



Materials Research in Microgravity 2012

R. Hyers, Editor

University of Massachusetts, Amherst, Massachusetts

V. Bojarevis, Editor

University of Greenwich, London, United Kingdom

J. Downey, Editor

Marshall Space Flight Center, Huntsville, Alabama

H. Henein, Editor

University of Alberta, Edmonton, Alberta, Canada

D. Matson, Editor

Tufts University, Medford, Massachusetts

A. Seidel, Editor

EADS Astrium, Friedrichshafen, Germany

D. Voss, Editor

ESA-ESTEC, Noordwijk, The Netherlands

M. SanSoucie, Compiler

Marshall Space Flight Center, Huntsville, Alabama

Proceedings of a symposium held at the
141st TMS 2012 Annual Meeting and Exhibition,
Orlando, Florida, March 11–15, 2012

The NASA STI Program...in Profile

Since its founding, NASA has been dedicated to the advancement of aeronautics and space science. The NASA Scientific and Technical Information (STI) Program Office plays a key part in helping NASA maintain this important role.

The NASA STI Program Office is operated by Langley Research Center, the lead center for NASA's scientific and technical information. The NASA STI Program Office provides access to the NASA STI Database, the largest collection of aeronautical and space science STI in the world. The Program Office is also NASA's institutional mechanism for disseminating the results of its research and development activities. These results are published by NASA in the NASA STI Report Series, which includes the following report types:

- **TECHNICAL PUBLICATION.** Reports of completed research or a major significant phase of research that present the results of NASA programs and include extensive data or theoretical analysis. Includes compilations of significant scientific and technical data and information deemed to be of continuing reference value. NASA's counterpart of peer-reviewed formal professional papers but has less stringent limitations on manuscript length and extent of graphic presentations.
- **TECHNICAL MEMORANDUM.** Scientific and technical findings that are preliminary or of specialized interest, e.g., quick release reports, working papers, and bibliographies that contain minimal annotation. Does not contain extensive analysis.
- **CONTRACTOR REPORT.** Scientific and technical findings by NASA-sponsored contractors and grantees.

- **CONFERENCE PUBLICATION.** Collected papers from scientific and technical conferences, symposia, seminars, or other meetings sponsored or cosponsored by NASA.
- **SPECIAL PUBLICATION.** Scientific, technical, or historical information from NASA programs, projects, and mission, often concerned with subjects having substantial public interest.
- **TECHNICAL TRANSLATION.** English-language translations of foreign scientific and technical material pertinent to NASA's mission.

Specialized services that complement the STI Program Office's diverse offerings include creating custom thesauri, building customized databases, organizing and publishing research results...even providing videos.

For more information about the NASA STI Program Office, see the following:

- Access the NASA STI program home page at <http://www.sti.nasa.gov>
- E-mail your question via the Internet to help@sti.nasa.gov
- Fax your question to the NASA STI Help Desk at 443-757-5803
- Phone the NASA STI Help Desk at 443-757-5802
- Write to:
NASA STI Help Desk
NASA Center for AeroSpace Information
7115 Standard Drive
Hanover, MD 21076-1320



Materials Research in Microgravity 2012

R. Hyers, Editor

University of Massachusetts, Amherst, Massachusetts

V. Bojarevis, Editor

University of Greenwich, London, United Kingdom

J. Downey, Editor

Marshall Space Flight Center, Huntsville, Alabama

H. Henein, Editor

University of Alberta, Edmonton, Alberta, Canada

D. Matson, Editor

Tufts University, Medford, Massachusetts

A. Seidel, Editor

EADS Astrium, Friedrichshafen, Germany

D. Voss, Editor

ESA-ESTEC, Noordwijk, The Netherlands

M. SanSoucie, Compiler

Marshall Space Flight Center, Huntsville, Alabama

Proceedings of a symposium held at the
141st TMS 2012 Annual Meeting and Exhibition,
Orlando, Florida, March 11–15, 2012

National Aeronautics and
Space Administration

Marshall Space Flight Center • Huntsville, Alabama 35812

September 2012

Available from:

NASA Center for AeroSpace Information
7115 Standard Drive
Hanover, MD 21076-1320
443-757-5802

This report is also available in electronic form at
<<https://www2.sti.nasa.gov/login/wt/>>

TABLE OF CONTENTS

1. MATERIALS RESEARCH IN MICROGRAVITY: SESSION I	1
1.1 Materials Science Experiments Under Microgravity—A Review of History, Facilities, and Future Opportunities C. Stenzel	1
2. MATERIALS RESEARCH IN MICROGRAVITY: SESSION II	12
2.1 Studies of Thermophysical Properties of Metals and Semiconductors by Containerless Processing Under Microgravity A. Seidel • W. Soellner • C. Stenzel	12
2.2 Advanced Measurement Devices for the Microgravity Electromagnetic Levitation Facility EML J. Brillo • H. Fritze • G. Lohöfer • M. Schulz • C. Stenzel	21
2.3 Electrostatic Levitation Furnace for the ISS K. Murakami • N. Koshikawa • K. Shibasaki • T. Ishikawa • J. Okada • T. Takada • T. Arai • N. Fujino • Y. Yamaura	29
3. MATERIALS RESEARCH IN MICROGRAVITY: SESSION III	33
3.1 Liquid Structures and Physical Properties—Ground Based Studies for ISS Experiments K. Kelton • J. Bendert • N. Mauro	33
3.2 Thermophysical Properties Measurement of High-Temperature Liquids Under Microgravity Conditions in Controlled Atmospheric Conditions M. Watanabe • S. Ozawa • A. Mizuno • T. Hibiya • H. Kawauchi • K. Murai • S. Takahashi	41
3.3 Microstructure Formations in the Two-Phase Region of the Binary Peritectic Organic System TRIS-NPG J. Mogeritsch • A. Ludwig	48
4. MATERIALS RESEARCH IN MICROGRAVITY: SESSION IV	56
4.1 ISS—Experiments of Columnar-to-Equiaxed Transition in Solidification Processing L. Sturz • G. Zimmerman • C. Gandin • B. Billia • N. Mangelinck • H. Nguyen-Thi • D. Browne • W. Mirihanage • D. Voss • C. Beckermann • A. Karma	56

TABLE OF CONTENTS (Continued)

4.2	Liquid Droplet Dynamics in Gravity Compensating High Magnetic Field V. Bojarevics • S. Easter • K. Pericleous	63
4.3	Measurements of Dendritic Growth Velocities in Undercooled Melts of Pure Nickel Under Static Magnetic Fields J. Gao • Z. Zhang • Y. Zhang	72
5.	MATERIALS RESEARCH IN MICROGRAVITY: SESSION V	80
5.1	X-Ray Radiographic Observation of Directional Solidification Under Microgravity: XRMON-GF Experiments on MASER12 Sounding Rocket Mission G. Reinhart • H. Nguyen-Thi • A. Bogno • B. Billia • Y. Houltz • K. Löth • D. Voss • A. Verga • F. de Pascale • R. Mathiesen • G. Zimmermann.....	80
5.2	Innovative Video Diagnostic Equipment for Material Science G. Capuano • D. Titomanlio • W. Soellner • A. Seidel	88
5.3	Containerless Measurements of Density and Viscosity of Fe-Co Alloys J. Lee • P. Choufani • R. Bradshaw • R. Hyers • D. Matson	97
5.4	TEMHD Effects on Solidification Under Microgravity Conditions A. Kao • K. Pericleous	105
6.	MATERIALS RESEARCH IN MICROGRAVITY: SESSION VI	113
6.1	Multi-Scale Modeling of Liquid Phase Sintering Affected by Gravity: Preliminary Analysis E. Olevsky • R. German	113
6.2	Self-Assembly of Ni Nanoparticles in Aerosols Produced Thermally on Ground and Under Microgravity Conditions S. Lösch • D. Nolle • E. Goering • B. Günther	120
6.3	Crystallographic Stability of Metastable Phase Formed by Containerless Processing in REFeO ₃ (RE: Rare-Earth Element) K. Kuribayashi • M. Kumar	128
6.4	On-Line, Real-Time Diagnostics of a Single Fluid Atomization System P. Khatibi • A. Ilbagi • H. Henein	136
6.5	Electrodeposition of Metals in Microgravity Conditions K. Nishikawa • T. Homma • E. Chassaing • M. Rosso • Y. Fukunaka	144
6.6	Propagation Regime of Iron Dust Flames F. Tang • S. Goroshin • A. Higgins	157
7.	MATERIALS RESEARCH IN MICROGRAVITY: POSTER SESSION	163
7.1	Containerless Processing on ISS: Ground Support Program for EML A. Diefenbach • S. Schneider • R. Willnecker	163

TABLE OF CONTENTS (Continued)

7.2 High-Precision Temperature Control of a Crystal Growth Furnace at 1,500 °C C. Stenzel • A. Hess • A. Cröll • D. Bräuer • H. Sauermann	170
7.3 Investigation of Thermocapillary Convection of High Prandtl Number Fluid Under Microgravity R. Liang • G. Duan	177
7.4 Real Time In Situ Observations of Equiaxed Dendrite Coherency in Al-Cu Alloys Using High-Brilliance, 3rd Generation Synchrotron Sources A. Murphy • D. Browne • W. Mirihanage • R. Mathiesen	185
7.5 Truncated Dual-Cap Nucleation Site Development D. Matson • P. Sander	193

MATERIALS SCIENCE EXPERIMENTS UNDER MICROGRAVITY - A REVIEW OF HISTORY, FACILITIES, AND FUTURE OPPORTUNITIES

Ch. Stenzel¹,

¹Astrium GmbH, D-88090 Immenstaad

Keywords: Diffusion, solidification, crystal growth, levitation

Abstract

Materials science experiments have been a key issue already since the early days of research under microgravity conditions. A microgravity environment facilitates processing of metallic and semiconductor melts without buoyancy driven convection and sedimentation.

Hence, crystal growth of semiconductors, solidification of metallic alloys, and the measurement of thermo-physical parameters are the major applications in the field of materials science making use of these dedicated conditions in space. In the last three decades a large number of successful experiments have been performed, mainly in international collaborations. In parallel, the development of high-performance research facilities and the technological upgrade of diagnostic and stimuli elements have also contributed to providing optimum conditions to perform such experiments. A review of the history of materials science experiments in space focussing on the development of research facilities is given. Furthermore, current opportunities to perform such experiments onboard ISS are described and potential future options are outlined.

Introduction

A microgravity environment facilitates processing of fluids without buoyancy driven convection and sedimentation. Ideally, the absence of gravity-driven buoyancy convection features a purely diffusive transport; the absence of sedimentation leads to homogeneous particle distribution in mixtures. For materials science these effects are mainly relevant for experiments aiming at crystallisation of bulk materials from the fluid state (melt or vapour phase) and on the determination of thermo-physical parameters in the under-cooled regime.

Materials science experiments have been therefore a prominent topic, already since the early days of research under microgravity (μg) conditions. The first experiments under reduced gravity were reported during the fly-back phase of the Apollo 14 moon mission in 1971 [1]. A couple of demonstration experiments have been performed by the astronauts A. Shephard, S. Roosa, and E. Mitchell to experimentally assess the advantage of materials processing in space. Composite casting has been selected as one reference experiment for materials science. 11 different samples were melted and re-solidified in order to permit evaluation of the particle re-distribution. For example, it could be shown that a mixture out of paraffin, Be-Cu particles and Ar gas displayed a somewhat homogeneous distribution after re-solidification under μg conditions. Fig. 1 shows a photograph of the mixture after cool-down and the simple setup to perform this experiment.

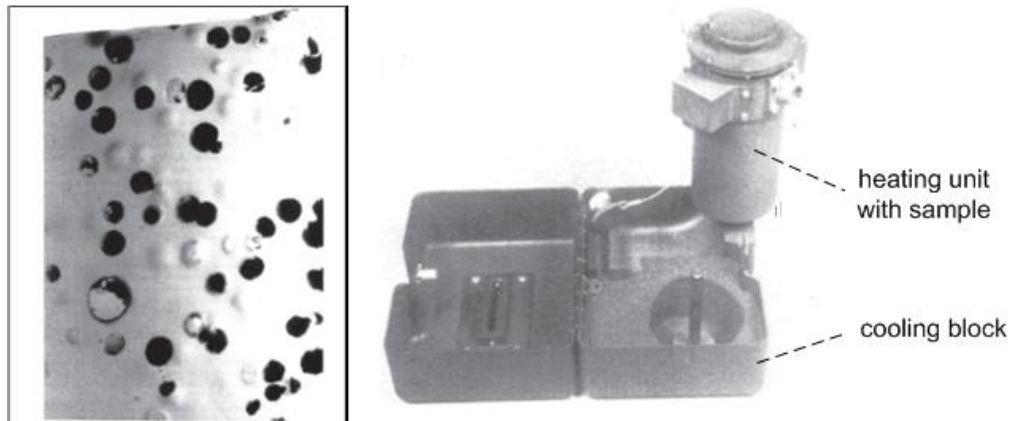


Figure 1. Composite casting experiment on Apollo 14. Left part: Re-solidified mixture out of paraffin, Be-Cu particles, and Ar gas bubbles; right part: Experimental apparatus

These experiments represented a pioneering work in terms of a first proof-of-principle and hence opened the door for a long series on investigations under space conditions on various carriers and missions, starting with Skylab, the Apollo/Soyuz mission, Spacelab, other shuttle experiments, sounding rockets, free flyers, and finally on space stations like Mir or ISS.

In this paper a review on the objectives, performance and results of high-lighted experiments in the main fields for materials science research is presented

- Crystal growth
- Solidification
- Diffusion processes
- Measurement of thermo-physical properties.

Furthermore key technology improvements which have lead to innovative scientific research are reported and finally an overview on currently available facilities, opportunities, and recognizable trends is given.

Materials Science Experiments

During the last three decades the general objectives that materials science experiment in space have thus been focussed

- To understand fundamental mechanism and processes
- To validate numerical models
- To provide benchmark data for industrially important materials
- To measure accurately thermo-physical properties which can not easily reached on earth.

In the following sections the different areas of materials science are reviewed and the results of high-lighted experiments are described.

Crystal growth

Crystal growth of single-crystalline materials from the liquid and gas phase as well is performed very close to the thermodynamic equilibrium, i. e., with very low growth rates and having a flat or only smoothly curved solid/liquid interface. Hence, these processes are rather sensitive to small perturbations of all kinds, maybe caused by short-term fluctuations in the temperature field of the furnace, variations in the ganging of the mechanical drive of the heater or sample, or by different types of time-dependent convective flows in the melt [2]. The first two issues must be addressed by the design and performance of the facility, processing under μg conditions could help to reduce the latter one.

In the early days the main target for crystal growth experiments in space - especially for semiconductors - was the improvement of material quality caused by the absence of buoyancy effects. The first experimental results however, were quite disillusioning: A. Eyer et al. discovered during the float-zone growth of Si that Marangoni convection is the dominant factor in the melt flow, more than outbalancing the absence of buoyancy-driven convective motions [3]. In a comprehensive survey K. W. Benz has described the consequences drawn by the community from Eyer's early experiment and the resulting metamorphosis of objectives for semiconductor crystal growth in space [4]. The most striking results for performing crystal growth experiments under reduced gravity conditions which have been obtained so far are summarised below:

- To attain larger diameter for float-zone crystals [5]
- To measure Marangoni numbers without overlaying buoyancy flows [6, 7]
- To study the influence of soluto-capillary flow [8, 9]

- To study the influence of fluid flow stimuli like magnetic fields or mechanical vibrations [10, 11, 12]
- To allow for numerical calculations under well-defined conditions [13]
- To study detached solidification [14]

As example the float zone growth of Ga-Sb [5] which yielded a significant reduction of striations in the space grown crystal compared to its earth-grown counterpart, is illustrated in Fig. 2.

These investigations were also fostered by a steady improvement in the technical capabilities of the respective facilities. For example, mirror furnaces were the working horses in the early days on S/L, sounding rocket, and EURECA missions. They were robust, easy to operate, and allow for a direct optical control of the solid/liquid [15]. But the thermal profile was fixed and the temperature gradient at the S/L IF could not be adjusted. Nowadays multi-zone furnaces built up by several individual heaters with a high-stability temperature control system are available onboard ISS. With these furnaces the thermal gradient at the phase boundary can be adjusted over a wide range, and perform various types of experiments can be performed [16, 17]. Furthermore, in order to suppress stochastic flows which are caused by residual accelerations, the implementation of magnet systems inducing a well-defined flow in the melt into these new facilities has been pursued in the last decade. First experiments performed on sounding rocket missions revealed indeed that the melt flow can be substantially affected by a rotating magnetic field [18] in microgravity, thus providing ideal reference cases for testing and improving numerical models on the melt flow.

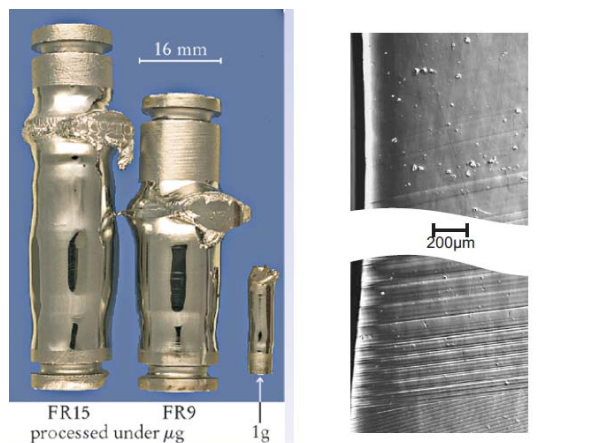


Figure 2. Crystal growth of GaSb on Spacehab-4 mission. Left part: Size comparison between earth grown and μg crystals. The right part illustrates the significantly reduced micro-segregation under μg (less striations in upper photograph)

Actually, two major experiments from field of the crystal growth are envisaged for the ISS: RDGS and SISSY. The first one is targeted to determine the effects of “detached” Bridgman growth in comparison to regular Bridgman growth and float-zone (FZ) growth on the defect formation and distribution in Ge-Si crystals [19]. The international cooperation SISSI aims at

investigating the gravitational effects on heat and mass transport phenomena in directional solidification of upgraded metallurgical silicon for photovoltaic applications [20].

Solidification

One key aspect of the solidification that influences the microstructure is the shape of the solid-liquid interface in a solidifying material. At low growth rates the interface is planar like for semiconductors. Industrially relevant metallic materials crystallise at much higher growth rates. As the rate of growth increases, the interface develops a corrugated texture until three dimensional cells form in the solid. Even higher growth rates cause the formation of dendrites. The development of these different interface shapes and the transition from one shape to another is controlled by the morphological stability of the interface. Gravity represents one of the most influencing factors to this stability. In particular, buoyancy-driven convection can influence the stability and, thus, the shape of the solidifying interface. Hence, processing under reduced gravity imposes therefore well-defined conditions for crystallisation. Thus, the results obtained so far from microgravity experiments about the conditions under which certain types of solidification boundaries appear could help to explain the formation of the crystalline structure of a material, to validate numerical models, and to improve terrestrial applications [21].

In the recent decades the subsequently listed most striking results have been obtained in microgravity experiments:

- Study of morphological stability in immiscible systems [22]
- Processing of eutectics [23]
- Melt interface stability studied by Seebeck coefficient variation [24]
- Dispersed systems [25]

In addition to the mentioned issues dendritic growth is the common mode of solidification applied for metals and alloys under low thermal gradients. The growth of dendrites in pure melts depends on the transport of latent heat from the moving crystal–melt interface and the influence of weaker effects like the interfacial energy. Experimental data for critical tests of dendritic growth theories remained limited because dendritic growth can be complicated by convection. A fundamental understanding of dendritic solidification is necessary to correct mathematical models that will provide a basis for improved industrial production techniques. Prof. M. Glicksman and his research team have performed a series of pioneering and quite successful experiments on the mechanisms of dendrite formation by eliminating buoyancy-induced convection in the Isothermal Dendritic Growth Experiment (IDGE). This facility has been flown three times as part of the United States Microgravity Payload (USMP) series. During the first two flights of IDGE on the shuttle, the IDGE flight hardware grew and photographed individual dendrites of the material succino-nitrile (SCN) as they solidified at various temperatures (see Fig. 3). The third flight of IDGE on USMP-4 has used a different sample material, pivalic acid. Dendrite growth velocities could be measured and the researchers were able to compare the results with theoretical predictions and to answer questions on fundamental characteristics on dendrite growth [26, 27, 28].

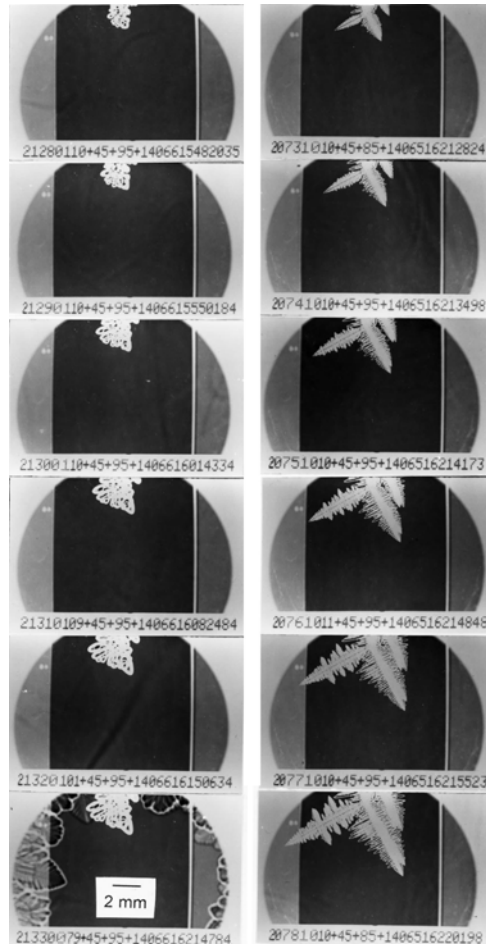


Figure 3. Example of two image sequences of dendritic growth for SCN at two supercoolings: Left: 0.1 K (photographs taken every 700 s); right: 1 K (photos every 6.75 s)

The modular experimental facility MSL (Materials Science Laboratory) [16] which is implemented in the US-module destiny of the ISS is successfully being operated since 2009. It enables in its current condition to perform investigations on

- Columnar to Equiaxed Transition in Solidification Processing (CETSOL) [29]
- Microstructure Formation in Casting of Technical Alloys under Diffusive and Magnetically Controlled Convective Conditions (MICAST) [30]
- Solidification Along A Eutectic Path in Ternary Alloys (SETA) [31]

In the near future it is considered to develop an MSL insert for in-situ diagnostic of dendritic growth by radiography [32].

Diffusion

The determination of diffusion constants in liquids allows for validating theoretical models on diffusive transport phenomena at one side. Furthermore, if a purely diffusion-controlled flow regime is established under μg conditions the exact knowledge of the diffusion constants is essential for modelling the fluid flow in the melt during crystal growth and solidification processes.

Under terrestrial conditions the measurement of diffusion constants in the liquid state is always overlaid by gravity-driven convective flows. For this reason the measurement of diffusion constants was already one of the major topics for performing experiments under microgravity conditions in the early years. The first measurements of diffusion constants were performed during S/L missions or on the MIR station using the long-capillary (LC) technique [33-35]. For single-component systems the experiments indeed disclosed much lower values for the diffusion constants than obtained in earth-bound experiments [33]. This technique, however, leads for multi-component systems to segregation effects resulting in an additional mass transport which give rise to a systematic measurement error. This drawback can be overcome by a stable density layering of the sample materials. Thereby the density has to increase parallel to the gravity vector resulting in a density gradient corresponding to the concentration gradient.

By the implementation of the shear-cell technique other drawbacks (free surface convection, diffusion during heat-up and cool-down) of the LC technique can be avoided: A rapid partitioning the sample material into several small volumes after processing but before cool-down by means of a dedicated mechanical mechanism leads to a quasi-frozen concentration distribution for off-line analysis. On the un-manned FOTON-12 mission pioneering measurements of diffusion constants employing the shear-cell technique up to a temperature of 1200°C have been successfully carried out [36, 37]. The diffusion constants of several multi-component systems have been successfully measured on the FOTON-M2 mission in 2005 [38].

A further innovation has moved in the field during the recent years, the in-situ determination of diffusion profiles via radiography. DLR has initiated the development of the DIXI heater insert for the MSL facility onboard ISS. This facility would allow performing in-situ diagnostics for high-temperature diffusion experiments as illustrated in Fig. 4 [32].

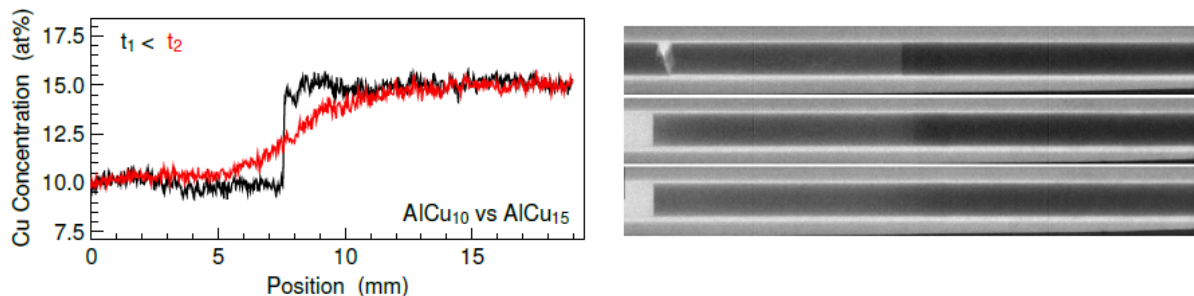


Figure 4. The concentration profiles of a Al-Cu alloys can be deduced from the grey values of an in-situ radiographic image (right) in the DIXI facility on ground [32]

The measurement of diffusion constants of self-diffusion in elements like Si and of multi-component systems where no stable density layering can be established (Si-Ge) represents the actual trends for future experiments. Today, all the envisaged experiments on the ISS from European- or Japanese-coordinated research groups favour the combination of the shear-cell technique with in-situ radiography.

Levitation techniques

Experiments on crystal growth and solidification are generally bound to a crucible containing the sample material. The crucible is integrated into a cartridge if a closed containment to the process environment has to be provided. This design affects the measurement of surface-sensitive properties like viscosity and surface tension and prevents to reach significant undercooling of the liquid sample as well. Furthermore, the chemical compatibility between the crucible and sample material at elevated temperatures imposes often severe problems leading in the worst case to a complete exclusion from processing for rather critical metals than Ti where no appropriate high-temperature resistant crucible materials is available.

To overcome these obstacles levitation methods have been established into materials science research facilities. Two main techniques have been successfully applied in the past:

- Electrostatic levitation
- Electromagnetic levitation

In electrostatic levitators the sample is electrically charged, levitated in a static electric field, and heated by a laser. This enables to process preferably non-metallic elements and oxide materials. Both, JAXA and NASA are fostering the development and operation of an *Electrostatic Levitator (ESL)* on ground for a potential later implementation on the ISS [39, 40].

Electromagnetic levitation allows processing of electrically conductive samples including pure metals, alloys and semiconductors. The sample is thereby placed in the center of a coil system which is part of an oscillating RF circuit and generates an RF electromagnetic field. The interaction of eddy currents induced in the sample with the electromagnetic field leads to a positioning of the sample at the center of the coil system. Heating is achieved by ohmic losses of the eddy currents flowing in the sample [41, 42].

For ground-based experiment strong levitation fields are needed for both techniques in order to counteract gravity. This leads to a number of drawbacks like large power consumption, difficult control of sample positioning, convective flows in the melt, and a deformed geometrical sample shape. These drawbacks can be eliminated if levitation is performed under microgravity conditions where only small levitation forces are required to compensate for the residual accelerations. Moreover, convective flows are significantly reduced and the sample shape is nearly spherical.

Electromagnetic levitation experiments in space have already a long-lasting successful history: The DLR facility TEMPUS (see Fig. 5) was operated on three Spacelab missions (IML-2 in 1994, MSL-1 and MSL-1R in 1997) and provided a wealth of scientific data [41, 43].

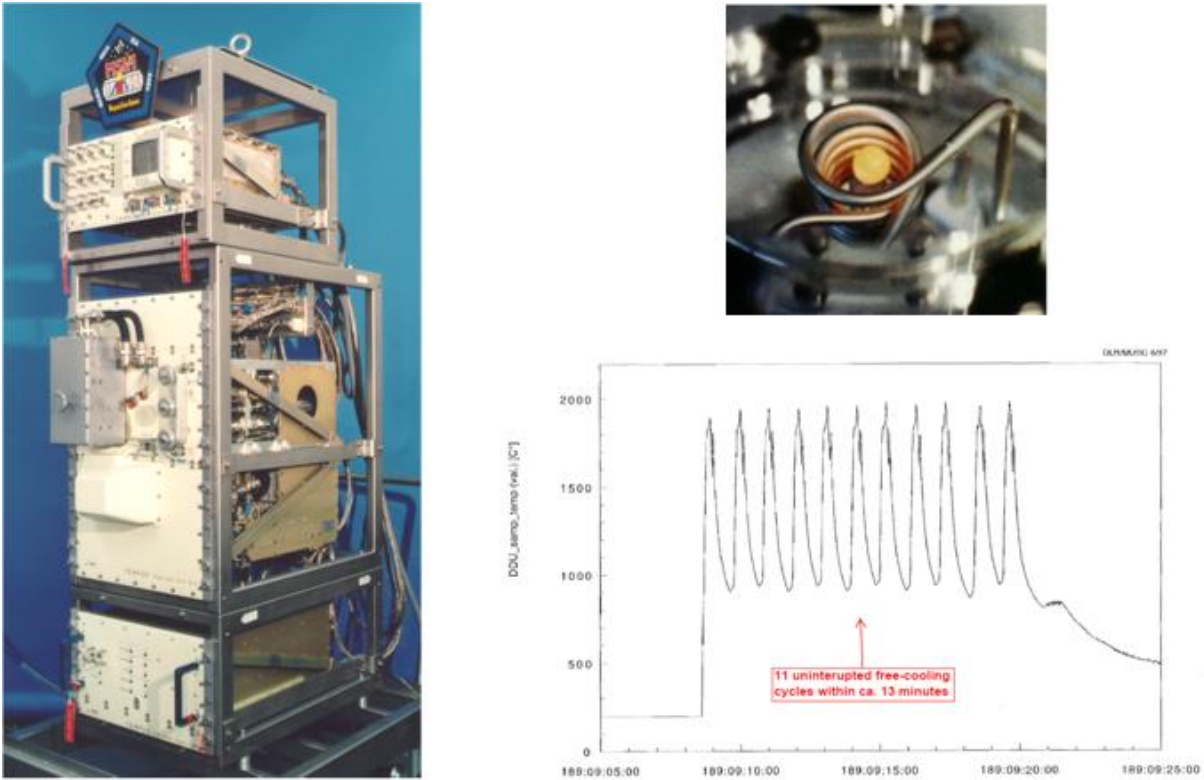


Figure 5: TEMPUS facility (left). In the upper right part the levitated molten sample is shown, the lower right part displays the undercooling of a levitated Zr sample as measured during the MSL-1 (see [44]).

One of the prominent scientific topics of these missions was the investigation on the kinetics of solid nucleation in Zr. Bayuzick and co-workers could perform 122 cycles of undercooling with a $\Delta T=333^{\circ}\text{C}$ below the nominal solidification temperature and could study the influence of fluid flow regimes on the nucleation kinetics via variation of the cooling rate [44].

Compared to crystal growth or solidification experiments the duration of a levitation run is short and the sample can be re-processed several times enabling to perform systematic investigations even on one single mission. For the purpose of extending the experimental capabilities even further, currently the ISS version of this facility the *Electromagnetic Levitator (EML)* is being developed and will be operational in space from 2014 [42].

In addition to the performed Spacelab experiments a number of campaigns have been conducted on sounding rockets and on parabolic flights as well in the recent decades. This makes electromagnetic levitation the most prevalent technique for materials science investigations in space.

Outlook

Microgravity has to be regarded as tool which can be employed to provide dedicated experimental conditions like the application of external fields or forces does. In all relevant research areas of materials science it could be shown that a microgravity environment is advantageous for the investigation of specific subjects. Numerous distinguished experiments have been performed and were well received within the science community. The character of these results, however, can be portrayed in most cases as proof-of-principle or benchmarks. Due to the lack of continuous experiment opportunities so far and also due to the long duration of experiments mainly single-shot experiments have been conducted - experiments using electromagnetic levitation being an exception here because of the reasons mentioned above.

The next coherent step in this context would be to convert the nature of material science research from primarily benchmarking to a more systematic research. Utilization of the ISS offers exactly this perspective and gives the unique possibility to initiate and perform intense research programs embedded in international frameworks especially if emphasizing the extended utilization period up to 2020. The facilities to perform the above described class of experiments are either already implemented (MSL, GHF, DECLIC), in preparation (EML), planned (ESL, TRANSPARENT ALLOYS), or addressed in several outstanding science proposals and consequently envisaged by the Agencies. The extended capabilities leave certainly much room for an extension of the science community resulting in a higher science output.

References

- [1] R. J. Sharpe, M. D. Wright, "*Analysis of Microgravity Experiments Conducted on the Appollo Spacecraft*", NASA/TM-2009-215905
- [2] Müller, G., *Convection and Inhomogeneities in Crystal Growth from the Melt*, in: *Crystal Growth, Properties and Applications*, Vol. 3, III-V Semiconductors, Springer-Verlag, Berlin, Heidelberg, New York, 1980
- [3] A. Eyer, H. Leiste, R. Nitsche, Proceedings of the Fifth European Symposium on Materials Science and Microgravity, ESA-SP222, Schloß Elmnau, 1984, p. 173
- [4] K. W. Benz, P. Dold, J. Cryst. Growth **237-239**, 2002, p. 1638-1645
- [5] A. Cröll, T. Kaiser et al., J. Cryst. Growth **191**, 1998, p. 365
- [6] A. Cröll, W. Müller-Sebert et al., Microgravity Sci. Technol. **III/4**, 1991, p. 204
- [7] G. Müller, R. Rupp, Cryst. Properties Prep., **35**, 1991, p.138
- [8] P. Tison, D. Camel et al., Proceedings of the First International Symposium on Hydromechanics and Heat/Mass Transfer in Microgravity, Perm/Moscow, 1991. p. 121
- [9] K. Arafune, A. Hirata, J. Cryst. Growth **197**, 1999, p. 811
- [10] F. M. Herrmann, J. Baumgartl et al., Proceedings of the VIIIth European Symposium on Materials and Fluid Sciences in Microgravity, ESA SP-333, Brussels, 1992, p. 57
- [11] F. R. Szofran, K. W. Benz et al., NASA Microgravity Materials Science Conference, NASA/CP-1999-209092, Huntsville, AL, 1998, p. 617
- [12] A. Cröll, F. R. Szofran et al., J. Cryst. Growth **183**, 1998, p. 554
- [13] T. Kaiser, A. Cröll et al., Proceedings of the Second European Symposium: Fluids in Space, Napoli, 1996, p. 245

- [14] L. L. Regel, W. R. Wilcox, 1998, *Microgravity Sci. Technol.* **14**, 1999, p.152
- [15] H. Lenski, *Microgravity Quarterly* **1**, 1990, p. 47
- [16] H. Lenski et al., *Proceedings of the 4th International Symposium on Physical Sciences in Space*, Bad Godesberg, 2011
- [17] A. Hess, A. Cröll et al., *Floating Zone Furnace with Rotating Magnetic Field*. Poster Presentation DGKK, 2010
- [18] P. Dold, A. Cröll et al., *J. Cryst. Growth* **231**, 2001, p. 95
- [19] M. P. Volz, A. Cröll, RDGS, <http://issresearchproject.nasa.gov/MSFC/RDGS/index.php>
- [20] SISSI project, AO-2009/ILSRA-09 Results and Selection, ESA/PB-HME/EUB(2010)28, May 2010
- [21] B. K. Dhindaw, *Sadhana*, Vol. 26, Parts 1&2, 2001, p. 59
- [22] J. B. Andrews, A. C. Sandlin et al., *Advances in Space research* **11**, 1991, p. 291
- [23] D. J. Larson, *NASA Conference Publication* 3342, 1996, p. 337
- [24] G. Cambon, G. Cadet et al., *Acta Astronautica* **17**, Issues 11-12, 1988, p. 1229
- [25] F. R. Juretzko, B. K. Dhindaw et al., *Met. Trans. A29*, 1997, p. 1691
- [26] M. E. Glicksman, M. B. Koss et al., *Phys. Rev. Lett.* **73**, 1994, p.573
- [27] J. C. LaCombe, M. B. Koss et al., *Phys. Rev. Lett.* **83**, 1999, p. 2997
- [28] M. B. Koss, J. C. LaCombe et al., *Metallurgical and Materials Transactions A*, **30A**, 1999, p. 3177
- [29] <http://www.spaceflight.esa.int/users/materials/research/solid/cetsol/cetsol.html>
- [30] <http://www.spaceflight.esa.int/users/materials/research/solid/micast/micast.html>
- [31] <http://www.spaceflight.esa.int/users/materials/research/solid/seta/seta.html>
- [32] F. Kargl, M. Balter et al., *Proceedings of the 4th International Symposium on Physical Sciences in Space*, Bad Godesberg, 2011
- [33] Y. Malmejac, G. Frohberg, in: *Fluid Science and Materials Science in Space*, Springer, 1987, p. 159-190
- [34] G. Frohberg, *Diffusion in solids: Scientific results of the German Spacelab mission D-2*, WPF/DLR, 1995, p. 275-287
- [35] R.W. Smith, *Microgravity Sci. Technol.* XI (2) 78-84 (1998)
- [36] T. Masaki, T. Fukuzawa et al., *Meas. Sci. Technol.* **16**, 2005, p. 327-335
- [37] A. Griesche, K.-H. Kraatz et al., *Proceed. First Intern. Symp. on Microgr. Res. and Appl. in Phys. Scienc.*, ESA-SP-454, 2000, p. 985
- [38] S. Suzuki, K.-H. Kraatz, G. Frohberg, *Micrograv. Sci. and Technol.* **16-1**, 2005, p. 120-126 and **18(3/4)**, 2006, p. 82
- [39] A. J. Rulison, J. L. Watkins, B. Zambrano, *Rev. Scient. Instrum.*, **68**, 1997, p. 2856
- [40] T. Ishikawa, J. T. Okada et al., ISSN 1349-1113, JAXA-RR-08-003E2009 ESL-JAXA
- [41] R. Knauf et al., *Containerless Processing Facility TEMPUS for Materials Science Research onboard Spacelab: 6th International Symposium on Experimental Methods for Microgravity Material Science (San Francisco)*, 1994
- [42] W. Soellner, A. Seidel et al., *J. Jpn. Soc. Microgravity Appl.* 27 No. 4, 2010, p. 183
- [43] Team TEMPUS, in: *Materials and Fluids under low gravity*, L. Ratke H. Walter, B. Feuerbacher, Springer-Verlag, Berlin, Heidelberg, New York, 1996
- [44] W. Hofmeister, J. Rogers, N. Singh, S. Marsh, P. Vorhees, eds., *Solidification 1999*, 1999, Warrendale, TMS

Studies of Thermophysical Properties of Metals and Semiconductors by Containerless Processing under Microgravity

A. Seidel, W. Soellner, C. Stenzel
Astrium Space Transportation
Claude Dornier Strasse, Immenstaad, 88090, GERMANY

Keywords: Electromagnetic Levitation, Microgravity, Materials Science, Thermophysical Properties

Abstract

Electromagnetic levitation under microgravity provides unique opportunities for the investigation of liquid metals, alloys and semiconductors, both above and below their melting temperatures, with minimized disturbances of the sample under investigation. The opportunity to perform such experiments will soon be available on the ISS with the EML payload which is currently being integrated. With its high-performance diagnostics systems EML allows to measure various physical properties such as heat capacity, enthalpy of fusion, viscosity, surface tension, thermal expansion coefficient, and electrical conductivity. In studies of nucleation and solidification phenomena the nucleation kinetics, phase selection, and solidification velocity can be determined. Advanced measurement capabilities currently being studied include the measurement and control of the residual oxygen content of the process atmosphere and a complementary inductive technique to measure thermophysical properties.

Introduction

Electromagnetic levitation provides unique opportunities for the investigation of electrically conductive liquid metals, alloys and semiconductors (if pre-heated or doped), both above and below their melting temperatures. In particular, the undercooled regime where the sample is liquid at temperatures below its equilibrium melting temperature is accessible through electromagnetic levitation thus allowing the determination of thermo-physical properties of materials in this particular state as well as studying of nucleation and solidification phenomena. Thermo-physical properties that can be measured comprise heat capacity, enthalpy of fusion, thermal transport coefficients in the liquid phase, viscosity, surface tension, thermal expansion coefficient, hemispherical emissivity, fraction solid and electrical conductivity. In studies of nucleation and solidification phenomena the nucleation kinetics and solidification velocity can be determined. [1], [2]

Ingredients

In order to prepare the undercooled state and to perform experiments aiming at the determination of the thermo-physical properties without adverse impacts related to chemical reactions, heterogeneous nucleation, or lack of visibility, the following ingredients are essential:

2.1. Electromagnetic levitation

Electromagnetic levitation allows processing of the samples without contact to a container. A wide range of electrically conductive samples including pure metals, alloys and semiconductors can be processed with this technique. The sample is placed in the center of a coil system which is part of an oscillating RF circuit and generates an RF electromagnetic field. The interaction of eddy currents induced in the sample with the electromagnetic field leads to a displacement force which keeps the sample at the center of the coil system. Heating is achieved by ohmic losses of the eddy currents flowing in the sample. In ground-based experiments the required levitation force and therefore electromagnetic field strength to counteract gravity is so large that many materials are melted just by applying the field to position them. Heating and positioning of the

sample are therefore not independent and the undercooled regime of samples with low melting temperatures is not accessible. Furthermore, the electromagnetic pressure exerted by the strong fields leads to strong convection and a deformation of the liquid samples which are not compatible with many experiment objectives such as the determination of viscosity and surface tension. The need for lower electromagnetic field strengths thus becomes evident which means that gravity has to be largely eliminated in order to perform experiments with undisturbed samples over a wide temperature range [4-8].

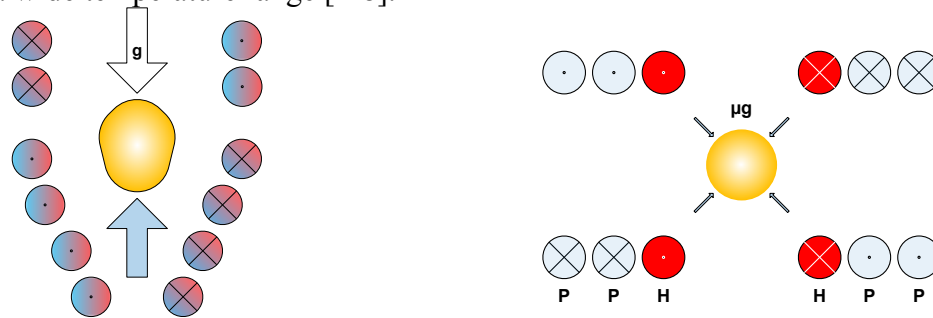


Figure 1. Principle design of levitation coils for levitation under $1g$ (left) and μg (right). In a $1g$ levitation coil the positioning force has to counteract gravity, therefore strong electromagnetic fields are needed just for the positioning of the sample, which leads to a strong heating and deformation of the sample (left). In contrast, the forces required to position a sample in a μg environment are orders of magnitude smaller, therefore the heating and deformation of the sample due the positioning field are negligible. As a consequence, heating and positioning of the sample can be controlled largely independently, e.g. by using dedicated coils for heating and positioning, respectively (right). Note that this illustrative sketch does not show the current EML flight coil geometry.

2.2. Ultraclean process environment:

In order to reduce the potential for heterogeneous nucleation as much as possible an ultra-high vacuum or ultra-pure noble gas process atmosphere is necessary. In particular, the amounts of reactive trace gases, like for example oxygen, need to be minimized.

2.3. Contactless diagnostics

The diagnostic instruments have to be compatible with the containerless processing principle as well, such as pyrometers for measurement of the sample temperature and various dedicated video cameras for specific purposes, e.g. cameras with high spatial or temporal resolution.

2.4. Sample handling

Even though the samples are processed without contact to a container wall they need to be carefully prepared and handled during the experiment. Typical experimental set-ups provide the possibility to store several samples, to select a dedicated sample for processing and to transfer the selected sample into the coil. Therefore, the samples are placed in so-called sample holders made of chemically inert thermal shock resistant material which are connected to a transfer mechanism and provide enough free space for the sample such that the containerless principle is respected during processing.

3. Undercooling at Work

Driven by the size of the RF coils which are optimized for positioning and heating efficiency under microgravity the samples are spherical with diameters typically ranging from 5 to 8 mm. The process environment for the samples is either UHV or ultra pure noble gas (He or Ar) up to 400 mbar.

A typical experiment consists of several melt cycles. Starting from the solid state the sample is heated up above the melting temperature (overheating of up to 300 K), and then the heater power into the sample is reduced. During the subsequent cooling phase, the majority of the experimental data are gathered. Depending on its properties the sample undercools to temperatures below the melting temperature until solidification sets in rapidly and the heat of fusion is released in a very short time such that the sample temperature rises again to the melting temperature, a phenomenon known as recalescence. During the following cool down of the solid sample the cooling rate can be enhanced by additional convective cooling with the process gas being circulated through a pipe and filter system and released through a nozzle at the sample's vicinity. A typical melt cycle is shown in figure 2.

Due to the small size and related low heat content of the sample the typical duration of a melt cycle is in the order of seconds to minutes, depending on the sample material and the definition of the process, such that many such melt cycles can be performed during a the time frame available for an on-orbit experiment which is in the order of hours.

At high temperatures samples processed in ultra-high vacuum may evaporate some material which leads to a deposition of evaporated material on the inner surfaces of the experiment set-up in a physical vapor deposition process. Components and assemblies in the vacuum chamber that are sensitive to deposition of evaporated sample material like the components of the optical path from the sample to the pyrometer and video cameras have to be protected from deposition by e.g. exchangeable double mirror systems. If samples are processed in a noble gas atmosphere the evaporated material does coagulate into microscopic dust particles which are toxic and need to be removed from the experiment setup by a dedicated gas cleaning system.

After processing samples can be retrieved from the facility and returned to ground for further evaluation.

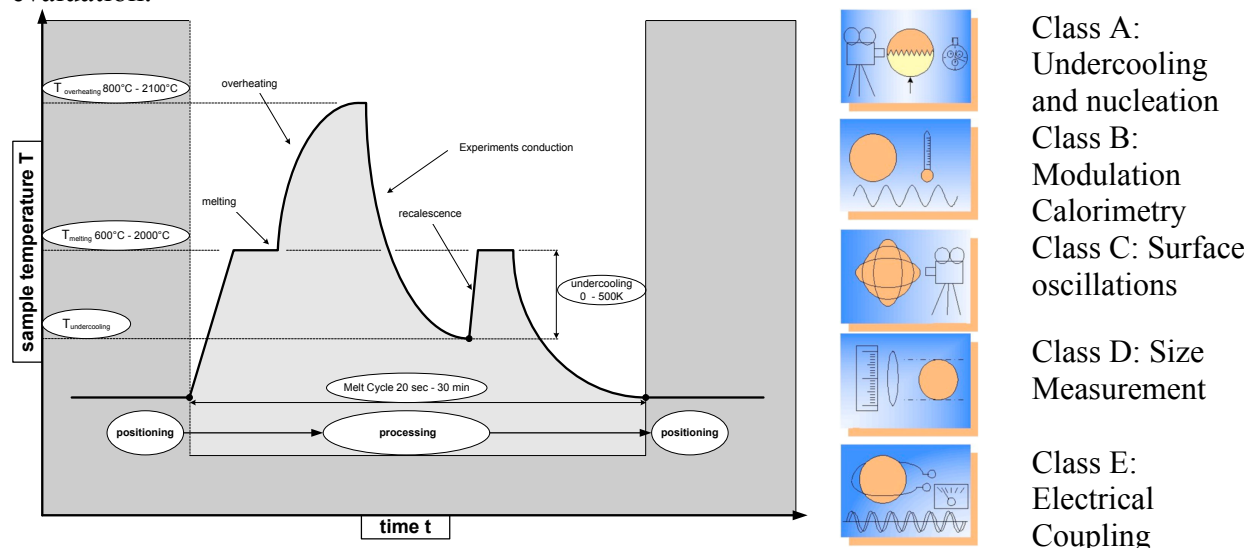


Figure 2. Principle sketch of the temperature-time profile of a typical melt cycle in the EML facility. Experiments are typically performed on the cooling flank when the sample is in the liquid state. Experiments in 5 different classes can be performed with EML, these classes are schematically introduced on the right side of the figure, and explained in detail in the text below.

4. EML on ISS: Experiment Classes and Measurement Capabilities

Based on a long and successful heritage of electromagnetic levitation facilities on various carriers and missions, the electromagnetic levitation facility EML for the International Space Station ISS is currently being developed by Astrium under contracts to ESA and DLR. A comprehensive discussion of the performance and design features of EML is provided in [8].

4.1. Experiment Class A: Undercooling and nucleation

The scientific objectives for this experiment are to:

1. measure solidification front speed
2. perform nucleation statistics (maximum undercooling)
3. study morphology and phase selection depending on undercooling and induced fluid flow [9]

An experiment of class A type is being executed as follows: The molten sample will be cooled by turning off the heater, whereas the cooling rate may be enhanced by dedicated convective cooling per adjustable gas flow. Recalescence may occur either spontaneously or it can be triggered by touching the undercooled sample with a custom-made trigger needle at a predefined undercooling temperature. The recalescence of the undercooled sample is detected automatically by an algorithm that detects the sudden increase of the pyrometer signal upon recalescence. A high-speed video camera is used to observe the sample from a direction perpendicular to the trigger needle such that the nucleation front passing from the nucleation point (trigger needle tip) across the surface of the sample can be observed. Once recalescence has been detected the high-speed video acquisition is stopped. Pre- and post-event storage of video data is facilitated by the use of a ring memory for the video data. See also the first pictogram in figure 2.

Typical duration of one melt cycle is in the range of 30-60 seconds. The temperature is recorded with a frequency of 100 Hz; video images are taken with up to 30.000 frames/s @ 256x256 pixel spatial resolution. An example of high-speed video recording is shown in figure 3.

The following equipment is needed for the execution of a class A experiment:

- high-speed and high resolution camera to resolve solidification process, this includes high digitalization of the camera chip to support good thermal resolution of the phases solidifying
- trigger needle to induce nucleation at desired temperatures of the undercooled liquid
- precision pyrometer

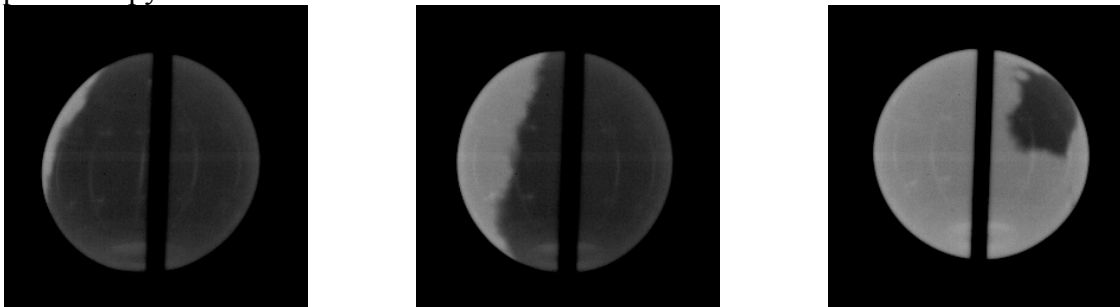


Figure 3. Class A Experiment: Sequence of a NiAl sample solidifying from the undercooled liquid captured by high-speed video camera @ 10.000 frames/s during parabolic flight. The total duration of the recalescence event was 29.1ms.

4.2. Experiment Class B: Modulation Calorimetry

The scientific objectives for this experiment class are to measure thermo-physical properties and if applicable their temperature dependence [10] such as:

1. heat capacity
2. enthalpy of fusion
3. total hemispherical emissivity
4. thermal transport coefficients
5. fraction solid

The class B experiment is carried out as follows: At a constant base temperature of the molten sample the heater power is modulated sinusoidally and the sample's temperature response is evaluated. The modulation can be repeated at different sample temperatures with different modulation frequencies in order to obtain several data points within one melt cycle. The typical duration of a melt cycle ranges from 10 to 20 minutes. The temperature data will be acquired with 100 Hz; furthermore input data of RF coil system (voltage, current) are needed.

The following equipment is mandatory to perform a class B experiment:

- high precision pyrometer
- calibrated modulated power input source (amplitude or power modulation is possible)

4.3. Experiment Class C: Surface Oscillations

The measurement of surface tension and viscosity and their temperature dependence are the main scientific objectives for these experiments.

The experiment starts with heating up the sample slightly above its melting point. During subsequent cooling of the molten sample a short heater pulse is applied which excites surface oscillations due to the dipole nature of the heating field, and the radial force of the field squeezing the sample. The surface oscillations are imaged by two video cameras in orthogonal views, as shown in figure 4. From the oscillating frequency the surface tension can be derived and from the oscillations decay the viscosity can be derived since this is the only damping mechanism involved for these oscillations. The temperature as well as the stimulus (pulse amplitude & shape) can be altered to achieve various measurement points during one melt cycle. For increasing viscosity the amplitude can be increased to observe a high enough oscillation signal. Instead of an excitation pulse also a frequency sweep can be applied to find the resonance frequency of the sample's surface oscillations. The typical duration of a melt cycle is in the range of 5-15 min.

The video images are usually taken with the radial camera @ 200 frames/s and 600x600 pixel spatial resolution and with axial camera @ 150 frames/s and 350x350 pixel spatial resolution. An example is shown in figure 4. The temperature is recorded with 100 Hz.

To perform a class C experiment the following equipment must be provided:

- fast and high resolution video cameras to resolve shape oscillations such that offline Fourier analysis on the sample diameter can be performed to derive the oscillation frequency and decay time
- high precision pyrometer
- free programmable power input source to apply either short pulses or a user defined signal shape as e.g. frequency sweep

4.4. Experiment Class D: Size Measurement

The scientific target for this class of experiments is to measure the thermal expansion coefficient and its temperature dependence. It is carried out as follows: The diameter of the solid and molten sample is precisely determined by the two video cameras in orthogonal view along the changing temperature of a melt cycle. For this purpose a high spatial resolution of the camera is necessary which will be even enhanced by a sub-pixel resolution algorithm which is applied to the video images off-line during evaluation. The algorithm requires the image of the sample's edge to be smeared out over a small number of camera pixels such that the algorithm can fit a 50% intensity value, as assumed sample edge, with a precision higher than the pixel resolution. The slightly blurred imaging of the sample's equator is achieved by setting the cameras focal plane slightly in front of it still achieving a sharp picture of the sample's surface. The typical duration of a melt cycle is in the range of 1-5 min. Video images captured by the axial camera are taken with typically 25 frames/s at up to 1000x1000 pixel resolution, whereas the radial camera offers

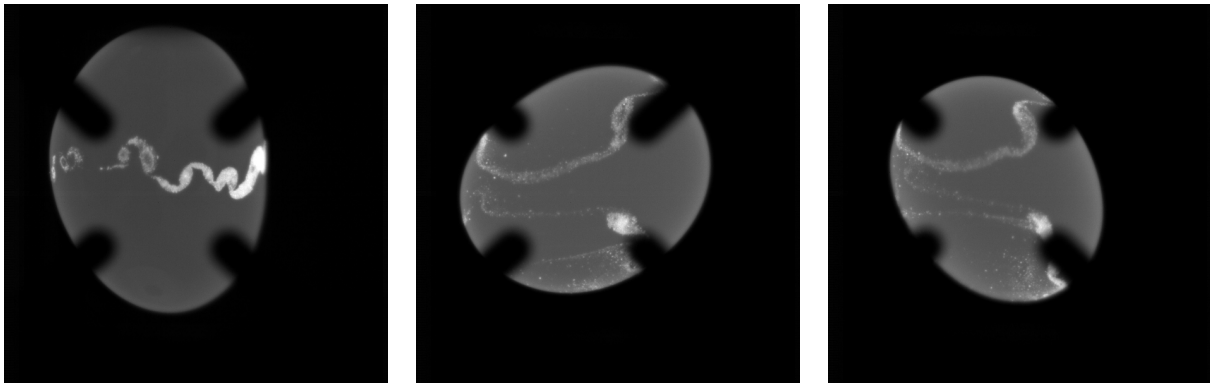


Figure 4. Class C experiment: Induced surface oscillations of a CuSnP sample (TEMPUS, 600x600x pixels @ 200 fps)

600x600 pixel spatial resolution. The selected frame rate depends on the temperature gradient and the desired temperature resolution of individual measurement points. The temperature data are recorded with 100 Hz.

The following equipment is needed for the execution of a class D experiment:

- high resolution video cameras to resolve sample diameter
- high precision pyrometer

4.5. Experiment Class E: Electrical coupling

The measurement of the electrical conductivity and its temperature dependence are the scientific targets for these investigations.

A class E experiment is carried out as follows: The electrical data of the RF oscillating circuit are used to derive the electrical conductivity of the sample since the sample itself is changing slightly the characteristics of the RF oscillating circuit by its inductance, which is determined by its geometry and electrical conductivity. Some calibration measurements on the empty coil have to be performed to distinguish between the coil's inductance and the one introduced by the sample. The relevant housekeeping data are measured by the levitation power supply which uses them mainly for internal control of the high RF power output. The basic resolution and accuracy can be further enhanced by using dedicated measurement equipment for this task- the so-called SCE which is described later.

The measurement can be performed together with other experiment classes since it requires only the high precision pyrometer as diagnostics, as all the other experiments too, and the RF oscillating circuit data which are part of the regular EML housekeeping data anyway. The acquisition frequency for the temperature data is 100 Hz, the RF oscillating circuit data (voltage, current, frequency) are recorded with 10 Hz.

5. Experiment preparation

Experiment preparation involves all aspects of transforming a scientific objective or idea into a fully developed flight experiment. Since EML provides a wide range of functions related to the definition of the sample processing including diagnostics, a deep understanding of the associated systems, their capabilities, functions, interrelations and constraints is needed in order to develop a successful flight experiment. Support to the scientists for the preparation of their experiments is given in the frame of the Ground Support Program GSP by a joint team consisting of Astrium and the DLR Microgravity User Support Center MUSC. Thereby the experience made in former TEMPUS missions is fully provided to the scientific community. A brief outline of the support tasks is given hereafter. The GSP is described in more detail in [12].

From the EML facility operation point of view the experiments are organized into melt cycles which in turn are decomposed into process steps. Each process step is characterized by a number of EML facility settings such as heater power, camera speed, etc. These settings are called Experiment Parameters or EP. In order to perform an experiment in the EML facility all EPs belonging to this experiment are needed since the EML facility is being operated using these parameters.

One of the major tasks of the GSP is therefore to translate an experiment idea into an EP set, a task that involves multiple steps and activities (see also figure 5), such as

- Definition of a rough outline of the experiment, in a so-called "science protocol"
- Characterization of sample properties relevant for processing in EML in a ground levitator
- Development of the Experiment Parameter (EP) set
- Verification of the EP set in a representative EML facility on ground
- Sample Integration and Launch

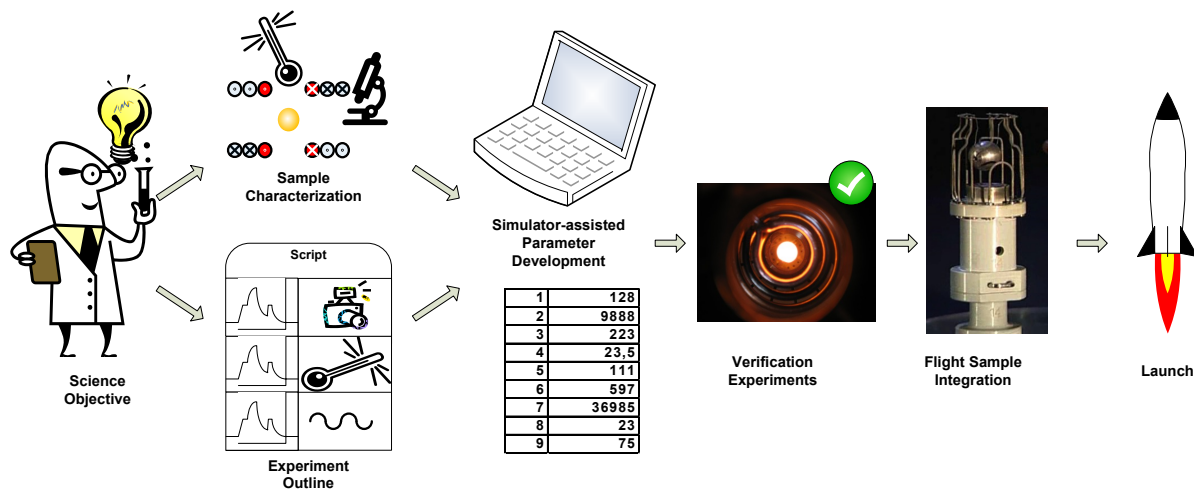


Figure 5. Preparation tasks for conducting experiments in EML onboard the ISS.

5. Mission Scenario

The EML facility will be launched and transported to the International Space Station ISS, where it will be installed in the European Drawer Rack (EDR). During its service lifetime of 5 years EML will be operated in the EDR. In order to be able to process a large number of scientific samples during the service lifetime, samples can be uploaded and downloaded between ground and EML on ISS according to the following scenario (see also figure 6):

- The flight samples which include pure metals, alloys and semiconductors, are spherical in shape with diameters ranging from 5 to 8 millimeters and are manufactured by the participating scientists in their labs.
- These samples are then integrated into dedicated sample holders and subsequently into a Sample Chamber (SCH) under very strictly controlled environmental conditions since the scientific results of the levitation experiments depend critically on the purity of the samples. Each Sample Chamber has a capacity of 18 samples which are stored in individual sample holders mounted on a magazine wheel in order to manipulate and select each sample individually for processing.
- The fully loaded Sample Chamber is uploaded to the ISS where it is attached to the EML facility.
- Sample processing is performed according to a sophisticated procedure which not only involves the settings of the levitator but also of diagnostics elements. The data delivered by the diagnostic

elements, mainly high-speed and high-resolution video cameras and pyrometers are the main scientific raw data gathered during the mission. Since the duration of a typical melt cycle of an EML sample is in the order of seconds or minutes and the processing procedure is very complex with hundreds of individual settings, the procedure is developed before the mission in a ground based experiment development program, converted into a parameter set for the facility, and is then automatically executed by the facility. Interactive control of running experiments can be performed e.g. to optimize parameters based on the results of the previous runs by tele-commanding from the user center on ground which is permanently monitoring and controlling the running experiments.

- After all samples in a Sample Chamber have been processed they are transferred to a Sample Download Container (SDC) by the flight crew for download to ground. The design of SDC has been optimized for the tight constraints of the download in terms of mass and size.
- After landing the processed flight samples are removed from the SDC and returned to the scientists for further analysis.

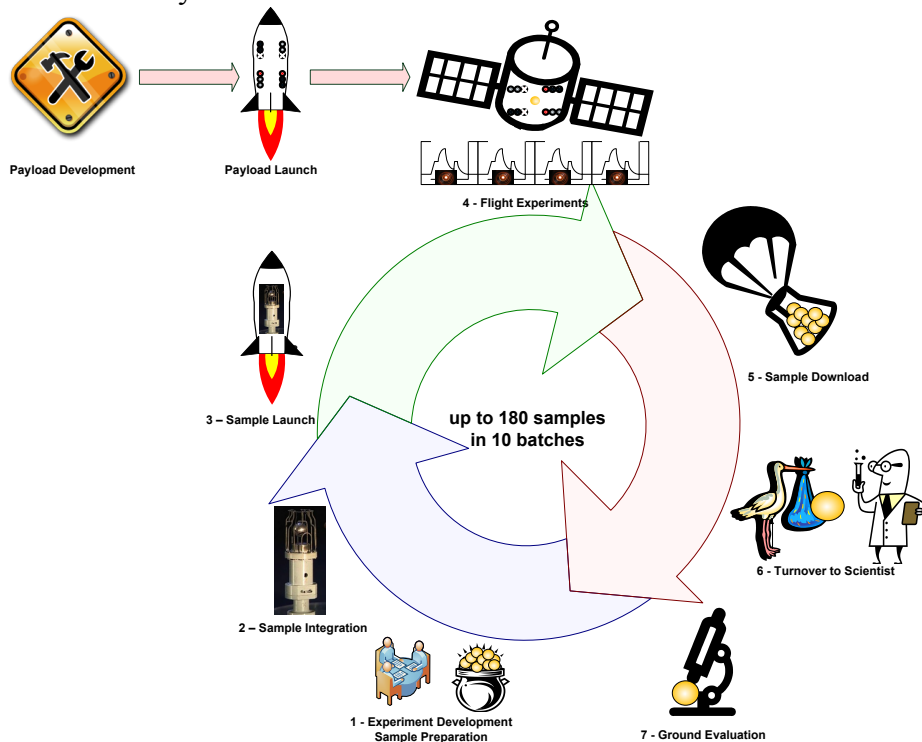


Figure 6. EML Mission Scenario, showing the complete life-cycle of the experiments from experiment preparation to post-flight evaluation.

According to the mission scenario up to two Sample Chambers per year will be uploaded to the EML facility, which translates to a total of 36 samples that can be uploaded, processed, and downloaded per year. Therefore, a maximum of 180 samples can be processed during the 5 year service lifetime of EML.

6. Advanced experimental techniques

The scientific outcome of the experiments as described herein may be significantly improved by implementing the following two upgrades of the EML facility [1], [9], [13], [14]: Oxygen Control System (OCS) & Sample Coupling Electronics (SCE). A description of these instruments and their capabilities is provided in [15].

Acknowledgement

TEMPUS and EML are developed by Astrium GmbH under programs of and funded by the European Space Agency (ESA) and by the Space Agency of the German Aerospace Center (DLR e.V.) with funds of the German Federal Ministry of Economics and Technology.

References

- [1] Soellner W, Seidel A, Stenzel C, Dreier W and Glaubitz B 2010 EML - Containerless Processing Facility for Material Science Research onboard The ISS J. Jpn. Soc. Microgravity Appl. 27 No. 4 183
- [2] Egry I and Voss D 2010 Present Activities fo the Investigators Working Group (IWG) for the Electromagnetic Levitator (EML) on ISS - A Status Report J. Jpn. Soc. Microgravity Appl. 27 No. 4 176
- [3] Team TEMPUS 1995 In Materials and Fluids Under Low Gravity: Proc. IXth Symp. on Gravity-Dependent Phen. in Physical Sciences ed L Ratke et al. (Berlin: Springer)
- [4] Piller J et. al. 1986 Electromagnetic Positioning and Inductive Heating under micro-g: 6th European Symposium on Materials Sciences under Microgravity (Bordeaux)
- [5] Knauf R, Piller J, Seidel A and Dreier W 1992 TEMPUS - An Electromagnetic Levitation Facility for Containerless Processing under Micro-g in Spacelab: Proc VIIIth European Symposium on Materials and Fluid Sciences in Microgravity (Brussels, Belgium) ESA SP-333
- [6] Geiger R and Thomas J 1993 Resonant High Power Supply for Electromagnetic Levitation and Melting of Metallic Samples European Space Power Conference (Graz)
- [7] Knauf R et. al. 1994 Containerless Processing Facility TEMPUS for Materials Science Research onboard Spacelab: 6th International Symposium on Experimental Methods for Microgravity Material Science (San Francisco)
- [8] Seidel A, Soellner W and Stenzel C 2011 EML - An Electromagnetic Levitator for the International Space Station, Proc. 4th International Symposium on Physical Sciences in Space (Bonn)
- [9] Matson D, Hyers R and Volkmann T 2010 Peritectic Alloy Rapid Solidification with Electromagnetic Convection J. Jpn. Soc. Microgravity Appl. 27 No. 4 238
- [10] Fecht H J, Wunderlich R, Ricci E, Etay J, Egry I, Seetharaman S and Battezzati L 2010 The Thermo-Lab Project: Thermophysical Property Measurement in Space for High-Temperature Alloys J. Jpn. Soc. Microgravity Appl. 27 No. 4 190
- [11] Study data package of ESTEC TRP study "Oxygen Sensing and Control" - ESTEC contract no. 19963/07/NL/PM
- [12] Diefenbach A, Schneider S, Willnecker R, Containerless Processing on ISS: Ground Support Program for EML, this proceedings
- [13] Ozawa S, Suzuki S, Hibiya T and Fukuyama H 2011 Influence of oxygen partial pressure on surface tension and its temperature coefficient of molten iron J. of Appl. Phys. 109 014902
- [14] Lohöfer G 2009 EML Sample Coupling Electronics Test Model Final Report EML/SCE-TM-Rep 1 (DLR, Cologne)
- [15] Brillo J, Fritze H, Lohöfer G, Schulz M, Stenzel C, Advanced Measurement Devices for the Microgravity Electromagnetic Levitation Facility EML, this proceedings

ADVANCED MEASUREMENT DEVICES FOR THE MICROGRAVITY ELECTROMAGNETIC LEVITATION FACILITY EML

Jürgen Brillo¹, Holger Fritze², Georg Lohöfer¹, Michal Schulz², Christian Stenzel³

¹Institut für Materialphysik im Weltraum, Deutsches Zentrum für Luft- und Raumfahrt (DLR),
51170 Köln, Germany

²Clausthal University of Technology, Institute of Energy Research and Physical Technologies,
38640 Goslar, Germany

³Astrium – Space Transportation, Department: TO 5, 88039 Friedrichshafen, Germany

Keywords: Electromagnetic levitation, micro gravity, inductive measurement technique, electrical resistivity, surface tension, liquid metals, oxygen sensing and control

Abstract

This paper reports on two advanced measurement devices for the microgravity electromagnetic levitation facility (EML), which is currently under construction for the use onboard the “International Space Station (ISS)”: the “Sample Coupling Electronics (SCE)” and the “Oxygen Sensing and Control Unit (OSC)”.

The SCE measures by a contactless, inductive method the electrical resistivity and the diameter of a spherical levitated metallic droplet by evaluating the voltage and electrical current applied to the levitation coil. The necessity of the OSC comes from the insight that properties like surface tension or, eventually, viscosity cannot seriously be determined by the oscillating drop method in the EML facility without knowing the conditions of the surrounding atmosphere. In the following both measurement devices are explained and laboratory test results are presented.

Introduction

The study of liquid metals and alloys is often in company with major challenges and difficulties, which is due to the high temperatures and, consequently, high reactivity of these materials. An elegant way to bypass these problems is the use of containerless methods. Among these, electromagnetic levitation is a well established and robust technique for electrically conducting melts [1]. By application of alternating magnetic fields of high frequency (~375 kHz), metallic samples are heated and positioned in electromagnetic levitation inductively without external contact by inductive means.

In order to exploit this containerless environment for thermophysical property measurements of liquid metals, electromagnetic levitation must be combined with non-contact diagnostic tools [1]. Generally, these tools are based on optical techniques like pyrometry, which applies Planck's law of radiation for temperature measurement, and videometry, which uses high-speed cameras for an analysis of the static and dynamic shape of the levitated drop.

However, in electromagnetic levitation under earthbound conditions, the sample droplets are not force free. The gravity deforms the droplet to a non-spherical shape and distorts the measurement of certain properties, like surface tension. Furthermore, the magnetic fields used to heat and levitate the sample will also generate turbulent fluid flows inside the melt, which strongly disturb measurements of e.g. growth velocities, or melt viscosities [2].

These problems are almost completely removed when electromagnetic levitation is performed in the essentially forceless microgravity environment. Here, the used positioning fields are strongly reduced and, consequently, also the side effects. This has led to the development of the

microgravity electromagnetic levitation facility “EML”. It is currently under construction for the use onboard the “International Space Station (ISS)”, and will provide an ideal processing environment for undisturbed measurements of thermophysical properties of electrically conductive melts.

In this paper, we report on two proposed extensions of the EML: One is the “Sample Coupling Electronics (SCE)” and the other is the “Oxygen Sensing and Control Unit (OSC)”. Both measurement devices have been proposed for integration into the EML facility.

The SCE measures by a contactless, inductive method the electrical resistivity and the diameter of a spherical levitated metallic droplet by evaluating the voltage and electrical current applied to the levitation coil. Any change in the electrical or volumetric properties of the sample can be measured this way. The SCE is therefore a comparatively simple but highly effective diagnostic tool which complements the existing video diagnostics and elegantly expands the spectrum of properties that can be measured.

The necessity of the OSC comes from the insight that properties like surface tension or, eventually viscosity cannot seriously be determined without knowing the conditions of the surrounding atmosphere. Oxygen is one of the most important surface active elements for liquid metals. Only a few ppm can decrease the surface tension by more than 10%. Such a dramatic effect can also lead to a sign reversal of its temperature coefficient and, hence, to a reverse Marangoni flow. In order to study and control these effects, not only the measurement, but also the control of the oxygen partial pressure plays an important role. Both can be achieved by the OSC.

Electromagnetic Levitation under Microgravity

For the stable electromagnetic positioning of the sample, the EML facility uses a magnetic quadrupole field, generated by two parallel and coaxial “positioning coils” carrying alternating currents of the same strength but opposite directions. Since the alternating electromagnetic levitation fields repel electrical conducting samples from areas of high field strengths, the weightless metallic sphere is fixed in the center of the two coils, where the magnetic field strength is weakest, see Fig. 1.

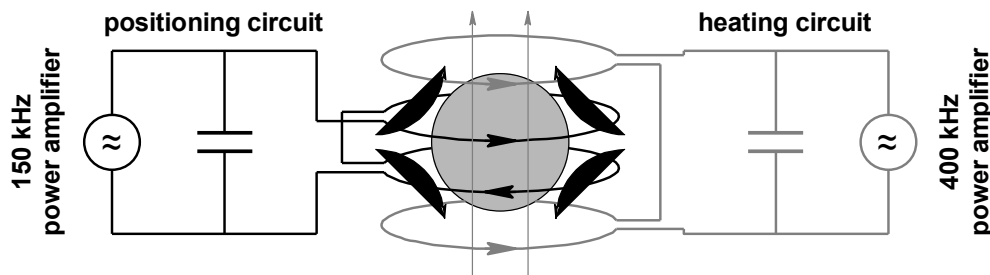


Fig. 1: Principal sketch of the electrical oscillating circuits of a microgravity levitation facility including the positioning coil (black, near the equator of the sample) generating an alternating (~ 150 kHz) magnetic quadrupole field (curved arrows), and the heating coil (gray, above and below the sample) generating an alternating (~ 375 kHz), homogeneous magnetic dipole field (straight arrows). Each of the circuits is powered by its own current supply. The actual EML circuits, basing on the superposition principle, differ in details from those shown above.

Since, moreover, the residual accelerations under microgravity, which have to be compensated by the positioning field, are relatively small, the remaining magnetic field strength around a droplet can be decreased under microgravity to values that are considerably weaker than those

necessary to position the same sample against earth gravity.

On the other hand, the positioning of the sample in a region, where the magnetic field strength is weakest, prevents an efficient heating and melting by the quadrupole field. Therefore, an additional, independent, highly efficient "heating coil", connected with its own power generator for the alternating current supply, has been provided in the EML facility. This coil arrangement has several advantages:

- The very poor heating efficiency of the positioning (quadrupole) field (see Fig. 1 left) and the very low center of gravity forces applied on the sample by the nearly homogeneous heating (dipole) field (see Fig. 1 right), enables an almost independent positioning and heating of the sample under microgravity.
- The high efficiency and the homogeneity of the heating field allows also its use as a detection field for a contactless, inductive determination of electrical and volumetric sample properties

Sample Coupling Electronics (SCE)

The "Sample Coupling Electronics (SCE)" uses simultaneously the high frequency magnetic heating field of the EML also for the inductive, contactless determination of the electrical resistivity of the levitated metallic droplet and its thermal expansion [3].

Inductive Measurement Principle

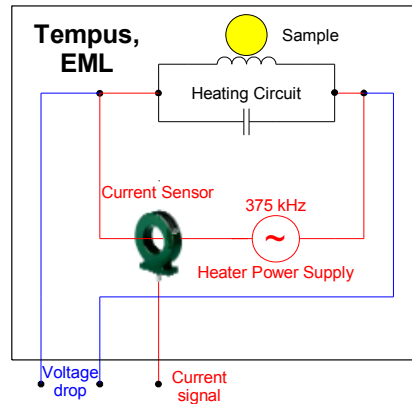


Fig. 2: Schematic sketch of the EML heating circuit with the electrical signal outputs. A power supply feeds a resonant current (~ 375 kHz) in the parallel oscillating circuit, the inductivity of which consists just of the heating coil and the inductively coupled metallic sample. The signal of the alternating current I through the circuit as well as the alternating voltage drop U across the circuit is conveyed to the outside.

As already indicated in Fig. 1 and shown in Fig. 2, the relation between the measurable quantities, i.e., U_0 : amplitude of the alternating voltage drop across the levitation circuit, I_0 : amplitude of the alternating current through the levitation circuit, φ : phase difference between voltage drop and current, as well as ω : angular frequency of voltage and current, and the sample properties, i.e. ρ : sample resistivity and a : sample radius, is given by the simple complex impedance relation

$$\frac{I_0}{U_0} e^{-i\varphi} = \frac{1}{Z_{cap}(\omega)} + \frac{1}{Z_{coil}(\omega) + Z_{sample}(\omega, \rho, a)},$$

where $Z_{cap}(\omega) = (i\omega C)^{-1}$ is the capacitor impedance, $Z_{coil}(\omega) = R + i\omega L$ is the impedance of the empty coil and $Z_{sample}(\omega, \rho, a)$ is that part of the coil impedance resulting from the inductively coupled sample. By a measurement of I_0 , U_0 , φ , and ω , real and imaginary part of the complex sample impedance $Z_{sample}(\omega, \rho, a)$, depending on the sample properties ρ and a , can be determined, after a preceding calibration measurement without sample provided the circuit parameters C , L and R .

For a spherical sample shape and a homogeneous magnetic induction field, two conditions which are largely satisfied in the EML facility under microgravity, $Z_{sample}(\omega, \rho, a)$ assumes a relatively simple mathematical form [4] allowing its inversion for a calculation of ρ and a from the “measured” values of $\text{Re}\{Z_{sample}\}$ and $\text{Im}\{Z_{sample}\}$. Both quantities are, however, relatively small compared to the real and imaginary part of Z_{coil} and Z_{cap} , respectively. Therefore, to obtain the temperature dependent electrical resistivity $\rho(T)$ of liquid samples with reasonable accuracy, the necessary resolution of the measurement quantities has to be correspondingly high:

$$\Delta U_0/U_0 < 8 \cdot 10^{-4}, \quad \Delta I_0/I_0 < 8 \cdot 10^{-4}, \quad \Delta\varphi < 0.15^\circ, \quad \Delta\omega/\omega < 2 \cdot 10^{-5}.$$

Test Results

A development model of the so called “Sample Coupling Electronics (SCE)” has been designed and constructed by DLR for the EML facility onboard the International Space Station (ISS). The SCE supplies dc voltages proportional to the measurement quantities: U_0 , I_0 , and φ with the above mentioned resolution from the alternating voltage and current signals of the levitation facility, see Fig. 2. These signals are then sent to the EML “Data Acquisition (DAQ)” unit, which converts the analogue dc voltages with a rate of 10 Hz into 16bit digital values. Finally, all digitized SCE data are stored synchronously with the sample temperature data, provided by the pyrometer of the levitation facility, to enable the calculation of the temperature dependent resistivity ρ and radius a of the sample with the help of the theoretical model of $Z_{sample}(\omega, \rho, a)$ given in Ref. [4].

To visualize the resolution of the SCE, Fig. 4 shows results of the electrical resistivity ρ and the radius a of a solid, spherical tungsten test sample for different sample temperatures.

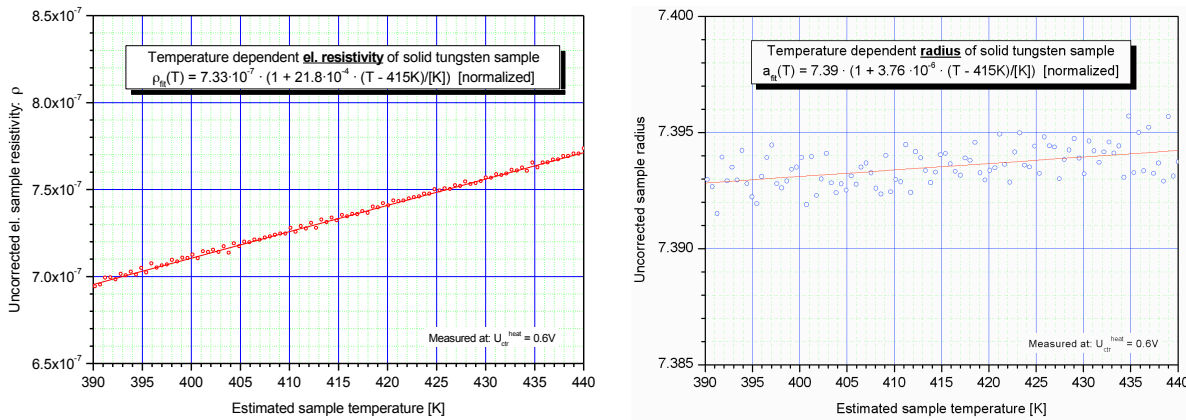


Fig. 4: Plot of the uncorrected electrical resistivity (left) and the radius (right) of the solid tungsten test sample against the estimated sample temperature. The open circles show the values evaluated from the measured SCE data. The straight lines present a linear fit of these data points.

The scatter of the resistivity data (Fig. 4 left) is extremely low. This is also due to the fact, that the sample itself is solid and fixed within the coil during the test. The fitted absolute values of the resistivity are arbitrary, because there was no previous calibration with a sample of known properties providing a correct “coupling constant”.

Due to the very low increase of the sample radius with the temperature: $\approx 3.76 \cdot 10^{-6} [K^{-1}]$ (see Fig. 4 right) and the necessarily much higher resolution of this diagram compared to that of Fig. 4 left, the data scatter of the radius values is higher. Nevertheless, the radius increase of the test sample with increasing sample temperature is clearly visible, proving that the above listed data resolution of the SCE is sufficient.

Oxygen Sensing and Control Unit (OSC)

Using the OSC, the oxygen partial pressure in the atmosphere of the EML experiment chamber can be measured and controlled. This enables a measurement of critical properties, such as surface tension and viscosity in dependence of an adjusted oxygen partial pressure.

Technical Realization

The OSC consists of an oxygen loading system (OLS), a solid state potentiometric sensor (SS1) and a gas circulation pump. The SS1 is located at the outlet of the EML chamber and the OLS at the inlet. Due to the design constrains in the EML facility, the OLS and SS1 are mounted outside the chamber and thus require gas circulation.

Both, the oxygen loading system (OLS) and the potentiometric solid state sensor (SS1) are based on an ionic conductor, yttrium-stabilized zirconium (YSZ), operated at the temperature sufficiently high to enable the transport of O^{2-} ions throughout the electrolyte, but low enough to suppress electronic conduction. The oxygen partial pressure adjusted by the pump depends on the electric current I , total pressure p_{tot} , total gas flow J_{tot} and the initial oxygen partial pressure in the carrier gas $p_{O_2}^0$ as follows:

$$p_{O_2} = p_{O_2}^0 + \frac{p_{tot}}{J_{tot}} \frac{I}{4F},$$

whereas F is the Faraday constant. As shown in Fig. 5, the tube of the oxygen ion pump is covered with platinum paste at three regions i.e. the large pumping area, the reference electrode and the counter electrode. The reference electrode is used to monitor the electromotive force, and thus p_{O_2} , which is given by the Nernst equation. Due to the large distance between the pumping and reference electrode, no impact of the pumping current on the Nernst potential is observed.

The oxygen partial pressure is also measured by an additional potentiometric solid state sensor (SS1) located at the outlet of the chamber.

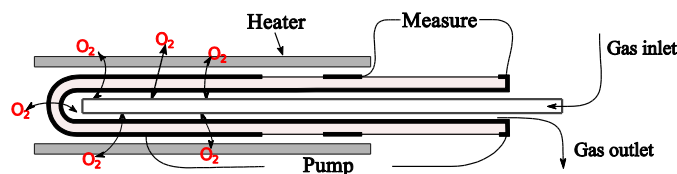


Fig. 5: The schematic view of oxygen ion pump. The carrier gas is delivered through a tube into the active area, where electric current I is applied and, therefore, oxygen ions are transferred throughout the electrolyte. An additional electrode is provided where the Nernst potential and, therefore oxygen partial pressure is measured.

Both, the oxygen ion pump and the sensor are operated at 870 K. This relatively low temperature ensures sufficiently high oxygen ion mobility and long-term stability of the system as required for the electromagnetic levitation experiments.

Since the system is operated in an environment, where strong electromagnetic noise occurs, commercial temperature controllers do not fulfill the stability requirements under such conditions. Therefore, a robust custom device is built. In order to reduce the cross-feed between the power supply and monitored temperature, commonly used thermocouples are replaced with resistive temperature sensors. Moreover, shielding for control electronics and for entire OLS is provided. The pumping current I of at most 40 mA is adjusted by a pulse width modulation control based on a PID algorithm. Thereby the polarity of the current can be changed. The controller achieves a resolution of about 1 μ A. At maximal current about 8 cm³ of O₂ can be transferred throughout the electrolyte within an hour. In order to adjust the oxygen partial pressure at two different potentiometric sensors, the system features a cascade PID controller.

Test Results

The OLS system is tested in two different environments. Laboratory conditions, free of strong electromagnetic fields and dust particles in carrier gas due to evaporation of liquid samples, enable precise determination of oxygen pump's performance, response time and signal stability. In case of the experiments, where the oxygen partial pressure is adjusted during levitation, strong electromagnetic fields impact potentially the stability of the control system.

The result of oxygen ion pump controlling p_{O_2} at the carrier gas (Ar 99.999 %, $p_{O_2}=1.6 \times 10^{-4}$ bar) is shown in Fig. 6. Here, the oxygen partial pressure is varied stepwise between 10^{-7} and 10^{-3} bar. Remarkable is the very short response time of less than 90 s and signal stability of $\Delta \log(p_{O_2}/\text{bar}) < 0.02$. Since the oxygen control system features switching of the pumping current polarity, it is possible to control p_{O_2} below and above oxygen's partial pressure in the carrier gas.

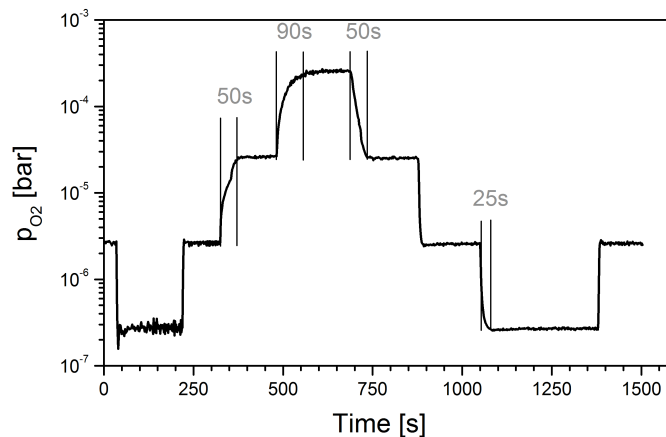


Fig. 6: The oxygen partial pressure adjusted by the OLS.

The results of OSC operated in parallel with a ground based electromagnetic levitator are shown in Fig. 6. The system proves to operate stable under these conditions, even if the levitator is operated at full power required to levitate and heat the sample in 1g conditions. Thanks to the use of resistive Pt100 sensors, the fluctuation of the temperature is negligible. The electromagnetic interference the OSC was exposed to in this test is much stronger than expected in EML (under μ g conditions) since the ground levitator uses fields that are approximately three orders of

magnitude larger than in the EML under μg . Therefore, this was a very harsh test providing a large confidence level that the OSC will work well in an μg -EML environment

The response time of OSC varies between several seconds and an hour. It depends strongly on the experimental conditions like e.g. the gas flow rate, kind and purify of levitated material as well as presence of unintended buffer mixtures like $\text{H}_2/\text{H}_2\text{O}$, CO/CO_2 or $\text{C}_x\text{H}_y/\text{CO}_2$. In particular, the liquid sample acts an oxygen buffer and its influence on the measurement and control of p_{O_2} cannot be ignored.

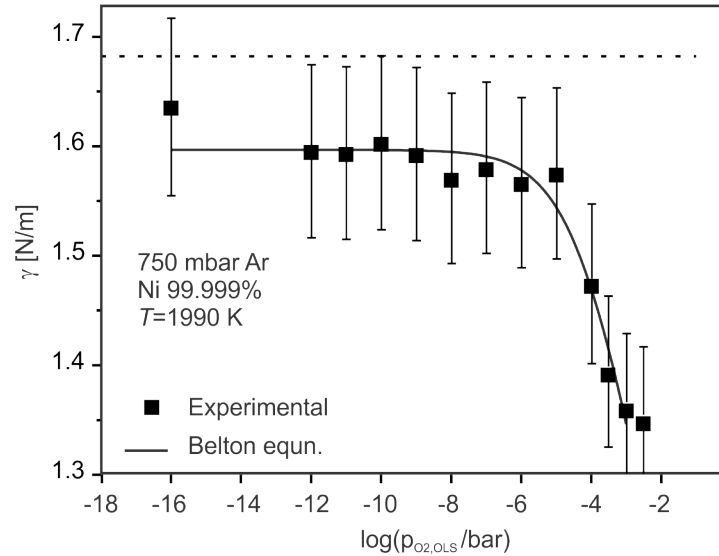


Fig. 7: Surface tension of liquid Ni at 1990 K versus $p_{\text{O}_2, \text{OLS}}$ together with data from Ref. [8] (dotted line).

During levitation, the liquid sample performs spontaneously excited surface oscillations. The sample is observed by a fast digital C-MOS camera (400 frames per second) and the frequency spectra of the surface oscillations are obtained from image analysis software. Using the sum formula of Cummings and Blackburn [6] the surface tension γ can be calculated from a spectrum. This is shown in Fig. 7 for a liquid Ni sample of 99.999 % purity at 1990 K where γ is plotted versus $p_{\text{O}_2, \text{OLS}}$.

For $p_{\text{O}_2} < 10^{-6}$ bar, γ remains constant at a value of 1.6 N/m. It decreases with increasing p_{O_2} when the oxygen partial pressure becomes larger than 10^{-6} bar. The results can be described by the Belton-equation [7] and the agreement is very good, as shown in Fig. 7b.

At the corresponding temperature of 1990 K, the surface tension of pure Ni is 1.68 N/m, Ref [8], which is slightly larger than the value of 1.6 N/m that was found in this experiment. However, this discrepancy is still within the error bar of ± 5 %, so that it can be stated that a good agreement with the reference data is obtained.

Summary

Two advanced measurement devices for the microgravity “electromagnetic levitation facility (EML)”, which is currently under construction for the use onboard the “International Space Station (ISS)”, have been presented. One is the “Sample Coupling Electronics (SCE)” and the other is the “Oxygen Sensing and Control Unit (OSC)”.

The SCE measures by a contactless, inductive method the electrical resistivity and the diameter of a spherical metallic droplet, levitated in the EML under microgravity conditions, by evaluating the voltage and electrical current applied to the levitation coil. A development model

of the SCE has been designed, constructed and tested under laboratory conditions by DLR. These tests show a sufficiently well resolution of the electronics for a temperature dependent determination of those measurement quantities.

The OSC measures the oxygen partial pressure of the atmosphere in the EML experiment chamber. The necessity of the OSC comes from the insight that properties like surface tension or, eventually viscosity by the oscillating drop method in the EML facility cannot seriously be determined without knowing the conditions of the surrounding atmosphere. A technology demonstrator of an OSC system for the use at the ISS-EML has been developed and successfully tested. The tests were carried out under ideal laboratory conditions as well as in real levitation environment under gravity conditions. In both test it was shown that the device works reliably. An example experiment, the measurement of the surface tension of liquid Ni as function of the oxygen partial pressure, succeeded convincingly. The obtained data could be described by the Belton equation.

References

- [1] Brillo J., Lohöfer G., Schmidt-Hohagen F., Schneider S. and Egry I., *Int. J. Materials and Product Technology* **26** (2006), 247-273.
- [2] Schneider S., *Viskositäten unterkühlter Metallschmelzen* (PhD Theses, RWTH Aachen 2002).
- [3] Lohöfer G., *Meas. Sci. Technol.* **16** (2005), 417-425.
- [4] Lohöfer G., *Int. J. Engng Sci.* **32** (1994), 107-117.
- [5] Ellingham, H. J. T., *J. Soc. Chem. Ind.* **63** (1944) 125.
- [6] Cummings D.L. and Blackburn D.A., *J. Fluid Mech.* **224** (1991) 395.
- [7] Belton G.B., *Metall. Trans.* **7B** (1976) 35.
- [8] Brillo J and Egry I., *J. Mater. Sci.* **40** (2005) 2213.

Electrostatic Levitation Furnace for the ISS

Keiji Murakami¹, Naokiyo Koshikawa¹, Kohichi Shibasaki¹, Takehiko Ishikawa¹, Junpei Okada¹
²Tetsuya Takada, ²Tatsuya Arai, ²Naoki Fujino, ²Yukiko Yamaura

¹JAXA, 2-1-1, Sengen, Tsukuba, Ibaraki,305-8505, Japan
²IHI Aerospace, 900,Fujiki, Tomioka, Gunma,370-2398, Japan

Keywords: ISS, JEM, Multiuser Facility

Abstract

JAXA (Japan Aerospace Exploration Agency) has just started the development of Electrostatic Levitation Furnace to be launched in 2014 for the ISS.

This furnace can control the sample position with electrostatic force and heat it above 2000 degree Celsius using semiconductor laser from four different directions. The announcement of Opportunity will be issued soon for this furnace.

In this paper, we will show the specifications of this furnace and also the development schedule.

Introduction

As for microgravity material science research, JAXA has started the development of Gradient Heating Furnace in 1993. The GHF has been launched by H-II Transfer Vehicle #2 last year(2011). At that time, Electrostatic levitation Furnace (ELF) was also the candidate of the JAXA multi-user facility for the ISS. Because of the technical difficulty of ELF, the start of the development of ELF has delayed, and also the ISS assembly schedule has delayed. Since then, many circumstance conditions has changed (such as rack location availability, crew time availability, maximum development cost and etc.), so the specification and requirements have also changed. Through these hard time, JAXA started the development of ELF in February 2011. The ELF will be integrated into Multi-purpose Small Payload Rack (MSPR) in KIBO. The launch target year is 2014.

History

In 1993, at Furnace Workshop which was held at ESTEC among the each space agency (CSA, ESA, NASA and JAXA), JAXA presented the intent of developing ELF and also preliminary specifications was presented. At that time, DLR has presented Electro-magnetic Levitator Furnace, based on the result of Shuttle equipment TEMPUS. In 2000, Levitation Furnace Workshop was held at San Diego, USA. There NASA, ESA and JAXA has discussed and came to some conclusion, that each agency's furnace contribution. The image of the contribution is shown in Table 1.

Specification

ELF has been developed based on a design by Rhim et al.¹⁾ from which several modifications were made. Fig. 1 depicts schematically the ELF and its optical diagnostic instruments. The electrostatic levitation method utilizes the Coulomb force between the sample and the surrounding electrodes. A positively charged sample was levitated between a pair of electrodes which were utilized to control the positions of the specimen.

Table 2 is the latest specification of the ELF. The heating lasers hit the sample from the top of regular tetrahedron to center, so that the sample temperature could be isothermal.

	Low Temp	High Temp
Conductors (Metal, Alloy)	Space DRUMS (NASA)	EML(ESA)
Insulators (Oxides)		ELF(JAXA)

Table 1 Levitation Furnace Contribution of each space agencies

To integrate the ELF into MSPR, vacuum pump was deleted, so the samples which requires high vacuum condition are impossible with ELF. The maximum environment pressure is 0.2 Mpa. And the best vacuum condition is worse than 0.13 Pa. ELF can control the environment pressure between those values with N₂ or Ar. We plan to conduct the oxides sample in the maximum pressure so that the outgas from the sample become minimum. When we process metal samples with ELF, we will choose Ar environment in which we can not levitate samples in 1-G condition. The cleanliness of the supply gas are shown in also table 2.

Figure 2 shows the rough images of ELF sample chamber. ELF experiment chamber is polyhedron shape so that the chamber accommodates many optical windows in minimum chamber size and enables us to set various functions(such as heating, sample position detection, observations and etc.) .

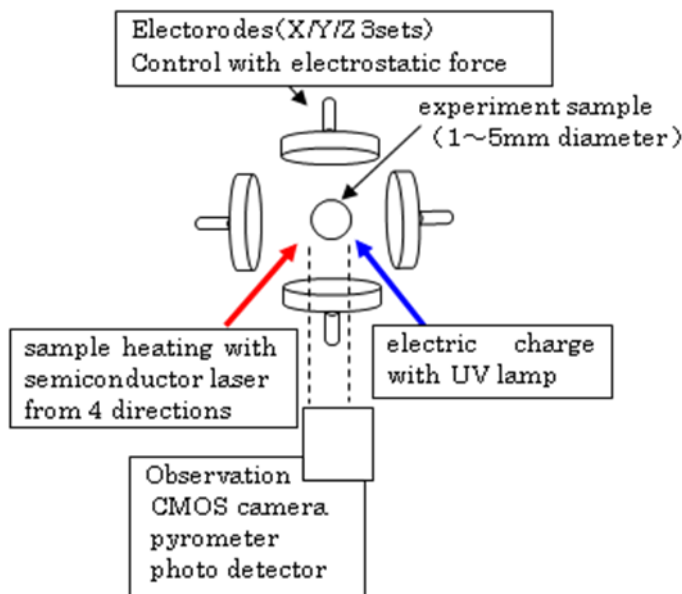


Figure 1 Schematic drawing of the ELF

ELF is equipped an UV lamp (peak wavelength;365nm) to assist the electric charge of the sample so that ELF electrostatic positioning control can maintain the sample position to correspond to the sample charge decrease, caused by such as outgas from the sample.

ELF usually control the sample positions at 1 kHz frequency. This position control frequency can be reduced by ground commanding as well as PID control parameters.

Utilization Concept of ELF

To demonstrate the ELF capability, we are now planning to process the oxide samples, whose melting temperature are over 2000 degree Celsius. The thermophysical properties such as density,

surface tension, and viscosity will be measured over wide temperature range including under cooled region. The density can be calculated using magnified image of the molten sample²⁾, while surface tension and viscosity can be measured by oscillating drop method³⁾. We will superimpose the oscillation signals to position control voltage. Then measure the sample oscillation with photo detectors with vertical slit. 5 kHz of oscillating data would be down linked to ground for the measurement. The processed samples will be retrieved to the ground. These process would be conducted as ELF initial check. Some thermophysical properties of molten oxides have not been measured on the ground and will be the first measurement in the world. Also we plan to investigate the detailed structure of the processed sample on ground.

By using ELF, we can obtain the cooling curve of the sample, with which we may calculate the heat capacity of the sample if we can estimate the conductive heat transfer by surrounding gas.

The processing sample would be installed into cartridge (up to 15 samples per cartridge), and then launched by HTV(H-II Transfer Vehicle) or other launch system. After installing the cartridge into ELF chamber, each sample can be processed by ground commanding. The images of the sample and equipment telemetry data would be down linked to ground automatically, when we oscillate the sample, we plan to get the resonance frequency and attenuation factor of the sample. After the experiment, the sample cartridge would be retrieved by Space-X or Soyuz to ground.

The ELF chamber equipped double seal and around the chamber connectors, there is decompression environment, so that ELF can provide three protecting method for the sample vapor gas. After each measurement, the inner gas could be replaced by ground commanding.

Table 2 Specification of ELF

Items		Requirements
Sample Size (diameter)		1 ~5mm
Accuracy of Positioning		±100micro meter
Heater	Laser (Wave Length/Power)	980nm(TBD) /40W x 4 directions
	Target Temperature	Melting Point of Zirconia (2710 degC)
Observation	Temperature Measurements	one thermometer (ORU)(range;1450-1800 nm(TBD)) Sampling Rate (more than 100Hz) equipped with one camera(NTSC)
	Magnified Image	One camera with zoom (NTSC) higher than 140 pixels/ half diameter (1mm)
	Observation of Overview	One camera with zoom (NTSC)
Measurements of Thermo-physical Properties	Density	through Image Analysis
	Surface Tension	Oscillating Droplet Method
	Viscosity	Oscillating Droplet Method
Others	Ambient	N ₂ Gas(Level300A)* Ar Gas(Level300A)*, Vacuum with Evacuation Line

*SN-C-0005C

Development Schedule

Figure 2 shows the development schedule of ELF. Launch target year of ELF is 2014. Using the engineering model, we plan to verify the sample control logic with parabolic flight. After that verification, the engineering model would be modified to training/ground model.

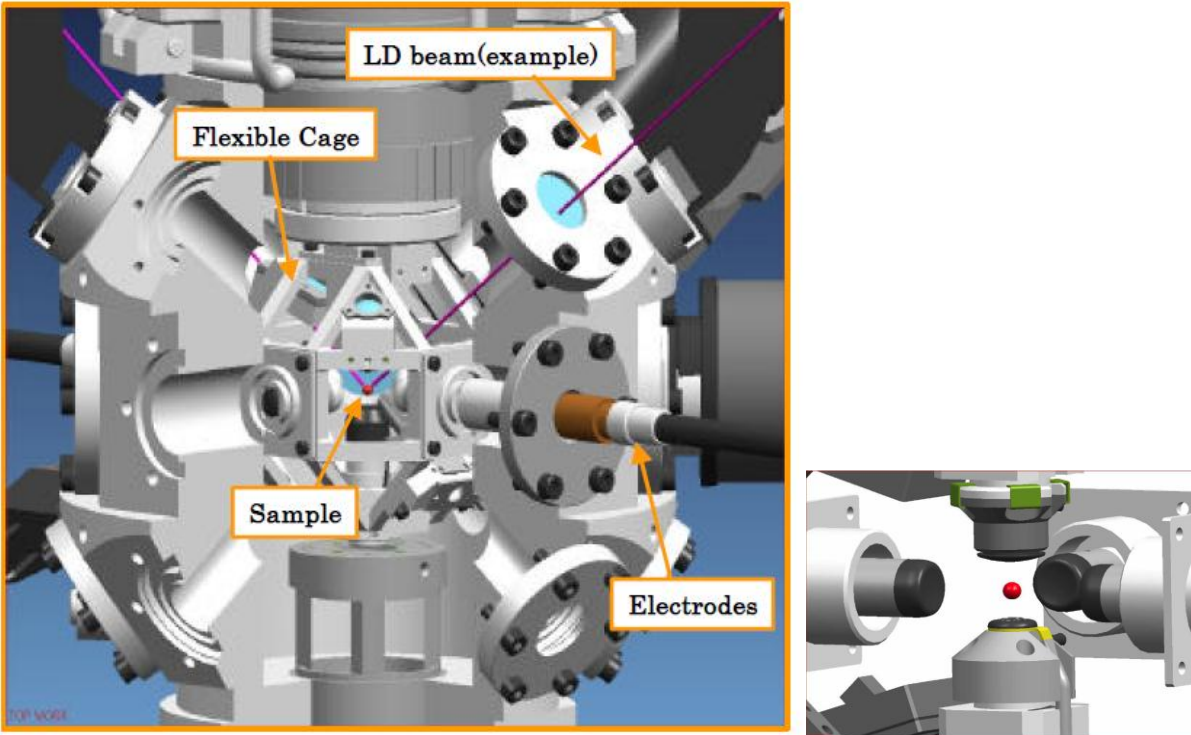


Figure 2 Sample chamber images of ELF

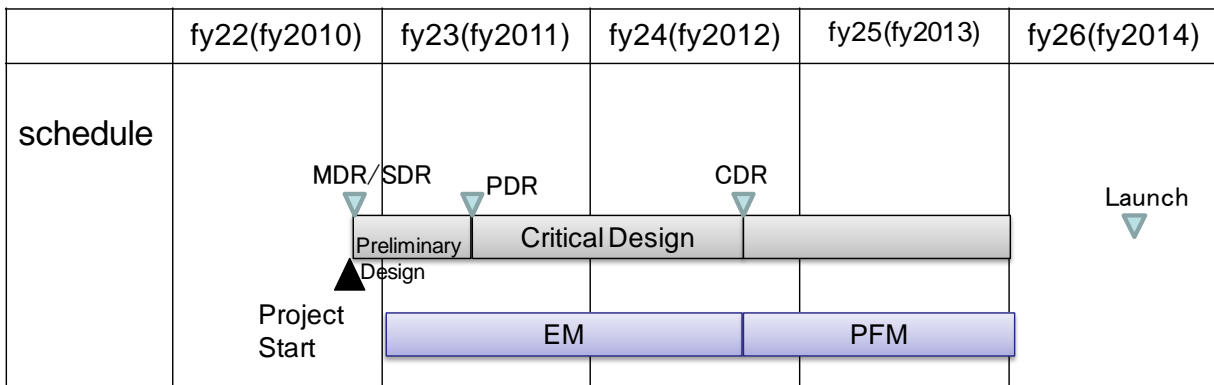


Figure 3 Development Schedule of ELF

Conclusion

Announcement of Opportunity (AO) will be issued for the ISS experiment (including the usage of ELF) at Japan in February 2012. We hope many researchers are interested in ELF and apply to the AO.

References

- 1) Rhim, W.-K., Chang, S. K., Barber, D., Man, K. F., Gutt, G., Rulison, A., and Spjut, R. E.: *Rev. Sci. Instrum.* 64 (1993), pp. 2961.
- 2) S. K. Chung, D. B. Thiessen, W.-K. Rhim, *Rev. Sci. Instrum.* **67** (1996), 3178.
- 3) W.-K. Rhim, K. Ohsaka, P.-F. Paradis, R. E. Spjut, *Rev. Sci. Instrum.* **70** (1999), 2796.

LIQUID STRUCTURES AND PHYSICAL PROPERTIES – GROUND BASED STUDIES FOR ISS EXPERIMENTS

K. F. Kelton, J. C. Bendert, and N. A. Mauro

Department of Physics, Washington University, St. Louis, MO 63130

Keywords: electrostatic levitation, liquid structure, short-range order, medium-range order, icosahedral order

Abstract

Studies of electrostatically-levitated supercooled liquids have demonstrated strong short- and medium-range ordering in transition metal and alloy liquids, which can influence phase transitions like crystal nucleation and the glass transition. The structure is also related to the liquid properties. Planned ISS experiments will allow a deeper investigation of these results as well as the first investigations of a new type of coupling in crystal nucleation in primary crystallizing liquids, resulting from a linking of the stochastic processes of diffusion with interfacial-attachment. A brief description of the techniques used for ground-based studies and some results relevant to planned ISS investigations are discussed.

I. Introduction

Fahrenheit [1] first demonstrated that under the right conditions water can be cooled far below its melting temperature without freezing, indicating a barrier to crystallization. That metallic liquids resisted supercooling was believed to indicate a small nucleation barrier, arising from similarities in the atomic structures of the liquid and crystal, a view supported by their similar densities and coordination numbers. However, if heterogeneous sites for nucleation are removed it is possible to deeply supercool liquid metals [2, 3]. This can be explained if undercooled liquids develop icosahedral short-range icosahedral order (ISRO), which is incompatible with crystalline periodicity [4]. Experimental data from liquids and glasses support this view [5-9]. This and subsequent work show that nucleation in liquids is more complicated than generally thought. It is well known that it can be coupled to other first-order processes, such as phase separation prior to crystallization and the precipitation of nano-sized heterogeneous sites, but these studies demonstrate that local order in a liquid can also couple to the nucleation barrier. Dynamical coupling effects can occur. For example, when the nucleating phase has a different chemical composition than that of the original phase, models predict that the interfacial flux, of central concern in the *classical theory of nucleation*, can couple to the long-range diffusion field [10, 11]. Ordering can also couple to atomistic dynamics, significantly influencing the nucleation kinetics and possibly giving rise to dynamical phase transitions, such as the fragile/strong transition. A more thorough investigation of these processes requires a microgravity environment to minimize stirring effects and allow key thermophysical properties to be measured. As a member of the THERMOLAB and ICOPROSOL teams, we will carry out these studies on the International Space Station. To support those activities, we are making extensive ground-based studies of liquid structures and some thermophysical properties. In this

manuscript, a brief overview of our ground-based techniques and activities and a brief review of some of the results obtained, are provided.

II. X-Ray Diffraction of Supercooled Liquids

Electrostatic levitation (ESL) is used for containerless investigations of the high temperature liquids of interest; most of our studies are now made using the recently constructed Washington University Beamline ESL, or WU-BESL (Fig. 1). In ESL, charged samples (2.0 – 4.0 mm diameter) are levitated in an electrostatic field (0 to 2 MV/m) under high vacuum ($\approx 10^{-7}$ torr). Three pairs of orthogonal electrodes and a robust control algorithm maintain the sample position during processing to better than 50 μ m. The samples are initially charged by induction and the charge is maintained during processing with an external UV source. Samples are melted using a 50 W diode laser and the sample temperature is measured across a range of 160 to 2300 $^{\circ}$ C using a combination of two infrared pyrometers with overlapping ranges. In addition to structural studies, WU-BESL is capable of making coordinated density, viscosity and surface tension measurements. More details on WU-BESL can be found elsewhere [12].

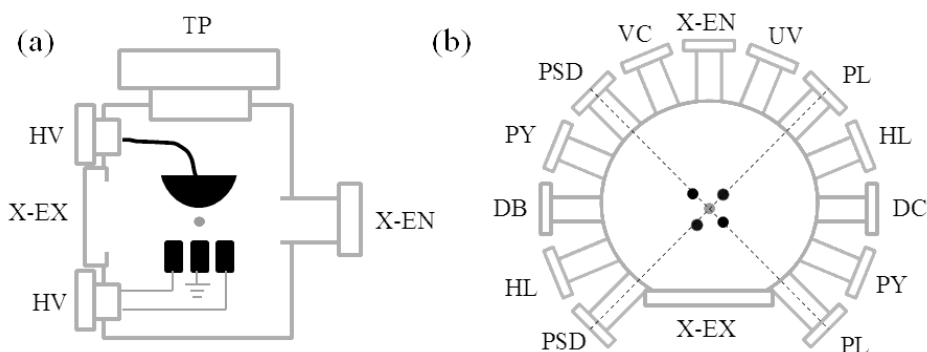


Figure 1 –Schematic drawing of the WU-BESL: (a) vertical and (b) horizontal cuts through the sample. The top and bottom electrode and two side electrodes are schematically indicated in (a) (solid black). Components: TP - turbo pump; HV - high voltage feed through; X-EN –X-ray entrance window; X-EX –X-ray exit window; PL - positioning laser; PSD - position sensitive detector, PY – pyrometer; DC – density camera; HL - heating laser; UV - ultra violet light source; VC - visualization camera; DB – backlight for density measurements.

X-ray scattering experiments are made in a transmission geometry (Fig. 2); a series of collimators and a beam-stop reduce the background to acceptable levels. For a typical study ($E = 129\text{keV}$, $\lambda = 0.09611\text{\AA}$), useful data can be obtained to 15 \AA^{-1} using a GE Revolution 41-RT amorphous Si flat panel X-ray detector at a sampling rate of up to 10 Hz.

The scattering data are used to obtain the total X-ray static structure factor, $S(q)$, from which structural information is inferred using either single cluster [7, 8] or Reverse Monte Carlo (RMC) [13, 14] approaches. When constrained with the measured liquid density and atomic sizes, an RMC fit yields a reasonable topological model for the liquid; it does not, however, yield realistic chemical correlations (such as the partial pair distribution functions). If the RMC can be

further constrained with information from molecular dynamics (MD) structural studies, elastic neutron diffraction, EXAFS, or anomalous scattering data, it becomes possible to obtain more accurate partial pair distribution functions. The order in the RMC structures is characterized using the Honeycutt-Andersen (HA) indices [15], bond orientation order parameters [16, 17] and Voronoi polyhedra (VI) construction [18]. The HA indices typically indicate a large amount of five-fold symmetry, which may not, however, signal complete icosahedral clusters. Consistent with this, the VI construction tends to show much smaller amounts of icosahedral order [19].

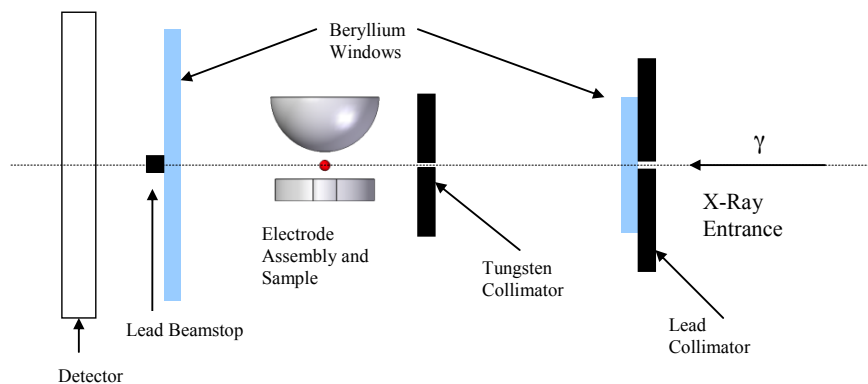


Figure 2 – Schematic of the X-ray optics in WU-BESL

Many studies indicate that icosahedral short-range order (ISRO) in metallic liquids increases with supercooling [7, 8, 20-22]. A developing shoulder on the high- q side of the second peak in $S(q)$ often correlates with ISRO. This is observed in the scattering data from liquid $Zr_{59}Ti_3Cu_{20}Ni_8Al_{10}$, a bulk metallic glass former (Fig. 3.a). An increase in the number of 1551 HA indices from atomic structures obtained from a RMC fit to the scattering data (Fig. 3.b) supports this conclusion in this case. However, it is important to point out that a developing shoulder should only be used as a rough guide. Other local structures can produce a similar shoulder, and in some cases ISRO may be dominant with no evidence of the shoulder. The latter is the case for liquid Al, which shows no asymmetric second peak, yet an HA analysis of the RMC structures indicates a high degree of ISRO [23]. When present, ISRO can couple to the nucleation barrier [8] and may play a role in the glass transition in some cases [9].

Many reports exist of medium-range order (MRO) in glasses, i.e. ordering beyond nearest neighbors, [24-28]. In some cases, evolution of MRO has been correlated with changes in plasticity [25] and viscosity [29]. Since reports of medium-range ordering in metal-metal liquids have been rare, it is of interest to determine under what conditions it can be observed. Binary liquids, such as Zr-Pd and Zr-Pt, provide good systems for such studies. The two alloys are very similar. Both have deep eutectics at similar Zr-rich compositions and both form glasses that devitrify first to the icosahedral quasicrystal phase [30]. Further, Pd and Pt have similar bonding properties with Zr and are of similar sizes. However, recent WU-BESL studies of the two eutectic liquids show qualitatively different X-ray static structure factors [31, 32]. As shown in Fig. 4, a pre-peak is clearly observed in the $S(q)$ data at all temperatures for $Zr_{80}Pt_{20}$ liquids (indicated by an arrow), while it is not observed in $Zr_{75.5}Pd_{24.5}$ liquids. Given the many similarities between these two systems, the presence of a pre-peak in one and not in the other is

at first difficult to understand. An analysis of constrained RMC fits to the data, made using partial pair-correlation functions obtained from MD simulations [31, 32] revealed a solute-solute (Pd-Pd or Pt-Pt) correlation in both cases, which manifests itself as a prepeak at $\sim 1.7\text{\AA}^{-1}$. Because Pd has a much smaller atomic form factor than Pt, however, the correlation is not evident in the experimental X-ray data for Zr-Pd, suggesting that MRO may be much more common in metal-metal liquids than previously thought.

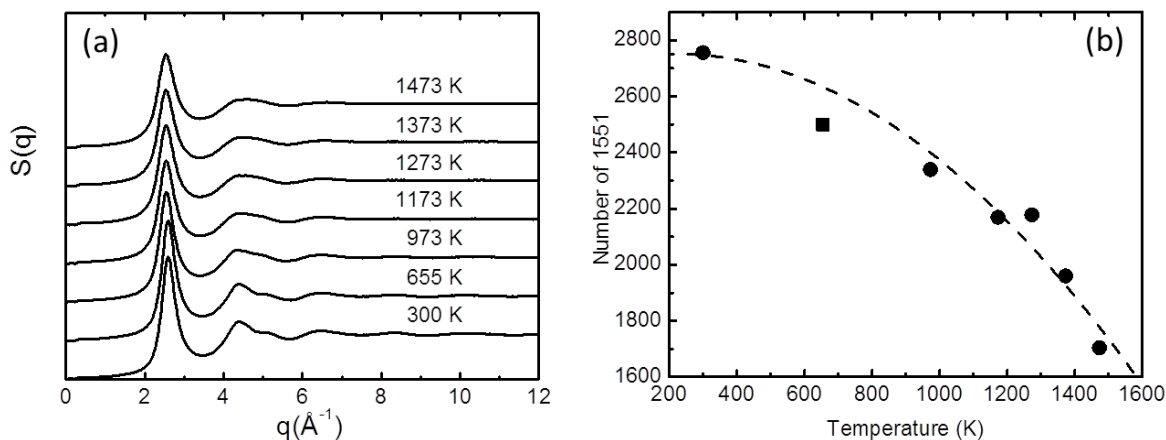


Figure 3 – (a) Experimental $S(q)$ data for liquid $\text{Zr}_{59}\text{Ti}_3\text{Cu}_{20}\text{Ni}_8\text{Al}_{10}$ as a function of temperature. (b) Number of 1551 HA indices (indicating ISRO) obtained from RMC fits to the $S(q)$ data as a function of temperature.

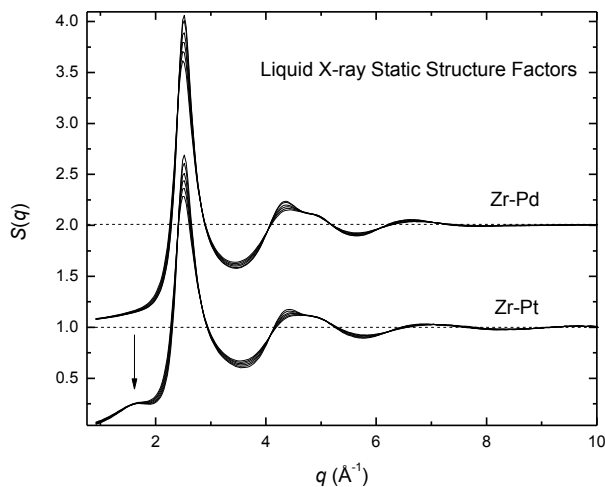


Figure 4 – Liquid X-ray static structure factor for Zr-Pt and Zr-Pd eutectic liquids. For each alloy, a series of $S(q)$'s are plotted corresponding to the temperature range over which the data were collected.

III. Thermophysical Property Measurements using ESL

Employing non-contact techniques, WU-BESL can be used to measure thermophysical properties such as density, thermal expansion, specific heat, viscosity and surface tension. A brief discussion of the techniques used for measurements of the density, thermal expansion coefficient and specific heat in WU-BESL is provided here.

Following techniques developed by others [33, 34], the density is measured from video data of the shadow of a levitated sample. A schematic layout of the WU-BESL density measuring system is shown in Fig. 5. Video data are taken at 25 frames per second (fps) with an exposure time of 0.8 ms using a 1.6 megapixel CMOS monochrome camera (pixeLINK®) and a K2/SC long distance video microscope lens, with a close focus objective that is capable of magnifications of 2.13 - 0.71 and a working distance of 222 - 418 mm. A 450 nm band pass having a 40 nm full-width-at-half-max is placed between the camera and the lens system to exclude interference from thermal radiation [34]. The samples are backlit through a transparent port that is opposite to the camera and lens with a 455 nm collimated microscope LED, having a total beam power of approximately 240 mW and a beam diameter of 37 mm. The pixel dimensions are calibrated between studies of samples of each composition using 3/32" diameter grade 3 ($\pm 3 \times 10^{-5}$ " diameter) tungsten carbide standards (Industrial Tectonics Inc).

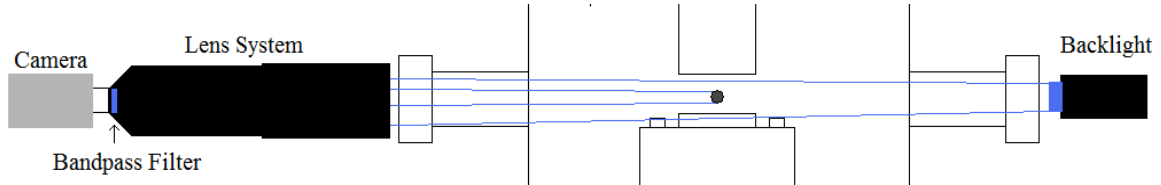


Figure 5 – Schematic diagram for density and volume expansion measurements in WU-BESL.

The video are analyzed to identify the edges of the 2D sample silhouette and then integrated about an axis of symmetry to calculate sample volume, following a method described by Bradshaw et. al. [35]. The coefficient of thermal expansion ($\beta = (\partial \ln V / \partial T)_p$) is determined from linear fits to regions of the volume-temperature data. The error in the density is dominated by the uncertainty in the volume and mass calibrations ($\pm \sim 0.4\%$). These uncertainties cancel in the thermal expansion calculations. There, the dominant contribution to the error are the uncertainty in the temperature calibration ($\sim \pm 1\%$) and the uncertainty in the linear fit to the data ($\sim \pm 1\%$), giving a total uncertainty in β of $\sim \pm 2\%$.

For illustration, the measured density of the best glass-forming Cu-Zr liquid ($\text{Cu}_{64}\text{Zr}_{36}$) during free cooling is shown in Fig. 6.a. The density increases approximately linearly with decreasing temperature (see inset in Fig. 6.a) and can be described by

$$\rho(T) = [7.316 \pm .023 \text{ gcm}^{-3}] \left[1 + \left([8.57 \pm 0.15] \cdot 10^{-5} \text{ K}^{-1} \right) (994^\circ \text{C} - T) \right]. \quad (1)$$

Since the sample is levitated in vacuum, when laser power is removed, the sample will cool by radiation loss described by the Stefan-Boltzmann equation, giving

$$mC_p dT / dt = -A\varepsilon\sigma(T^4 - T_R^4) \quad , \quad (2)$$

where T_R is the effective room temperature of the chamber, A is the sample surface area, ε is the hemispherical emissivity, σ is the Stefan-Boltzmann constant, m is the sample mass, and C_p is the sample specific heat capacity. By determining the temperature derivative from the measured temperature as a function of time during cooling, the ratio C_p / ε is readily obtained. As an example, the C_p / ε values measured as a function of temperature for $\text{Cu}_{64}\text{Zr}_{36}$ are shown in Fig. 6.b. As observed in other alloy liquids, C_p / ε increases approximately linearly with decreasing temperature, with the rate of increase becoming slower at lower temperatures. Were the emissivity approximately constant across this temperature range, this would suggest a rise in the specific heat, which would be consistent with the ordering of the liquid.

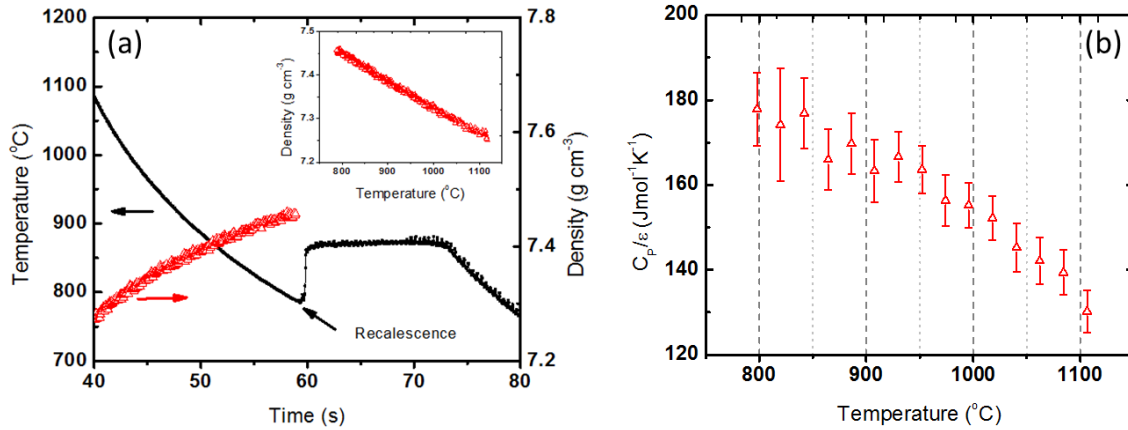


Figure 6 – (a) Temperature as a function of time during free cooling of the sample and the corresponding change in density. The density as a function of temperature is shown in the inset to the figure. (b) Measured C_p / ε as a function of temperature with the estimated error.

IV. Summary and Future Directions

New methods for obtaining structural information have been applied to supercooled metallic glass-forming liquids. These studies have demonstrated that these liquids typically develop significant short-range order, often with an icosahedral character. Some liquids also develop medium-range ordering, extending beyond nearest-neighboring atoms; our studies indicate that this may occur in more metallic liquids than is generally thought. Structural ordering has an impact on phase transitions occurring in the liquid and likely on liquid properties. We have developed capabilities that allow the density, volume expansivity, specific heat, viscosity and surface tension to be measured simultaneously with the structural studies to investigate this.

Since neutrons scatter differently from X-rays, they provide additional information about chemical ordering in a sample. Further, since the neutron scattering cross section differs among

different isotopes, it is possible to obtain additional information from elastic neutron scattering studies on samples made with isotopic substitution. These data can be used to constrain RMC fits to the X-ray scattering data, allowing structures with realistic topological/chemical order to be inferred. Neutron scattering studies can also provide information about dynamics. Due to their lack of periodicity, only long wavelength phonons are present in liquids; the strong temperature dependence of the liquid structure makes it difficult to predict the vibrational properties. Inelastic neutron scattering experiments allow these and related issues in liquids, such as atomic diffusion and the existence of dynamical transitions, like mode-coupling and the glass transition, to be quantitatively investigated. We are currently constructing an ESL for neutron scattering studies (Neutron ESL, NESL). NESL has been designed take full advantage of the high neutron flux and the exceptionally high solid angle detector coverage at several of the beamlines at the Spallation Neutron Source (SNS) at Oak Ridge National Laboratory, including VULCAN, ARCS, CNCS, BASIS and NOMAD.

Using the quiescent microgravity environment on the ISS, experiments are planned to investigate the role of stirring on the amount of supercooling possible in metallic liquids that crystallize to phases of different composition. This will allow the effects of diffusion on the nucleation rate to be studied. Modulated specific heat and other thermophysical property measurements in metallic glass-forming liquids will enable studies of possible liquid/liquid phase transitions and their relation to structure, determined from the ground-based WU-BESL and NESL studies. The results of these studies will improve our knowledge of phase transitions that occur in liquids and help develop methods that can lead to improved microstructural control.

Acknowledgements

The research presented here has been supported by NASA (NNX07AK27G & NNX10AU19G) and the National Science Foundation (DMR-08-56199). We thank R. W. Hyers for his collaboration on many of the past and ongoing ESL studies; he is a co-investigator on the upcoming ISS experiments designed to investigate the role of diffusion on nucleation.

References

1. D. B. Fahrenheit, *Phil. Trans. Roy. Soc.*, **39**(1724) 78-89.
2. D. Turnbull, *J. Chem. Phys.*, **20**(1952) 411-424.
3. K. F. Kelton and A.L. Greer, *Nucleation in Condensed Matter - Applications in Materials and Biology*, Pergamon Materials Series (Amsterdam: Elsevier, 2010).
4. F. C. Frank, *Proc. Roy. Soc. LondonA*, **215** (1952) 43-46.
5. J. C. Holzer and K.F. Kelton, *Acta Metall. et Mater.*, **39** (1991) 1833-1843.
6. D. Holland-Moritz, *International Journal of Non-Equilibrium Processing*, **11** (1998) 169-199.
7. T. Schenk, D. Holland-Moritz, V. Simonet, R. Bellissent and D.M. Herlach, *Phys. Rev. Lett.*, **89**(2002) 075507/1-4.
8. K. F. Kelton, G.W. Lee, A.K. Gangopadhyay, R.W. Hyers, T.J. Rathz, J.R. Rogers, M.B. Robinson and D.S. Robinson, *Phys. Rev. Lett.*, **90**(2003) 195504/1-4.
9. Y. T. Shen, T.H. Kim, A.K. Gangopadhyay and K.F. Kelton, *Phys. Rev. Lett.*, **102** (2009) 057801 /1-4.

10. K. C. Russell, *Acta Metall.*, **16** (1968) 761-769.
11. K. F. Kelton, *Acta Mater.*, **48** (2000) 1967-1980.
12. N. A. Mauro and K.F. Kelton, *Rev. Sci. Instrum.*, **82** (2011) 035114/1-6.
13. R. L. McGreevy, R.L., *Nuc. Instrum. Methods in Phys. Res. A*, **354** (1995) 1-16.
14. R. L. McGreevy and J.D. Wicks, *J. Non-Cryst. Solids*, **192-193** (1995) 23-27.
15. J. D. Honeycutt and H.C. Andersen, *J. Phys. Chem.*, **91** (1987) 4950-4963.
16. P. J. Steinhardt, D.R. Nelson and M. Ronchetti, *Phys. Rev. B*, **28** (1983) 784-805.
17. P. J. Steinhardt, D.R. Nelson and M. Ronchetti, *Phys. Rev. Lett.*, **47**(1981) 1297-1300.
18. J. L. Finney, *Proc. Roy. Soc. London A*, **319**(1970) 479-493.
19. S. G. Hao, M.J. Kramer, C.Z. Wang, K.M. Ho, S. Nandi, A. Kreyssig, A.I. Goldman, V. Wessels, K.K. Sahu, K.F. Kelton, R.W. Hyers, S.M. Canepari and J.R. Rogers, *Phys. Rev. B*, **79** (2009) 104206/1-7.
20. G. W. Lee, A.K. Gangopadhyay, K.F. Kelton, R.W. Hyers, T.J. Rathz, J.R. Rogers and D.S. Robinson, *Phys. Rev. Lett.*, **93**(2004) 037802/1-4.
21. T. H. Kim, G.W. Lee, A.K. Gangopadhyay, R.W. Hyers, J.R. Rogers, A.I. Goldman and K.F. Kelton, *J. Phys. Condens. Matter*, **19**(2007) 452112/1-10.
22. T.H. Kim and K.F. Kelton, *J. Chem. Phys.*, **126** (2007) 054513/1-7.
23. N. A. Mauro, J.C. Bendert, A.J. Vogt, J.M. Gewin and K.F. Kelton, *J. Chem. Phys.*, **135**(2011) 044502/1-6.
24. T. Nakamura, E. Matsubara, M. Sakurai, M. Kasai, A. Inoue and Y. Waseda, *J. Non-Cryst. Solids*, **312-314**(2002) 517-521.
25. J. M. Park, J.H. Na, D.H. Kim, K.B. Kim, N. Mattern, U. Kuhn and J. Eckert, *Phil Mag.*, **90**(2010) 2619-2633.
26. W. G. Stratton, J. Hamann, J.H. Perepezko, P.M. Voyles, X. Mao and S.V. Khare, *Appl. Phys. Lett.*, **86**(2005) 141910/1-3.
27. H. K. Breitzke, Luders, S. Scudino, U. Kuhn and J. Eckert, *Phys. Rev. B*, **70**(2004) 014201/1-12.
28. A. P. Sokolov, A. Kisliuk, M. Soltwisch and D. Quitmann, *Phys. Rev. Lett.*, **69** (1992) 1540-1543.
29. B. Xiufang, S. Minhua, X. Xianying and Q. Xubuo, *Mater. Lett.*, **57**(2003) 2001-2006.
30. J. Saida, M. Matsushita and A. Inoue, *J. Appl. Phys.*, **90** (2001) 4717-4724.
31. N.A. Mauro, V. Wessels, J.C. Bendert, S. Klein, A.K. Gangopadhyay, M.J. Kramer, S.G. Hao, G.E. Rustan, A. Kreyssig, A.I. Goldman and K.F. Kelton, *Phys. Rev. B*, **83**(2011) 184109/1-8.
32. N.A. Mauro, W. Fu, J.C. Bendert, Y. Chen, E. Ma and K.F. Kelton, "Local atomic structure in equilibrium and supercooled liquid $Zr_{75.5}Pd_{24.5}$," *Phys. Rev. B*, (submitted).
33. W.-K. Rhim, S.K. Chung, D. Barber, K.F. Man, G. Gutt, A.J. Rulison and R.E. Spjut, *Rev. Sci. Instrum.*, **64**(1993) 2961-2970.
34. T. Ishikawa, P.F. Paradis and S. Yoda, *Rev. Sci. Instrum.*, **72**(2001) 2490-2495.
35. R. C. Bradshaw, D.P. Schmidt, J.R. Rogers, K.F. Kelton and R.W. Hyers, *Rev. Sci. Instrum.*, **76**(2005) 125108/1-8.

Thermophysical Properties Measurement of High-Temperature Liquids under Microgravity Conditions in Controlled Atmospheric Conditions

Masahito Watanabe¹, Shumpei Ozawa², Akitoshi Mizuno¹, Taketoshi Hibiya³,
Hiroya Kawauchi¹, Kentaro Murai¹, Suguru Takahashi²

¹Department of Physics, Gakushuin University;
1-5-1 Mejiro, Tokyo, 171-8588, JAPAN

²Department of Aerospace Engineering, Tokyo Metropolitan University;
6-6 Asahigaoak, Hino, Tokyo, 191-0065, JAPAN

³SDM Research Institute, Keio University;
4-1-1 Hiyosi, Yokohama, 223-8526, JAPAN

Keywords: Electromagnetic Levitation, Surface Tension, Viscosity.

Abstract

Microgravity conditions have advantages of measurement of surface tension and viscosity of metallic liquids by the oscillating drop method with an electromagnetic levitation (EML) device. Thus, we are preparing the experiments of thermophysical properties measurements using the Materials-Science Laboratories ElectroMagnetic-Levigator (MSL-EML) facilities in the international Space station (ISS). Recently, it has been identified that dependence of surface tension on oxygen partial pressure (P_{O_2}) must be considered for industrial application of surface tension values. Effect of P_{O_2} on surface tension would apparently change viscosity from the damping oscillation model. Therefore, surface tension and viscosity must be measured simultaneously in the same atmospheric conditions. Moreover, effect of the electromagnetic force (EMF) on the surface oscillations must be clarified to obtain the ideal surface oscillation because the EMF works as the external force on the oscillating liquid droplets, so extensive EMF makes apparently the viscosity values large. In our group, using the parabolic flight levitation experimental facilities (PFLEX) the effect of P_{O_2} and external EMF on surface oscillation of levitated liquid droplets was systematically investigated for the precise measurements of surface tension and viscosity of high temperature liquids for future ISS experiments. We performed the observation of surface oscillations of levitated liquid alloys using PFLEX on board flight experiments by Gulfstream II (G-II) airplane operated by DAS. These observations were performed under the controlled P_{O_2} and also under the suitable EMF conditions. In these experiments, we obtained the density, the viscosity and the surface tension values of liquid Cu. From these results, we discuss about as same as reported data, and also obtained the difference of surface oscillations with the change of the EMF conditions.

Introduction

Microgravity conditions have advantages of measurement of surface tension and viscosity of metallic liquids by the oscillating drop method with an electromagnetic levitation (EML) device [1]. Thus, we are preparing the experiments of thermophysical properties measurements using the Materials-Science Laboratory ElectroMagnetic-Levigator (MSL-EML) in the international space station (ISS). Recently, it has been identified that dependence of surface tension on oxygen partial pressure must be considered for industrial application of surface tension values [2]. Effect of oxygen partial pressure (P_{O_2}) on surface tension would apparently change viscosity from the damping oscillation model. Because viscosity values are obtained from damping time of surface oscillations, the change of surface tension with oxygen partial pressure would change the

damping time of surface oscillation. However, viscosity is bulk properties, so the values affected by oxygen partial pressure are not real properties. Therefore, surface tension and viscosity must be measured simultaneously in the same atmospheric conditions. In our project using the parabolic flight levitation experimental facilities (PFLEX), the effects of P_{O_2} and external forces by EML are systematically investigated for the precise measurements of surface tension and viscosity of high temperature liquids. From the above purpose, we performed the observation of surface oscillations of levitated liquid Cu and Ag in the controlled P_{O_2} atmosphere and various electromagnetic forces (EMF) under the microgravity conditions by parabolic airplane flight in order to decide the suitable conditions of thermophysical properties measurements by EML. On the suitable conditions, we measured the surface tension and viscosity of liquid Cu. From the results, we propose the refinement of the surface oscillation measurement under the microgravity for precise measurements of thermophysical properties of high-temperature liquid, such as industrial application materials and scientifically interested materials, on the future ISS experiments using MSL-EML facilities.

Experiments

a. Oxygen partial pressure control

To control P_{O_2} conditions in microgravity, we used Ar+H₂ gas as atmospheric condition gas around the levitated liquid samples. The control of P_{O_2} by Ar+H₂ gas is used the reaction of $H_2+1/2O_2=H_2O$, so P_{O_2} values has the temperature dependence. However, surface tension of liquid Ag is weak dependence on P_{O_2} in wide range of P_{O_2} (10^{-2} - 10^{-20} Pa) [3], so we can separate between temperature dependence and P_{O_2} dependence of surface tension values. On the other hand, liquid Cu has large dependence of surface tension in the range from 10^{-10} to 10^5 Pa [4]. In the range from 10^{-20} to 10^{-10} Pa, the surface tension of liquid Cu does not depend on the P_{O_2} values. For liquid Cu we can perform the measurements of surface tension under the controlled P_{O_2} conditions below 10^{-10} . Therefore, the method using Ar+H₂ gas is not best way to control P_{O_2} , so for the future experiments we must use oxygen pump using electrochemical reaction based on the solid-state electrolyte.

b. Electromagnetic levitation experiments on board parabolic flight

We performed electromagnetic levitation experiments under microgravity by parabolic flight of airplane (Gulfstream-II) operated by Diamond Air Service Co. (DAS) using PFLEX. PFLEX has electromagnetic levitation coil in high vacuum chamber, 2kW radio frequency (RF) power supply with 300Hz, control system for electromagnetic levitation conditions, water cooling system for coil cooling, and sample droplet observation system. The observation system has single color pyrometer for temperature measurement of samples and high-speed camera with sampling rate of 250Hz and shutter speed of 100msec and also we monitor oxygen partial pressure in vacuum chamber by the zirconia based solid electrolyte sensor. The surface oscillation of levitated liquid droplets was observed from the top view by high-speed camera with the frame rate of 250kHz by the recording system of the flash solid-state drive (SSD) system. For electromagnetic levitation experiments under microgravity, TEMPUS facilities have been used for long time in European research group [5]. TEMPUS has two coils system for separation between heating and positioning. Thus, since the magnetic field shape is different in the one coil system used in ground experiments, we cannot identify the effect of electromagnetic force on modification of liquid droplet shape. From the above reason, we adopted the one coil system same as the ground experiments. Using one coil system, we can levitate a sample before microgravity conditions during parabolic flight, so the samples can be melted just at the start of microgravity conditions. However, for the one coil system, weak electromagnetic force applies

to liquid droplet even in microgravity conditions in order to keep position of droplets, so we cannot reduce the electromagnetic force to completely zero. The effect of the weak electromagnetic force on liquid droplet oscillation, we checked the effect of electromagnetic force on the surface oscillation of liquid droplets before thermophysical properties measurements. For this purpose, we changed electrical current applying to the coil from 0 to 10A.

Experimental Results

We observed surface oscillation of liquid Cu in Ar+H₂ atmospheres under microgravity with different electromagnetic force conditions. The surface oscillation was obtained from the analysis of the change of liquid droplet shape with time. Figure 1 shows the result of the dumping of surface oscillation of liquid Cu droplet with change of electric current applying to levitation coil. From the results, on the large EMF case surface oscillation was long damping time and was not completely damped. This is due to that the EMF continuously generated the surface oscillation during sample levitation. For the case of long time dumping, we cannot obtain correct viscosity. Also, the EMF affects on the surface oscillation frequency shown in Fig.2. Figure 2 shows the power spectrum of surface oscillation of both conditions. From Fig.2, we found that the small EMF had single peak of surface oscillation but for the large EMF case multi peaks found and the main peak position was shifted. This means that the electromagnetic force by applying small EMF case did not modify the surface oscillation of liquid droplets. However, for the case of large EMF, the electromagnetic force modified the surface oscillation. The effects of gravity and electromagnetic force cause the modification of the surface oscillation of electromagnetically levitated liquid droplets in the ground. For the case of electromagnetically levitated liquid droplets under microgravity, only electromagnetic force caused for the effect of modification of the surface oscillation. Thus, details of the modification of surface oscillation are different between microgravity and ground conditions. The modification of surface oscillation of liquid droplets by gravity and EMF must be clarified for the preparation of ISS experiments in near future. Based on the conclusion we selected the levitation condition for precise measurement of surface oscillation for thermophysical properties measurements. Figure 3 shows the results of viscosity of liquid Cu measured with the change of EMF. In Fig.3, previous reported viscosity of liquid Cu [6] was also plotted. From the results, on the small EMF case viscosity values almost the same as the previous reported values. From our results, temperature dependence of liquid Cu viscosity was fitted by Arrhenius type formula with the activation energy of 25kJ/mol. From these measurements, in order to obtain correct viscosity we found the critical EMF conditions for keeping the sample position was below 3% of maximum EMF for heating.

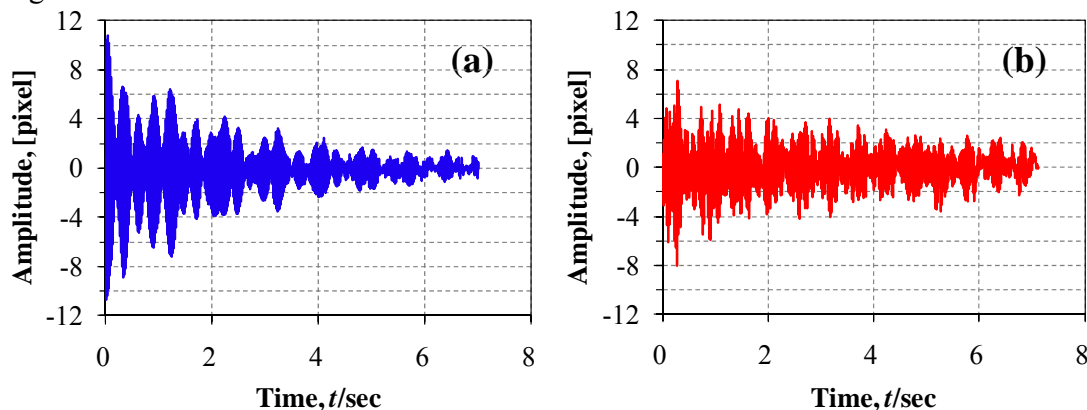


Fig.1 Surface oscillation dumping of liquid Cu at 1620K under microgravity conditions with different electric current applying to RF coil, (a) 0.2A and (b) 7A

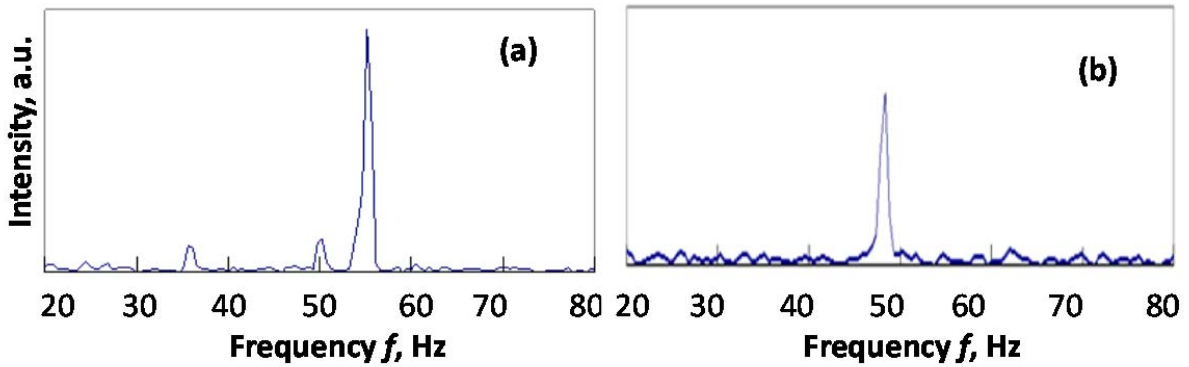


Fig.2 Power spectrum of surface oscillations of liquid Cu shown in Fig.1.

In order to find the affect of EMF on the surface oscillation frequency fro surface tension measurements, we calculated the surface tension values of liquid Cu from the surface oscillation frequency shown in Fig.2 with different EMF conditions. For these measurements of surface oscillations of liquid Cu, we controlled P_{O_2} condition in 10^{-20} Pa. Figure 4 shows the results of temperature dependence of surface tensions liquid Cu [7] with previous reported values. Figure 4 exhibits the surface tension of liquid Cu calculated from the single frequency peak of the droplet under small EMF case using the Rayleigh equation [8] (■) and that calculated from the frequencies of the $m = 0, \pm 1$, and ± 2 oscillations for the $l = 2$ mode of the droplet on the ground using the Cummings and Blackburn calibration (▲) [9]. The surface tension is also calculated from the frequency of the main peak (●) in the spectrum which shows three peaks as shown in figure 4a. Even though the droplet oscillation does not degenerate completely under microgravity in the EMF conditions shown in figure 8a, the main peak may correspond to the frequency of the $l = 2$ mode if it is predominant in the oscillation of the droplet. For the case, the surface tension is calculated from the frequencies assigned same as the $m = 0, \pm 1$, and ± 2 oscillations observed in the terrestrial experiment. The temperature dependence of surface tensions of liquid Cu obtained from single peak of surface oscillation agrees well with the literature values [10,11,12] and the surface tension decreases from about 1300mN/m to 1200mN/m as the sample temperature rises from 1515K to 1815K. However, the calculated surface tension shows a large scatter when it is calculated from the frequency of the main peak in the frequency spectrum that also has small two additional peaks.

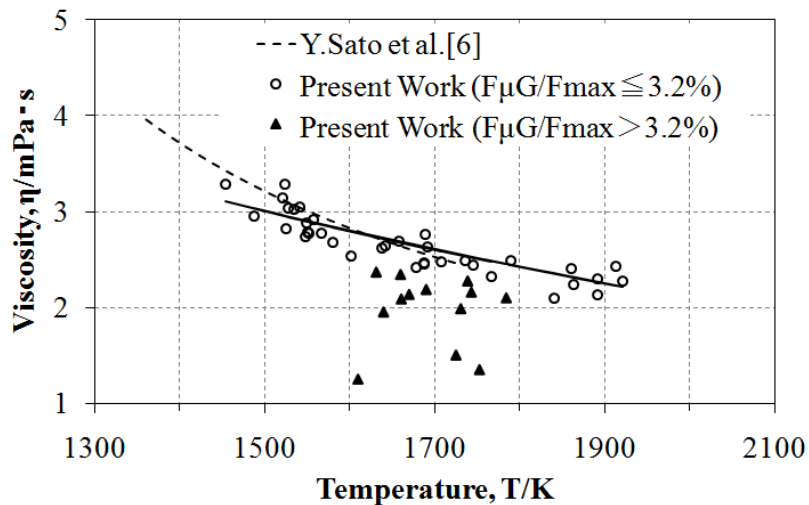


Fig.3 Viscosity of liquid Cu measured under microgravity with different EMF conditions.

This suggests that the main peak does not correspond to the frequency of the $l = 2$ mode. The surface oscillation of the droplet would not degenerate as long as a few additional peaks are observed in the frequency spectrum even if it is very small.

When the surface tension of the droplet is calculated from the single frequency peak of the surface oscillation observed under the microgravity experiment, it is almost the same as that measured in the terrestrial experiment though it shows a small scattering. This implies that the Cummings and Blackburn equation can calibrate the effect of the deformation of the droplet due to the gravitational acceleration and the external electromagnetic force.

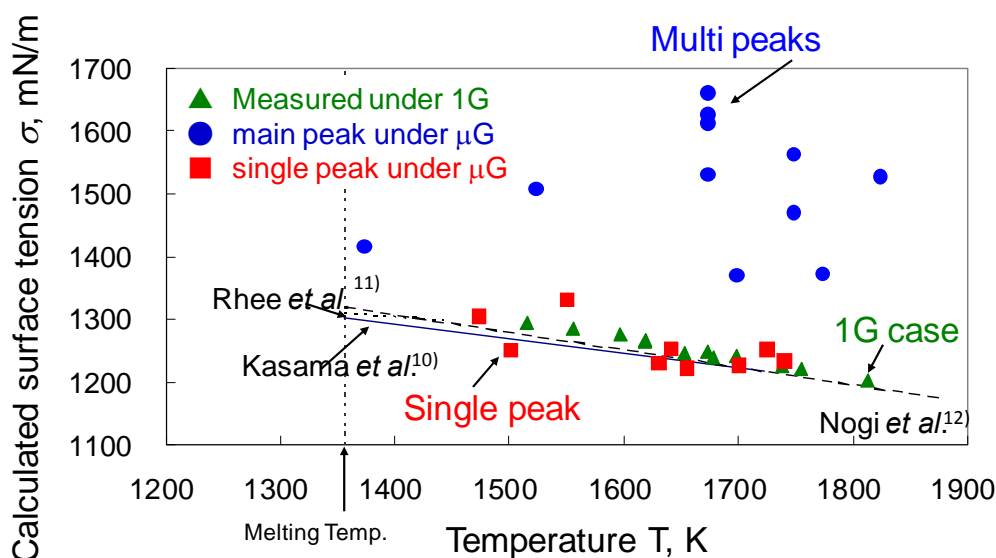


Fig.4 Surface tension of molten copper calculated from the single frequency of the surface oscillation observed under microgravity (■) and that calculated from the frequencies of $m = 0$, ± 1 , and ± 2 oscillations under 1G (▲). The calculated surface tension from the main peak in the frequency spectrum which shows three peaks as shown in figure 6a is also exhibited (●).

Discussion

As mentioned above, we succeeded in a significant decrease in the electromagnetic force given to the droplet during the viscosity and the surface tension measurements by the oscillating droplet method using EML under microgravity. Furthermore, the oxygen partial pressure of the ambient atmosphere was monitored and controlled simultaneously. The surface tension of the liquid Cu calculated from the single frequency peak of the surface oscillation of $l = 2$ mode observed under the microgravity condition became almost the same as that calculated from the frequencies of the $m = 0$, ± 1 , and ± 2 oscillations on the ground. However, the surface tension calculated from the frequency of the single peak for the microgravity experiment showed a small scattering due to the incorrect estimation of the sample mass because the sample could not be collected after the experiment. Furthermore, the calculation result of the surface tension of liquid Cu under microgravity included the influence of the temperature variation of the sample due to the decrease in the electromagnetic force. Since a large electromagnetic force was applied to the sample to levitate it under the high gravity condition of 1.5G before the microgravity condition starts, in many cases the surface oscillation did not degenerate within the short microgravity period prepared by the parabolic flight of the airplane. A long microgravity experiment without any gravity change is expected in the International Space Station (ISS). In this case it is easy to

levitate the sample in a stable state. Furthermore, there is a lot of flexibility for the design of the RF coil because a large electromagnetic force is not necessary to levitate the sample. As a result, the sample would be heated and kept at certain temperature easily. Since the sample can be collected after its solidification due to a sufficient experiment time, it would become easy to estimate the change of the sample mass during the measurement. Further investigation is required under a long microgravity environment in the ISS so that the oscillation behavior of the droplet, which is used for calculation of surface tension, can be understood more clearly. We are planning the microgravity experiment in the ISS as collaboration of ESA (European Space Agency), JAXA (Japan Aerospace Exploration Agency), and NASA (the National Aeronautics and Space Administration). For ISS experiments, the present status of our planning was shown below. Our project of thermophysical properties measurements of high-temperature liquid using the materials-science-laboratory electromagnetic-levitator (MSL-EML) in ISS initially focus on the semiconducting materials liquid, so our project name is SEMITHERM. SEMITHERM is concerned with the THERMophysical properties of SEMIconductors, specifically Ge, and Si-Ge.

Conclusion

Using the parabolic flight levitation experimental facilities (PFLEX), the effects of P_{O_2} and external EMF on surface oscillation of levitated liquid droplets were investigated for the measurements of surface tension and viscosity of liquids Cu. The surface oscillations of levitated liquid Cu using PFLEX on board flight experiments by G-II were observed in Ar+H₂ and pure Ar gas atmospheric conditions. From these observations, we obtained the density, the viscosity and the surface tension values as same as reported data, and also obtained the difference of surface oscillations with the change of the P_{O_2} . For these thermophysical properties measurements, we investigated the effect of EMF on the surface oscillations in controlled P_{O_2} conditions. This clarified the effect of EMF on the surface oscillation of levitated under microgravity. This is different from the ground conditions. Therefore, if large EMF applying cases, we need modified the surface oscillation analysis method from the present method based on the Cummings and Blackburn analysis. We future more systematically perform precise measurements surface oscillation in different P_{O_2} conditions. On the basis of present experimental results, we are discussing about ISS experiments of MSL-EML with controlled atmospheric P_{O_2} conditions with Investigator Working-Group of EML (IWG-EML) in order to progress high temperature liquid science.

Acknowledgments

This work was performed in JAXA research-working group of “Measurement of Oxygen Partial Pressure Dependence of Surface Tension for High Temperature Melts under Microgravity”, and also supported by SENTAN, JST. We appreciate these supports for this work.

References

- [1] Egry, I., Lohoefer, G. and Jacobs, G., Phys. Rev. Lett., 75(1995) pp. 4043- 4046.
- [2] Mito, M., Tsukada, T., Hozawa, M, Yokoyama, C., Li, Y-R., and Imaishi, N., Meas. Sci. Technol., 16 (2005) pp.457-466.
- [3] Lee, J., Tanaka, T., Yamamoto, M. and Hara, S., Materials Tran., 45 (2004) pp.625-629.
- [4] Lee, J., Tanaka, T., Asano, Y. and Hara, S., Materials Trans., 45 (2004) pp.2719-2722.
- [5] Fecht, H.-J., Wunderlich, R., Battezzati, L., Etay, J., Ricci, E., Seetharaman, S., Egry, I., Europhysics News, 39 (2008) pp.19-21.

- [6] Sato, Y *et al.*, Proc. 24th Jpn. Symp. Thermophysical Properties, 24 (2003) pp.68-71.
- [7] Lord Rayleigh, Proc. Roy. Soc. London, 29 (1879) pp.71-97.
- [8] Ozawa, S., Watanabe, M., Kiyamura, K., Morohoshi, K., Aoyagi, T., Tanno, M., Matsumoto, T., Adachi, M., Mizuno, A., Fujii, H., and Hibiya, T., J. Jpn. Soc. Microgravity Appl., 27 (2010) pp.215-219
- [9] Cummings, D. L., and Blackburn, D. A., J. Fluid Mech., 224 (1991) pp.395-416.
- [10] Kasama, K., Iida, T., and Morita, Z., J. Jpn. Inst. of Metals, 16 (1976) pp.787-790 (in Japanese)
- [11] Rhee, S. R., J. American Ceramic Soc., 53 (1970) pp.639-642.
- [12] Nogi, K., Oishi, K., Ogino, K., J. Jpn. Inst. of Metals, 52 (1988) pp.72 -75 (in Japanese).
- [13] Ozawa, S., Koda, T., Adachi, M., Morohoshi, K., Watanabe, M., and Hibiya, y., J. Appl. Phys., 106 (2009) 034907-1.

MICROSTRUCTURE FORMATIONS IN THE TWO PHASE REGION OF THE BINARY PERITECTIC ORGANIC SYSTEM TRIS-NPG

Johann Mogeritsch, Andreas Ludwig

University of Leoben, Department Metallurgy,
Franz-Josef-Strasse 18, 8200 Leoben, Austria

Keywords: Peritectic solidification, in-situ observations, microgravity

Abstract

In order to prepare for an onboard experiment on the International Space Station (ISS), systematic directional solidification experiments with transparent hypoperitectic alloys were carried out at different solidification rates around the critical velocity for morphological stability of both solid phases. The investigations were done in the peritectic region of the binary transparent organic TRIS-NPG system where the formation of layered structures is expected to occur. The transparent appearance of the liquid and solid phase enables real time observations of the dynamic of pattern formation during solidification. The investigations show that frequently occurring nucleation events govern the peritectic solidification morphology which occurs at the limit of morphological stability. As a consequence, banded structures lead to coupled growth even if the lateral growth is much faster compared to the growth in pulling direction.

Introduction

Experimental investigations under reduced gravity condition lead to a better understanding of the influence of gravitational related phenomena as natural convection and sedimentation on the solidification morphologies of peritectic alloys. For an alloy of peritectic composition the liquid [L], the primary solid [α] phase, and the peritectic [β] phase are in equilibrium at the peritectic temperature, T_p . The focus of the present investigation is put on the solidification morphologies at growth rates where one or both phases might reveal a planar solid/liquid interface. Such morphologies reveal a complex dynamic which is still not fully understood in detail.

Trivedi [1] published a conceptual model which predicts cyclic nucleation and overgrowth under purely diffusive growth conditions in the hypoperitectic region where both [α] and [β] phases would grow independently as planar fronts. Evidence for such bands were found in experiments where convection is suppressed by using thin samples [2,3]. Hunzinger et al. [4] developed a microstructure map with the nucleation and constitutional undercooling criterion under the assumption of infinitely high nuclei density and steady-state growth. Chalmers [5] predicted the simultaneous growth of both phases in form of lamellae or fibers and Lo et al. [6] show by simulation that bands are formed only for approximately equal volume fraction of the two phases otherwise islands are formed.

Directionally solidification experiments with metal alloys were carried out and published in [2, 3,7-17], but in-situ observations of peritectic solidification with transparent organic compounds were done recently only by the authors. Organic alloys with a high temperature non-faceted phase solidify in a metal-like manner and thus enable the detailed observation of the dynamic of the solid/liquid interface morphology during solidification. The transparent non-faceted/non-

faceted peritectic system TRIS–NPG [18,19] was selected for in-situ observations of solidification experiments with near peritectic compositions. The peritectic region of the TRIS-NPG phase diagram is shown in Fig. 1. Preliminary studies of the phase diagram show a thermal sensibility of the organic substance TRIS at temperatures close to the melting point which constrains the experimental process conditions. The diffusion coefficient in the liquid within the peritectic region could be measured as $D_L \approx 1.5 \cdot 10^{-11} \text{ m}^2/\text{s}$.

The observation was realized with a micro Bridgman-furnace and a light microscope in combination with a CCD camera. For the selected process conditions growth competition between the primary phase and the peritectic phase is expected and the growth of discrete bands are predicted [20-23]. Our experimental results show oscillatory and isothermal coupled growth morphologies within the peritectic region, published and discussed in details in [24-27].

In the present paper, we report the results of investigations for a hypoperitectic alloy with $x = 0.5$ mol fraction NPG at a fixed temperature gradient and variable solidification rates. Furthermore, the impact of different initial solid/liquid interfaces morphologies on the dynamic of peritectic solidification near the morphological stability limit of both phases was evaluated.

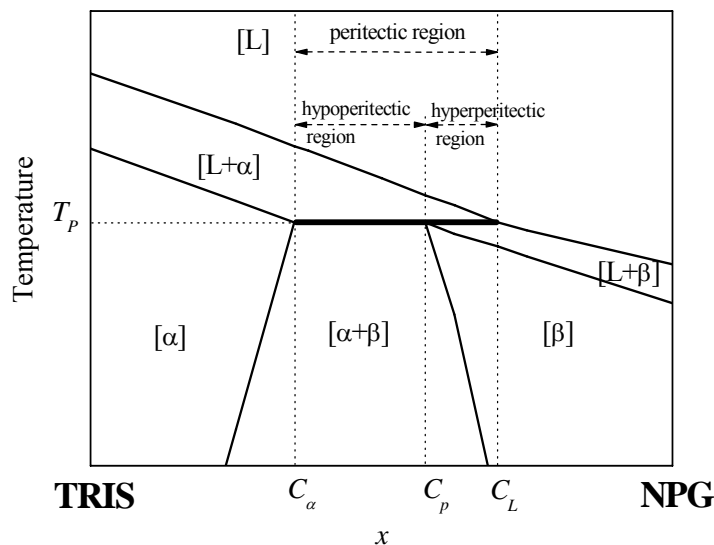


Figure 1. Detail of the TRIS –NPG phase diagram. At the peritectic temperature T_p and the peritectic concentration C_p the primary $[\alpha]$ phase, the peritectic $[\beta]$ phase, and the liquid phase $[L]$ are in equilibrium.

Experimental procedure

The organic substances TRIS and NPG were delivered as powder from Adrich [28] with an indicated purity of 99% and 99.9+%, respectively. Both substances are highly hygroscopic [29], whereby, the water content of the organic substance NPG was reduced by a drying process at 310 K for 24 hours. TRIS, sensitive to long time annealing and delivered with high-purity, was used without further purification. All operations were done in an argon atmosphere within a glove box.

The alloy preparation for the hypoperitectic concentration was done by mixing the powder of both organic substances in a glass container. Subsequently, the powder was heated up to the liquid state and cooling down to room temperature and stored for further use.

Extra large but thin rectangle glass samples ($0.1 \times 2.0 \text{ mm}^2$ inner dimensions with $100 \mu\text{m}$ wall thickness) were filled with liquid alloy by capillary force on a heater within the glove box. The sample itself has a length of more than 20 cm and 4 cm observation length can be used within the micro Bridgman-furnace. The movement of the glass sample through the furnace is PC-controlled which allows the application of different cooling rates.

The furnace itself consists of a heating and a cooling zone departed by a small adiabatic observation gap of $3.6 \pm 0.1 \text{ mm}$, see Fig. 2.

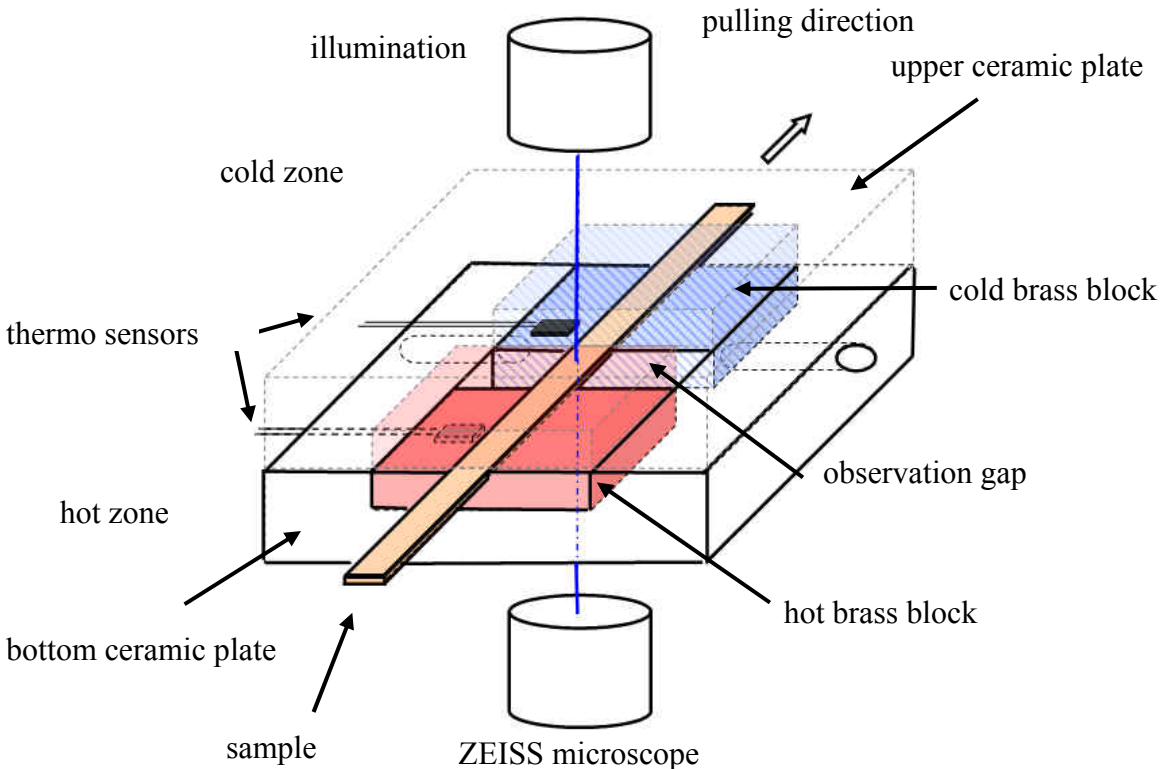


Figure 2: Sketch of the micro Bridgman-furnace.

The hot parts of the Bridgman-furnace are controlled by electrical resistant heaters and the cold parts are cooled by circulating water. The temperatures of the hot zone were measured with Pt 100 temperature sensors placed inside each brass block and regulated independently by a EUROTHERM 2408 controller [30] with an accuracy of $\pm 0.1 \text{ K}$. The temperature of the cold zone was measured with a Pt 100 temperature sensor placed between the brass blocks and regulated by a water cooling system with an accuracy of $\pm 0.5 \text{ K}$ measured within the water tank of the pump. A slot of $0.4 \times 2.5 \text{ mm}^2$ is milled in the hot and cold brass block of the bottom plate to host the sample.

The sample are illuminated from the top and observed from the bottom with the used ZEISS microscope. The construction of the Bridgman-furnace enables a field of view of $3180 \times 2760 \mu\text{m}^2$.

For the optical investigations, the microscope was equipped with a ½” Pulnix TMC-6700 digital camera with a resolution of 648 x 484 pixels. During solidification the taken images were recorded simultaneously with relevant temperatures from the furnace.

For the experiments, the micro Bridgman-furnace is preheated to bring the entire system, furnace and microscope, in a thermally equilibrated stage. After 1 hour the desired temperature gradient of $G_T = 14.5$ K/mm in the furnace is stable and a sample is placed into the furnace. The sample was held at least 30 minutes to prepare a planar solid/liquid interface. Now, the sample is ready for the solidification experiment and the optical system is started to record pictures and temperatures. Solidification experiments were carried out in two different ways: (i) at a constant pulling rate close to the constitutional undercooling limit with a corresponding concentration profile in front of the planar solid/liquid interface, or (ii) the sample was moved with a high pulling rate above the morphological stability limit (here $V_p = 115$ $\mu\text{m/s}$) for 30 seconds to create localized concentration fields around dendrites tips. Afterwards, the sample was moved with a pulling rate clearly below the morphological stability limit (here $V_p \leq 0.89$ $\mu\text{m/s}$) through the furnace.

Results and discussion

The investigations of a hypoperitectic alloy with $x = 0.5$ mol fraction NPG with solidification rates from 1.28 $\mu\text{m/s}$ to 0.06 $\mu\text{m/s}$ and two different initial solid/liquid interfaces show a wide range of solidification morphologies. We are able to observe simultaneous growth of $[\alpha]$ and $[\beta]$ phases in form of an oscillating coupled growth and isothermal coupled growth. The results are published and discussed in [25, 27].

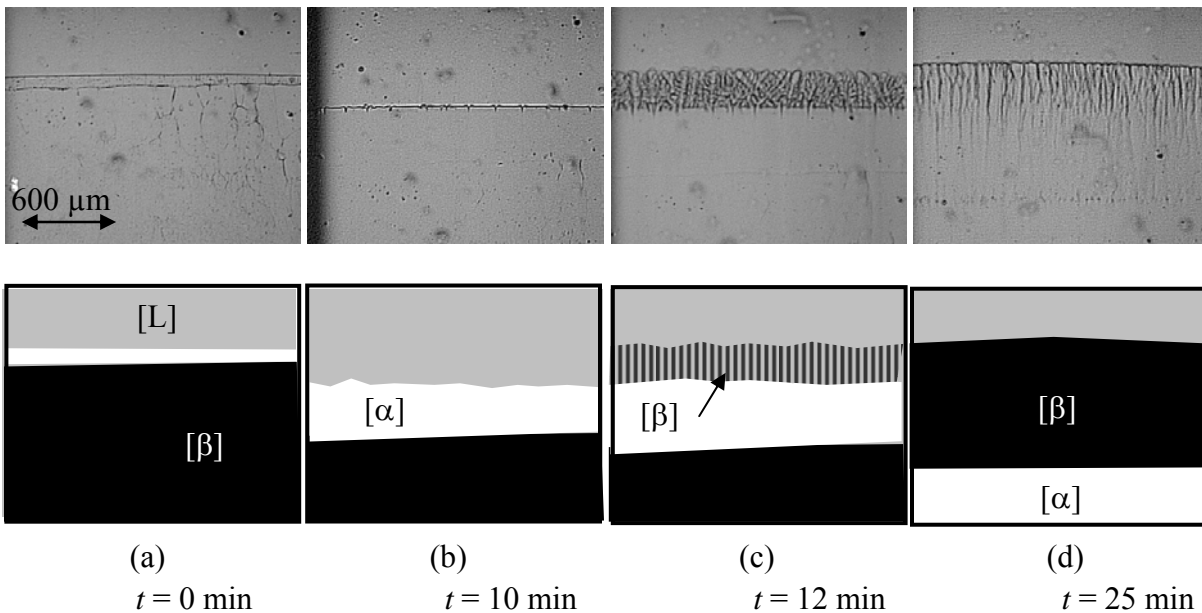


Figure 3. Development of layered solidification structure.

In some cases only the change from $[\alpha]$ planar growth to $[\beta]$ planar growth or vice versa was observed. In other cases we found the formation of layers by the mechanism shown in Fig.3a-d.

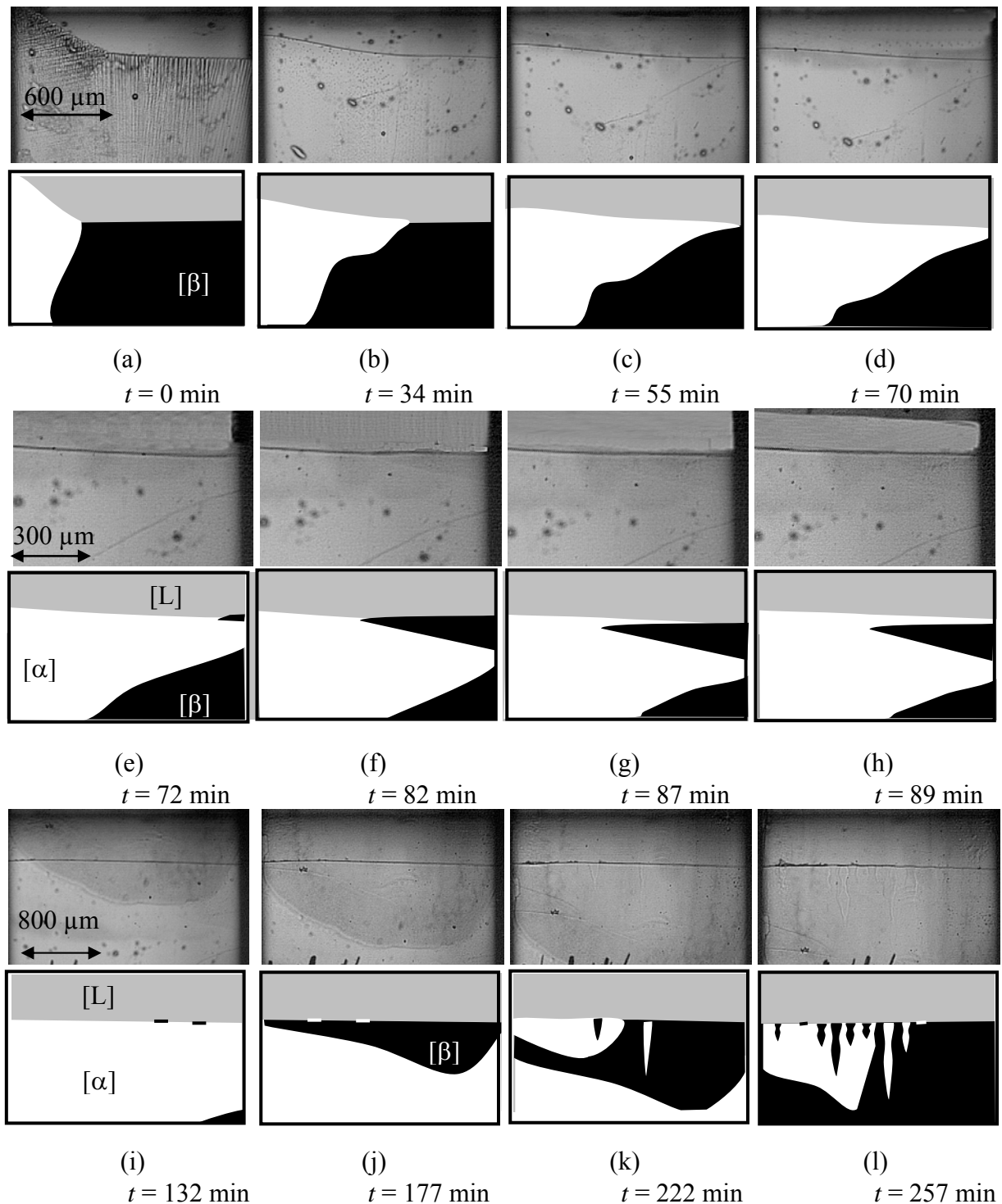


Figure 4. Evolution of the solidification morphology from a planar solid/liquid interface to an isothermal coupled growth. Note that the dark and bright grey shadows visible in Fig. 4i-k result from an uneven sample illumination.

Here, the solidification starts with a planar interface of the $[\beta]$ phase and the formation of an $[\alpha]$ band along the solid/liquid interface (Fig. 3a). Now, the solid/liquid interface goes to a lower temperature and became unstable (Fig. 3b). In this moment, the $[\beta]$ phase nucleates multiple on

the liquid/[α] interface and start to propagate as dendrites (Fig. 3c). As soon as the dendrite tips reach the solidus line of the [β] phase the solidification morphology transforms to a planar solid/liquid interface, see Fig. 3d. The cycle from Fig. 3b to Fig. 3d was observed 3 times with different time intervals in between.

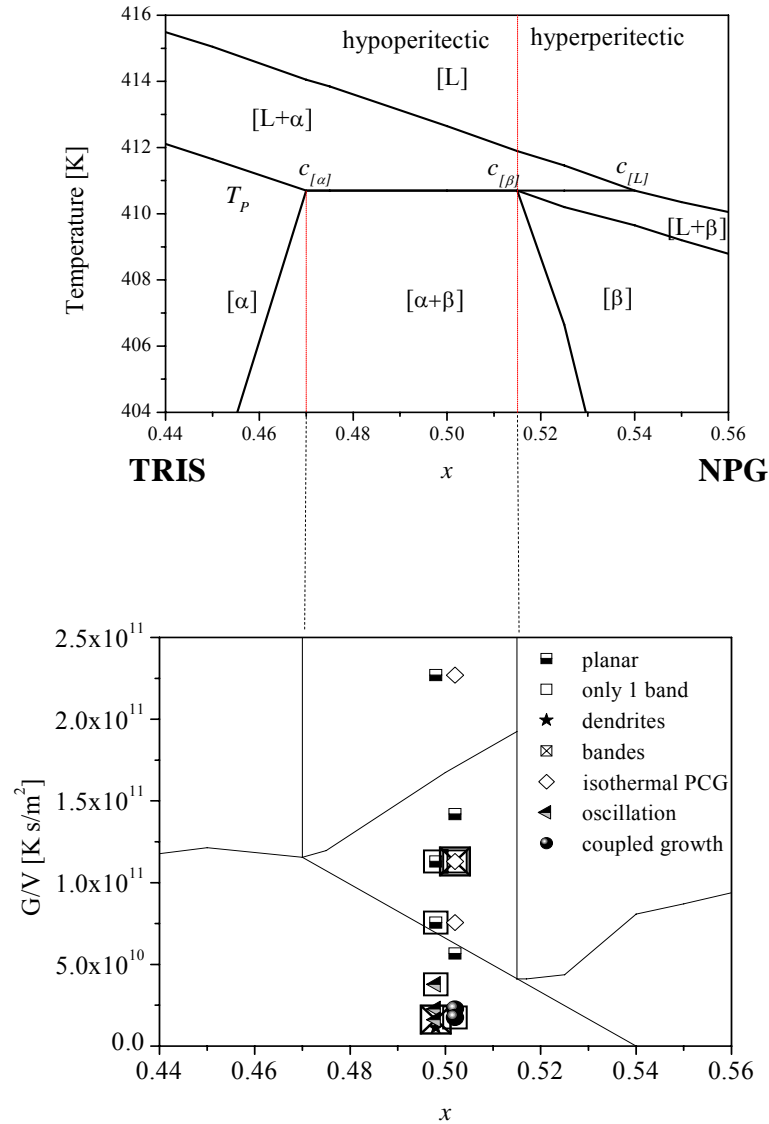


Figure 5: Peritectic region of the phase diagram and calculated microstructures depending on the applied G/V and the mol fraction x as full lines. The solidification morphologies for a hypoperitectic concentration are given as symbols. Experiments with a initial planar front are in the left column and results with a dendritic/cellular initial interface are on the right one.

Another form of layered solidification structures is shown in Fig. 4. Here, the initial solid/liquid interface is dendritic/cellular. During the fast movement of the sample the [α] phase nucleates on the wall or on the wall-solid-liquid junction, see Fig 4a. Following this, the pulling rate is changed from fast movement with $V_p = 115 \mu\text{m/s}$ to a slow movement with $V_p = 0.13 \mu\text{m/s}$.

Within the first 10 minutes the interface changes into a planar solidification morphology. The $[\alpha]$ phase, visible on the left corner of the picture in Fig. 4a, grows laterally with $V_\alpha = 0.34 \pm 0.05 \mu\text{m/s}$ along the solid/liquid interface of the $[\beta]$ phase, see Fig. 4a-c. The entire $[\beta]$ phase is overgrown in Fig. 4d and only the $[\alpha]$ phase grows further on. After the growth of an $[\alpha]$ phase band of $133 \pm 22 \mu\text{m}$ the $[\beta]$ phase nucleates on the solid/liquid/wall junction and starts to grow from the right side to the left side of the sample with $V_\beta = 1.11 \pm 0.1 \mu\text{m/s}$ (see Fig. 4e-f). Whereby, the $[\beta]$ phase is overgrown by the $[\alpha]$ phase, with $V_\alpha = 0.69 \pm 0.1 \mu\text{m/s}$, before the $[\beta]$ phase reaches the other side of the sample, as visible in Fig. 4g-h. Only a section with a maximum width of $166 \pm 22 \mu\text{m}$ is created. The $[\alpha]$ phase grows stable for further $200 \pm 22 \mu\text{m}$ before the $[\beta]$ phase nucleates again. Now, nucleation takes place on the solid/liquid interface with a distance between the nucleation events of $500 \pm 120 \mu\text{m}$ (Fig. 4i). The $[\beta]$ phase overgrows with $V_\beta = 0.46 \pm 0.05 \mu\text{m/s}$ the $[\alpha]$ phase along the entire solid/liquid length and creates a new $[\beta]$ phase band with a maximum of $535 \pm 20 \mu\text{m}$ and a minimum of $20 \mu\text{m}$. Further on, the $[\alpha]$ phase nucleates at the solid/liquid interface of the $[\beta]$ phase (Fig. 4j) and starts to grow laterally with $V_\alpha = 0.51 \pm 0.05 \mu\text{m/s}$. Before the $[\alpha]$ phase overgrows the $[\beta]$ phase multiple nucleation events happen on the solid/liquid interface (Fig. 4k). The distance between the nucleation events is now gradually reduced and the solidification morphology changes to isothermal coupled growth.

It is important to notice that all lateral growth velocities are faster than the solidification velocity in pulling direction. Further more, the small thickness of the sample suppresses convection. Nevertheless, only parts of bands were grown. Instead, the layered structure of bands changes to isothermal peritectic coupled growth [22]. It seems that in the present NPG-TRIS system nucleation dominates against lateral growth. The results of our investigations for a hypoperitectic concentration with $x = 0.5$ are gathered in the microstructure map shown in Fig. 5. For a better visualization experiments with an initial planar front are put on the left side and the ones with an initial dendritic/cellular interface are put on the right side.

Conclusions

We have investigated the relationship between solidification velocity and the solid/liquid interface morphology during solidification of an alloy of hypoperitectic composition at $x = 0.5$. Experiments were carried out in a micro Bridgman-furnace at different solidification rates and a constant temperature gradient. For pulling rates above the morphology stability limit of both solid phases we found an oscillatory solidification dynamic of dendritic/cellular kind [25]. For pulling rates below these limits we observed (i) a change of planar growth from on to the other solid phase, (ii) isothermal coupled growth, and (iii) lateral bands which finally also turn into isothermal coupled growth. The results show no significant dependence on whether the initial solid/liquid interface was planar or dendritic/cellular. Although we found that the lateral growth of the respective other phase is much faster than the forwards solidification rate, multiple nucleation promote the formation of isothermal couple growth.

Acknowledgements

This work was supported in part by the European Space Agency ESA and in part by the Austrian Space Agency ASA through means of the ESA map project METCOMP.

References

- [1] R. Trivedi, *Metall. Mater. Trans.*, 26A (1995) 583-90.
- [2] J.S. Park, R. Trivedi, *J. Cryst. Growth*, (1998) pp. 511.
- [3] H. Yasuda, I. Ohnaka, K. Tokieda, Solidification processing. University of Sheffield 1997, 44-8.
- [4] O. Hunziker, M. Vandyoussefi, W. Kurz, *Acta Mater*, 46 (1998) 6325-36.
- [5] B. Chalmers, *Physical Metallurgy*, New York Wiley (1959)
- [6] T.S. Lo, A. Karma, M. Plapp, *Phys Rev E*, 63 (2001) pp. 031504.
- [7] Y. Li, S.C. Ng, H. Jones, *Scripta Mater.*, 39 (1998) 7-11.
- [8] P. Busse, F. Meissen, *Scripta Mater.*, 36 (1997) 653-8.
- [9] L.S. Luo, Y.Q. Su, J.J. Guo, X.Z. Li, S.M. Li, H. Zhong, L. Liu, H.Z. Fu, *J. Alloys Comp.*, 461 (2008) 121-7.
- [10] Y.Q. Su, L.S. Luo, X.Z. Li, J.J. Guo, H.M. Yang, H.Z. Fu, *Appl. Phys. Lett.*, 89 (2006) 2319181-3.
- [11] L.S. Luo, Y.Q. Su, X.Z. Li, J.J. Guo, H.M. Yang, H.Z. Fu, *Appl. Phys. Lett.*, 92, (2008) 0619031-3.
- [12] T.S. Lo, S. Dobler, M. Plapp, A. Karma, W. Kurz, *Acta Mater.*, 51 (2003) 599-611.
- [13] S. Dobler, T.S. Lo, M. Plapp, A. Karma, W. Kurz, *Acta Mater.*, 52 (2004) 2795-808.
- [14] J.H. Lee, J.D. Verhoeven, *J. Cryst. Growth*, 144 (1994) 353-66.
- [15] H.W. Kerr, W.Kurz, *Int. Mater. Rev.*, 41 (1996) 129-64.
- [16] W.Luo, J.Shen, Z.Min, H.Fu, *J. Cryst. Growth*, 24 (2008) 5441-6.
- [17] W.Z. Luo, J. Shen, Z.X. Min, H.Z. Fu, *Mater. Lett.*, 63 (2009) 1419-21.
- [18] L. Sturz, V.T. Witusiewicz, U. Hecht, S.Rex, *J. Crystal Growth*, 270 (2004) 273-82.
- [19] M. Barrio, D.O. Lopez, J.L. Tamarit, P. Negrier, Y. Haget, *J. Solid State Chem.*, 124 (1996) 29-38.
- [20] W.J. Boettinger, *Metall.Trans.*, 5 (1974) 2023-31.
- [21] R. Trivedi, J.S. Park, *J. Cryst. Growth*, 235 (2002) 572-88.
- [22] F. Kohler, L. Germond, J.D. Wagnière, M.Rappaz, *Acta mater*, 57 (2009) 56-68.
- [23] R. Trivedi, *Scripta Mat.* 53 (2005) 47-52.
- [24] J. Mogeritsch, A. Ludwig, S. Eck, M. Grasser, B. McKay, *Scripta Mater.*, 60 (2009) 882-5.
- [25] A. Ludwig, J. Mogeritsch, M. Grasser, *Trans. Indian Inst. Met.*, 62 (2009), 433-6
- [26] J. Mogeritsch, S. Eck, M. Grasser, A. Ludwig, *Mater. Sci. Forum*, 649 (2009) 159-64.
- [27] J. Mogeritsch, A. Ludwig, John Hunt International Symposium, London (2011), in print.
- [28] <http://www.sigmaaldrich.com> (access date: 30.10.2011).
- [29] NPG CAS-No 126-30-7 and TRIS CAS-No 77-86-1.
- [30] <http://www.eurotherm.com> (access date: 30.10.2011).

ISS-EXPERIMENTS OF COLUMNAR-TO-EQUIAXED TRANSITION IN SOLIDIFICATION PROCESSING

Laszlo Sturz¹; Gerhard Zimmermann¹; Charles-Andre Gandin²; Bernard Billia³; Nathalie Mangelinck³; Henry Nguyen-Thi³; David John Browne⁴; Wajira U. Mirihanage⁴; Daniela Voss⁵; Christoph Beckermann⁶; Alain Karma⁷

¹Access e.V.;

²MINES ParisTech CEMEF Sophia Antipolis;

³Université P. Cézanne, Marseille;

⁴University College Dublin;

⁵European Space Agency - ESA/ESTEC;

⁶University of Iowa, USA;

⁷Northeastern University, USA;

Keywords: Solidification, Microgravity, Grain structure

Abstract

The main topic of the research project CETSOL in the framework of the Microgravity Application Promotion (MAP) programme of the European Space Agency (ESA) is the investigation of the transition from columnar to equiaxed grain growth during solidification. Microgravity environment allows for suppression of buoyancy-driven melt flow and for growth of equiaxed grains free of sedimentation and buoyancy effects. This contribution will present first experimental results obtained in microgravity using hypo-eutectic AlSi alloys in the Materials Science Laboratory (MSL) on-board the International Space Station (ISS). The analysis of the experiments confirms the existence of a columnar to equiaxed transition, especially in the refined alloy. Temperature evolution and grain structure analysis provide critical values for the position, the temperature gradient and the solidification velocity at the columnar to equiaxed transition. These data will be used to improve modeling of solidification microstructures and grain structure on different lengths scales.

Introduction

Casting of metallic alloys often results in a structure which consists of several dendritic grains. This grain structures is the result of a competition between the growth of several arrays of dendrites that develop under constrained and unconstrained conditions. In case of unidirectional solidification typically columnar dendritic grains exist. At high cooling rates or low temperature gradients nucleation and growth of equiaxed grains in the undercooled melt may occur. The often observed change in grain structure is described as a columnar-to-equiaxed transition (CET) [1-4].

The effect of CET was intensively investigated in the last decades because it's of high relevance in industrial application. Therefore, several computational models of the CET were developed. Volume-averaged multi-phase/-scale models [5-8] calculate the transport phenomena on the scale of an entire casting. Here, the CET can be determined based on the volume fractions of columnar and equiaxed grains. Meso-scale models track the growth of the envelope of each individual grain. Examples are the cellular-automaton finite-element (CAFE) model [9] or the front-tracking models [10-12]. Micro-scale models and phase field models resolve details of the

solid-liquid interface and, thus, do not require a separate expression for dendrite tip growth or a criterion for the CET [13, 14]. In spite of the fact that these numerical models are able to describe the CET quite well, there are some shortcomings in the modeling studies. Especially the treatment of nucleation and growth of equiaxed grains is the purpose of numerical studies. In the presence of a gravitational field, settling or floatation of solid particles in the melt and their interaction with the development of the columnar grain structure as well as natural convection of the melt itself must be taken into account in order to predict the grain structure of a casting.

Here, a microgravity environment allows for suppression of buoyancy-driven melt flow and so for growth of equiaxed grains free of sedimentation and buoyancy effects. Therefore, experiments in microgravity provide unique data for testing fundamental theories of grain structure formation. To carry out such experiments and to model the process of columnar to equiaxed transition is the topic of the research project Columnar-to-Equiaxed Transition in SOLidification Processing (CETSOL) in the framework of the Microgravity Application Promotion (MAP) programme of the European Space Agency (ESA). Some results of experiments performed in microgravity on the International Space Station (ISS) are shown in the paper.

Set-up of the microgravity experiments

To investigate the columnar-to-equiaxed transition under diffusive conditions for heat and mass transport, experiments in microgravity were performed in the Materials Science Laboratory (MSL) with the Low Gradient Furnace (LGF) module onboard the International Space Station (ISS). For a first batch, six samples from Al-7wt%Si alloy (refined and non-refined) were processed. Rod-like samples of diameter 7.8mm and length 245.0mm were integrated in tantalum cartridges, which were also equipped with 12 thermocouples to measure the axial temperature distribution along the sample. **Figure 1** shows such a fully integrated MSL-SCA cartridge. More details are given in [15]. For sample processing the MSL-SCA set-up is inserted into the furnace, which consists of a ‘cold zone’ with 3 heaters, a ‘hot zone’ with 4 heaters, separated by an “adiabatic zone”. By controlling the temperatures of the cold and the hot zone a temperature gradient along the sample axis is applied. Melting or solidification of the metallic alloy is realized by a movement of the furnace insert along the axis of the fixed sample with a defined speed.

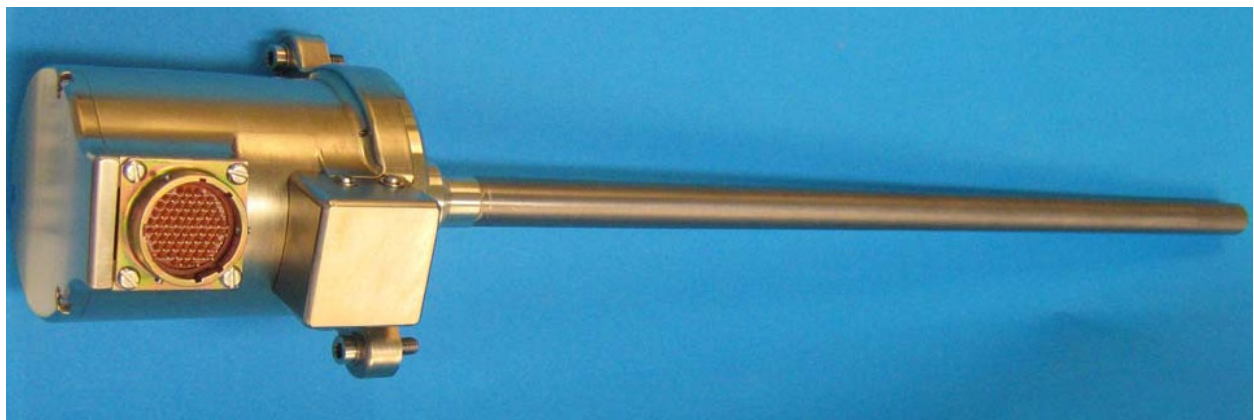


Figure 1: Fully integrated MSL-SCA cartridge to be processed in the MSL-LGF furnace on ISS.

The first phases of the experimental procedure were identical for all six samples FM#1 to FM#6 and result in an initial temperature gradient in the sample of 0.9K/mm. In samples FM#3 and FM#4 non-refined binary Al-7wt%Si alloys were used, while all other samples contain 0.5wt% of TiB₂ for grain refinement (AlSi7 + g.r.). The main process parameters are summarized in **Table 1**. The experiments differ mainly in the homogenization time t_H and in the parameters for the solidification phase 2. In this phase a transition from columnar dendritic growth to equiaxed growth (CET) should be triggered either by increasing the furnace velocity to $v_2=200\mu\text{m/s}$ or by decreasing the temperature gradient [15].

Table 1: Process parameters of the CETSOL1 flight experiments

Sample No.	Alloy	Homogenization time t_H (min)	Solidification phase 1		Solidification phase 2			Fast movement v_3 ($\mu\text{m/s}$)
			v_1 ($\mu\text{m/s}$)	z_1 (mm)	v_2 ($\mu\text{m/s}$)	z_2 (mm)	dT/dt (K/min)	
FM#1	AlSi7+g.r.	10	10	20	200	50	-4	3000
FM#2	AlSi7+g.r.	300	10	20	200	50	-4	3000
FM#3	AlSi7	300	10	20	200	50	-4	3000
FM#4	AlSi7	300	10	20	10	20	-4	3000
FM#5	AlSi7+g.r.	10	10	20	10	20	-4	3000
FM#6	AlSi7+g.r.	300	10	20	10	20	-4	3000

Grain structure evaluation

As an example, **Figure 2** shows the processed sample CETSOL1 FM#2. The maximum melting position at $z=68\text{mm}$ can be identified, which separates the non-molten region and the mushy zone region. The adjacent solidification phases are also shown qualitatively (see also Table 1).

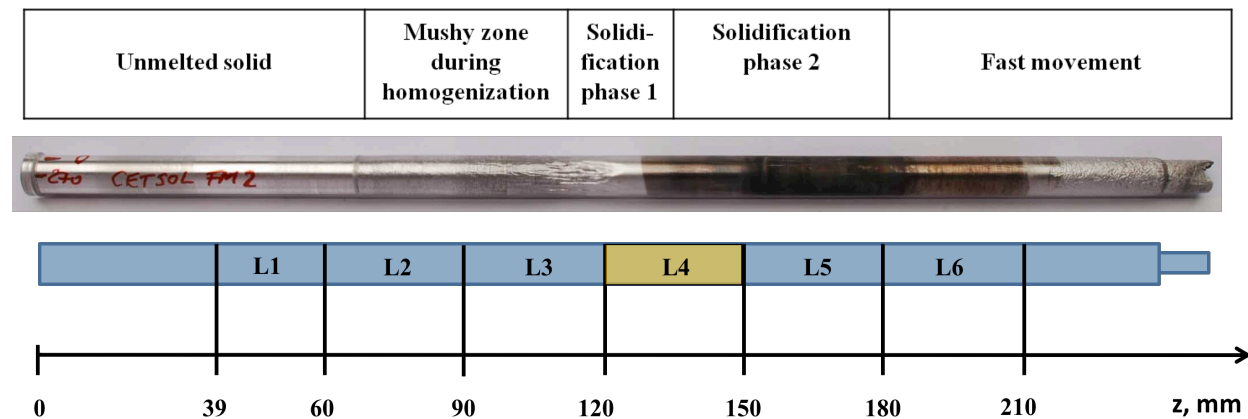


Figure 2: Image of the processed sample CETSOL1 FM#2 with indication of the different regions related to the solidification process (top) and markings for metallographic preparation of longitudinal cross-sections (below).

For analyzing the microstructure and the grain structure the samples have to be sectioned. First, the samples were cut into pieces of length 30mm to analyze the transversal cross-sections. Second, each of these pieces was sawed along the axis to get two halves for analysis of the longitudinal cross-sections L1 to L6 (see also Figure 2).

To determine the microstructure the samples were polished, slightly etched and observed with a microscope. **Figure 3** shows the longitudinal cross-section L4 of FM#2 sample. The length of the cross-section is 30mm, the position values are referred to the non-molten end of each sample. The left part of the cross-section shows a structure with rather large primary dendrites which corresponds to the solidification phase 1 with furnace velocity $v_1=10\mu\text{m/s}$. The increase in furnace velocity to $v_2=200\mu\text{m/s}$ results in the development of a much finer dendritic microstructure.

To identify the grain structure qualitatively the cross-sections were electrolytically etched and analyzed in a polarized light microscope. Then, different colors represent different crystallographic orientations of the dendritic grains [16]. As a result, in cross-section L4 of sample FM#2 two large columnar grains can be identified on the left side (**Figure 4**). The increase of the furnace velocity from $v_1=10\mu\text{m/s}$ to $v_2=200\mu\text{m/s}$ results in the development of many smaller grains with different orientations.

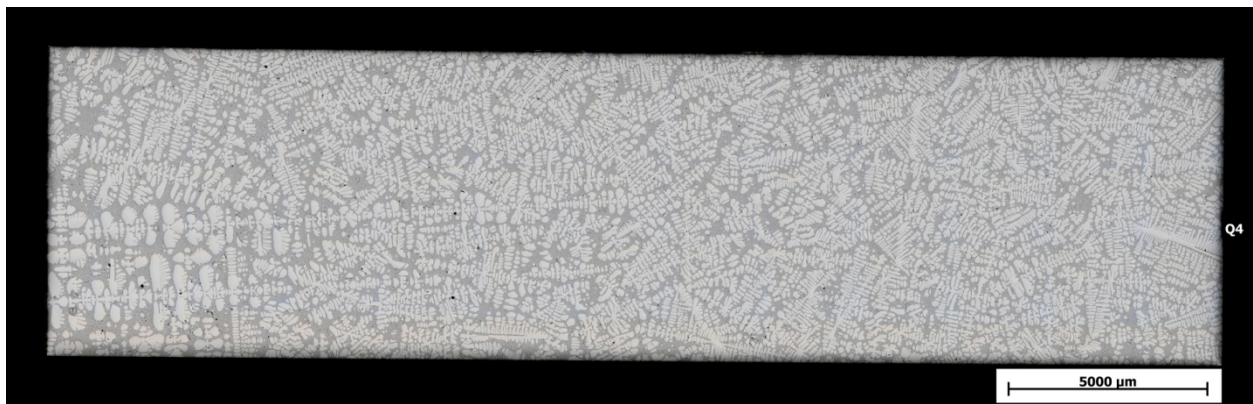


Figure 3: Microstructure in the longitudinal cross-section L4 ($z = 120\text{mm}$ to 150mm) of FM#2 flight sample; direction of solidification from left to right.

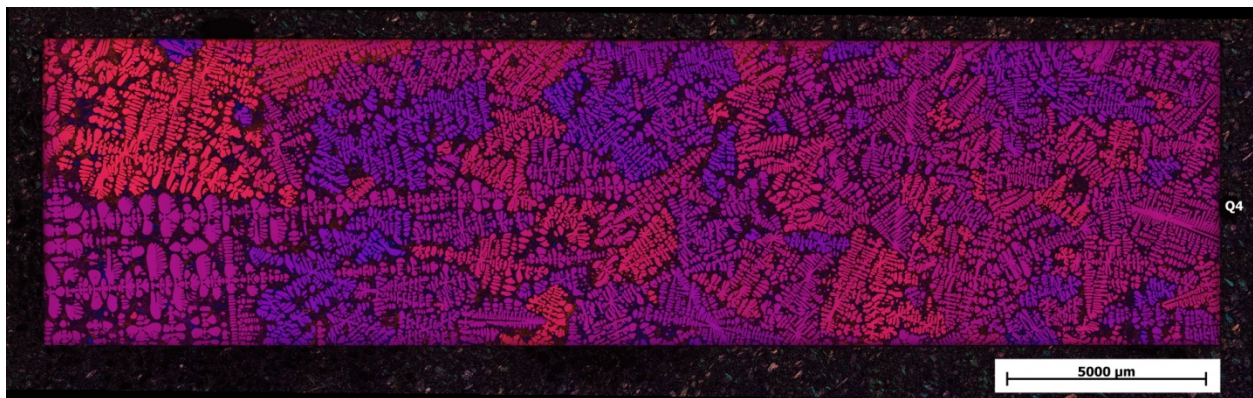


Figure 4: Grain structure in cross-section L4 ($z = 120\text{mm}$ to 150mm) of FM#2 sample obtained from electrolytical etching.

For quantitative evaluation of the grain structure the cross-section was vibratory polished for many hours. This allows for a surface which is exceptional flat and nearly free of stress. Grain orientation measurements were performed in a scanning electron microscope using an electron backscatter diffraction device (SEM-EBSD) [17]. The size of the field of view is typically $4\text{mm} \times 8\text{mm}$. From 8 subsequent measured fields of view the grain structure in the cross-sections L4 of FM#2 sample was analysed quantitatively. For each grain the fibre direction (pole 100) in transverse direction was determined. Related to the rod-like sample this direction corresponds to the sample axis. **Figure 5** shows the resulting grain structure in cross-sections L4 of FM#2 sample. The grey level indicates the deviation of the crystallographic axis of each grain from the sample axis. Black colour corresponds to 0° deviation angle and white colour to the maximum deviation angle of 54.74° . The different grey levels indicate a variety of grains with different orientations, which is characteristic for equiaxed grain growth.

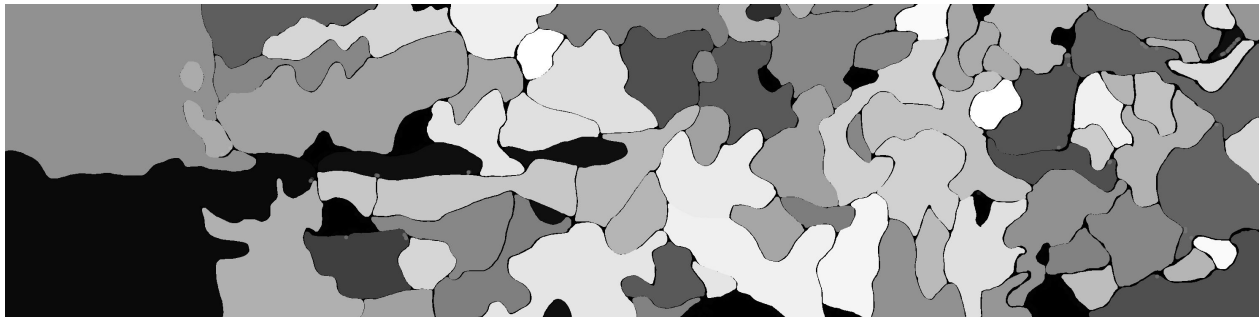


Figure 5: Grain structure in cross-sections L4 ($z = 120\text{mm}$ to 150mm) of FM#2 sample obtained from EBSD measurements with crystallographic orientation related to the sample axis (white: deviation angle 0° ; black: maximum deviation angle 54.74°).

Determination of CET

For determination of the columnar-to-equiaxed transition in FM#2 flight sample the grain structure was evaluated quantitatively from the electrolytically etched longitudinal cross-sections L3 to L5 (**Figure 6**). The grain sizes were measured using digital image analysis. Averaging was performed over all grains being totally or partly within a sheet of $\pm 2\text{mm}$ around the actual position. The maximum value corresponds to columnar growth of just two large grains in the first solidification phase. Equiaxed growth is characterized by a significant decrease of the average grain size. Thus, based on this criterion and this type of evaluation, the region of CET is determined and is centered at $z = 126 \pm 2\text{mm}$.

The critical parameters for CET, i.e. a critical temperature gradient of about $G_c = 0.75\text{K/mm}$ and a critical velocity of the isotherm of about $v_c = 87\mu\text{m/s}$, were determined from the temperature measurements along the sample axis and were already given in [15].

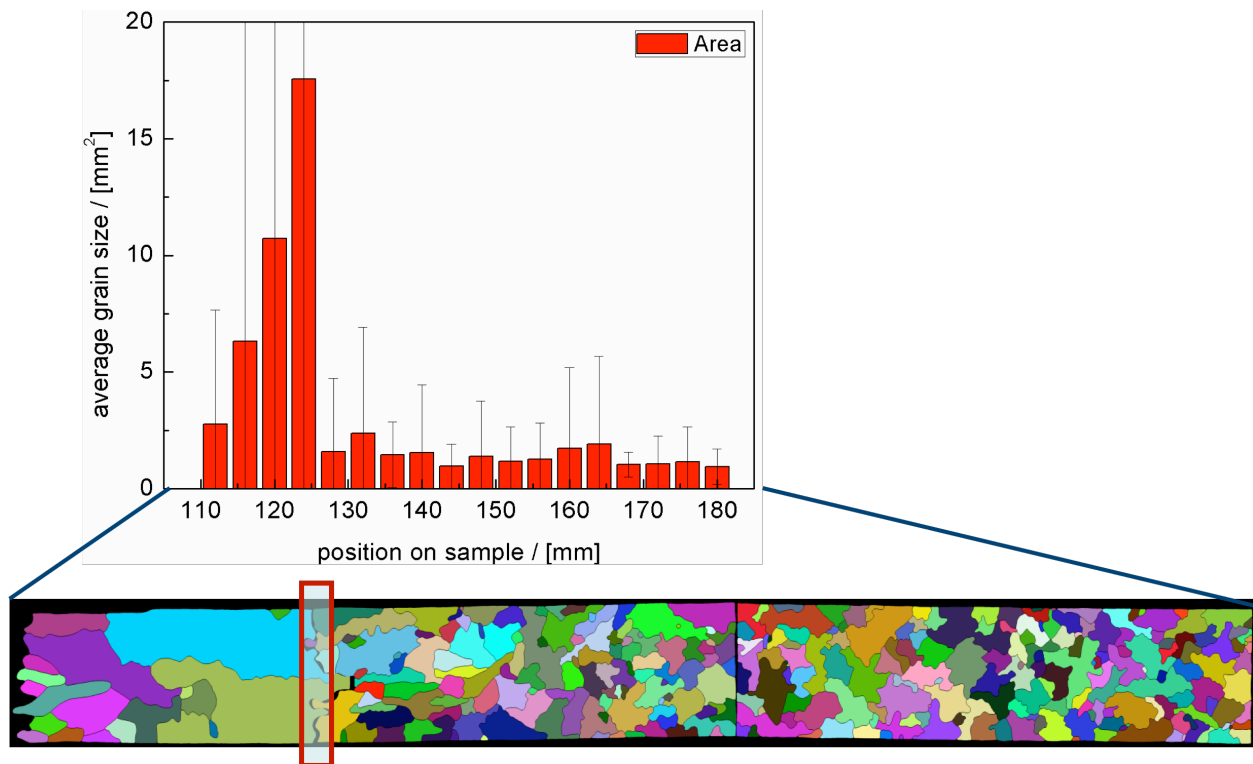


Figure 6: Grain structure identified from longitudinal cross-sections L3 to L5 ($z =90\text{mm}$ to 180mm) of FM#2 sample (below) and determination of averaged grain size (top).

Conclusions

This paper reports on results obtained during metallic alloy solidification experiments onboard the International Space Station in the Materials Science Laboratory using the Low Gradient Furnace module. Within a first batch six experiments with Al-7wt%Si alloy were performed successfully to investigate columnar-to-equiaxed (CET) solidification behaviour in microgravity. Qualitative and quantitative grain structure analysis using electrolytical etching and EBSD-technique show that CET is observed in the grain refined samples. Here, the microgravity environment allows for pure diffusive conditions for heat and mass transfer in the melt and therefore for investigation of CET without buoyancy convection and sedimentation of equiaxed grains in the melt. The critical parameters for CET were determined from analysis of thermal data and taking into account the grain structure. These data basis will be used for calibration and further development of numerical model predicting CET.

Acknowledgments

This work was conducted within the ESA MAP programme ‘CETSOL’, the ESA PRODEX programme, and also funded by the German Space Agency DLR and the French Space Agency CNES.

References

1. J.D. Hunt, "A numerical analysis of time dependent isolated dendritic growth for conditions

- near the steady state," *Acta Metall. Mater.*, 38 (1990), 411-418.
2. Ch.-A. Gandin, "From constrained to unconstrained growth during directional solidification," *Acta Materialia* 48 (2000), 2483-2501.
 3. D.J. Browne and J.D. Hunt, "A fixed grid front-tracking model of the growth of a columnar front and an equiaxed grain during solidification of an alloy," *Numerical Heat Transfer, Part B: Fundamentals* 45 (2004), 395-419.
 4. L. Sturz and G. Zimmermann, "Investigations on Columnar-to-Equiaxed Transition in Binary Al Alloys with and without Grain Refiners," *Materials Science Forum* 508 (2006), 419-424.
 5. C. Beckermann and C.Y. Wang, "Multi-Phase/-Scale Modeling of Transport Phenomena in Alloy Solidification," *Annual Review of Heat Transfer VI*, ed. C.L. Tien, Begell House, New York, NY, (1995), 115-198.
 6. M.A. Martorano et al., "A solutal interaction mechanism for the columnar-to-equiaxed transition in alloy solidification," *Metall. Mater. Trans. A*, 34A (2003), 1657-1674.
 7. A. Ludwig and M. Wu, "Modeling the columnar-to-equiaxed transition with a three-phase Eulerian approach," *Mater. Sci. Eng.*, A413-414 (2005), 109-114.
 8. A. Noepfel et al., "Numerical modelling of columnar to equiaxed transition – application to microgravity experiments," *Int. Journal of Cast Metals Research* 22 (2009), 34-38.
 9. Ch.-A. Gandin and M. Rappaz, "A coupled finite element-cellular automaton model for the prediction of dendritic grain structures in solidification processes," *Acta Metall. Mater.* 42, (1994), 2233-2246.
 10. I. Steinbach et al., "Three-dimensional modeling of equiaxed dendritic growth on a mesoscopic scale," *Acta Mater.* 47, (1999), 971-982.
 11. P. Delaleau et al., "Mesoscopic Simulation of Dendritic Growth Observed in X-ray Video Microscopy During Directional Solidification of Al–Cu Alloys," *ISIJ International* 50 (2010), 1886-1894.
 12. J. Banaszek et al., "Natural Convection and Columnar-to-Equiaxed Transition Prediction in a Front-Tracking Model of Alloy Solidification," *Metallurgical Materials Transact.* A38 (2007), 1476-1484.
 13. H.B. Dong and P.D. Lee, "Simulation of the columnar-to-equiaxed transition in directionally solidified Al–Cu alloys," *Acta Mater.* 53 (2005), 659-668.
 14. A. Badillo and C. Beckermann, "Phase-field simulation of the columnar-to-equiaxed transition in alloy solidification," *Acta Mater.* 54 (2006), 2015-2026.
 15. G. Zimmermann et al., "Investigation of columnar-to-equiaxed transition in solidification processing of AlSi alloys in microgravity – The CETSOL project", accepted in *IOP Conference Series Materials Science and Engineering, ISPS4*.
 16. E. Schaberger, F. Grote and A. Schievenbusch, "Farbätzung und Farbbildanalyse - Ein Weg zur Charakterisierung von Gefügen innovativer Gusswerkstoffe," *Prakt. Metallographie* 37 (2000), 419-434.
 17. A.J. Schwartz et al., *Electron Backscatter Diffraction in Materials Science* (Springer Science+Business Media, 2nd edition, 2009)

Liquid droplet dynamics in gravity compensating high magnetic field

V. Bojarevics, S. Easter and K. Pericleous

University of Greenwich, Park Row, London SE10 9LS, UK

Keywords: Magnetic levitation, droplet oscillations, free surface dynamics, magnetohydrodynamics

Abstract

Numerical models are used to investigate behavior of liquid droplets suspended in high DC magnetic fields of various configurations providing microgravity-like conditions. Using a DC field it is possible to create conditions with laminar viscosity and heat transfer to measure viscosity, surface tension, electrical and thermal conductivities, and heat capacity of a liquid sample. The oscillations in a high DC magnetic field are quite different for an electrically conducting droplet, like liquid silicon or metal. The droplet behavior in a high magnetic field is the subject of investigation in this paper. At the high values of magnetic field some oscillation modes are damped quickly, while others are modified with a considerable shift of the oscillating droplet frequencies and the damping constants from the non-magnetic case.

Introduction

The electromagnetic (EM) and electrostatic levitation experiments with liquid metal droplets show difficulties related to confinement stability and a need for complex correction functions to establish a correlation between the measurements and the droplet material properties [1,2]. Intense internal fluid flow is visually observed, apparently being in the turbulent regime for earthbound conditions. The combination of AC and DC magnetic fields was recently recognized as an efficient tool for the thermo-physical property measurements without a contact to contaminating walls [3,4]. The intense AC magnetic field required to produce levitation results in turbulent large-scale toroidal recirculation within the droplet, which prevents accurate measurements. The use of a homogenous DC magnetic field allows the toroidal flow to be damped. However the turbulence generated in these conditions makes the effective viscosity to behave in a non-linear fashion depending on the DC and AC magnetic field intensity [4]. The flow in a typical droplet is approaching the conditions with laminar viscosity and heat transfer when a uniform DC magnetic field exceeds about 4-5 T. For even higher DC magnetic field the levitation, using para- and dia-magnetic properties of the materials, can be used for advanced material research [5,6]. The vertical field gradient permits to compensate gravity along the central axis, while the radial variation acts to centre it on the axis for stable levitation. In practice a small vibration of the droplet as a whole remains even in carefully conducted experiments [6]. Frequency measurements using the oscillating drop technique have been conducted for water droplets by Beaunon et al. [5], where estimates were made as to the frequency modification due to the magnetic field. More recent experiments have been conducted by Hill & Eaves [6], in which a derivation of the frequency modifications due to the magnetic field are made and compared with the experimental results.

The oscillations in a high DC magnetic field are quite different for an electrically conducting droplet. In a recent publication [7] an asymptotic solution for very high magnetic field shows damping of the even axisymmetric modes, but the odd modes are not damped or damped

moderately. The asymptotic linear theory predicts a considerable shift of the oscillating droplet frequencies from the non-magnetic case. The droplet behavior in high magnetic field is the subject of investigation in this paper. Numerical models of the flow coupled with the moving free surface give an insight to the dynamics of levitated droplets of various sizes and magnetic field intensities. The realistic gradient fields, as in the solenoidal coils of superconducting magnets, are used for the modeling experiments with electrically non-conducting (water) and conducting (liquid silicon) droplets.

Droplet oscillation numerical model

The free surface shape of the droplet is defined by a deviation from a sphere of radius R_0 . The surface position can be represented in the spherical co-ordinates by a function S of time and the angular coordinates:

$$r_s = R_0 [1 + S(\theta, \phi, t)]. \quad (1)$$

The mode dependent oscillation frequency and damping constants are generally derived by following a perturbation approach. The S function can be represented as a series of spherical harmonics:

$$S(\theta, \phi, t) = \sum_{L=0}^{\infty} \sum_{M=0}^L A_L^M(t) P_L^M(\cos \theta) e^{iM\phi}. \quad (2)$$

The $Y_0^0 = P_0^0$ mode is included to account for conservation of mass (volume) of the sphere with radius R_0 if an initial perturbation of the surface is given. The time-dependent surface coefficients are assumed to be harmonic with exponential damping:

$$A_L^M(t) = e^{(i\omega_L^M - \gamma_L^M)t}. \quad (3)$$

The zero order (in powers of the perturbation amplitude) result for the frequency was obtained by Rayleigh, and is given for a droplet with density ρ and surface tension Γ by:

$$\omega_L^M = \sqrt{L(L-1)(L+2)\Gamma / (\rho R_0^3)}. \quad (4)$$

The damping coefficient for a droplet of viscosity ν was determined by Lamb:

$$\gamma_L^M = (L-1)(2L+1)\nu / R_0^2. \quad (5)$$

The zero order approximation for both the frequency and the damping constant are independent of the azimuthal number M . These formulae provide a good first approximation for low amplitude oscillations of droplets in microgravity conditions where the effects of any external forces used to position the droplet are negligible compared with surface tension and viscous forces. However it is worth noting that these formulae are restricted and are only valid in the limit that the amplitude of oscillation and also non-linear effects tend to zero. Modifications to these have been derived by Tsamopoulos & Brown [8] for ‘moderate amplitude’: the frequency decreases with increasing amplitude and a coupling of modes appears at the second order.

In a recent paper Priede [7], considers the effect of a constant high intensity magnetic field on the oscillation frequency and damping rate of an electrically conducting drop. The magnetic field is shown to significantly alter the dynamics of the droplet with some interesting results. There are two distinct cases: the longitudinal modes when $(L-M)$ is odd and the transversal modes when $(L-M)$ is even. The frequencies for the odd modes including the axisymmetric ($M=0$, of the greatest interest for this paper) are given by:

$$\omega_L^M = \sqrt{(L-1)(L+2)\Gamma / (\rho R_0^3)}, \quad (6)$$

which is \sqrt{L} less than the normal mode frequencies (4). In the following section an outline is given of an axisymmetric and a 3D numerical model that will be used to investigate these effects. Following results are presented that demonstrate quantitatively the theoretical predictions and the

deviations from the zero order asymptotic theory due to the presence of the gravity field and finite amplitude oscillations.

The numerical model uses a grid point formulation of the spectral collocation method [10] with the Chebyshev grid for the radial direction and Fourier in the angular directions. The model uses a coordinate transformation for the free surface, which allows the problem to be solved on a unit sphere. The equations solved by the numerical model are the momentum and mass conservation equations with the modified pressure, $P_{\text{mod}} = P + \rho g R \cos \theta - \chi_v |B|^2 / (2\mu_0)$:

$$\partial_t \mathbf{V} + (\mathbf{V} \cdot \nabla) \mathbf{V} = -\rho^{-1} \nabla P_{\text{mod}} + \nu \nabla \cdot (\nabla \mathbf{V} + \nabla \mathbf{V}^T) + \rho^{-1} \mathbf{J} \times \mathbf{B}; \quad \nabla \cdot \mathbf{V} = 0. \quad (7)$$

The total force due to the magnetic field consists of two components, the Lorentz force due to the conducting properties, which is added to the momentum equations as a body force and the diamagnetic force, which is potential and is implemented in the model as boundary condition to the pressure equation along with the gravitational force, which is also potential. The full boundary conditions for the equations (7) relate the normal stress to the surface tension:

$$\mathbf{e}_n \cdot \Pi \cdot \mathbf{e}_n = \Gamma K, \quad (8)$$

continuity of the velocity field and the tangential stress conditions:

$$\nabla \cdot \mathbf{V} = 0, \quad \mathbf{e}_n \cdot \Pi \cdot \mathbf{e}_{\tau_1} = 0, \quad \mathbf{e}_n \cdot \Pi \cdot \mathbf{e}_{\tau_2} = 0, \quad (9)$$

where $\mathbf{e}_n, \mathbf{e}_{\tau_1}, \mathbf{e}_{\tau_2}$ are the unit vectors normal and tangential to the free surface, Π is the stress tensor, K is the surface curvature, and χ_v is the volumetric magnetic susceptibility. The free surface shape given by (1) is updated at each time step using the kinematic condition:

$$\partial_t \mathbf{r}_s \cdot \mathbf{e}_n = \mathbf{V} \cdot \mathbf{e}_n. \quad (10)$$

The magnetic field in a solenoid is modelled as a superposition of the magnetic field generated by axisymmetric coil filaments of finite cross-section (see Figure 1 as an example). The axisymmetric magnetic field is obtained from the analytical formulae [9].

The stable levitation conditions can be established by adjusting the electric current in the coils to form a minimum in the magneto-gravitational potential:

$$U = g R \cos \theta - \chi_v |B|^2 / (2\rho\mu_0). \quad (11)$$

The electromagnetic body force requires in general an additional equation to be solved for the electric potential (only in the 3D case). The electric current density is given by:

$$\mathbf{J} = \sigma (-\nabla \phi_E + \mathbf{V} \times \mathbf{B}). \quad (12)$$

The equation for the electric potential is obtained from the charge conservation $\nabla \cdot \mathbf{J} = 0$. Taking the divergence of the electric current density gives:

$$\nabla^2 \phi_E = \nabla \cdot (\mathbf{V} \times \mathbf{B}). \quad (13)$$

This equation is solved subject to the condition at the instantaneous drop surface: $\mathbf{J} \cdot \mathbf{e}_n = 0$.

Results & Discussion

The following section contains the results of numerical simulations made using both the 2D axisymmetric [10] and 3D modes compared with experimental results [6] and theoretical asymptotic results [7]. The material chosen for the numerical test cases is either water (diamagnetic, electrically non-conducting) or molten silicon (diamagnetic, electrically conducting) having the material property values given in the Table 1.

Symbol	Quantity	Water	Silicon	Units
Γ	Surface Tension Coefficient	0.0733	0.865	N m^{-1}
ρ	Density	999.0	2510.	Kg m^{-3}
ν	Kinematic Viscosity	1.11e-6	1.0e-6	$\text{m}^2 \text{s}^{-1}$
χ_v	Volumetric Magnetic Susceptibility	-9.0e-6	-4.2e-6	N/A

Table 1. The material property values used for the numerical test cases.

The numerical simulation uses the superposition of the modes $L = 2,3,4,5,6,7$ for axisymmetric surface shape, or $L=2, M=1$ for the 3d test as the initial condition. The amplitude coefficient is chosen to give a deformation of 1% of the unperturbed radius ($R_0 = 5\text{mm}$ or 10mm). A spherically symmetric constant component ($L=0$) is also required to ensure the initial surface shape conserves the mass of the droplet based on the equilibrium spherical radius.

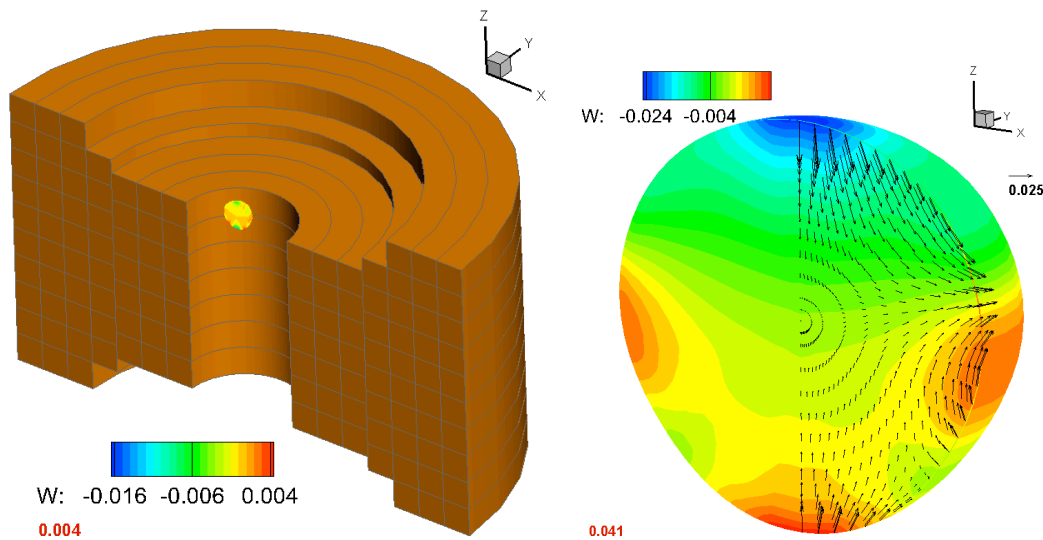


Figure 1. Water droplet $R_0 = 10\text{mm}$ in the bore of solenoid magnet and the initial velocity field (color contours for vertical velocity component W and the scale vector in m/s).

Water Droplet in Solenoid Magnet

Figure 1 shows the droplet in the solenoid magnet and the zoom-in view to the initial velocity field after 41 ms, generated by the axisymmetric surface deformation condition in the simulation. The droplet is positioned in the upper part of the magnet 8 cm above the magnet centre. We attempted to preserve dimensions similar to the experiment [6], however the exact design of the magnet is a proprietary information not available for this modelling work. The magnetic field and the required magneto-gravitational potential (11) are updated at each time step of maximum length 0.000125s. The instantaneous distributions of the magnetic field are computed only in the volume occupied by the droplet as shown in the Figure 2. The magnetic field at the top part of the solenoid is reduced in magnitude relative to the central part where it is about 16.5 T.

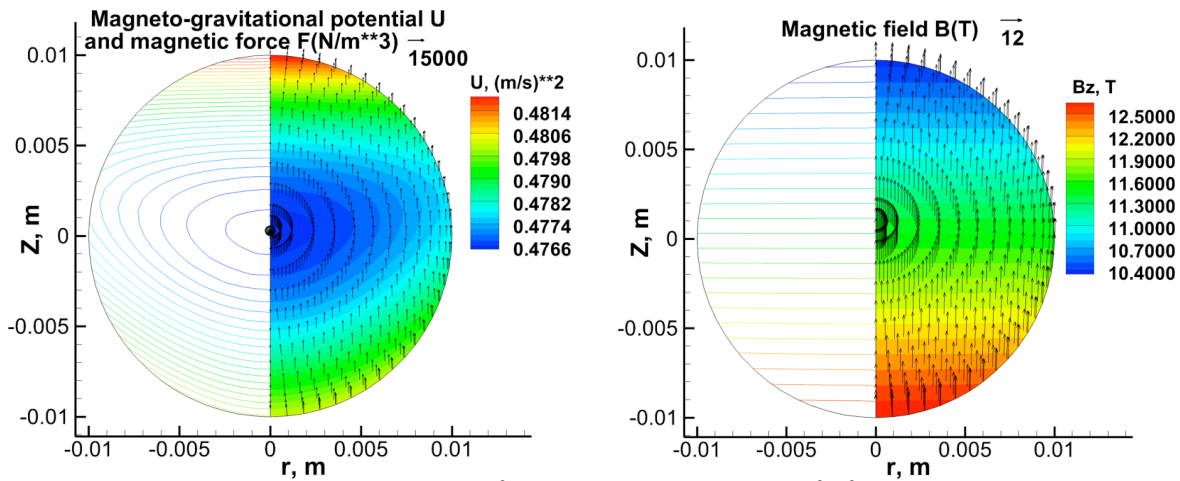


Figure 2. Magnetic field in T, force (N/m^3) and the potential U (m^2/s^2) in the water droplet $R_0 = 10$ mm at the top part of the solenoid magnet. (The reference vector scales in respective units.)

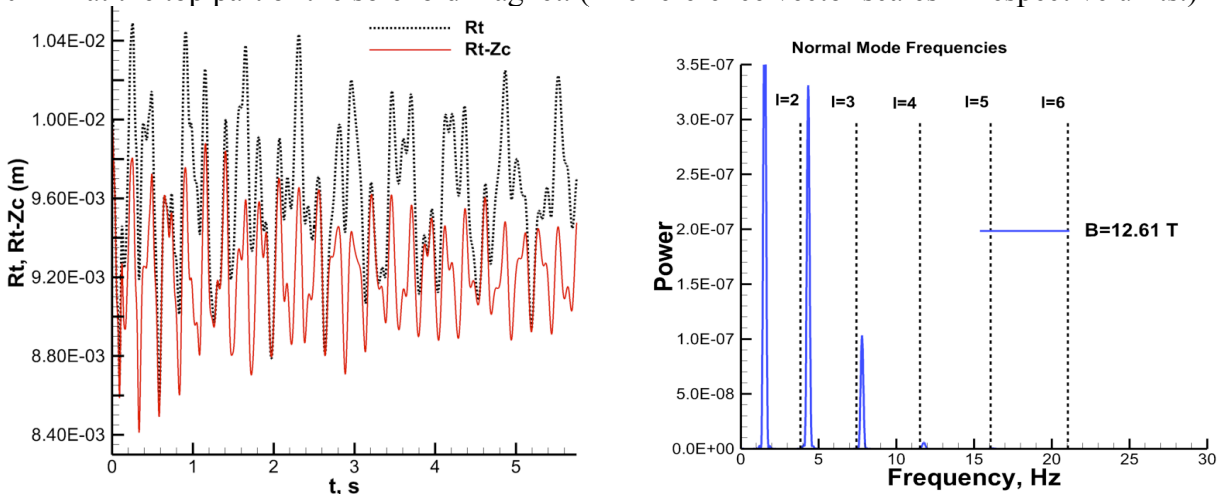


Figure 3. Oscillations of the surface top position R_t and $R_t - Z_c$ (difference to centre of mass position), and power (relative units) spectra computed for water droplet $R_0 = 10$ mm.

The computed oscillation pattern appears to be of similar nature as observed in the experiments [6], i.e., the frequency spectra peaks are slightly shifted to increase the mode frequencies relative to the non-magnetic Rayleigh values (4). The oscillation pattern shown in the Figure 3 indicates a considerable centre of mass position influence on the surface variation. The droplet position as a whole vibrates with a very small amplitude, typically less than 1 mm [6]. The numerical results in the Figure 3 give the oscillation of the surface top position difference to the centre of mass position: $R_t - Z_c$ (t). This function clearly shows the decay of the surface oscillation, while the Z_c continues to move without an apparent damping.

Figure 4 illustrates the centre of mass oscillation for a smaller size water droplet $R_0 = 5$ mm. In this numerical run we additionally modified the electric current in the solenoid so that the droplet is stably levitated in a region of higher magnetic field (max $B = 15.46$ T). In this case the centre of mass oscillates with a small amplitude of about 0.01 mm. The surface oscillation is damped at different rate for various amplitudes, apparently the mode $L = 3$ is the dominant as the power spectra for this case shows (Figure 4). The other remarkable feature for this case is the systematic reduction of all the frequencies relative to the non-magnetic values (4) and contrary to the observations in [6]. The explanation for this discrepancy is the effect of the finite amplitude shifting the frequency to smaller values [8] as supported by our tests running the same simulation with $B = 0$ (not shown due to space restrictions).

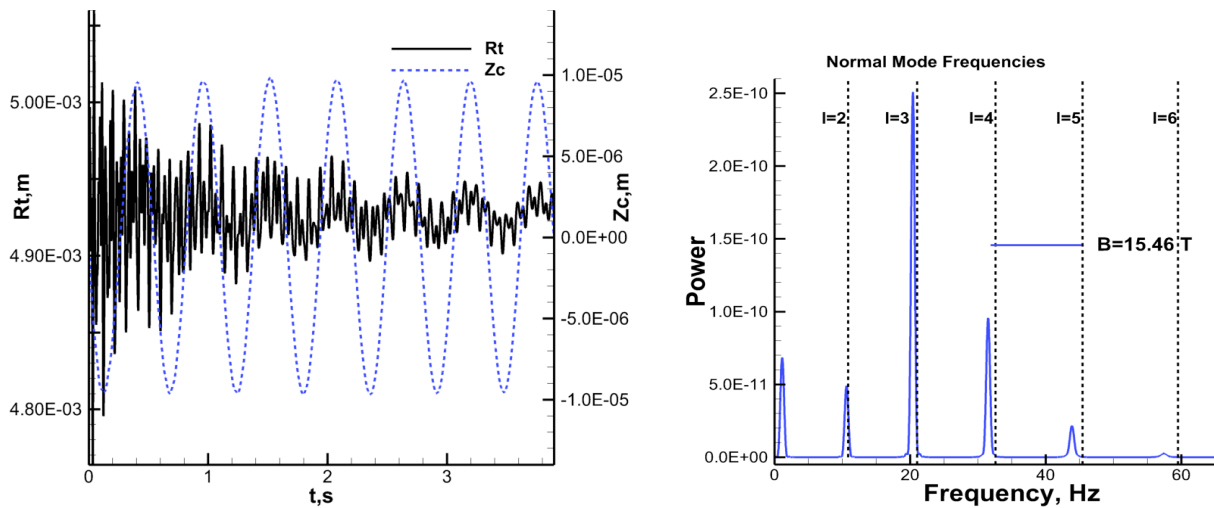


Figure 4. Oscillations of the surface top R_t and the centre of mass Z_c , and R_t power spectra (in relative units) computed for the water droplet $R_0 = 5$ mm.

3d Water Droplet Oscillations in Solenoid Magnet

A 3d test case generally supports the more accurate axisymmetric simulations. A numerical procedure is used to analyze the surface shape at each time-step in order to determine the relative contribution of each mode. This results in time dependent coefficient for each of the spherical harmonic modes. The dominant components are the $L = 2, M = 1$ mode, which corresponds to the initial condition, axisymmetric modes $L = 2, M = 0$, and $L = 3, M = 0$, which are introduced by the external forces, and the $L = 1, M = 0$ translational mode. Other small components are also present that ensure the conservation of mass. Figure 5 shows the computed instantaneous 3d velocity field and the oscillations corresponding to the dominant mode with the respective power spectra. The theoretical value for the normal mode, derived for the magnetic modification to the first order [6], is indicated in the power spectra with dashed line.

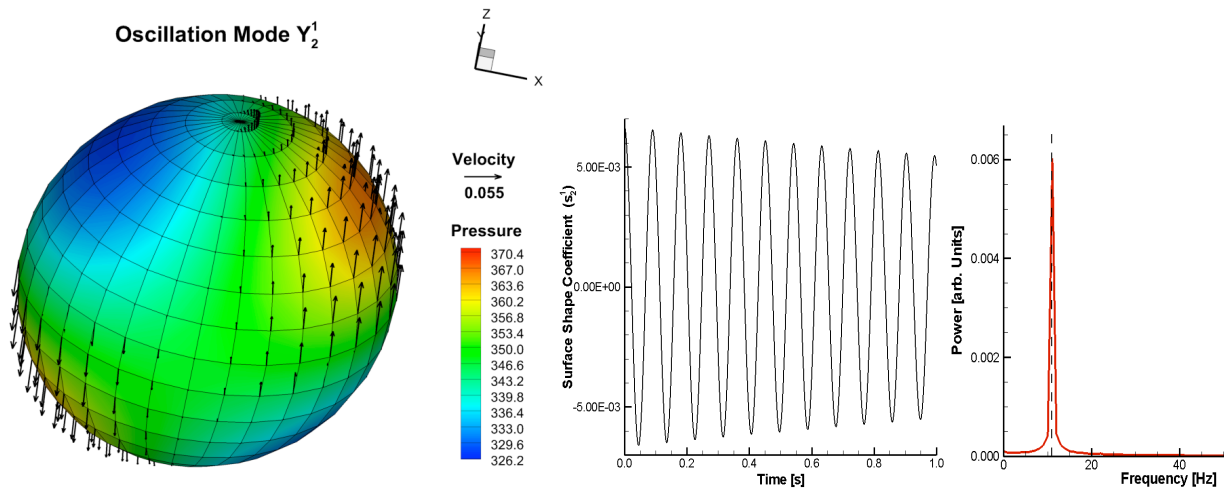


Figure 5. The 3d instantaneous velocity and pressure on the surface, and the oscillations of the top with the power spectra computed for the water droplet $R_0 = 5$ mm.

Table 2 compares the theoretical frequencies and the frequencies calculated numerically. There is a reasonable agreement between the theoretical and numerical values. The frequency shifts are small, but not insignificant when considered in the context of surface tension measurements.

	Y^0_1	Y^0_2	Y^l_2	Y^0_3
Normal Mode, see (4)	N/A	1.09e+1	1.09e+1	2.11+1
Theoretical [6]	N/A	1.12e+1	1.11e+1	2.14e+1
Numerical	1.62e+0	1.11e+1	1.11e+1	2.13e+1

Table 2. The frequency calculations for 3d water droplet oscillations.

Liquid Silicon Droplet in Solenoid Magnet

An electrically conducting levitated droplet motions are expected to be damped in strong DC magnetic field, however some types of movement are not affected in a particular field configurations. In the microgravity case ($g = 0$) and a uniform vertical magnetic field the asymptotic solution [7] shows that odd axisymmetric oscillation modes are very moderately damped and the frequencies are reduced by a factor of \sqrt{L} (6). It is not immediately clear if this behavior will stay in the presence of terrestrial gravity and the gradient magnetic field required for the magnetic levitation. The numerical experiments with liquid silicon appear to support the general conclusions of the asymptotic solution as demonstrated by the Figure 6. The $L = 3$ (see the velocity field in the Figure 7) and the longitudinal centre of mass $L = 0$ modes are the only ones not damped immediately in the 17 T magnetic field required to levitate the 5 mm radius liquid silicone droplet. The frequency of the $L = 3$ mode is reduced about $\sqrt{3}$ times relative to the non-magnetic case (4) and closely matches the theoretical value [7]. The small deviation can be explained by the presence of the gradient part of the magnetic field. By readjusting the electric current in the solenoid the gradient part can be reduced at the expense of increased uniform B_z component. When the magnitude of the field is 28 T the computed frequency is practically coinciding with the theoretical value to the accuracy of 0.01%. However in this case the droplet weight is balanced only at the initial time, then vigorous oscillations of the modes $L = 3$ and $L = 1$ (centre of mass) follow (Figure 7), and the droplet very slowly slides downwards (Figure 8). The magneto-gravitational potential on the surface $U(R = r_s) = \sum_{n=0} U_n(t) P_n(\cos \theta)$ experiences similar oscillations to the free surface shape as shown in the Figure 8.

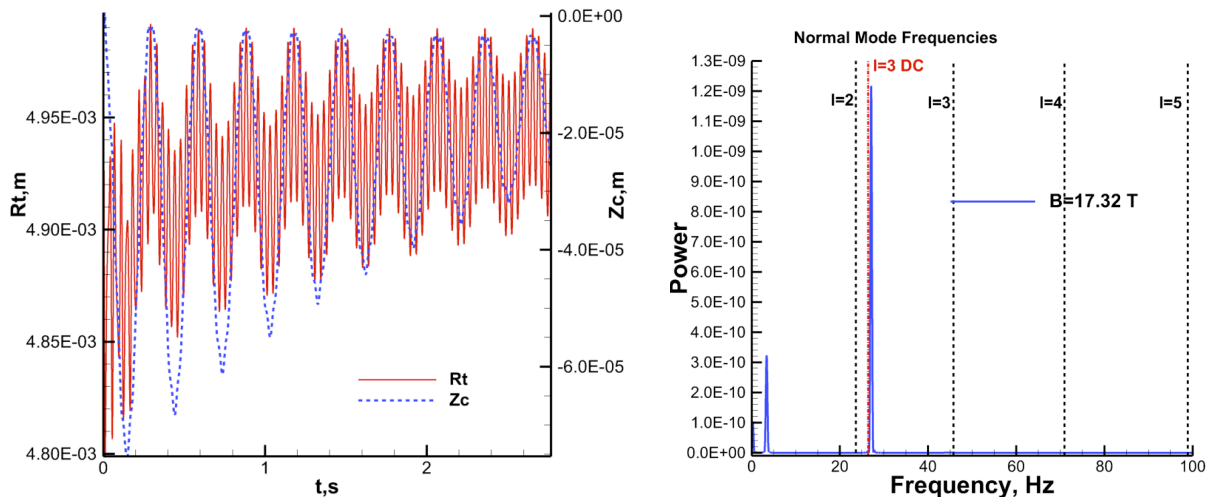


Figure 6. Oscillations of the surface R_t and the centre of mass Z_c , and R_t power spectra computed for the liquid silicon droplet $R_0 = 5$ mm in 17 T field.

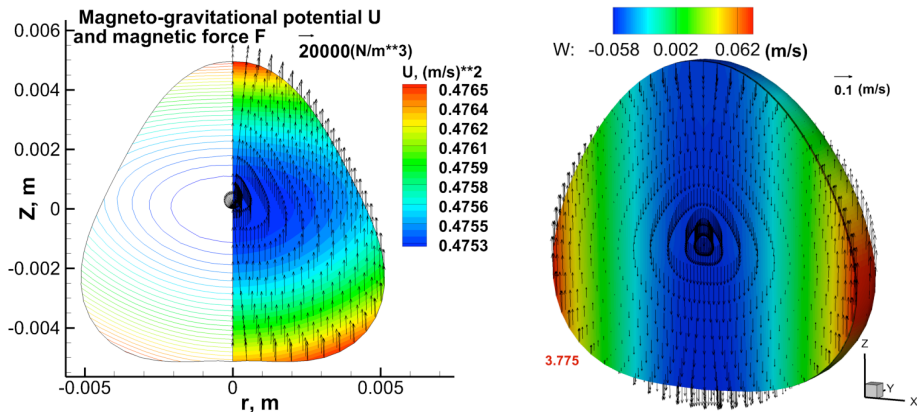


Figure 7. Magnetic potential, force and velocity field in the liquid silicon droplet $R_0 = 5$ mm.

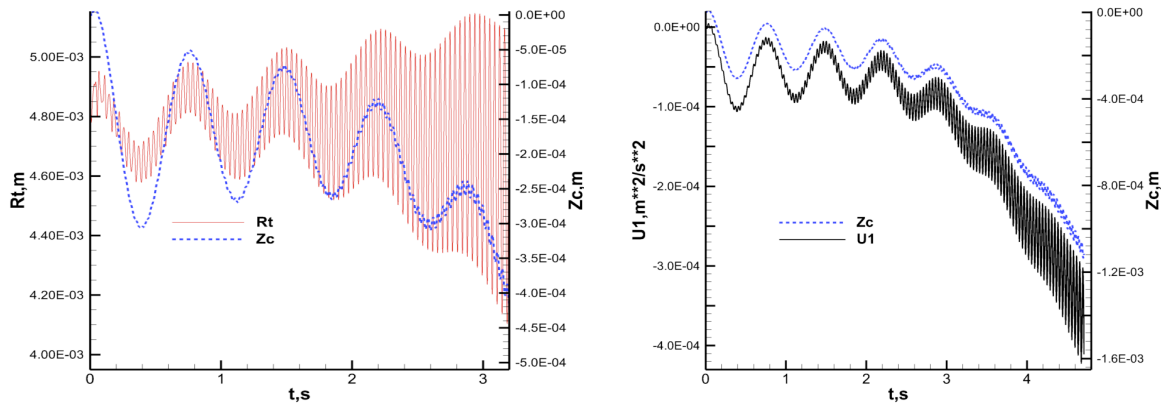


Figure 8. Oscillations of the surface R_t , centre of mass Z_c , and the magnetogravitational potential expansion linear coefficient U_1 for the liquid silicon droplet $R_0 = 5$ mm in 28 T field.

References

- [1] Egry I, Lohofner G, Seyhan I, Schneider S and Feuerbacher B 1999 "Viscosity and surface tension measurements in microgravity" *Int. J. Thermophys.* 20 (4) 1005-1015
- [2] Cummings D L and Blackburn D A 1991 "Oscillations of magnetically levitated aspherical droplets" *J. Fluid Mech.* 224 395-416
- [3] Kobatake H, Fukuyama H, Minato I, Tsukada T and Avaji S 2007 "Noncontact measurement of thermal conductivity of liquid silicon in a static magnetic field" *Applied Physics Letters* 90 094102
- [4] Bojarevics V, Easter S, Roy A and Pericleous K 2009 "Levitated Liquid Droplets in AC and DC Magnetic Field" *Proc. Int. Symp. Liquid Metal Processing and Casting, Santa Fe, TMS, ed-s Lee P, Mitchell A, Williamson R, 319-326*
- [5] Beaugnon E, Fabregue D, Billy D, Nappa J and Tournier R 2001 "Dynamics of magnetically levitated droplets" *Physica B* 294-295 715-720
- [6] Hill R J A and Eaves L 2010 "Vibrations of a diamagnetically levitated water droplet" *Phys. Rev E* 81 (5) 056312
- [7] Priede J 2010 "Oscillations of weakly viscous conducting liquid drops in a strong magnetic field" *J. Fluid Mech.* 671 399-416
- [8] Tsamopoulos J A and Brown R A 1983 "Nonlinear oscillations of inviscid drops and bubbles" *J. Fluid Mech.* 127 519-537
- [9] Smythe W R 1950, *Static and Dynamic Electricity*, McGraw-Hill, London
- [10] Bojarevics V and Pericleous K 2003 "Modelling electromagnetically levitated liquid droplet oscillations" *ISIJ International* 43 (6) 890-898

MEASUREMENTS OF DENDRITIC GROWTH VELOCITIES IN UNDERCOOLED MELTS OF PURE NICKEL UNDER STATIC MAGNETIC FIELDS

Jianrong Gao¹, Zongning Zhang¹, Yingjie Zhang¹

¹ Key Laboratory of Electromagnetic Processing of Materials (Ministry of Education)
3-11 Wenhua Road; Shenyang 110004, China

Keywords: Pure metal, Dendritic growth velocity, Fluid flow, Impurity

Abstract

Dendritic growth velocities in undercooled melts of pure Ni have been intensively studied over the past fifty years. However, the literature data are at marked variance with the prediction of the widely accepted model for rapid dendritic growth both at small and at large undercoolings. In the present work, bulk melts of pure Ni samples of high purity were undercooled by glass fluxing treatment under a static magnetic field. The recalescence processes of the samples at different undercoolings were recorded using a high-speed camera, and were modeled using a software to determine the dendritic growth velocities. The present data confirmed the effect of melt flow on dendritic growth velocities at undercoolings below 100 K. A comparison of the present data with previous measurements on a lower purity material suggested an effect of impurities on dendritic growth velocities at undercoolings larger than 200 K as well.

Introduction

Many studies have been carried out to measure dendritic growth velocities in undercooled melts for an understanding of the mechanism of dendritic growth [1]. Pure nickel has attracted constant attention over the past fifty years [2-16]. The main reason is because its materials properties both in the liquid and in the solid states are well known so that the measured growth velocities can be referred to for a rigorous test of physical models for rapid dendritic growth. A review of previous measurements on pure nickel could be found elsewhere [12,16]. The latest studies [9,15,16] showed reduced scatter as well as an improved agreement with the widely accepted dendritic growth model (known as LKT model [17]) owing to the use of a series of advanced techniques including those for undercooling and those for in-situ observations. However, the measured data were yet at marked variance with the predictions of the LKT model. A positive and a negative deviations were observed for the small (below 100 K) and for the large undercooling regions (above 200 K), respectively [9,15]. Efforts were already made to account for these discrepancies. Eckler et al. [8,9] first proposed two alternative explanations for the positive deviation: impurity and fluid flow effects. Galenko et al. [18] extended the LKT model by taking into account the contribution of fluid flow and showed a reduction of the discrepancy. Herlach and Galenko [19] further incorporated the impurity effect and explained the residual discrepancy. Using a phase field method, Bragard et al. [20] and Nestler et al. [21] explored effects of capillary and kinetic anisotropy on dendritic growth to understand the deviation in the large undercooling region. The former group suggested that the deviation might also be related to fluid flow or impurities in liquid samples. Thus, it is of great interest to determine the effects of fluid flow and impurities on dendritic growth velocities in undercooled Ni samples experimentally.

A fluid flow effect on dendritic growth velocities has been observed for electromagnetically levitated samples of few intermetallic compounds under reduced gravity conditions [22-23]. However, no experimental data for pure nickel samples processed under similar experimental conditions are available. Recently, a few studies [24-26] have shown that a static magnetic field of few Tesla is able to damp convective flow in electromagnetically levitated samples under terrestrial conditions. Such advancement opens a new opportunity for investigations of fluid flow effects on dendritic growth velocities in undercooled metals. Very recently, the present authors designed a novel glass-fluxing facility, which combined an inducting heating furnace with a superconducting magnet. A preliminary study on nickel samples of 99.99% purity (referred to 4N Ni below) showed evidence for a detectable effect of fluid flow on dendritic growth velocities in the small undercooling region [16]. In the present work, the measurements were extended to samples of higher purity, 99.999% purity (referred to 5N Ni below) to investigate the effects of fluid flow and impurities simultaneously.

Experimental Details

The experimental facility used for measurements of dendritic growth velocities comprised a vacuum induction melting furnace, a superconducting magnet, a shielding tube, an Ultima-APX type digital high-speed camera (HSC), a METIS MS09 type single-color pyrometer, and two computers. The details of the facility can be found elsewhere [16]. In the present measurements, individual samples of 1.0 g were cut from a 5N purity Ni rod of 5 mm in diameter offered by Alfa Aesar. Under each condition, the measurements were made on one sample only. The cut samples were polished using an abrasive paper and cleaned in an ultrasonic bath for few minutes. Before melting, a single sample was placed onto an alumina crucible containing soda lime glass lumps. The crucible was positioned in a heating coil. After evacuation to a vacuum pressure of 5×10^{-3} Pa, the chamber of the facility was back-filled with argon of 99.999% purity to a pressure of 5×10^4 Pa. The superconducting magnet was ramped to a magnetic field of 1.0 T. Then, the sample was heated and melted inductively. The sample temperature was measured using a single-color pyrometer at a frequency of about 100 Hz. The glass powders were fused by conducted heat. The sample was overheated and soaked for a few minutes. After soaking, the power to the coil was switched off. The sample was cooled and solidified spontaneously. A recalescence event took place during solidification of the undercooled sample due to rapid release of latent heat. For measurements of dendritic growth velocities, the recalescing sample surface was in-situ observed using a high-speed camera with a resolution of 256×32 pixels at a frame rate of 87600 fps. A pixel corresponded to an area of $100 \mu\text{m} \times 100 \mu\text{m}$. The sample was subjected to more than 40 melting-solidification cycles. In order to determine the nucleation site and therefore the growth velocity of each recalescence process, the recorded images of the sample surface was modeled using computer software named POV Ray 3.7 [23]. The recalescence front was assumed to travel through the bulk volume of the undercooled sample at a constant rate like a spherical wave. Thus, the three-dimensional recalescence front traveling through the sample volume could be reconstructed by a continuous analysis of the recorded loci of the recalescence front sweeping across the sample surface with the aid of the software. The dendritic growth velocity was calculated by dividing the total traveling distance of the three-dimensional recalescence front by the consumed time in a given recalescence process.

Results and Discussion

Figure 1 illustrates cooling curves of a Ni sample of 5N purity. The recalescence temperature, i.e., the temperature reached at the end of recalescence, often showed a deficit with respect to a

well-determined melting temperature of 1728 K. The deficit generally increases with increasing undercooling. A similar phenomenon was observed by the present authors for the Ni sample of 4N purity [16] and by other researchers for glass-fluxed Ni-Cu single-phase alloys [27] and Ni-Sn eutectic alloys [28]. The most probable reason for the deficit is a thermal loss of the sample to the crucible through the molten glass during recalescence. Other reasons include creation of numerous defects and stresses in the solid phase, which might reduce the energy difference between the solid and the liquid phases during recalescence [27]. Because of this deficit, the measured sample temperature was calibrated with respect to a maximum recalescence temperature derived from a statistical analysis of all data.

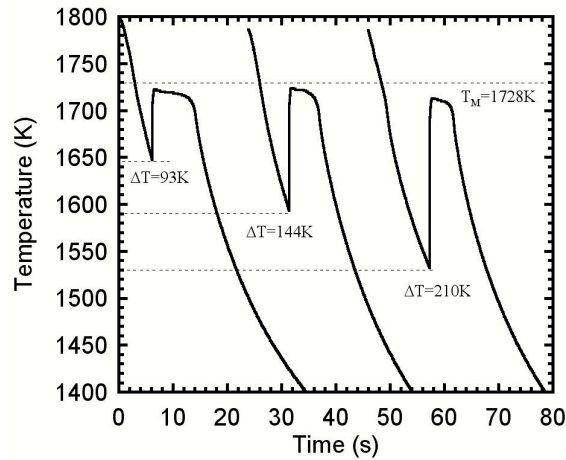


Figure 1 Illustration of cooling curves of 5N Ni sample at different undercoolings

Figure 2 illustrates the corresponding sequential images of the top surface of the recalescing sample recorded by the high-speed camera. In agreement with many previous studies (e.g. Refs. [12] and [15]), the observed recalescence front shows an angular morphology and a smooth morphology for small and large undercoolings, respectively. The transition does not correspond to a sharp undercooling, but occurs over a span of 15 K. The imposition of the static magnetic field did not produce any visible changes either in the morphology or in the transition. It is

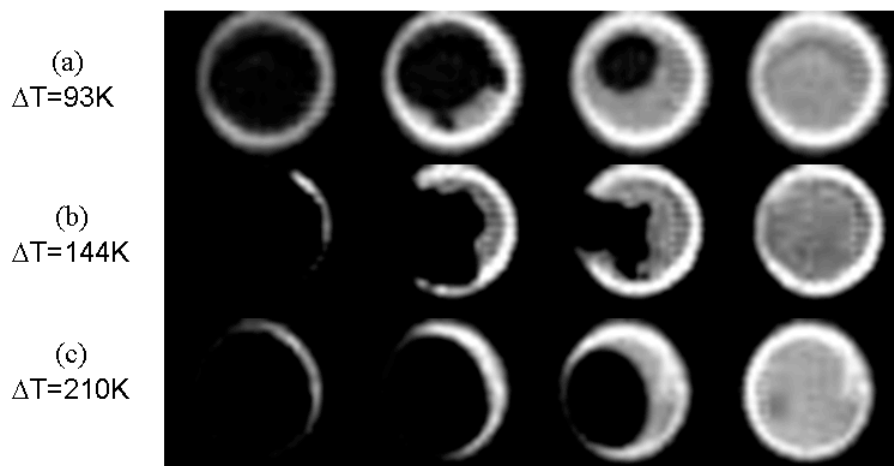


Figure 2 Illustration of HSC images of the 5N Ni samples at different undercoolings

worthy of mentioning that the irregular morphology of the recalescence front for small undercoolings brought about a difficulty in modeling of the recalescence process. However, this difficulty could be overcome by modeling the major contour of the recalescence front instead of the whole front. In this sense, the derived traveling distance of the recalescence front represented a mean value, rather than a specific value for local regions.

Figure 3 shows the measured dendritic growth velocities of the 5N Ni samples as a function of undercooling. As seen in Figure 3a, the data measured under the static magnetic field show a reduced scatter with respect to those measured without the static magnetic field. Apart from this aspect, it is hardly to see a difference between the two sets of the data in the normal-scale plot. In agreement with many previous studies, the present data show a power-law behavior and a linear law behavior for small and large undercoolings, respectively. Such a transition of the growth velocities, however, is sharper than the morphological transition of the recalescence front is. The former occurs at a well-defined undercooling of 200 K. If compared with the previous data for the 4N purity samples [16], one can find a striking difference in the large undercooling region. The velocities measured on the 5N purity samples are considerably higher than those measured on the 4N purity sample. Such a difference highlights that the effect of unknown impurities on growth velocities of undercooled nickel melts is tremendous. In the following, attention is focused onto the data measured at small and medium undercoolings.

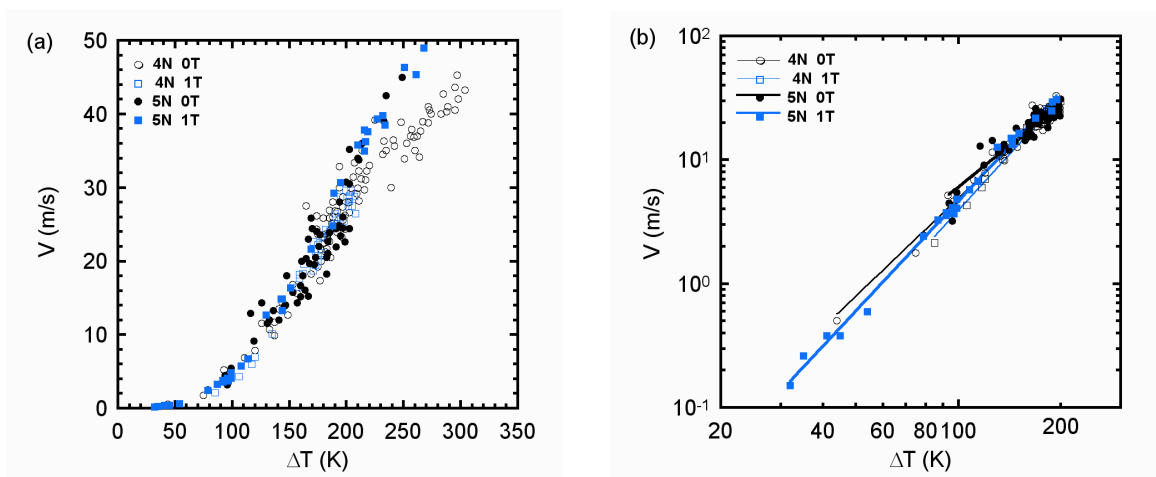


Figure 3 Growth velocity – undercooling relationship measured on the 5N Ni samples with and without imposition of a static magnetic field of 1 T. For comparison, two sets of the previous data measured on 4N purity samples [16] are also shown.

Due to relatively small values in magnitude, the differences of the growth velocities in the small undercooling region cannot be readily distinguished on a normal-scale plot. For this reason, the data are re-plotted on a dual-logarithm scale. However, the data are too few to allow us to directly extract the effect of impurities and residual fluid flow on the growth velocities in the small undercooling region of high interest. Thus, the data are all truncated at 200 K and fit to different power laws. As seen in Fig. 3b, each power law is represented by a straight line. Two clear tendencies are shown by these lines. One is that the imposition of the static magnetic field decreases the slope of the power law fitting line independent of the sample purity. The other is that the improvement of sample purity increases the slope of the power law fitting line under identical magnetic field conditions. The first tendency means that damping of fluid flow in the undercooled samples lowers the dendritic growth velocities. Reversely, the introduction of fluid flow increases the dendritic growth velocities as expected. Such a tendency agrees reasonably

with the prediction of the extended LKT model [18]. The second tendency means that the reduction of impurities increases the dendritic growth velocities. Reversely, the presence of the impurities lowers the dendritic growth velocities. This tendency, however, is in contrast to the theoretical prediction for a strongly partitioning impurity [8,19]. Probably the species or the amount of the impurity is different from that assumed in the previous studies [8,19]. Consequently, the reversed effect of the impurities occurs to the present samples.

It is also noted in Figure 3b that two power law fitting lines for the samples of different purities intersect at an undercooling of 168 K in the absence of the static magnetic field. However, the other lines never intersect. This difference between the fitting lines implies that the lower purity sample can reach a growth velocity comparable to that of the higher purity sample with the aid of fluid flow, but never can reach the same velocity without the aid of fluid flow. For the higher purity 5N sample, the two power law fitting lines intersect at an undercooling of 145 K. In contrast, the two power law fitting lines of the lower purity 4N sample intersect at an undercooling of 405 K, where the power laws do not apply any longer. Such a difference suggests that the fluid flow effect becomes negligible at a medium undercooling for the higher purity 5N sample, but does not vanish for the lower purity 4N samples for all accessible undercoolings.

In order to produce more insight into the effects of impurities and fluid flow, dendritic growth velocities of the Ni samples are calculated for five different undercoolings in terms of the above power law fittings. Relative changes of the growth velocities are determined. The results are listed in Table 1. At an undercooling as small as 10 K, the imposition of the static magnetic field decreases the growth velocities by 76% and by 85% for the 4N and 5N purity samples, respectively. With increasing undercooling, the effect of the static magnetic field on the 4N purity sample shows a continuous decrease. For the 5N purity sample, the effect of the static magnetic field decreases faster and reaches a minimum at an undercooling of 150 K. After that, the effect resumes but changes its direction. On the other hand, the impurities produce the strongest effect on the growth velocities at small undercoolings. In the absence of the static magnetic field, the effect of the impurities decreases quickly with increasing undercooling and changes its direction at 200 K. Under the action of the static magnetic field, the effect of impurities decreases slightly with increasing undercooling. Such different behavior highlights that the impurities interact strongly with fluid flow during dendritic growth at small undercoolings. In many of the previous studies, these two quantities were not controlled strictly. Thus, it is not surprising that a large discrepancy had arisen between the measured growth velocities and the prediction of the LKT model. A detailed analysis of the present data within the framework of the LKT model is under way. In the following, the present data measured under the static magnetic field are further discussed with respect to two recent studies and one phase field modeling.

Table 1 Relative changes of dendritic growth velocities of pure nickel in response to altering of the experimental conditions

Sample conditions		Relative change of growth velocity (%)				
		10 K	50 K	100 K	150 K	200 K
0T→1T	4N	-76	-55	-42	-32	-24
	5N	-85	-53	-23	2	26
5N→4N	0T	-67	-38	-19	-5	7
	1T	-47	-41	-38	-37	-35

As shown in Figure 4a, the present data measured under the static magnetic field are in good agreement with the previous measurements by Lum et al. [12] for undercoolings larger than 180 K. However, there is a large discrepancy in the medium undercooling region. Since those researchers employed the same glass-fluxing method for undercooling, the convection in their samples is assumed to be comparable to that in the present samples. Under this assumption, the large discrepancy may be ascribed to a difference in the method for calibration of the temperature measurements. Actually, if the deficit of the recalescence temperature of the present samples with respect to the melting temperature was eliminated deliberately, the derived growth velocity-undercooling relationship would show an excellent agreement with those researcher's data over the whole undercooling regime. However, such calibration may not be necessary. Note that the present data coincide with the lower limits of the latest data measured by Funke et al. [15] for electromagnetically levitated samples. As concluded from the above discussion, residual fluid flow in the present samples can enhance growth velocities of pure nickel. Convective flow in the electromagnetically levitated samples is much stronger [24,29] and should make a larger contribution to the growth velocities than in the present samples. From this point of view, the present method for calibration of the sample temperature is reasonable. More importantly, the present data show an excellent agreement with the recent phase field modeling [21] up to an undercooling of 220 K (see Fig. 4b). The contributions of fluid flow and impurities were not incorporated in the modeling. Therefore, the conditions hypothesized therein were well satisfied through the present experiments under the static magnetic field. The discrepancy remaining at extremely large undercoolings can be ascribed to the impurity effect because it is smaller for the higher purity sample. It will vanish if the material purity can be improved further. In other words, the deviation of the growth velocities from a power law at large undercoolings is largely due to the impurities dissolved in the pure Ni samples.

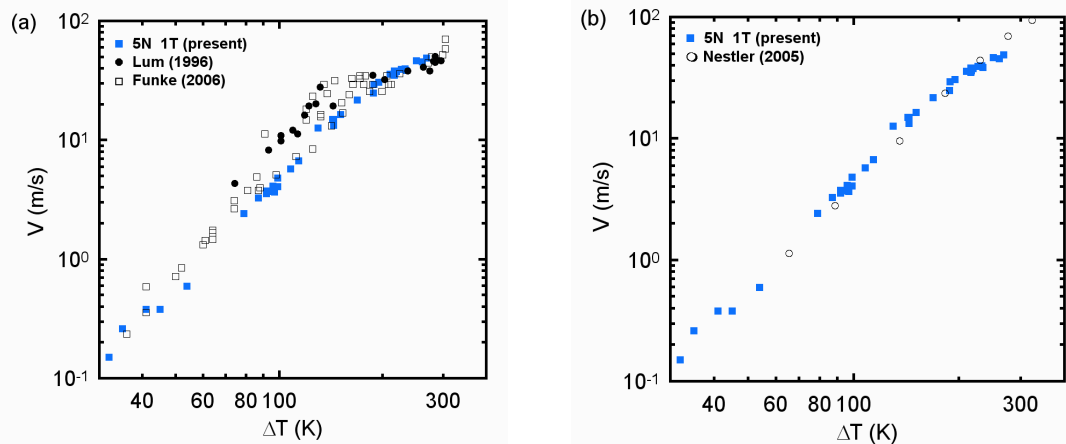


Figure 4 Comparison of the present data with two sets of literature data [12,15] (a) and the results of the recent phase-field modeling [21] (b). For clearance, the data measured in the present of the static magnetic field are shown only.

Conclusions

Dendritic growth velocities in undercooled melts of high purity nickel samples have been measured with and without the imposition of a static magnetic field of 1 T. Similar to the latest measurements on the samples of lower purity, the present data have confirmed the long-term suspected effect of fluid flow on growth velocities in the small undercooling region. The present data have also shown that the impurity effect plays a role both in the small and in the large

undercooling regions. Although the species of the impurities are unknown, they tend to lower the dendritic growth velocities under the present experimental conditions. Additionally, the present data measured under the static magnetic field show an excellent agreement with the prediction of the recent phase field modeling [21] up to an undercooling of 220 K. The remaining discrepancy at larger undercoolings has been attributed to the impurity effect.

Acknowledgements

This work is financially supported by the National Natural Science Foundation of China (Grant No. 51071043) and by the Fundamental Research Funds for the Central Universities (Grant Nos. N090509001 and N090109001). The authors thank D. M. Herlach, P. Galenko, T. Volkman, A. Kao for helpful discussions. The authors thank S. Binder for offering the computer code and X. T. Deng, H. F. Li, P. Zhang and Y. Xiao for their assistance in the experimental work.

References

- [1] D. M. Herlach, P. Galenko and D. Holland-Moritz, *Metastable Solids from Undercooled Melts*, Pergamon Materials Science, Amsterdam, 2007.
- [2] J. L. Walker, in: *Principles of Solidification*, ed. B. Chalmers, Chapter 4, Wiley, New York, 1964.
- [3] G. A. Colligan and B. J. Bayles, *Acta Metall.* 10 (1962) 895.
- [4] E. Schleich, R. Willnecker, D. M. Herlach and G. P. Görlner, *Mater. Sci. Eng. A* 98 (1988) 39.
- [5] T. J. Piccone, Y. Wu, Y. Shiohara and M. C. Flemings, in: *Solidification Processing 1987*, The Institute of Metals, London, 1988, p. 268.
- [6] R. Willnecker, D. M. Herlach and B. Feuerbacher, *Phys. Rev. Lett.* 62 (1989) 2707.
- [7] W. H. Hofmeister, R. J. Bayuzick and M. B. Robinson, *Rev. Sci. Instrum.* 61 (1990) 2220.
- [8] K. Eckler, D. M. Herlach, R. G. Hamerton and A. L. Greer, *Mater. Sci. Eng. A* 133 (1991) 730.
- [9] K. Eckler and D. M. Herlach, *Mater. Sci. Eng. A* 178 (1994) 159.
- [10] B. T. Bassler, W. H. Hofmeister, G. Carro and R. J. Bayuzick, *Metall. Mater. Trans. A* 25 (1994) 1301.
- [11] S. Walder and P. L. Ryder, *Mater. Sci. Eng. A* 203 (1995) 197.
- [12] J. W. Lum, D. M. Matson and M. C. Flemings, *Metall. Mater. Trans. B* 27 (1996) 865.
- [13] B. T. Bassler, W. H. Hofmeister and R. J. Bayuzick, *Mater. Sci. Eng. A* 342 (2003) 80.
- [14] P. R. Algosio, W. H. Hofmeister and R. J. Bayuzick, *Scrip. Mater.* 51 (2004) 539.
- [15] O. Funke, G. Phanikumar, P. K. Galenko, L. Chernova, S. Reutzel, M. Kolbe and D. M. Herlach, *J. Cryst. Growth* 297 (2006) 211.
- [16] J. Gao, Z. N. Zhang, Y. K. Zhang and C. Yang, in: *Solidification of Containerless Undercooled Melts*, ed. D. M. Herlach and D. Matson, Chapter 13, Wiley, in press.
- [17] J. Lipton, W. Kurz and R. Trivedi, *Acta Mater.* 39 (1994) 49.
- [18] P. K. Galenko, O. Funke, J. Wang and D. M. Herlach, *Mater. Sci. Eng. A* 375-377 (2004) 488.
- [19] D. M. Herlach and P. K. Galenko, *Mater. Sci. Eng. A* 449-451 (2007) 34.
- [20] J. Bragard, A. Karma, Y. H. Lee and M. Plapp, *Interface Sci.* 10 (2002) 121.
- [21] B. Nestler, D. Danilov and P. Galenko, *J. Comput. Phys.* 207 (2005) 221.
- [22] S. Reutzel, H. Hartmann, P. K. Galenko, S. Schneider and D. M. Herlach, *Appl. Phys. Lett.* 91 (2007) 41913.
- [23] S. Binder, Ph.D. Thesis of Ruhr University of Bochum, 2010.
- [24] V. Bojarevics and K. Pericleous, *ISIJ Inter.* 43 (2003) 890.

- [25] H. Yasuda, I. Ohnaka, Y. Ninomiya, R. Ishii, S. Fujita and K. Kishio, *J. Cryst. Growth* 260 (2004) 475.
- [26] Y. K. Zhang, J. Gao, D. Nagamatsu, T. Fukuda, H. Yasuda, M. Kolbe and J. C. He, *Scrip. Mater.* 59 (2008) 1002.
- [27] W. Yang, F. Liu, H. F. Wang, Z. Chen, G. C. Yang and Y.H. Zhou, *J. Alloys Compd.* 470 (2009) L13.
- [28] J. F. Li, W. Q. Jie, S. Zhao and Y. H. Zhou, *Metall. Mater. Trans. A* 38 (2007) 1806.
- [29] R. W. Hyers, *Meas. Sci. Technol.* 16 (2005) 394.

X-RAY RADIOGRAPHIC OBSERVATION OF DIRECTIONAL SOLIDIFICATION UNDER MICROGRAVITY: XRMON-GF EXPERIMENTS ON MASER12 SOUNDING ROCKET MISSION

G. Reinhart^{1,2}, H. Nguyen Thi^{1,2}, A. Bogno^{1,2}, B. Billia^{1,2}, Y. Houltz³, K. L oth³,
D. Voss⁴, A. Verga⁴, F. de Pascale⁴, R.H. Mathiesen⁵, G. Zimmermann⁶

¹Aix Marseille Univ & ⁽²⁾ CNRS, IM2NP UMR 6242

Campus Saint-J r me, Case 142, 13397 Marseille Cedex 20, France

³Swedish Space Corporation, P.O. Box 4207, SE-171 04 Solna, Sweden

⁴European Space Research & Technology Centre, Keplerlaan 1 Postbus 299, 2200 AG Noordwijk, the Netherlands

⁵Dept. of physics, NTNU, N-7491 Trondheim, Norway

⁶ACCESS e.V, Intzestrasse 5, 52072 Aachen, Germany

Keywords: X-ray radiography, Microgravity, Sounding Rocket, Convection, Fragmentation, Solidification, Aluminium

Abstract

The European Space Agency (ESA) - Microgravity Application Promotion (MAP) programme entitled XRMON (*In situ* X-Ray MONitoring of advanced metallurgical processes under microgravity and terrestrial conditions) aims to develop and perform *in situ* X-ray radiography observations of metallurgical processes in microgravity and terrestrial environments. The use of X-ray imaging methods makes it possible to study alloy solidification processes with spatio-temporal resolutions at the scales of relevance for microstructure formation.

XRMON has been selected for MASER 12 sounding rocket experiment, scheduled in autumn 2011. Although the microgravity duration is typically six minutes, this short time is sufficient to investigate a solidification experiment with X-ray radiography. This communication will report on the preliminary results obtained with the experimental set-up developed by SSC (Swedish Space Corporation). Presented results dealing with directional solidification of Al-Cu confirm the great interest of performing *in situ* characterization to analyse dynamical phenomena during solidification processes.

Introduction

Many phenomena involved during solidification are dynamic, such as dendrite fragmentation [1; 2], columnar-to-equiaxed transition [3; 4], and equiaxed growth [5-7]. The study of such phenomena by classical approaches like quenching or decanting is not well adapted. Therefore, *in situ* and real-time X-ray imaging should be retained as the method of choice for investigating the solidification front evolution of metallic alloys grown from the melt [8-10]. In addition, for most real solidification processes involving a liquid phase, natural buoyant convection plays an important role and may interact with the microstructure. An important pending issue is to clarify the role of convection on macrosegregation and on microstructure formation of the solidification process [11; 12]. It has been shown that microgravity (μg) environment is an efficient way to eliminate buoyancy and convection to provide benchmark data for the validation of models and numerical simulations [13-17]. In addition, a comparative study of solidification experiments at 1g and μg can also enlighten the effects of gravity. Therefore, in the frame of the XRMON

project, an experimental set-up has recently been developed to perform directional solidification in microgravity conditions with *in situ* X-ray radiography observation. The first solidification experiment in microgravity using this facility is scheduled during MASER 12 sounding rocket mission, in autumn 2011.

This paper is divided into two parts. The first part will present a brief review of some gravity-induced effects on solidification process, investigated by means of synchrotron X-ray radiography. Experiments were carried out at ESRF (European Synchrotron Radiation Facility) in thin Aluminium-based alloys. In the second part of this paper, we will describe the breadboard tests carried out in Stockholm (Sweden) with a prototype of the XRMON-Gradient Furnace set-up. Preliminary results show the high capabilities of this experimental set-up in terms of thermal behaviour, as well as X-ray observation.

1. Influence of convection on solidification process

The synchrotron experiments are carried out at the European Synchrotron Radiation Facility (ESRF), inside a Bridgman furnace [18]. *In situ* and real time observation of the solidification process is possible by the use of synchrotron X-ray radiography. The main surface of the sheet-like sample (40 mm x 6 mm x 0.2 mm) is set perpendicular to the incident monochromatic X-ray beam, with energy in the range 14-18 keV. Absorption is the main source of the image contrast and depends on the atomic number of the elements and the solute content. In all radiographic pictures, the solid aluminum microstructures appear in white and the copper-rich liquid in dark grey after an image processing [19]. The optics is chosen to obtain a good compromise between a large field of view (15 x 6 mm²) and a sufficient resolution (pixel size: 7.46 μm).

Initial Solidification Transient

It is well known that even when solidification is performed under both thermal and solutal stabilizing configuration, convection in the melt can nevertheless be strong due to residual transverse gradient, in particular at low growth rates [16; 20]. Indeed, in real experimental configurations there are generally small departures of the initial interface from planarity, even after a long thermal stabilization phase. As solidification proceeds, the solute is rejected at the solid-liquid interface. Due to gravity, the denser Cu-enriched liquid flows towards depressed regions of the front, which results in solute accumulation in those regions. According to the phase diagram, solute accumulation in depressed regions retards solidification and further deepens the solid-liquid interface modulations. This leads to a large macroscopic deformation of the solidification front (steepening phenomena). In addition, the transverse solute gradient gives rise to a transverse microstructure gradient (clustering phenomena), as already shown by *post-mortem* analysis [16].

Figure 1 shows a sequence of images recorded during the initial transient solidification of Al-4wt% Cu. The temperature of the hot zone of the furnace was lowered at a given cooling rate $R_H = 1$ K/min, while the temperature of the cold zone of the furnace was maintained constant $R_C = 0$ K/min. The average temperature gradient G is about 35.5 K/cm. In this experiment an initially slightly curved smooth interface is observed (figure 1a), owing to a residual transverse temperature gradient G_y of about 1 K/cm [21]. When the cooling of the sample begins the growth rate gradually increases as solidification proceeds, leading to the destabilization of the interface first in the center of the sample. The propagation of the morphological instability towards the two sides of the sample is visible in figure 1, as well as the transverse gradient of microstructure (i.e. clustering phenomena). Concomitantly, macroscopic distortion of the solid-liquid interface becomes larger and larger with time, due to fluid flow in the melt (i.e. steepening phenomena). In figure 1, it can be seen that the liquid phase in the two channels becomes darker as solidification proceeds, which confirms an increase in the liquid solute concentration there.

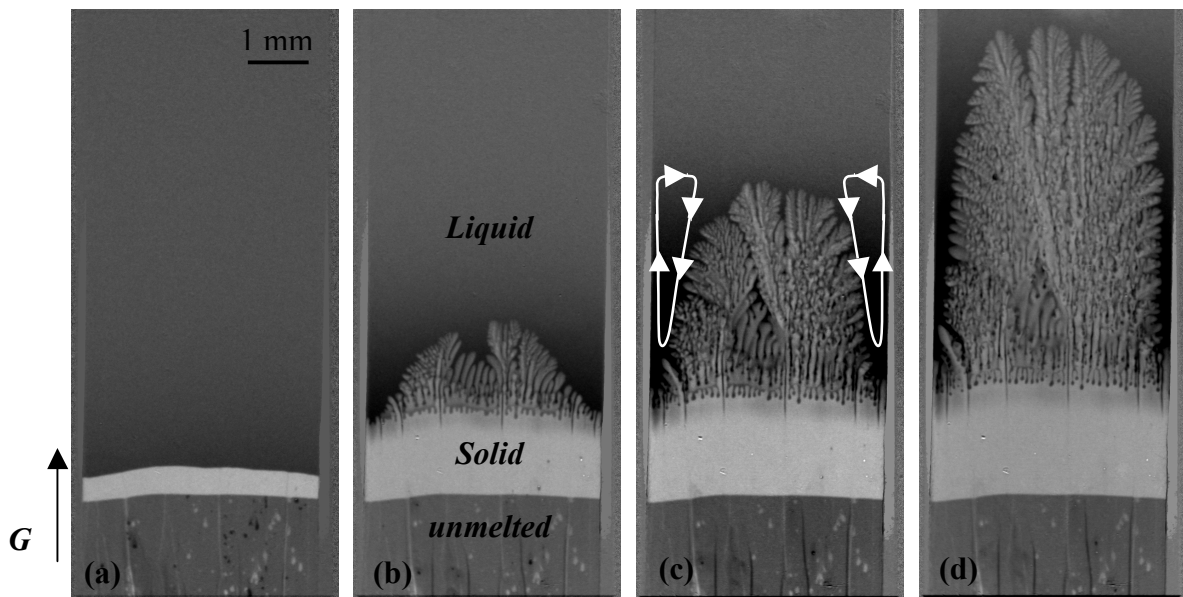


Figure 1: Sequence of 4 images showing the progressive deformation of the solid-liquid interface during the initial transient of solidification for Al-4wt% Cu ($R_H = 1$ K/min; $R_C = 0$ K/min, $G=35.5$ K/cm). (a) $t \approx 20$ min; (b) $t \approx 40$ min; (c) $t \approx 50$ min; (d) $t \approx 60$ min

Sedimentation and buoyancy in Al-Cu alloys

Sedimentation or floating of solid parts (i.e. dendrite fragments or equiaxed grains) are two key issues to understand the final microstructure or grain arrangement and can only be analyzed by *in situ* observation [22-25]. In the case of Al-Cu alloys, Ganesan and Poirier [26] calculated the densities of the solid and the liquid phases as function of temperature and composition. They found that below approximately 10 wt% Cu, solid density is larger than liquid density so that we may expect to have solid sedimentation. Above this threshold value, the opposite behavior is anticipated and solid floating assumed. The gravity-settling behavior of equiaxed grains is shown in figure 2, with a sequence of radiographs recorded during an Al – 4 wt% Cu solidification experiment. In this experiment, a few equiaxed grains nucleated above the columnar front (Fig.2a). Some of them remained stuck on crucible wall, but others can fall down due to gravity like the grain indicated by the white circle on the right side of the sample.

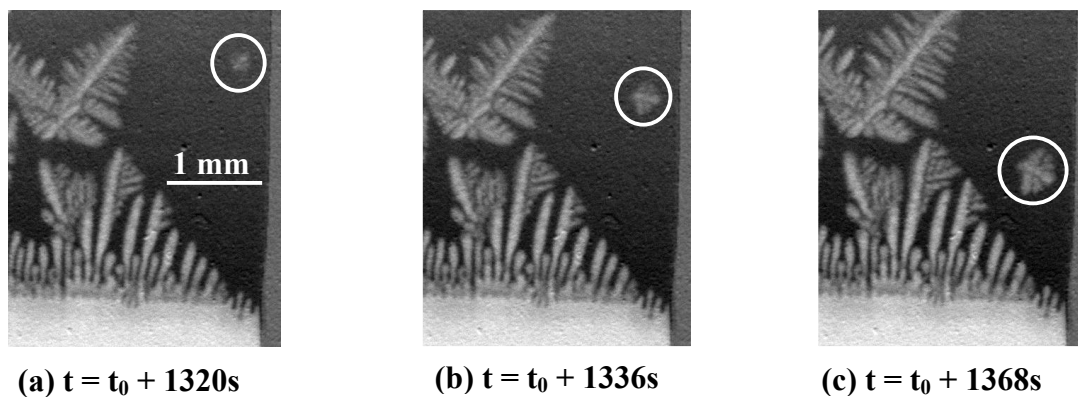


Figure 2: Sequence of 3 radiographs showing sedimentation of an equiaxed grain under the effect of gravity during directional solidification of Al-4wt% Cu ($R_H = 1.5$ K/min, $R_C = 0$, $G = 35.5$ K/cm) (t_0 is the beginning of the cooling).

Live monitoring showed that equiaxed grains grew faster and faster during sedimentation, which is in agreement with the fact that they moved in a richer and colder liquid (Fig.2b and 2c). In addition, they may rotate because of uneven lengthening of their dendrite arms. Finally, the grains stopped to move when they met the columnar front or when their size was comparable to the crucible thickness (Fig.2c). A rough estimate of the sedimentation velocity, typically about 25 $\mu\text{m/s}$, could be obtained based on successive radiographs. It should be stressed that the falling down of equiaxed grains is enhancing grain packing on the columnar front and may lead to the Columnar – to – Equiaxed Transition when their number and size were large enough [3; 4]. According to this, CET is expected to occur earlier on earth than in microgravity.

The floating behavior of dendrite fragments is shown in figure 3, with a sequence of radiographs recorded during an Al – 10 wt% Cu solidification experiment. In this experiment, fragmentation phenomena of the dendritic columnar microstructure were visible on the left side of the dendritic microstructure (Fig.3a and 3b). The dendrite fragments moved upward because it was buoyant with respect to the surrounding fluid. On contrary to the sedimentation case, the size of the dendrite fragments slightly decreased during their upwards movement because they were gradually melted. A rough estimate of the sedimentation velocities between two successive radiographs gave an approximate value of 60 $\mu\text{m/s}$. It is worth noticing that these dendrite fragments could not promote Columnar-to-Equiaxed Transition, because they were carried up far into the liquid where they were re-melted. Our conclusions are in agreement with Griffiths et al [27], who analyzed in details the influence of initial solute composition on the formation of equiaxed regions in Al-Cu and Al-Si alloys but during downwards solidification.

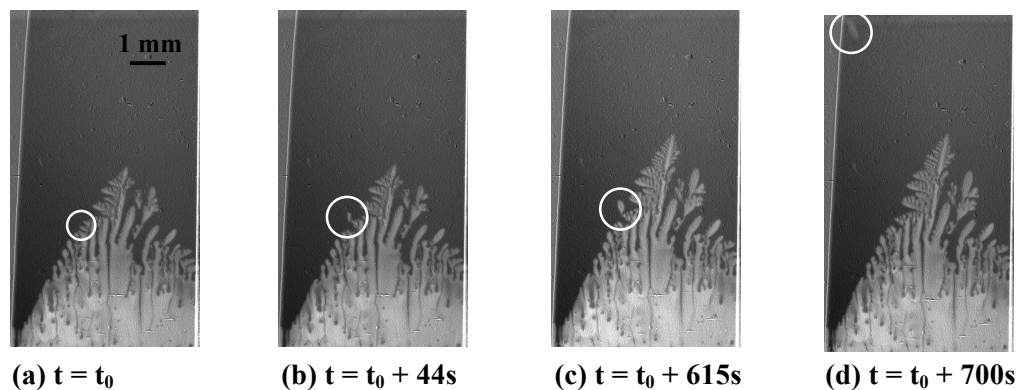


Figure 3: Sequence of radiographs showing dendrite fragments moving upwards under the effect of buoyancy during columnar growth of Al-10wt% Cu ($R_H = 0.1\text{K/min}$, $R_C = 0.1\text{K/min}$, $G = 23.5\text{ K/cm}$).

2. XRMON – GF project

XRMON-GF device

The conceptual design of the breadboard setup is given in figure 2. It consists of a gradient furnace system for solidification of Al-Cu based alloys and an attached high-resolution X-ray diagnostic system. The metallic samples had a sheet-like geometry with a length of 50mm, a width of 5mm and a roughly constant thickness of less than 0.2mm along the sample. Each sample was mechanically polished down to the desired thickness and then sandwiched between two rectangular glassy carbon plates. To investigate the dynamics of solidification processes, the field of view for the X-ray diagnostics was larger than 5 x 5 mm^2 with a spatial resolution of

about 5 μm and a temporal resolution of 2-3 Hz. The X-ray source was based on a microfocus transmission target in molybdenum using polychromatic radiation with a peak at 17.5 keV.

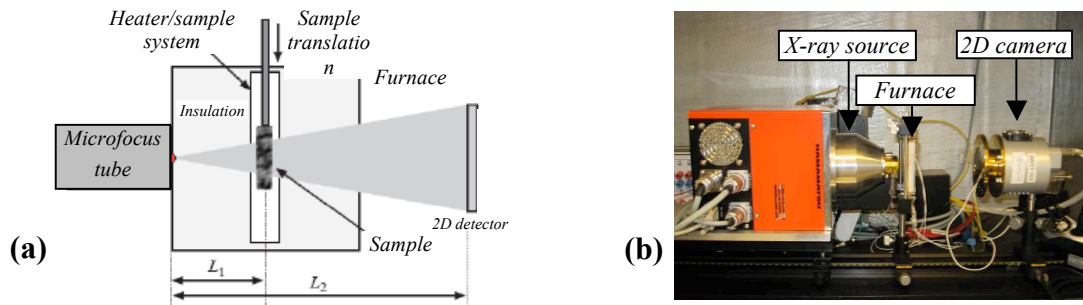


Figure 4. (a) Design of the breadboard set-up, (b) picture of the breadboard set-up showing the X-ray source (left), the furnace (very close to the microfocus source) and the detector (right).

Initial transient during directional solidification of Al - 10 wt% Cu alloy

Fig.5 shows a sequence of radiographs recorded during the initial solidification transient of an Al - 10 wt% Cu alloy for a temperature gradient of 43 K/cm and a cooling rate of the hot heater element of 6 K/min. In Fig.5a ($t = t_0 + 150\text{s}$, with t_0 the reference time, just before the beginning of the solidification) the first disturbances are visible along the whole interface, following the planar front breakdown induced by the Mullins–Sekerka instability [28]. One can already see in Fig.5a that side branches begin to grow on most of the perturbations, which indicates the inception of the formation of dendrites. At this stage, it is possible to determine an average wavelength λ_i for the microstructure, $\lambda_i \approx 180 \mu\text{m}$.

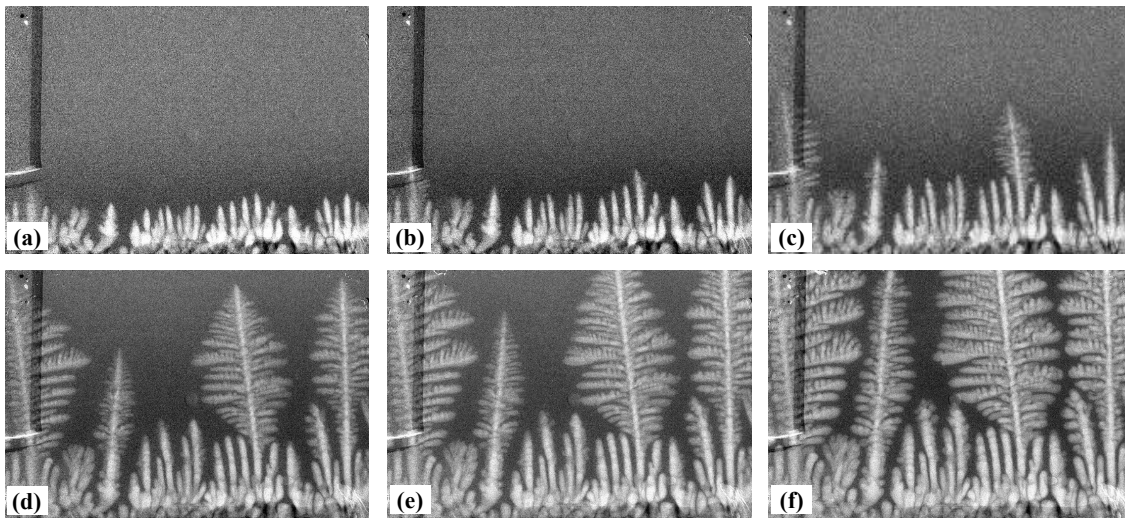


Figure 5. Sequence of radiographs showing the formation of a columnar structure of Al-10wt% Cu (cooling rate = 6 K/min; $G \approx 43 \text{ K/cm}$) (a) $t=t_0+150\text{s}$; (b) $t=t_0+170\text{s}$; (c) $t=t_0+200\text{s}$; (d) $t=t_0+260\text{s}$; (e) $t=t_0+300\text{s}$; (f) $t=t_0+400\text{s}$. t_0 is the reference time, just before the beginning of the solidification. Image width=4.5 mm.

Further development of the pattern occurs with a progressive increase of the amplitude of the disturbances (Fig. 5b, $t = t_0 + 170\text{s}$), while the liquid ahead of the columnar front becomes darker and darker, due to the solute rejection during the liquid-solid transformation. In the subsequent stages, both the amplitude and lateral size of dendrite increase concomitantly, with solute

screening causing a strong decrease of the growth of the neighboring dendrites. The last observed microstructure is mainly composed of several dendrites protruding markedly into the liquid phase with an average final primary spacing $\lambda_f \approx 1\ 260\mu\text{m}$ (Fig.5f).

Fragmentation phenomenon during solidification of Al – 20 wt% Cu alloy

One mechanism for the formation of equiaxed grains during the Columnar-to-Equiaxed Transition is the dendrite fragmentation, which is believed to be at the origin of the central equiaxed core region in casting processes [1; 2]. The details of the fragmentation phenomenon are insufficiently understood and controlled. Thus, it is compulsory to confirm the predominance of the fragmentation phenomenon in CET and also to improve the characterisation and understanding of its mechanism, in particular the role of gravity at each step of CET. To achieve this goal, an efficient approach is to perform a comparison between solidification experiments carried out at 1g and in μg , in both cases with *in situ* characterization by means of X-ray radiography. In Fig.6a one can see the gradual establishment of columnar microstructure, as described in the previous section. In this experiment, an equiaxed grain nucleated ahead of the columnar front, on a small heterogeneity. This grain remained fixed and simply continued to grow in interaction with the columnar front. In Fig.6b and Fig.6d, the black circles pinpoint the presence of several dendrite fragments. For Al – 20 wt% Cu, the solid being much lighter than the surrounding liquid, dendrite fragmentation was promoted by buoyancy forces acting on secondary dendrite arms. After the fragmentation, the dendrite pieces were immediately carried away to the upper part of the sample. In this experiment, fragmentation occurred continuously during the growth process. Radiographs made it possible to have a rough estimation of the fragments velocity, about $60\mu\text{m/s}$. It is worth noticing that these dendrite fragments could not promote CET, because they were carried up far into the liquid where they were re-melted.

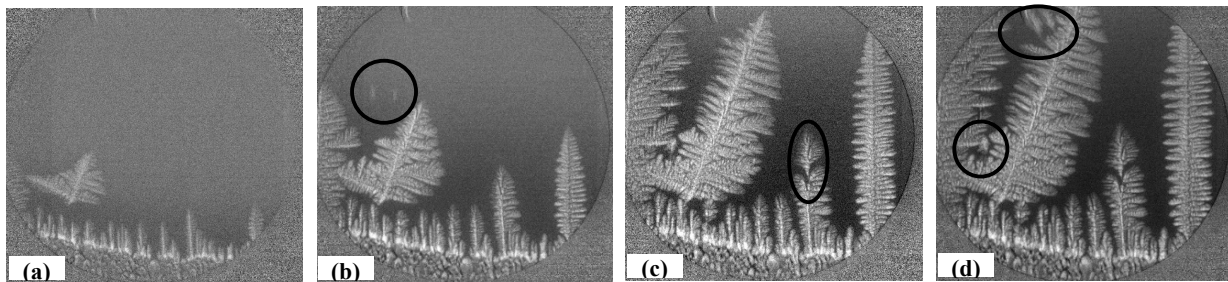


Figure 6. Sequence of radiographs during columnar growth of Al – 20 wt% Cu showing several dendrite fragmentations (cooling rate = 20K/min; $G = 400\ \text{K/cm}$) (a) $t=t_0+50\text{s}$; (b) $t=t_0+100\text{s}$; (c) $t=t_0+150\text{s}$; (d) $t=t_0+168\text{s}$. t_0 is the reference time, just before the beginning of the solidification.

In Fig.6c, the fragmentation of a dendrite primary trunk can also be noticed, indicated by a black ellipse. Its size being close to the sample thickness, the primary trunk fragment could not move far into the liquid phase. This phenomenon was rarely observed compared to the secondary dendrite arm fragmentation, certainly because of the difference in diameter between primary trunk and secondary arms. It has recently been observed by using combined radiography and topography that the rotation of some tenth of degrees around the growth axis of the entire primary trunk during the growth process can occur [29]. This rotation has been interpreted as a consequence of a torque induced by shear stress that builds up with the growth [30]. In our experiments, it was also observed that this phenomenon occurred mainly for a specific crystallographic dendrite direction $\langle 110 \rangle$, which suggests an effect of dendrite morphology.

Conclusions

This paper reports on a selection of results obtained during metallic alloy solidification experiments characterized *in situ* and in real time by X-ray radiography. Experiments were carried out with both a synchrotron source and a microfocus tube, with a dedicated novel experimental set-up developed in the frame of the ESA-MAP XRMON. These results emphasize the great impact of gravity and convection on the dynamics of the solidification front by showing the influence of convection on the initial solidification transient, the sedimentation/buoyancy of equiaxed grains or dendrite fragments. The next step of the project is to perform an experiment in microgravity environment to obtain purely diffusive transport conditions and then to provide benchmark data for the validation of models and numerical simulations. In addition, a comparative study of solidification experiments at 1g and μg will also enlighten the effects of gravity. This is the goal of the solidification experiment scheduled during MASER 12 sounding rocket mission, in autumn 2011.

Acknowledgments

This research work is supported by the XRMON project (AO-2004-046) of the MAP program of the European Space Agency (ESA) and by the French National Space Agency (CNES).

References

1. H. Jung et al. "Fragmentation in an Al-7 wt-%Si alloy studied in real time by X-ray synchrotron techniques", *International Journal of Cast Metals Research*, 22(1-4).(2009). 208-211.
2. D. Ruvalcaba et al. (2007). Fragmentation due to the interaction of solute flow with the dendritic network during the solidification of aluminum alloys. In: *5th Decennial Conference on Solidification processing* (pp. 321-325). Sheffield, U.K.: University of Sheffield, U.K.
3. H. Nguyen Thi et al. "In-Situ and Real-Time Investigation of Columnar to Equiaxed Transition in Metallic Alloy", *Metall. Mater. Trans. A*, 38-7.(2007). 1458-1464.
4. G. Reinhart et al. "in-situ observation of transition from columnar to equiaxed growth in Al-3.5 wt% Ni alloys by synchrotron radiography", *Modeling of Casting, Welding and Advanced Solidification Processes, XI*.(2006). 359-366.
5. A. Bogno et al. "Application of synchrotron X-ray radiography to the study of dendritic equiaxed microstructure formation in Al-Cu alloys", *Nuclear Instruments and Methods in Physics Research Section B: Beam Interactions with Materials and Atoms*, 268(3-4).(2010). 394-398.
6. A. Bogno et al. "In situ analysis of dendritic equiaxed microstructure formation in Al-Cu alloys by synchrotron X-ray radiography", *Transactions of the Indian Institute of Metals*, 62(4-5).(2009). 427-431.
7. A. Badillo, & C. Beckermann (2007). Growth of equiaxed dendritic crystals settling in an undercooled melt. In: *5th Decennial International Conference on Solidification processing* (p. 316). Sheffield, UK: University of Sheffield, UK.
8. R. H. Mathiesen et al. "Time-resolved X-Ray Imaging of Dendritic Growth in Binary Alloys", *Phys. Rev. Lett.*, 83.(1999). 5062-5065.
9. H. Yasuda et al. "Direct Observation of stray crystal formation in unidirectional solidification of Sn-Bi alloy by X-ray imaging", *Journal of Crystal Growth*, 262.(2004). 645-652.
10. T. Schenk et al. "Application of synchrotron X-ray imaging to the study of directional solidification of aluminium-based alloys", *Journal of Crystal Growth*, 275.(2005). 201-208.
11. S. H. Davis "Hydrodynamics Interactions in Directional Solidification", *J. Fluid Mech.*, 212.(1990). 241-262.

12. D. T. J. Hurlle (1992). *Interactive Dynamics of Convection and Solidification*. Pays-Bas: Kluwer Academic.
13. C. Giummarra et al. "Sidebranch characteristics of pivalic acid dendrites grown under convection-free and diffuso-convective conditions", *Journal of Crystal Growth*, 274(1-2).(2005). 317-330.
14. J. C. LaCombe et al. "Nonconstant tip velocity in microgravity dendritic growth", *Physical Review Letters*, 83(15).(1999). 2997-3000.
15. M. B. Koss et al. "Dendritic growth tip velocities and radii of curvature in microgravity", *Metallurgical and Materials Transactions a-Physical Metallurgy and Materials Science*, 30(12).(1999). 3177-3190.
16. H. Nguyen Thi et al. "Directional Solidification of Al-1.5wt% Ni alloys under diffusion transport in space and fluid flow localisation on Earth", *J. of Crystal Growth*, 281.(2005). 654-668.
17. B. Drevet et al. "Solidification of Aluminum-Lithium Alloys near the Cell/Dendrite Transition - Influence of Solutal Convection", *J. Crystal Growth*, 218.(2000). 419-433.
18. A. Buffet et al. "Real-time and in situ solidification of Al-based alloys investigated by synchrotron radiation: a unique experimental set-up combining radiography and topography techniques", *Phys. Stat. Sol.*, 204(8).(2008). 2721-2728.
19. A. Buffet et al. "Measurement of solute profiles by means of synchrotron X-ray radiography during directional solidification of Al - 4 wt% Cu alloys", *Materials Science Forum*, 649.(2010). 331-336.
20. M. H. Burden et al. "Macroscopic Stability of a planar, cellular or dendritic interface during directional freezing", *J. Cryst. Growth*, 20.(1973). 121-124.
21. A. Bogno et al. "Analysis by synchrotron X-ray radiography of convection effects on the dynamic evolution of the solid-liquid interface and on solute distribution during the initial transient of solidification", *Acta Materialia*, 59(11).(2011). 4356-4365.
22. B. Appolaire et al. "Free growth of equiaxed crystals settling in undercooled NH₄Cl-H₂O melts", *Acta Materialia*, 46(16).(1998). 5851-5862.
23. A. Ramani, & C. Beckermann "Dendrite tip growth velocities of settling NH₄Cl equiaxed crystals", *Scripta Materialia*, 36(6).(1997). 633-638.
24. A. Badillo et al. "Growth of equiaxed dendritic crystals settling in an undercooled melt, Part 2: Internal solid fraction", *Journal of Crystal Growth*, 309(2).(2007). 216-224.
25. N. Mangelinck-Noël et al. "In situ analysis of equiaxed growth of aluminium-nickel alloys by x-ray radiography at ESRF", *J. Phys. D: Appl. Phys.*, 38.(2005). 28-32.
26. S. Ganesan, & D. R. Poirier "Densities of Aluminum-Rich Aluminum-Copper Alloys during Solidification", *Metalurgical Transaction A*, 18A.(1987). 721-723.
27. W. D. Griffiths et al. "The influence of bulk liquid natural convection on the formation of the equiaxed regions in Al-Cu and Al-Si alloys", *Materials Science and Engineering: A*, 205(1-2).(1996). 31-39.
28. W. W. Mullins, & R. F. Sekerka "Stability of a planar interface during solidification of a dilute binary alloy", *J. Appl. Phys.*, 35.(1964). 444.
29. G. Reinhart et al. "In-Situ and real-time analysis of the formation of strains and microstructure defects during solidification of Al-3.5 wt pct Ni alloys", *Metallurgical and Materials Transactions a-Physical Metallurgy and Materials Science*, 39A(4).(2008). 865-874.
30. B. Billia et al. "Cumulative moments and microstructure deformation induced by growth shape in columnar solidification", *Phys. Rev Lett.*, 93(12).(2004). 126105.

"Innovative Video Diagnostic Equipment for Material Science"

G. Capuano¹, D. Titomanlio¹, W. Soellner², A. Seidel²

¹TSD - Techno System Dev. s.r.l.;
Via Provinciale Pianura, 2 - Z.I. S. Martino, 23 - Pozzuoli, 80078, ITALY

²ASTRIUM Space Transportation
Claude Dornier Strasse, Immenstaad, 88090, GERMANY

Keywords:

High-Resolution High-frame rate imaging, Real-time Image Compression and Storage

Abstract

Materials science experiments under microgravity increasingly rely on advanced optical systems to determine the physical properties of the samples under investigation. This includes video systems with high spatial and temporal resolution. The acquisition, handling, storage and transmission to ground of the resulting video data are very challenging. Since the available downlink data rate is limited, the capability to compress the video data significantly without compromising the data quality is essential.

We report on the development of a Digital Video System (DVS) for EML (Electro Magnetic Levitator) which provides real-time video acquisition, high compression using advanced Wavelet algorithms, storage and transmission of a continuous flow of video with different characteristics in terms of image dimensions and frame rates. The DVS is able to operate with the latest generation of high-performance cameras acquiring high resolution video images up to 4Mpixels@60 fps or high frame rate video images up to about 1000 fps@512x512pixels.

Introduction

Microgravity provides a number of unique advantages for performing materials science investigations. For example, electromagnetic levitation experiments with undercooled melts can be performed under microgravity conditions with very weak levitation fields compared to experiments on ground leading to a situation where the disturbances induced in the samples by the levitation fields are very small and the temperature range accessible during the experiments can be extended to much lower values compared to ground-based experiments. This allows performing experiments that are targeted to measure a wide range of solidification phenomena and thermophysical properties, such as the direct observation of the solidification front upon recalescence, as well as the measurement of the heat capacity, surface tension, viscosity, and thermal expansion [1].

Due to the nature of the experiments and the measurement objectives, non-contact diagnostics systems are needed to perform such measurements. Among others very often high-resolution and high-frame rate video cameras are used producing a very high data amount. Therefore, advanced video compression and handling systems are essential for many diagnostic systems of materials science payloads. An example of such a video system and its application is presented in this paper.

Measurement Objectives and System Requirements

The main scientific data provided by electromagnetic levitation experiments are data on the size, shape, brightness distribution and temperature of the sample and their evolution over time. Physical data that can be extracted by analyzing the shape of the sample include surface tension and viscosity, which are derived from sample shape oscillations (see figure 2), and the thermal

expansion which is directly derived from the diameter of the sample. Other physical data such as the solidification speed is derived from direct observation of the solidification front (see figure 1). To perform these measurements with the required accuracy either a high spatial or a high temporal resolution is needed or intermediate settings of both, whereas these settings may need to be drastically changed within single measurements to cope with various scientific goals. Typically digital video cameras with advanced optics are used meeting these needs due to their high flexibility in spatial and temporal resolution [2].

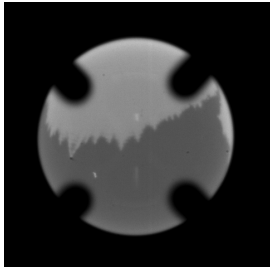


Figure 1 – Solidification (bright area) of undercooled sample

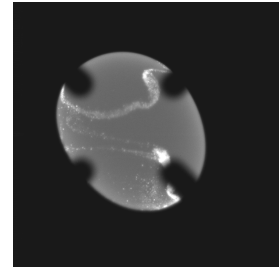
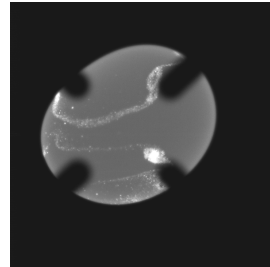
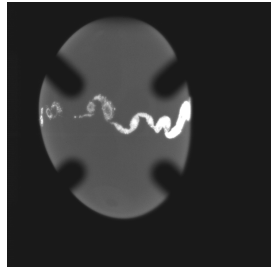


Figure 2 – Induced sample shape oscillations of a liquid sample, oxide particles are observed as bright white structures visualizing the fluid flow

The samples in both figures are levitated in an EML-like facility for parabolic flights; the 4 dark patterns in front are parts of the sample holder preventing the hot sample from leaving the confined area for levitation.

Moreover, monitoring of the levitation process needs a real-time downlink of the captured video, within the limitations of the currently available downlink capacity, for process control purposes and near real-time evaluation. The limited downlink capacity also motivates the need for storage of data on-board the spacecraft of the high amounts of captured video data. Data compression applied due to constraints on the on-board storage resources shall not impair the video images' quality because of the scientific need of image evaluation accuracy on pixel scale. Playback of these high quality video data stored on-board is needed for non real-time evaluation on ground allowing improving experiment settings for upcoming experiment runs.

Technological Challenges

The operation scenario demands from the video acquisition system not only a high data acquisition rate but also flexibility and fast reaction time on changed camera settings. Moreover the system has to duplicate the video into two streams, real-time and playback, which puts an even higher requirement on the data throughput of the system. Both streams have to be handled differently in terms of compression, frame rate adjustment and routing to meet the downlink requirements for the real-time video on one hand and the requirements for video storage on-board on the other hand. Further, the entire handling of the acquired video stream needs to be performed without delay since the camera does not provide for any video buffer and no image captured shall be lost. Provided this, the video system must fit within a small available volume and a tight mass and power budget.

Design Solution and Technology

TSD (Techno System Dev.) has been working since 1991 on the development of digital video systems for space applications, exploiting different hardware and software architectures. The DVS (Digital Video System), subject of the present paper, is based on a compact and very powerful platform, named H²VMU (High Resolution/High Frame Rate Video Management Unit), developed by TSD, and whose first generation implementation flew on board a Sounding Rocket on May 2005 [3]. The H²VMU has been designed for real-time video acquisition, lossy and/or loss-less compression and transmission/storage of a continuous video data flow. The

H²VMU platform is periodically enhanced and in the current third generation it is able to operate with very high performance cameras (both high resolution and high frame rate) with an input data throughput up to 240Mpixels/s. The H²VMU is based on a modular architecture comprising compact and low power modules implementing a wide set of functions:

- Camera interface & video acquisition
- Wavelet lossy and/or loss-less compression
- Custom image processing
- Volatile or no volatile video data storage on different technologies
- Command reception and decoding for unit configuration and control according to CCSDS (Consultative Committee for Space Data Systems) standard
- Video Data packetization and encoding according to CCSDS standard
- Low power management

The modules can be arranged in different configurations in order to fulfill different and specific user requirements. The modules are also available with different qualification levels, including radiation tolerant versions. Table 1 reports the maximum specifications that can be achieved. Since budgets strongly depend on the configuration, the values reported in the table 2 are provided for three typical configurations.

Table 1 - H²VMU maximum specifications

Video input data rate:	up to 240 [Mpixel/s] for each video input module
Image resolution	up to 4[Mpixel] @ 60[frame/s]
Frame rate	1000[fps] @ ≈512x512 [pixel] (higher frame rate at lower resolution available)
Pixel depth:	up to 12[bit]
Compression rate:	<ul style="list-style-type: none"> - up to 60[Mpixel/s] in loss-less mode for each compression module - up to 300[Mbyte/s] in lossy mode for each compression module
Storage rate and capacity:	<ul style="list-style-type: none"> - 60[Mbyte/s] and 64[Gbyte] for each custom high rel solid state storage module - 100[Mbyte/s] and 250[Gbyte] for each COTS (Commercial Off The Shelf) removable SATA hard disk

Table 2 - H²VMU Budgets

Configuration	60 [Mpixel/s] single Channel & 32 GB custom storage module	240 [Mpixel/s] four Channels & 148 GB custom storage module	60 [Mpixel/s] single Channel & Removable SATA disk (250 GB)	
			H ² VMU	HDD
Mass [kg]	2.7	4.7	5.8	2.2
Dimensions [mm]	150x140x150	149x252x140	186x114x254	58x140x220
Power@28V [W]	13.4	40	46 (including HDD)	

Internal Communication Architecture

The DVS is based on a novel approach for board interconnection and data communication. Depending on the unit configuration, an application-specific back-plane is designed based on:

- high-speed point-to-point SerDes (Serializer/Deserializer) links with multi-drop bus configuration for data transfer
- low-speed redundant CAN (Controlled Area Network) network for control and configuration

The SerDes links are based on the National ChannelLink technology that provides high speed data transfer (up to 1,785 Gbps) over a reduced size interconnection (a reduction up to 80% is possible with respect to the classic parallel bus approach), thus allowing the implementation, in a single back-plane PCB (printed circuit board) of a significant number of those links working at the same time. The physical level is LVDS (low voltage differential signaling) that provides differential signaling with small swing, low noise and good noise tolerance. The unit implements ChannelLink communication channels between modules with multi-drop configuration, thanks to a careful PCB design that requires to follow demanding guidelines to ensure signal integrity; these include, for instance, hand routing, impedance control, electrical length matching, proper track separation and loading balance.

The source module requiring transmitting data acts as driver of the communication channel while destination nodes are on the receiver side. As these modules support different input data rates (either as sustained or peak rate) a simple request/grant scheme is then implemented to manage the communication flow. The driver asserts the request line whenever it has valid data to transfer. A dedicated module generically acts as router (implemented as a stand-alone module or embedded in one of the already existing others) moving those requests to the destination nodes. The receivers, whose input request lines are set, acknowledge the request by asserting their relevant grant lines whenever they're available to accept the incoming data. They can release the grant line during the data transmission, as well, to add wait state to the communication. The router implements the logical and of the grant lines of the receivers that are involved in the communication and asserts thereafter the grant line towards the driver to start the data transmission. It can also implement the masking of the request and grant lines to/from one or more receivers. So, according to the chosen configuration, data can be moved to all the receivers physically connected to the multi-drop bus or only to a subset of them. All the same, faulty receivers that are no more capable of receiving data can be isolated to prevent any dead-lock in the communication.

Video Compression

Video data reduction techniques are of utmost importance in space applications, due to the often reduced on-board resources devoted to data storage and transmission to ground. The importance for data reduction is increasing over time as modern diagnostic instruments like high resolution digital cameras provide increasingly large amount of data.

The choice of compression factors to be applied to video data obviously depends on the use to be made of the images. As a rule of thumb one can say that for scientific images that have to be stored on-board a lossless or quasi-lossless compression is often required in order to guarantee the maximum scientific return. This imposes the use of compression factors in the range 2÷5. On the other hand, for images to be transmitted to ground in real-time to be used for control and monitoring purposes it is often possible to achieve much higher reduction levels. By applying different techniques like image lossy compression, image binning, frame rate reduction it is possible to have overall reduction factors in the range 100÷300.

Most of the image compression techniques use the signal expansion as major component. Generally this is achieved via digital filter banks. The reasons for expanding the video signals and process them in the transform domain are numerous. Usually the signal processing in the transform domain allows us to achieve a better data compression for a prefixed encoder complexity. The signal in the transform domain can be submitted to a more efficient quantization that takes into account also criteria about the human vision perception.

The most common transform is the DCT (Discrete Cosine Transform); it is still used for image compression standard like MPEG and JPEG. This type of compression technique exhibits several limitations from the implementation point of view. The algorithm needed to perform the DCT

requires a great amount of calculations to obtain the transformed image. This is due to the nature of the basis function used for signal expansion that has not a finite time extension (Cosine function is periodic). Therefore, in order to limit the amount of calculations to a reasonable level, the image is decomposed in 8x8 block of pixels. When high compression ratio is applied, this results in block artifacts that are typical of this compression technique.

In the recent years the image compression technique based on Wavelet transform has been considered an extremely interesting alternative due to the several advantages that it offers with respect to the DCT. This technique also uses signal expansion, but the basis function employed appears more appropriate in order to achieve the following goals:

- high quality image compression
- considerable reduction of transform computational complexity

As clearly visible in figure 3, the block artifacts are present, at high compression factors, only in the image compressed with JPEG; the same image compressed with the same factor using Wavelet, exhibits only a very small degradation.

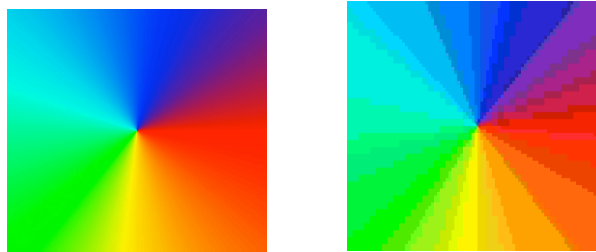


Figure 3 – Image compressed (170:1) by Wavelet (left) vs. JPEG (right)

The reduction of the amount of calculation to perform the image transformation is due essentially to an important property of the wavelet basis functions: their finite time extension.

A compression system based on the discrete transform consists mainly of 3 blocks:

- mapper
- quantizer
- entropy encoder

The mapper transforms the image from a space/time domain in a new domain where the redundant information between the pixels is reduced. In the case of a wavelet compressor, the mapper is represented by the discrete wavelet transform that transforms the image from a space/time domain in a time/frequency domain. The quantizer reduces the redundant psychological-visual information; the entropy encoder reduces the redundant numerical information. The solution that TSD has tuned over several years is a Wavelet compressor based on an EZW (embedded zerotree wavelet) encoder. The EZW is an algorithm for data compression derived from a scheme designed by J.M. Shapiro [4] especially to work with the discrete wavelet transform. The EZW coder is progressive in nature. This means that as more data is added to the compressed stream, the more detailed the reconstructed image will be. Progressive coding is also known as embedded coding - thus the E in EZW. EZW utilizes the observation that in natural images most of the energy (or information) is in the low frequency spectrum. After a wavelet transform has been calculated, the coefficients in the lower frequency subbands tend to be larger (in absolute value) than the coefficients in the higher frequency subbands. This allows for the creation of structures called zerotrees. Another observation used by EZW is that larger valued coefficients are more important than small value coefficients. Therefore EZW codes the larger coefficients first. The TSD solution offers significant higher quality especially at high compression factors than other Wavelet compressors, as visible in the example pictures of figure 4 using a factor of 160:1.



Original photo



TSD Wavelet



JPEG2000 Wavelet

Figure 4 – Comparison between TSD Wavelet and JPEG2000 Wavelet at extreme compression factor 160:1.

All the functional blocks needed to carry out the above described image compression algorithm, have been implemented, by TSD, in a hardware solution using high-density FPGAs, employed as complete System-On-Chip solutions. The newest implementation, running on Xilinx Virtex4 FPGA, is able to perform lossy compression at a rate of 300 Mbytes/s.

Video Storage

The video data storage functionality can be implemented with either custom solutions based on an array of flash memory devices or with commercial solutions like SATA disks. Custom arrays of flash devices are to be preferred in applications requiring high levels of reliability, while SATA mechanical disks offer higher storage density and better radiation tolerance.

TSD has developed products in both categories, reaching high levels of storage rates. For custom arrays of flash devices the latest implementation allows to store up to 240Mpixel/s, thanks to a proprietary pipelined architecture, with storage capacity up to 64GByte per module, while in the case of SATA disks it is possible to store more than 100MByte/s per disk with up to 4 disks running in parallel. The disk is used as a raw device, i.e. without a file system, so to maximize the performances.

Usability

One of the most appealing characteristics of the DVS for the end user is its high degree of flexibility. The on board software provides a rich set of commands and house keeping data that allows the facility controller to configure the DVS on-the-fly according to the user needs.

Among the various features, the most remarkable are:

- Possibility to modify various parameters while a video acquisition is running, like compression factors, binning, frame skipping, test patterns generation
- Possibility to route the different video streams (loss-less science video, lossy real-time video, etc.) to the on board storage devices and to the payload data transmitter in a number of different configurations
- Possibility to perform the software update during flight
- Possibility to interrogate any processing node (either main CPU or FPGAs) by means of low level CAN bus commands in case of troubleshooting
- Possibility to power off the video processing modules in case a low power mode is needed

Apart from its flexibility, the DVS is remarkable for the responsiveness: all the operations are executed in “real-time”; no latency is expected when a command is issued, regardless of the operations that are being performed in that moment. This is due to the hardware and software architecture of the DVS that features a powerful CPU, a highly deterministic real-time operating system, a number of highly specialized FPGAs and very fast internal communication links.

Applications

Main task of the H²VMU is to compress huge amounts of acquired data in real-time to make them accessible to users whenever the data transmission rate between facility and control station is limited. This feature is often employed to scientific systems using video diagnostics but also for data of X-ray detectors. The H²VMU has been successfully employed on-board several MASER Sounding Rockets [3], [5] and Foton Russian capsule [6], providing video diagnostic capabilities to different microgravity experiments. Figure 5 refers to the CDIC-2 experiment (Chemically Driven Interfacial Convection) while figure 6 refers to the SOURCE experiment (SOUnding Rocket Compare Experiment) which studies heat and mass transfer in a heated tank with a liquid pressurized by non-condensable gas. Both performed on board MASER 11.

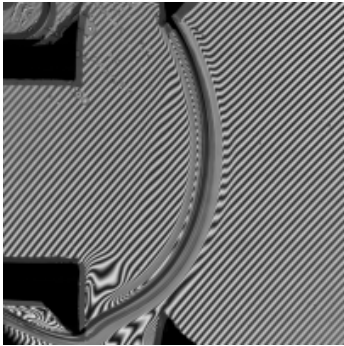


Figure 5 – Interferometric image of fluid interface, Compression factor 48:1

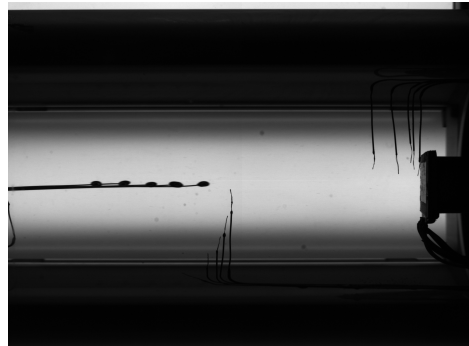


Figure 6 – Shadowgraph image of fluid science experiment cell, Compression factor 68:1

Other H²VMU based specific configurations are currently flown on board the ISS and on the main spacecraft of the PRISMA formation flying mission [7]. Next applications are foreseen for Maser 12 and for the ISS, supporting the EML Material Science Experiment [2].

Electro Magnetic Levitator (EML) on the International Space Station (ISS)

For EML the DVS plays a central role in the chain of optical diagnostics acquiring the digital video stream of a highly flexible camera wrt spatial and temporal resolution [2]. Since the acquired video stream is used twofold, for scientific and for process control purposes, the H²VMU (see figures 7 and 8) has to duplicate the video stream and have the capability to treat both streams (scientific & process control) in different ways wrt compression, pixel reduction and frame rate reduction. All the above actions have to be performed in real-time, storing the scientific data on the DVS owned hard drive and provide the process control video at the video interface for downlink to ground control. Moreover, playback of the scientific data from HDD via the downlink interface is possible offline, i.e. between two experiment runs, and the DVS configuration can be quickly changed to match the current scientific needs and camera settings.

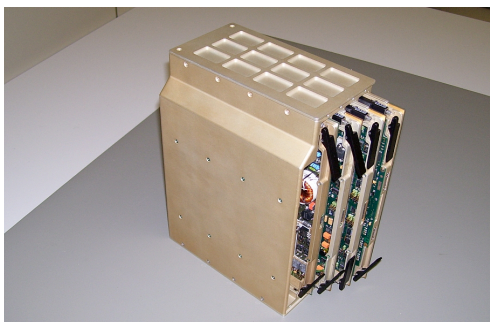


Figure 7 – The engineering model of the H²VMU for EML (internal view of the boards)

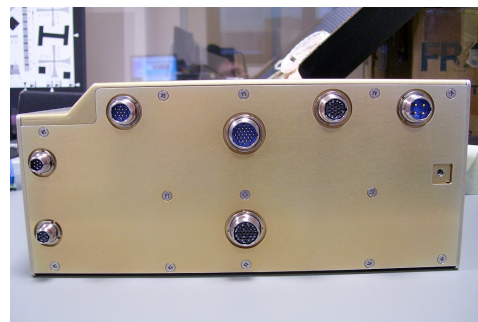
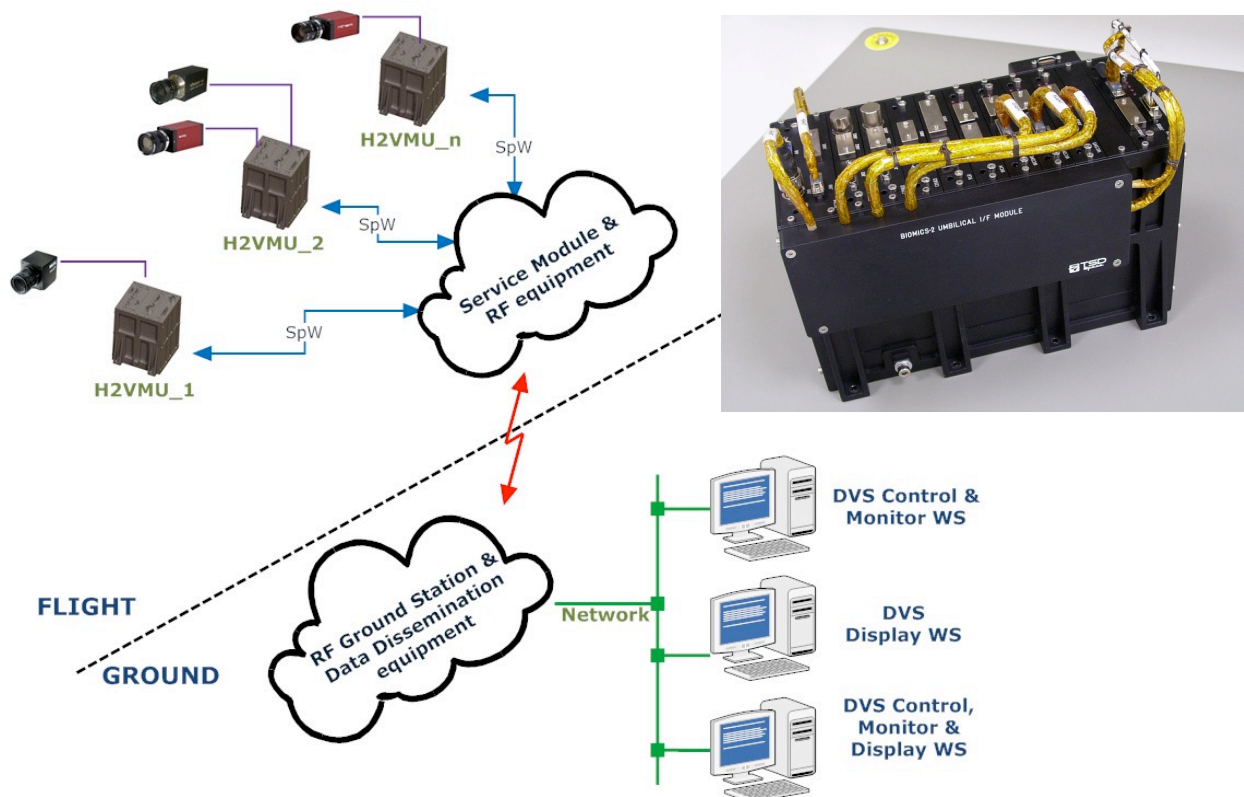


Figure 8 – The engineering model of the H²VMU for EML (rear view showing the connectors)

H²VMUs on board Sounding Rockets

The H²VMU represents the core of the DVS employed in all the MASER Sounding Rocket Program since 2005. A number of H²VMUs are used on board the MASER supporting all the Experiment Modules requiring video functionalities such as real-time image processing, on board storage, compression and downlink. Figure 9 below shows typical concept of DVS as applied to the MASER missions. The performance requirements of the experiments are more and more increasing and currently culminating to 313Mpixel/s (pixel depth up to 12 bit) on MASER12. The DVS architecture is decentralized and each Experiment Module is provided with a local H²VMU with multichannel capability in accordance with the requirement of the specific video diagnostic systems; a three channel H²VMU used on board MASER 12 is hereinafter shown in the insert of figure 9.



**Figure 9 – DVS architecture for Sounding Rocket missions as e.g. MASER
Insert: 3 channel H²VMU for BIOMICS-2 experiment on MASER 12**

ERB-2 Stereoscopic Camera

The Erasmus Recording Binocular 2 (ERB-2) is a digital stereoscopic camera, based on the H²VMU platform, allowing the simulation of human binocular vision. The ERB-2 has been proposed by ESA-ESTEC as a technology experiment to be flown on board the ISS able to capture and send to ground 3D films and related audio of the scenes filmed by the camera (see figure 10).

The ERB-2 is presently on-board the ISS. The first tests were successfully performed in July and August 2010. During March 2011 the Astronaut Paolo Nespoli conducted a fly-through filming program, starting in Kibo JPM (JEM Pressurized Module) and proceeding through Node-2, US Lab, and Node-3 with Cupola to COLUMBUS Laboratory (see figure 11). ERB-2 is also provided with two motorized objectives, driven by the H²VMU electronics, providing auto-iris and auto-focus functionalities.



Figure 10 – The flight model of ERB-2 at TSD premises



Figure 11 – Astronaut P. Nespoli with ERB-2 on board the ISS

Conclusions

Data compression has become a key technology for applications which produce high amounts of data and also suffer from a low data transmission rate. The technique introduced in this paper using EZW Wavelet compression is capable of maintaining the original data information by applying medium compression factors and achieves an unparalleled image quality for high compression factors compared to other Wavelet techniques.

The compression algorithm, as well as other customized features, is embodied in a hardware solution, called H²VMU, using state of the art and radiation hardened components. This modular and very flexible platform allows for real-time video acquisition, customized processing, lossy and/or loss-less compression and transmission/storage of a continuous video data flow.

The successful application of the H²VMU on board different space platforms (Sounding Rockets, Capsule, ISS, and Satellites) has demonstrated firstly its maturity to be now widely employed on board of various space platforms and secondly that it is best suited for material science facilities utilizing demanding image diagnostics.

References

1. “Materials Science Investigations using Electromagnetic Levitation”, A. Seidel, W. Soellner and C. Stenzel, Proceedings to 4th ISPS conference – Bonn, July 2011
2. “EML - Containerless Processing Facility for Material Science Research onboard The ISS”, W. Soellner, A. Seidel, C. Stenzel, W. Dreier and B. Glaubitz, J. Jpn. Soc. Microgravity Appl. 27 No. 4 183, 2010
3. “Digital Video System on-board Maser10”, G. Capuano et. al., 17th ESA Symposium on European Rockets and Balloon related research – Sandefjord, Norway 30 May – 2 June 2005
4. “Embedded Image Coding Using Zerotrees of Wavelet Coefficients”, Jerome M. Shapiro, IEEE Transactions on Signal Processing, December 1993
5. “Digital Video System on-board Maser11”, G. Capuano et. al., 18th ESA Symposium on European Rockets and Balloon related research – Visby, Sweden 3 - 7 June 2007
6. “Data Handling Unit for Foton-M3 Mission”, D. Titomanlio et. al., DASIA 2007, June 2007, Naples (Italy).
7. “Video System for PRISMA Formation Flying Mission”, G. Capuano, M. Severi, F. Cacace, et. al., 4th Symposium on Small Satellite, Systems and Services – Rhodes (Greece), May 2008

Containerless Measurements of Density and Viscosity of Fe-Co Alloys

Jonghyun Lee¹, Paul Choufani¹, Richard C. Bradshaw², Robert W. Hyers³, Douglas M. Matson¹

¹Tufts University;

Department of Mechanical Engineering;

200 College Avenue; Medford, MA 02155, USA

²Bradshaw Consulting

108 Harnden Avenue; Watertown, MA 02453, USA

³University of Massachusetts;

Department of Mechanical Engineering;

160 Governors Drive; Amherst, MA 01003, USA

Keywords: Fe-Co Alloys, Density, Viscosity, Containerless measurements, Double recalescence

Abstract

During the past years, extensive collaborative research has been done to understand phase selection in undercooled metals using novel containerless processing techniques such as electrostatic and electromagnetic levitation. Of major interest is controlling a two-step solidification process, double recalescence, in which the metastable phase forms first and then transforms to the stable phase after a certain delay time. The previous research has shown that the delay time is greatly influenced by the internal convection velocity. In the prediction of internal flow, the fidelity of the results depends on the accuracy of the material properties. This research focuses on the measurements of density and viscosity of Fe-Co alloys which will be used for the fluid simulations whose results will support upcoming International Space Station flight experiments.

Introduction

Molten metallic alloys can be undercooled if the preferred sites for nucleation such as crucibles and impurities are effectively removed. One effective way of achieving undercooling is containerless processing. When the undercooled liquid solidifies, the heat of fusion is rejected and the temperature increases suddenly. This phenomenon is referred to as recalescence. The solidification of undercooled alloys can occur in two ways: either the stable phase nucleates directly from the liquid (single recalescence) or the metastable phase forms first followed by the growth of the stable phase into the mushy zone (double recalescence). The metallography reveals that alloys which have undergone double recalescence show fine and globular grains, which can result in better mechanical properties. Since the growth rate of the metastable phase is lower than that of the stable phase, it is important to attain a certain amount of delay time between the

nucleation events. If there is enough delay time, most part of the alloy will double recalesce, otherwise, the stable phase begins to grow and overtakes the metastable phase solidification front as shown in Figure 1 [1]. Previous research has shown that the delay time is greatly affected by the internal convection in the molten alloy. If the convective velocity is large, the primary arms of dendrites can be bent by the drag forces and eventually collide with each other. The collision between neighboring dendrite arms can serve as a preferred site for the unwanted early nucleation of stable phase [2]. Therefore characterization of fluid flow in the molten alloys is important in understanding the phase selection during solidification.

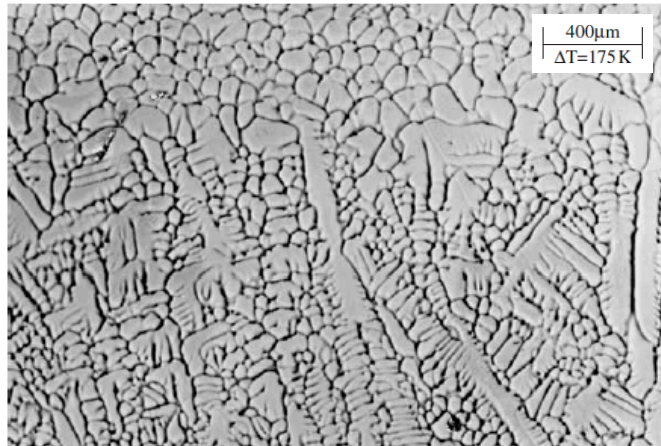


Figure 1. Microstructure of steel alloy: The solidification proceeded from top to bottom. The upper portion of the figure underwent double recalescence and thus shows globular and fine microstructures. As the solidification proceeded, the stable phase overtook the metastable solidification resulting in the dendritic structure shown in the lower portion of the figure. This corresponds to single recalescence behavior.

In the near future, a series of solidification experiments will be performed in space over a wide range of internal convective velocities to acquire data for comprehensive understanding of solidification processes. For the success of the International Space Station (ISS) mission, the identification of the correlation between test parameters and internal fluid flow is of great importance.

Hyers *et al* [3] have developed mathematical models which describe the convection inside the droplet while processed in both electromagnetic (EML) and electrostatic (ESL) levitators. These models can be solved using appropriate numerical techniques. To obtain satisfactory numerical results, it is important to secure reliable material properties. Using containerless measurement techniques [4], material properties of Fe-Co alloys, one of the candidate alloys for the ISS mission, are measured. These values will be used for the computational fluid dynamics simulations in support for the ISS mission.

Experimental Apparatus

The experiment was performed with the electrostatic levitation (ESL) facility at NASA Marshall Space Flight Center (MSFC) in Huntsville, AL. The weight of the sample was cancelled by Coulomb forces exerted by a pair of vertical electrodes. Two additional pairs of electrodes on the horizontal plane were used to stabilize the sample using the PID (Proportional, Integral, and Derivative) control scheme. After levitation and stabilization, the sample was heated by a 200 W YAG laser and the temperature was monitored by optical pyrometers (Mikron Infrared Inc.) which detects the wavelength of emitted light from the sample. The processing was achieved in a high vacuum chamber ($\approx 10^{-8}$ torr) to avoid chemical reactions. Figure 2 shows a schematic of ESL apparatus in NASA MSFC.

During the processing, images of the sample were captured by a high speed camera (Redlake Motion Pro 1000) and analyzed to obtain measurement of density and viscosity as a function of temperature. For analysis of images, the edges of the sample in the images were detected and fitted with sixth order Legendre polynomials for the calculations of projected areas and volumes of samples. The details of image processing techniques can be found in [5].

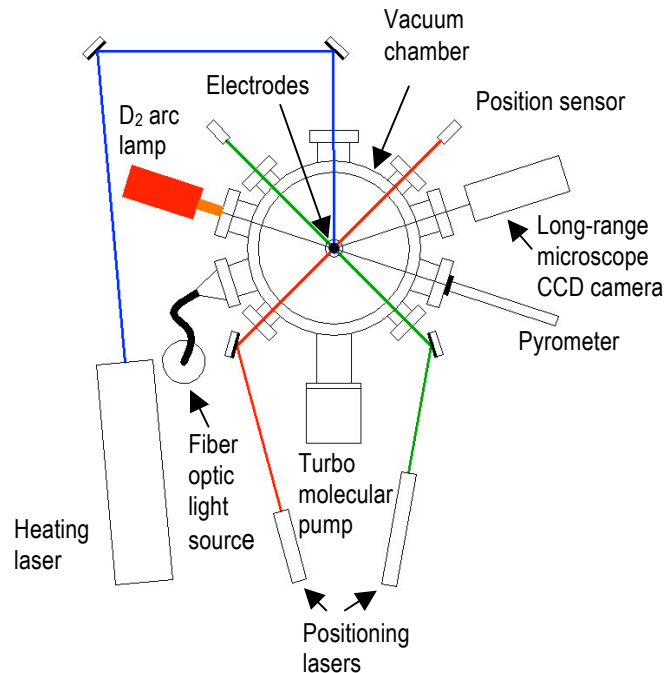


Figure 2. A schematic of ESL apparatus in NASA MSFC.

Measurement of Density

To estimate the density of the sample, it is essential to know the volume and mass of the sample for each time step in a thermal cycle. As the molten sample free cooled video images were acquired at a rate of 25 Hz and edge-detection software was used to tract sample shape. While the volume can be easily obtained by integrating the fitted functions (6th order Legendre polynomials), a care must be taken in dealing with the mass. Throughout the density test, the reduction in mass due to evaporation was observed. Adopting the Langmuir's equation for evaporation, the loss of mass for a given time was calculated.

$$\frac{\dot{m}}{A_s} = \frac{\alpha(p_{\text{vapor}} - p_{\text{atm}})}{\sqrt{2\pi kT}} \quad (1)$$

where \dot{m} is the rate of loss of mass due to evaporation, A_s is the surface area, p_{vapor} is the vapor pressure, p_{atm} is the partial pressure of the atmosphere, α is the correction factor to account for the mass transport diffusion layer resistance, k is the gas constant, and T is the absolute temperature. Having the volume and mass as functions of time, the density of the sample could be estimated as a function of time. Combining the estimated density and temperature as functions of time t , density-temperature plots were generated.

$$\rho(T(t)) = \frac{m(T(t))}{\text{volume}(T(t))} \quad (2)$$

Measurement of Viscosity

Since the viscosity acts as a resistance to fluid motion, the decay time for an oscillating sample can be used to measure the viscosity. The sample was excited by applying periodic changes in the vertical electrostatic field. The excitation started with the lower frequencies and was gradually increased until the sample showed noticeable oscillations; the excitation frequency was near the sample natural frequency ($\approx 200\text{Hz}$). Once the desired level deformation is achieved, the excitation was stopped and the sample was allowed to dampen out freely. The sample oscillations were captured at the rate of 1000 Hz.

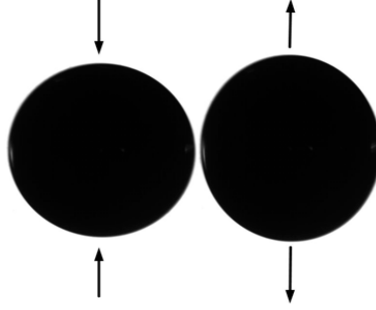


Figure 3. Shapes of an oscillating sample.

By analyzing the captured images, the areas of the oscillating sample were calculated for each frame. After the area of the oscillating sample was plotted in the time domain, the Fast Fourier Transform was applied to extract the natural frequency of the sample and then a sinusoidal curve as expressed in Equation (3) was fitted to the decaying portion of the amplitude $y(t)$.

$$y(t) = \cos(\omega t + \phi) \exp\left(\frac{t}{\tau}\right) \quad (3)$$

where ω is the natural frequency, ϕ is the phase angle, and τ is the damping coefficient which characterizes how fast the sample dampens out. The viscosity can be determined using its relationship with the damping coefficient as below.

$$\mu = \frac{\rho R_0^2}{(l-1)(2l+1)} \cdot \frac{1}{\tau} \quad (4)$$

where ρ is the density, R_0 is the radius of the undeformed droplet, l is the mode of oscillation ($l=2$).

Results and Discussion

The density of $\text{Fe}_{45}\text{Co}_{55}$ was measured as a function of temperature and plotted in Figure 4. As indicated above, during the experiment 6.86% of mass was lost due to the mass evaporation. According to the temperature-time plot, the sample was melted and superheated up to $T_m+130\text{K}$ for 66 seconds and cooled for 6 seconds during which the density was measured. Considering the fact that the time duration for the density measurement is only 9% of that for melting and superheating, it is reasonable to assume that the majority of mass evaporation had occurred before the measurement of density. Thus, the post-mass was used for calculation of density and this technique should result in a slight underestimation of density results. For comparison, the red line in the graph indicates the predicted values for density using rule of mixtures (ROM). For the

prediction, the density and the rate of change in density with respect to temperature ($\partial\rho/\partial T$) of Fe and Co shown were taken from the literature [6] and these values are shown in Table 1.

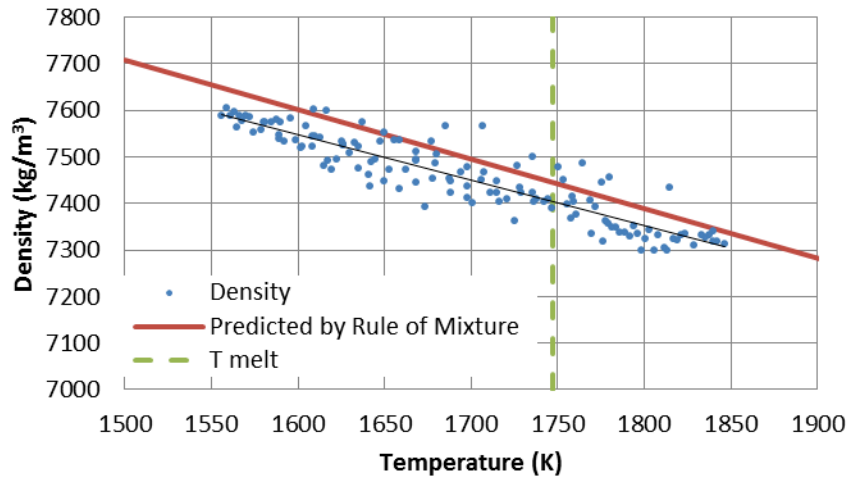


Figure 4. Variation of density as a function of temperature. The black line is a least-squares line fit to the measurements.

Table 1. Densities and the slopes of density with respect to temperature of Fe, Co, and Fe₄₅Co₅₅.

	Fe	Co	Fe ₄₅ Co ₅₅
T_m (K)	1808	1765	1747
ρ at T_m (kg/m ³)	7030	7750	7458
$-\partial\rho/\partial T$ (kg/m ³ ·K)	0.880	1090	0.996

The density at the melting point was estimated to be 7405 kg/m³ and it was slightly greater than the predicted value by 0.7%. The rate of change in density with respect to the temperature at the melting point was estimated to be -0.9741 kg/m³·K and the difference from ROM predicted slope was thus 2.1%. It can be stated that the experimental results and ROM predictions agree well with each other and.

Two samples of Fe₄₅Co₅₅ were used for the measurements of viscosity. Figure 4 shows the viscosity of Fe₄₅Co₅₅. The viscosity data was fitted with an Arrhenius relation.

$$\mu = \mu_0 \exp\left(\frac{E}{k_b T}\right) \quad (5)$$

where E is the activation energy, k_b is the Boltzmann constant (8.61730×10^{-5} eV/molecule-K). The fitted values are $\mu_0 = 4.912 \times 10^{-6}$ Pa·s and $E = 1.24891$ eV/molecule. The viscosity at the melting point was estimated to be 0.0197 Pa·s.

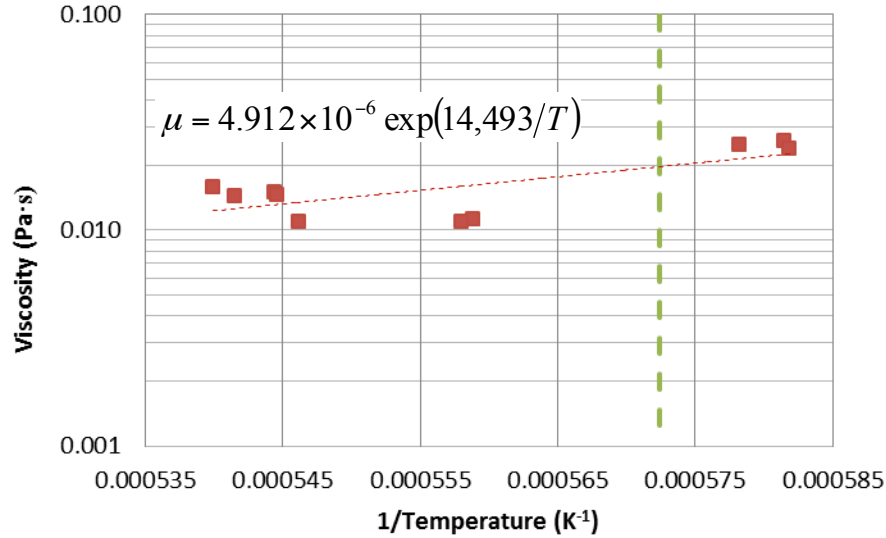


Figure 5. Variation of viscosity as a function of temperature.

Summary

As support and preparation for ISS mission, the density and viscosity of $\text{Fe}_{45}\text{Co}_{55}$ were measured with the novel containerless processing technique. The measured density and its rate of change with respect to the temperature at the melting point ($\partial\rho/\partial T$) were $7,405 \text{ kg/m}^3$ and $-0.9741 \text{ kg/m}^3\cdot\text{K}$ and these values show an excellent agreement with the predicted values by the rule of mixtures and their differences were to be 0.7% and 2.1% respectively. The viscosity of $\text{Fe}_{45}\text{Co}_{55}$ was measured and fitted with the Arrhenius relation as $\mu = 4.912 \times 10^{-6} \exp(14,493/T)$. The measured density and viscosity values will be used for the simulations of convection inside the droplets.

Acknowledgements

This project is sponsored by NASA under grants NNX08AL21G and NNX10AV27G. Experimental portions of this research were performed at NASA Marshall Space Flight Center. The authors wish to thank Trudy Allen and Glenn Fountain for extensive technical advice.

References

1. A.B. Hanlon, R.W. Hyers, and D.M. Matson, "Modeling the Effects of Internal Convection on Dendritic Evolution in Stainless Steel Alloys," *EPD Congress – Proceedings of the Symposium by the Extraction and Processing Division of the Minerals, Metals and Materials Society*, 2005, pp. 501-507.
2. A.B. Hanlon, D.M. Matson, and R.W. Hyers, "Internal Convective Effects on the Lifetime of the Metastable Phase Undercooled Fe-Cr-Ni Alloys," *Philosophical Magazine Letters*, vol. 86, no. 3, 2005, 165-174.
3. R.W. Hyers, Douglas M. Matson, Kenneth F. Kelton, and Jan R. Rogers, "Convection in Containerless Processing," *Annals of New York Academy of Science*, 2004, pp. 474-494.
4. R.C. Bradshaw, "Automatic Containerless Measurements of Thermophysical Properties of Quasicrystal Forming Metals," PhD Dissertation, The University of Massachusetts Amherst, 2006.
5. R.C. Bradshaw, D.P. Schmidt, J.R. Rogers, K.F. Kelton, and R.W. Hyers, "Machine Vision for High-Precision Volume Measurement applied to Levitated Containerless Material Processing," *Review of Scientific Instruments*, vol. 76, no. 12, 2005.
6. T. Iida and R.I.L. Guthrie, "The Physical Properties of Liquid Metals," Oxford University Press, Oxford, 1988.

TEMHD Effects On Solidification Under Microgravity Conditions

Andrew Kao, Koulis Pericleous

University of Greenwich, Old Royal Naval College, Park Row, Greenwich, London, SE10 9LS, United Kingdom

Keywords: Dendritic Growth, Solidification, Thermoelectricity, Magnetohydrodynamics, Undercooling

Abstract

An unexplored potential exists to control microstructure evolution through the use of external DC magnetic fields. Thermoelectric currents form during solidification and interact with this external field to drive microscopic fluid dynamics within the inter-dendritic region. The convective heat and mass transport can lead to profound changes on the dendritic structure. In this paper the effect of high magnetic fields is demonstrated through the use of both 3-dimensional and 2-dimensional numerical models. The results show that the application of a magnetic field causes significant disruption to the dendritic morphology. Investigation into the underlying mechanism gives initial indicators of how external magnetic fields can either lead to unexpected growth behaviour, or alternatively can be used to control the evolution of microstructure in undercooled melts as encountered in levitated droplet solidification

Introduction

Levitation/confinement is often achieved through the combined use of both AC and DC magnetic fields [8]. Under these conditions it is possible to undercool the droplet into a metastable state, where the droplet is still liquid but its temperature is below the solidus temperature. Upon nucleation, rapid dendritic solidification occurs. These conditions are of scientific interest; to understand the fundamental behaviour of solidification in both pure materials and alloys. A common addition is to apply a high DC magnetic field to damp macroscopic fluid flow and create a purely diffusion driven situation. However under certain conditions this magnetic field will interact with microscopic thermoelectric currents that are a natural and inherent part of solidification; generating a Lorentz force and driving microscopic fluid flow. This fluid flow can be sufficient to disturb the heat and solute boundary layers significantly altering the solidification process. In the absence of gravity a weak AC field can be used purely for positioning, while the DC field can be chosen to be significantly large to interact with the thermoelectric currents. The focus of this work is to explore what effect this may have and to provide the first study of how this phenomenon will affect droplet solidification. To do this a dimensionless 3D enthalpy based model is used and scaled to represent an AlSi hypo-eutectic alloy.

Theory

The Seebeck effect [1] describes how an e.m.f ($\Delta\Psi$) forms when two materials with varying Seebeck coefficients (S) are placed in thermal contact and that at the boundary this e.m.f varies with the surface temperature. The generalised form of Ohm's law includes a contribution from the Seebeck effect.

$$\mathbf{J} = \sigma (\mathbf{E} + \mathbf{u} \times \mathbf{B} - S\nabla T) \quad (1)$$

At the interface the potential difference can be written as

$$\Delta\Psi = \Delta ST \quad (2)$$

The evolution of the dendrite morphology is calculated by an enthalpy-based method [2]. The interfacial temperature (T^i) is defined by the Gibbs-Thompson condition

$$T^i = T_m - \frac{\gamma(\theta, \phi) T_m}{L} \kappa - m (C_0 - C_l^i) \quad (3)$$

where the second term accounts for local free energy through surface energy anisotropy and curvature and the final term accounts for solute partitioning in binary alloys. This equation leads to a variation in surface temperature and the formation of thermoelectric currents irrespective of an external magnetic field.

Results

Free Growth of a Single Crystal

To understand the mechanism that will lead to morphological changes a simplified situation of a single crystal freely growing in the bulk is considered. Previous work [3–7] has shown that the thermoelectric currents circulate between the cold tips and the hot roots of the crystal. In figure 1 a similar situation can be observed for a developing dendrite. In this example an additional positive curvature exists at the base of each arm near to the root. This is analogous to the formation of a secondary branch and the resulting undercooling gives rise to a relatively higher surface potential and the formation of another current circulation. As a dendrite continues to develop and many secondary branches form, this can have a significant impact on magnitude and direction of the thermoelectric currents. A more in depth description of this effect is presented in [6]; in summary a larger variation in surface temperature (i.e. an increase in hot and cold regions along the interface due to secondary arms) gives a higher average magnitude of \mathbf{J} . In the presence of a low magnetic field aligned along the tip in the $+z$ -direction, such that $Re \rightarrow 0$ and $Pe \rightarrow 0$ the growth can be considered to be diffusion driven; giving an idea of the direction and relative magnitude of the fluid flow. The flow is given in figure 2, where circulations form around each of the tips and circulations around the entire dendrite. For the tips tangential to the field a pair of vortices form, passing from the tip, under and over the arm. For the tips parallel to the field the circulation forms around the arm. The highest velocities can be seen in the root of the dendrite, passing over the tangential arms and at the z tips.

As the magnetic field is increased to 10T convective transport becomes important. The incident flow onto the tangential arm perturbs the interface causing secondary growth and a deflection of the tip. This is highlighted in figure 3, showing the transient growth from both an isometric perspective and also the perspective along the magnetic field. The secondary branches have a direct impact on the formation of thermoelectric currents; as the tips evolve from the surface of the arm the local curvature increases resulting in a decrease in the surface temperature and consequently a change of the potential boundary condition. The net effect

is the formation of a potential sources (tips) and sinks (local roots) where thermoelectric currents will begin to circulate around the secondary tips. This is highlighted in figure 4, which shows the surface potential. The currents formed from this potential will also interact with the magnetic field producing Lorentz forces and the situation becomes increasingly complex.

Thermoelectric currents also exist in the inter-dendritic region and the 3-dimensional simulation shows that a high velocity can also exist in this region. To highlight this, a cross-section in the x, z plane through the centre of the dendrite is given in figure 5, showing the y component of velocity. The flow between the first secondary branch and the tangential primary arms persists all the way into the root. A second cross section, in the x, y plane and in between these two branches shows the velocity and how it is not simply confined between the two branches, but forms a global circulation. However this is expected due to the rotational symmetry of the problem.

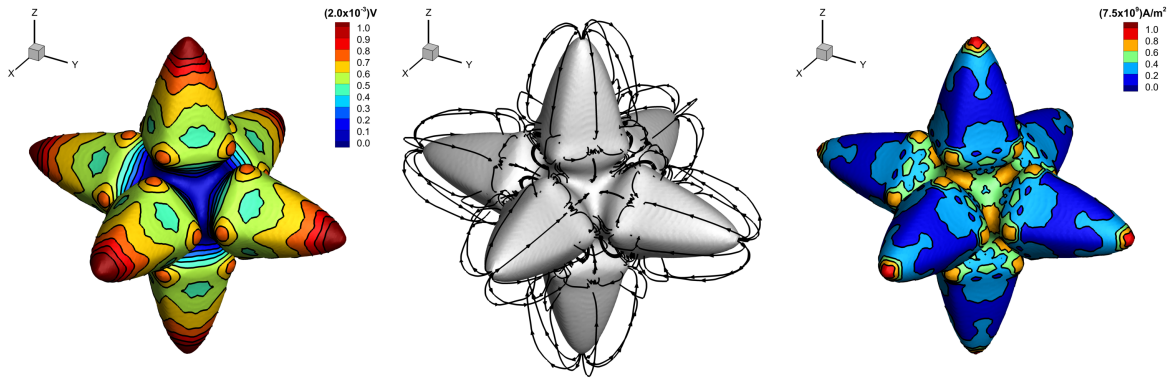


Figure 1: Stagnant growth. Left: Electric potential. Centre: Direction of \mathbf{J} . Right: $|\mathbf{J}|$.

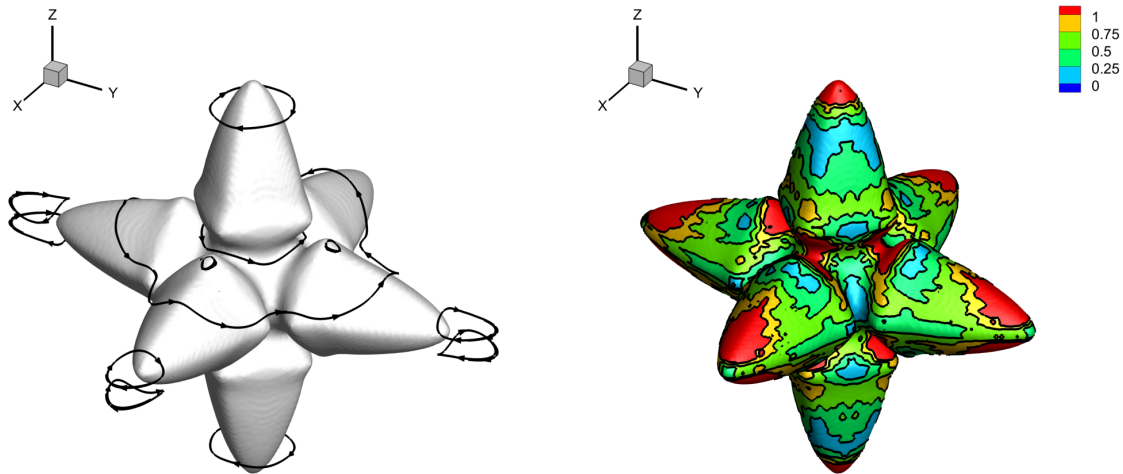


Figure 2: Stagnant growth velocity. Left: Direction of \mathbf{u} . Right: Normalised $|\mathbf{u}|$.

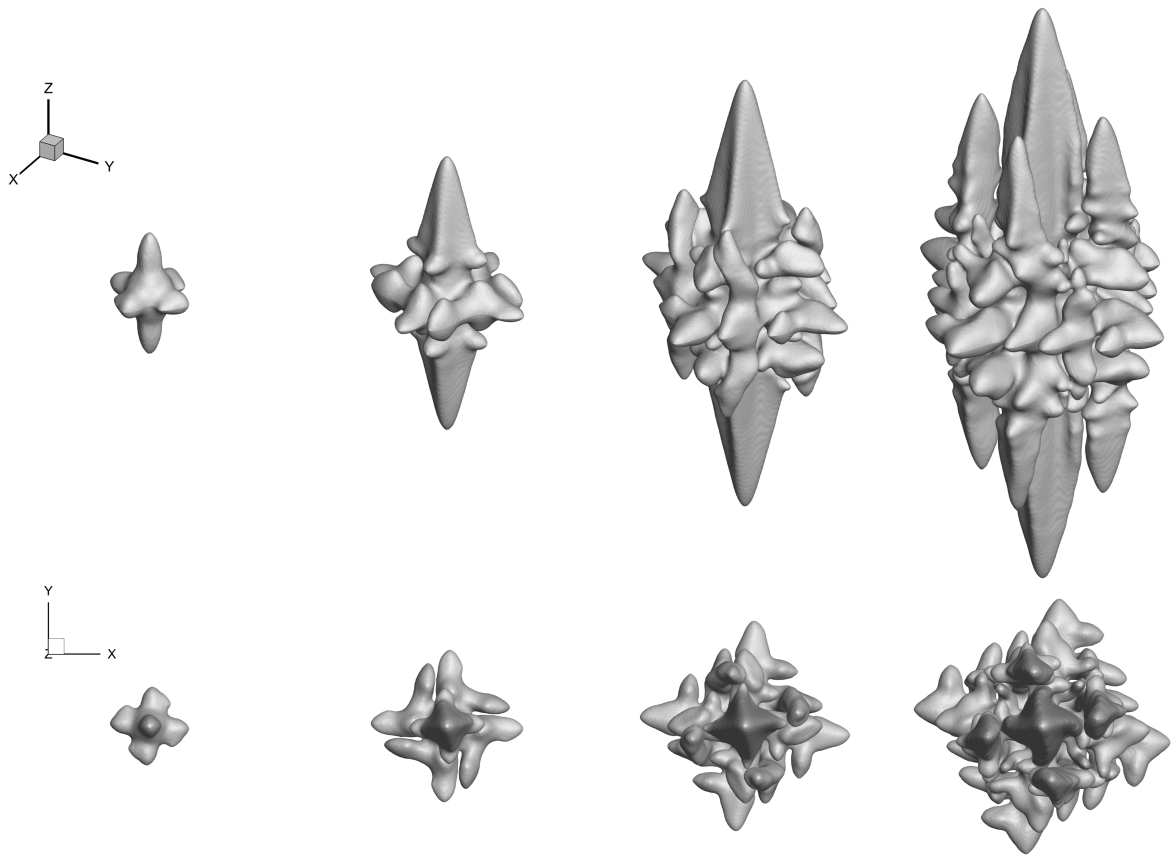


Figure 3: 10T Transient Growth. Top: Isometric perspective. Bottom: Along magnetic field direction.

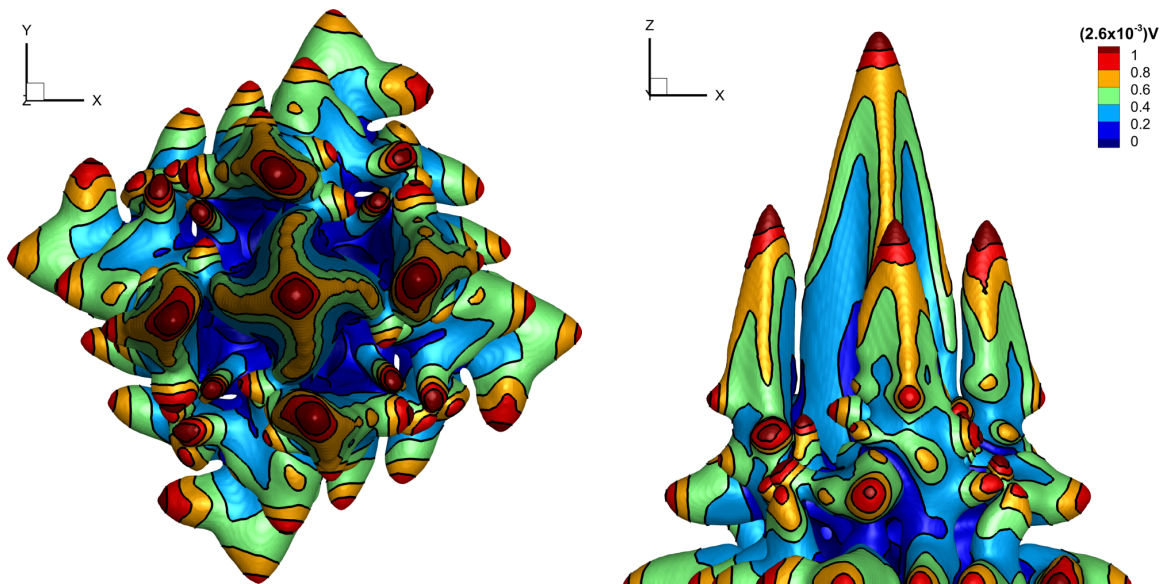


Figure 4: Electric potential of growth in the presence of a 10T magnetic field. Left: x, y plane. Right: x, z plane.

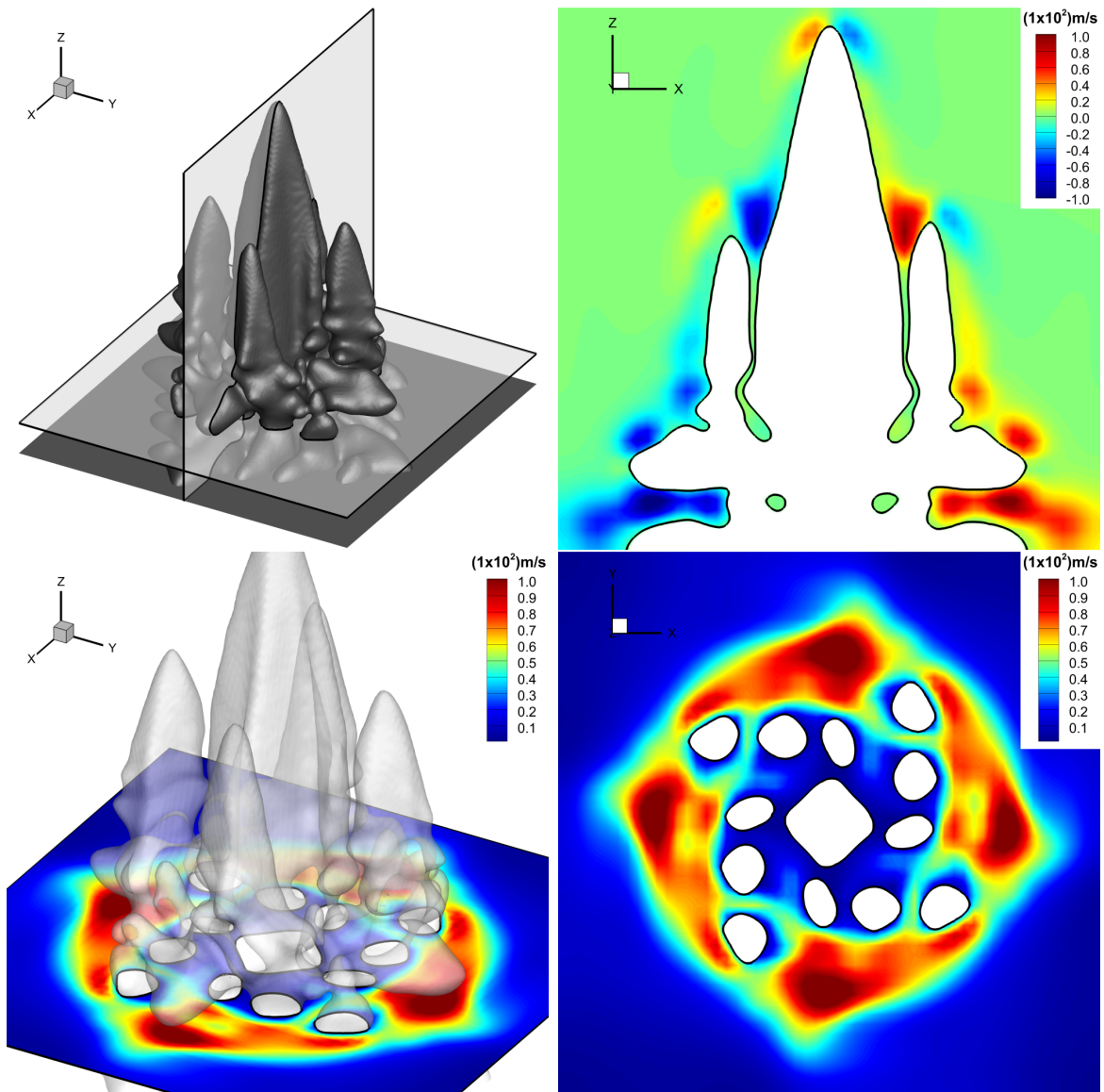


Figure 5: Velocity of growth in a 10T field. Top left: Location of planes. Top right: u_y in the x, z plane. Bottom: $|\mathbf{u}|$ in the x, y plane.

Droplet Solidification

Under microgravity conditions, with no external body forces a droplet of liquid metal will form a spherical equilibrium shape. Consider a droplet with a diameter of 0.4mm. The surface of the droplet is assumed to be adiabatic as the droplet is placed in a vacuum and due to the short duration of solidification heat loss through radiation may be neglected. The droplet begins in a supercooled state and nucleation is triggered on the surface at the positive x pole. Figures 6 and 7 show the evolution of the solidification within the droplet for cases without a magnetic field and with a 10T transverse magnetic field (perpendicular to the plane of growth). In the absence of a magnetic field the dendrite grows statistically symmetric exhibiting 4-fold symmetry. In the case where a magnetic field is present the solidification path takes a preferential route around the surface of the droplet. The change to the morphology is a consequence of the fluid dynamics generated through the interaction of thermoelectric currents and the magnetic field. At the tips of the dendrite the direction of the Lorentz force has the same sense, where each tip forms a clockwise micro circulation of flow. As multiple tips grow these circulations will interact forming a single circulation. The net effect is a larger mesoscopic circulation traversing multiple tips and transporting solute rich fluid downstream of the nucleation site; resulting in a plume of solute ejected from the bulk. The velocity is given in figure 8, where flow that appears to exist within the solid regions has entered a quasi 3-dimensional plane above and below the structure. This is analogous to the inter-dendritic flow of the 3D single crystal shown in figure 5. Figure 9 shows the magnitude of the thermoelectric currents; it is important to note that the normalised scale is logarithmic, highlighting the short range in which these currents act under these conditions. The highest \mathbf{J} is located at the tips growing into the bulk (along the top of the droplet), where micro circulations are perturbing the interface encouraging secondary growth and increasing \mathbf{J} . This give a large Lorentz force, but acting over a short distance.

This model suggests two plausible mechanisms. The first is a consideration to the extent of the plume of solute. Through continuity the localised high velocity forces solute into the bulk, however in this region electromagnetic damping becomes dominant and the velocity decreases sharply away from the microstructure. For low magnetic fields, where bulk flow can be significant the extent of this plume is governed by the inertia generated by the Lorentz force and the time for the flow to accelerate under a lower driving force. Ultimately this could lead to macro segregation, while for high magnetic fields the effect is limited to micro segregation. The second mechanism is a change to the inter-dendritic structure. Consider an inter-dendritic region with many secondary arms. Surface energy shows that thermoelectric currents and fluid flow will persist. The flow will act to homogenise the liquid destabilising the equilibrium of the secondary arms, causing some regions to re-melt and others to solidify. This will continue until the velocity becomes zero, which if it is assumed occurs when the region becomes devoid of thermoelectric currents then the surface temperature must become constant. For a homogeneous solute concentration and neglecting surface energy anisotropy, this occurs when the local curvature becomes constant. Thus over an extended period of time, it is anticipated that this region will slowly minimise its surface area; this is highlighted in figure 7, where the absence of secondary branches within the microstructure is evident. Therefore, initially secondary branching may be encouraged and later suppressed.

Conclusion

The focus of this paper is to look at the complex nature of the interaction of thermoelectric currents and a magnetic field in undercooled liquid metal droplets in the absence of gravity.

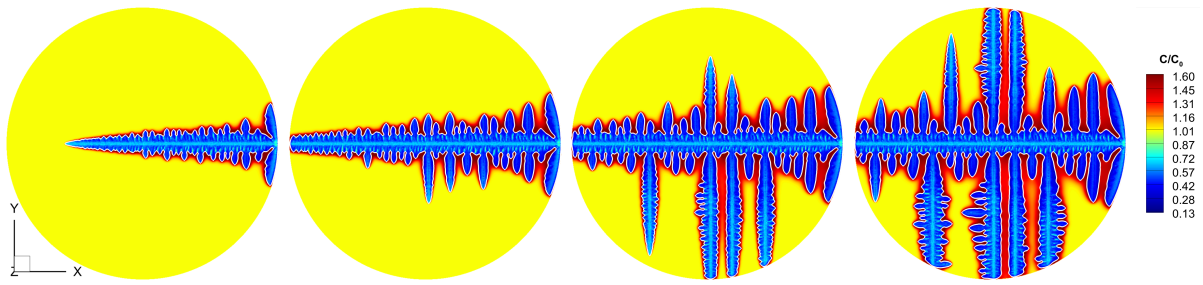


Figure 6: Solute field of droplet solidification with no external magnetic field.

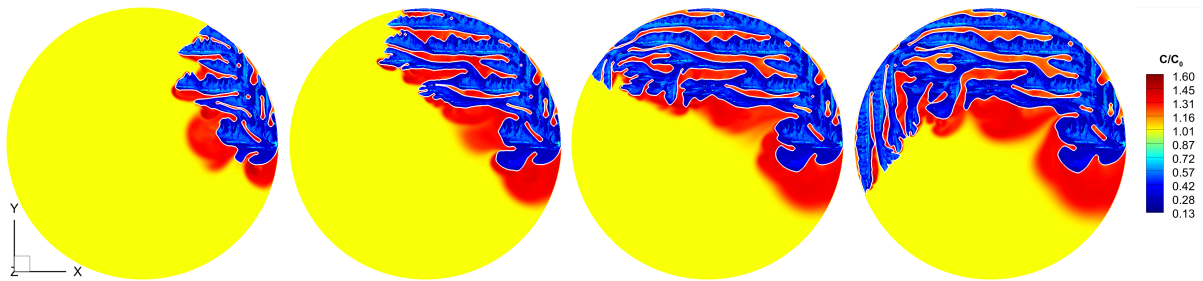


Figure 7: Solute field of droplet solidification with a 10T external transverse magnetic field.

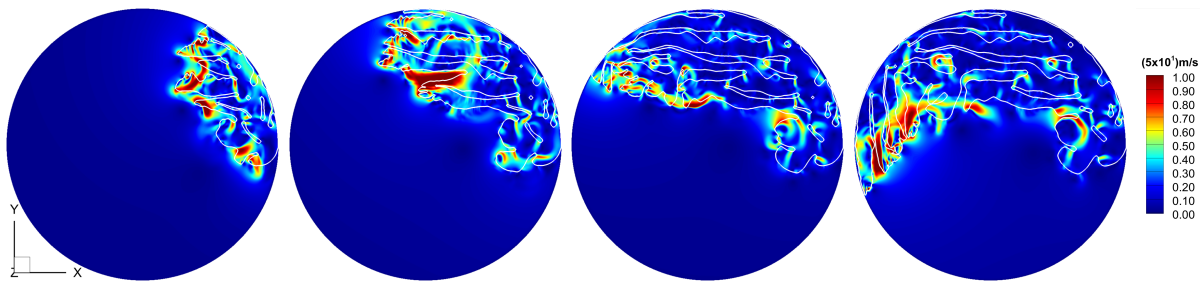


Figure 8: Relative $|\mathbf{u}|$ in an external magnetic field.

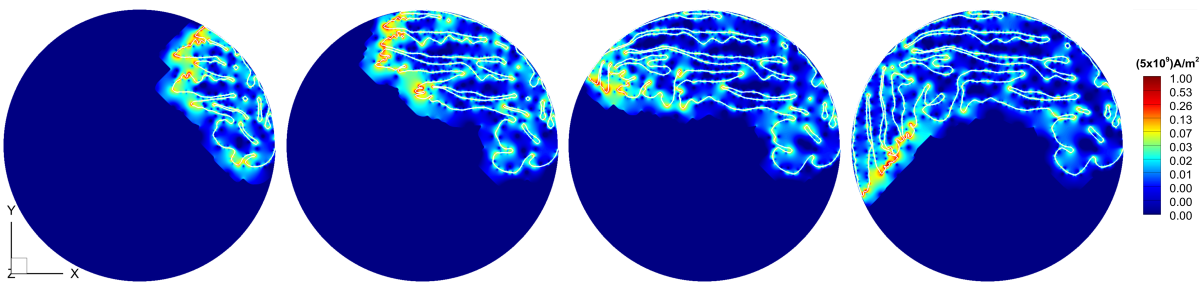


Figure 9: Relative $|\mathbf{J}|$ in an external magnetic field.

The 3-dimensional model highlights a variety of fluid microcirculations that all contribute to altering the convective transport and the evolution of dendritic growth. Perturbations from the flow of the thermal and mass boundary layer at the interface initiate secondary growth, altering the formation of thermoelectric currents, the Lorentz force and the velocity. Under a high magnetic field this intimate coupling results in a significant change to the dendritic structure and the numerical results indicate that an unexpectedly strong convection can develop within the inter-dendritic region. Using a quasi 3-dimensional approximation solidification of a droplet under a high magnetic field is also considered. The additional geometric constraints of the droplet surface give rise to a mesoscopic rotational flow, causing the dendrite to preferentially grow around the surface of the droplet. Downstream of this flow the thermal and mass boundary layers are extended as hot solute is ejected, stunting growth. As the solidification front propagates the microstructure continues to evolve through inter-dendritic flow and a hypothetical mechanism of the effect of this flow has been proposed.

References

- [1] J. A. Shercliff, "Thermoelectric magnetohydrodynamics", *Journal of Fluid Mechanics*, 1978, 91 part 2, 231-251.
- [2] V. R. Voller, "An enthalpy method for modelling dendritic growth in a binary alloy", *International Journal of Heat and Mass Transfer*, 2008, 51, 823-834.
- [3] A. Kao, G. Djambazov, K. A. Pericleous and V. Voller, "Thermoelectric MHD in Dendritic Solidification", *Magnetohydrodynamics*, 45 No.3, 305-315, 2009.
- [4] A. Kao, K. A. Pericleous, M. K. Patel and V. Voller, "Effects of magnetic fields on crystal growth", *International Journal of Cast Metal Research*, 22 No 1-4, 147-150, 2009.
- [5] A. Kao "Thermoelectric magnetohydrodynamics in dendritic solidification", (Ph.D. thesis, University of Greenwich, 2010)
- [6] A.Kao and K. Pericleous "The Effect of Secondary Arm Growth on Thermoelectric Magnetohydrodynamics", (Paper presented at the 8th International PAMIR Conference on Fundamental and Applied MHD, Borgo, Corsica, France, 5-9 September, 2011)
- [7] A.Kao and K. Pericleous, "A numerical model coupling thermoelectricity, magnetohydrodynamics and dendritic growth", *Journal of Algorithms and Computational Technology*, 2012, Vol 6 (1), 50-77
- [8] T.Tsukada, H.Fukuyama and H.Kobatake, "Determination of Thermal Conductivity and Emissivity of Electromagnetically Levitated High-Temperature Droplet based on the Periodic Laser-Heating Method: Theory.", *International Journal of Heat and Mass Transfer*, 2007, 50, 3054-3061

MULTI-SCALE MODELING OF LIQUID PHASE SINTERING AFFECTED BY GRAVITY: PRELIMINARY ANALYSIS

Eugene Olevsky and Randall M. German

San Diego State University
Mechanical Engineering Department
5500 Campanile Dr., San Diego, CA 92182-1323, USA

Keywords: Sintering, Microgravity, Finite-Element Method, Multi-Scale

Abstract

A multi-scale simulation concept taking into account impact of gravity on liquid phase sintering is described. The gravity influence can be included at both the micro- and macro-scales. At the micro-scale, the diffusion mass-transport is directionally modified in the framework of kinetic Monte-Carlo simulations to include the impact of gravity. The micro-scale simulations can provide the values of the constitutive parameters for macroscopic sintering simulations. At the macro-scale, we are attempting to embed a continuum model of sintering into a finite-element framework that includes the gravity forces and substrate friction. If successful, the finite elements analysis will enable predictions relevant to space-based processing, including size and shape and property predictions. Model experiments are underway to support the models via extraction of viscosity moduli versus composition, particle size, heating rate, temperature and time.

Introduction

One of the most important findings from the earlier conducted combined ground-based and microgravity studies [1,2] is that the rules isolated by mankind over many years of Earth-based processing do not carry over into the microgravity environment. New pathways are needed to obtain densification and satisfactory mechanical properties while minimizing distortion and attaining the desired dimensional precision for operating components. In this connection, the understanding of the link between the events occurring at the level of microstructure and the macroscopic behavior of powder specimens during liquid phase sintering (shape distortion, porosity spatial distribution) is of vital importance. This understanding can be gained through the development of a multi-scale model framework taking into account microscopic phenomena and macroscopic shape evolution.

Modeling of micro-scale evolution

At the microscale, simulations should be constructed to show how individual grains bond during sintering by the combined motion of thousands of atoms. Three types of simulations can be applied to this problem in liquid phase sintering:

- *atomistic level* (molecular dynamics) - applied to the study of sintering based on a large ensemble of individual vibrating atoms, providing a means to study time dependent particle coalescence, neck growth and bonding between grains, dihedral angle stabilization, and the roles of factors such as dopants or temperature on sintering [3];
- *viscous models* (surface energy minimization) - wherein an initial configuration is input with prescribed volume fractions, surface energy, and other boundary conditions and allowed to

morph as a viscous solid through a sequence of small steps to a lowest energy configuration, providing a means to identify terminal configurations in multiple grain and multiple phase systems [4];

- *hybrid model* (fine grained Monte Carlo) - relies on computational cells larger than atoms but still involves discrete jumps based on energy minimization rules and appropriate boundary conditions; provides time dependence to the microstructure transformation, enables extraction of important constitutive parameters relating to grain size, grain growth, grain agglomeration, neck growth, and liquid or pore distribution and sizes [5].

The atomistic level simulations provide a means to study the particle coalescence and redistribution of phases, including how additives change particle-particle sintering [3]. Unfortunately, to be relevant these simulations require accurate atomic interaction potentials to compute the total energy of the system. First-principles calculations can provide the most reliable interatomic potentials. An alternative is to use empirical interaction potentials such as the embedded atom method. However, a simulation of sintering requires a very large number of atoms and considerable computational time, making these methods rather slow.

To address these challenges, a hybrid solution to the micro-scale aspects can be employed. The discrete atom level calculation can be replaced by a coarser grid to expedite the simulation, but the time based discrete simulations should enable identification of morphology versus time needed for the mesoscale and component scale models.

Modeling of meso-scale evolution

Kinetic Monte-Carlo (KMC) models have been used extensively to simulate problems of microstructure evolution in multiple grain and multiple phase materials. The first KMC models were used to simulate normal grain growth in single-phase materials [6,7]. It has been shown [8] that very good representation of grain structure, topology and kinetic data could be obtained from KMC simulations. Since then, KMC models have been used to study many other types of microstructure evolution including abnormal grain growth, recrystallization [9], phase transformations, Ostwald ripening [10], pore migration [11] and final-stage sintering [12]. The earliest attempt to simulate sintering using KMC models was limited to final stage sintering and implemented densification by expanding the area of the simulation as densification proceeded. The criterion for densification was to reduce porosity in proportion to the mean distance between pores in the simulation.

While KMC models are fundamentally stochastic, the results of the studies cited above are very stable and have been found to always converge to the same topological and kinetic solutions [13].

Starting from the late 1940's, many researchers, including Kuczynski [14], Kingery [15], Exner [16] Johnson [17], Coble [18], Ashby [19] and others [20,21,22], have studied microstructure evolution during sintering. These studies initially considered sintering of idealized powder compacts consisting of 2 or 3 spherical particles of equal size, subjected to sintering by various diffusion mechanisms. The main accomplishment of these early models was an understanding of the driving forces, transport mechanisms and densification processes for sintering of crystalline materials. Next, sintering models consisting of repeating unit cells of the same geometry were proposed by DeHoff [23], Bouvard and McMeeking [24], Riedel and co-workers [25,26,27], Slaughter and Nettleship [28], and others [29,30,31]. In these models, researchers extended the two and three particle systems to idealized repeating unit cell models where each cell consists of a grain and the porosity around it. Molecular dynamics simulations used to study the sintering of nano-particles [32,33] showed that additional mechanisms such as particle rotation is active, as previously observed in tungsten heavy alloy LPS.

Continuum mechanics modeling of sintering of two [34], three [35] and a row [36] of particles have given very accurate particle shapes evolution. The application of continuum thermodynamic principles by the finite difference method to simulate the sintering of two particles [37], a row and close-packed particle [24], and unit cells of different packing [29] have given accurate data on the shrinkage kinetics during sintering. A cellular model [38] was used to study sintering by surface diffusion in a multiple particle system and an MC model [12] was used to simulate final-stage sintering of multiple grains. Some of these idealized geometric simulations [24] have been used to obtain the sintering stress, or capillary stress, necessary for modeling sintering at the continuum level.

When including a link to the deterministic micro-scale stress analysis, Monte Carlo model can be used to obtain more general and accurate thermodynamic (sintering stress, bulk and shear moduli) and kinetic data (densification rate, *etc.*) for liquid-phase sintering taking into consideration the gravity influence.

Modeling of macro-scale shape distortion during sintering

Sintering kinetics of real porous bodies is determined by temperature, the properties of the powder particles, and the nature of property interactions during microstructure evolution. Among some of the important aspects are kinematic constraints (*e.g.*, adhesion of porous component's end face and its support surface, which depends on gravity and the component mass), externally applied forces and, also, inhomogeneity of properties in the volume under investigation (for example, inhomogeneity of the initial density distribution in the green body).

The complex problems can be solved in terms of a macro-scale description if the local events at the micro-scale are known from a parallel set of local simulations. An approach capable of solving these problems is the continuum theory of sintering [39].

The main constitutive relationship of the continuum theory of sintering is represented below:

$$\sigma_{ij} = \frac{\sigma(W)}{W} \left[\varphi \dot{\epsilon}_{ij} + \left(\psi - \frac{1}{3} \varphi \right) \dot{\delta}_{ij} \right] + P_L \delta_{ij} \quad (1)$$

where φ and ψ are the normalized shear and bulk viscosity moduli, which depend on porosity θ and other structure parameters such as grain size, relative interparticle neck radius, *etc.*; δ_{ij} is a Kronecker symbol; $\dot{\epsilon}$ is the first invariant of the strain rate tensor. The effective equivalent strain rate W is connected with temperature, the current porosity, and with the invariants of the strain rate tensor. The effective equivalent stress $\sigma(W)$ determines the constitutive behavior of a porous material. P_L is an effective Laplace stress (sintering stress), which depends on the local sintering stress P_{Lo} , porosity and various pore structure parameters such as relative interparticle neck radius. The porosity θ is the ratio of the pore volume to the volume of a porous body.

The formulation (1) is used for the description of a wide range of powder processing techniques. Parameter σ_{ij} corresponds to the macroscopic stress applied to a representative volume element. The first term of the right-hand part characterizes the porous material's flow resistance, and the second term corresponds to the influence of capillary (sintering) stresses. In the case where the macroscopic stress σ_{ij} is equal to zero, Eq. (1) describes free sintering. In the case when the effective sintering stress P_L is equal to zero, Eq. (1) describes treatment by pressure without sintering. In general, Eq. (1) describes sintering under pressure.

It should be noted that existing model concepts and numerical codes, in particular those based upon the continuum theory of sintering, depend on the accurate determination of the constitutive parameters such as the bulk and shear moduli (ψ and φ) and the sintering stress P_L . This determination, relying on realistic pore-grain structures, can be provided by the microscale simulations (see above). A new synergistic combination of the macroscopic continuum model,

meso-scale Monte Carlo model, and microscale hybrid model simulations should enable a coupled description of liquid phase sintering at different scale levels with effective integration of gravity as an adjustable parameter.

The gravity influence

Studies on microstructural and configuration changes in liquid phase sintering have provided insight into the sintering and composition factors that influence distortion [40-48]. Most of the research in this area analyzed microstructure gradients as influenced by gravity. The influence of gravity-induced grain settling was examined by Kohara and Tatsuzawa [40], Niemi and Courtney [41], and German *et al.* [42-49]. The last group also studied gravity effects on the grain structure under liquid-phase sintering, with emphasis on grain packing [46] and grain coarsening [48]. Experimental evidence of gravity-induced shape distortions is given in several studies [43,47]. A geometry described as an “elephant foot” shape was frequently observed for distorted W-Ni-Fe powder compacts.

A publication by Raman and German [46] provided a first mathematical model for gravity-induced shape distortion during liquid-phase sintering. In this study, the evolution of the shape of a “top hat” (cylinder with flange) was modeled and experimentally observed. However, one of the model assumptions is constant density during the distortion process. This is based upon the hypothesis that bulk densification occurs during heating and is essentially complete prior to liquid formation [49]. In light of this idea, shape change is calculated for an incompressible viscous material in a gravity field [46]. Although qualitative successful for liquid phase sintered tungsten heavy alloys with excessive liquid quantities, such an assumption substantially restricts the model basis and excludes shrinkage and its interplay with gravity forces. The first study which included the analysis of a coupled impact of sintering stresses and gravity has been conducted by Olevsky and German [50,51]. This work, however, was a purely macro-scale analysis, focused on specimen shape distortions without taking into account the evolution of the micro- and meso-structure.

For a full-scale analysis, the gravity influence should be taken into account at both micro- and macro-scales. At the micro-scale, the respective bond energies are to be directionally modified to include the impact of gravity on the site exchanges. The buoyancy and grain settling has to be taken into account by introducing an additional Hamiltonian-based term in the bond energy expressions. In addition, the Potts model should be linked to the finite-element code calculating stresses and strains at the micro-scale in order to determine the gravity stress-effected state of the microstructure and to obtain the final form of the sintering body. The next step in the implementation of these ideas is the utilization of finite-element calculations allowing viscoplastic stress-strain analyses.

At the macro-scale, the continuum model of sintering can be embedded in the following finite-element framework:

$$\left[\int_{\mathcal{g}} [B]^T [D] [B] d\mathcal{g} \right] \{V_n\} = - \int_{\mathcal{g}} [B]^T P_L \{1\} d\mathcal{g} + \int_{\mathcal{g}} g \rho_T (1 - \theta) [N] \{n_g\} d\mathcal{g} \quad (2)$$

where [B] is the matrix correlating the strain rates with the nodal velocities V_n ; [D] is the matrix correlating the stresses with the strain rates (“matrix of viscosities”); \mathcal{g} is a macroscopic porous volume under investigation; g is the gravity acceleration; ρ_T is the theoretical density of a fully-dense material; N is the matrix of the finite element shape functions; {1} designates the unit column-vector; and $\{n_g\}$ is a unit vector oriented in the direction of the gravity forces’ action.

The development of the respective computer codes based on the described multi-scale modeling concepts is a part of the on-going research. Model experiments are underway to support the models via extraction of viscosity moduli versus composition, particle size, heating rate, temperature and time.

Conclusions

A multi-scale modeling framework for simulation of liquid phase sintering at micro-, meso-, and macro-scale structure levels is described. Both micro- and meso-scale modeling levels can rely on Monte-Carlo simulations, while macro-scale modeling is based on the finite-element approach. The development of the respective computer codes based on the described multi-scale modeling concepts is a part of the on-going research. Model experiments are underway to support the models via extraction of viscosity moduli versus composition, particle size, heating rate, temperature and time.

Acknowledgements

The support of the National Aeronautics and Space Administration, Grant G00008863, is gratefully acknowledged.

References

- [1]. R.M. German, Microstructure of the gravitationally settled region in a liquid-phase sintered dilute tungsten heavy alloy, *Met. Mat. Trans. A*, 26, 279-288 (1995).
- [2]. A. Tewari, A.M. Gokhale, R.M. German, Effect of gravity on three-dimensional coordination number distribution in liquid phase sintered microstructures, *Acta Mater.*, 47, 3721-3734 (1999).
- [3]. J. Houze, S. Kim, S. G. Kim, S. J. Park, R. M. German, The Effect of Fe Atoms on the Adsorption of a W Atom on W(100) Surface, *J. Appl. Phys.*, 103, 1061030 (2008).
- [4]. K. Lu and R.M. German, Microstructure analysis of samples sintered at different gravitational conditions, *J. Mater. Sci.*, 45, 4454 (2010)
- [5]. E.A. Olevsky, V. Tikare, and T. Garino, Multi-scale modeling of sintering – A Review, *J. Amer. Ceram. Soc.*, 89 (6), 1914-1922 (2006).
- [6]. M.P. Anderson, D.J. Srolovitz, G.S. Grest, and P.S. Sahni, Computer simulation of recrystallization. I. Homogeneous nucleation and growth, *Acta Metall.* 32, 783-791 (1984)
- [7]. J. Wejchert, D. Weaire, J.P. Kermode, Monte Carlo simulation of the evolution of a two-dimensional soap froth, *Phil. Mag. B53*, 15-24 (1986)
- [8]. E. A. Holm, J. A. Glazier, D. J. Srolovitz, and G. S. Grest, Effects of lattice anisotropy and temperature on domain growth in the 2-dimensional Potts model, *Phys. Rev. A*, 43, 2662-2668 (1991)
- [9]. D. J. Srolovitz, G. S. Grest, M. P. Anderson, and A.D. Rollett, Computer simulation of recrystallization. II. Heterogeneous nucleation and growth, *Acta Metall.*, 36, 2115-2128 (1988)
- [10]. V. Tikare and J.D. Cawley, Application of the Potts model to simulation of Ostwald ripening, *Acta Metall.*, 46, 1343-1356 (1998)
- [11] V. Tikare and E.A. Holm, Simulation of grain growth and pore migration in a thermal gradient, *J. Am. Ceram. Soc.*, 81, 480-484 (1998)

- [12]. G.N. Hassold, I-W, Chen. D.J. Srolovitz, Computer simulation of final-stage sintering. I. Model, kinetics, and microstructure, *J. Am. Ceram. Soc.*, 73, 2857-64 (1990)
- [13]. F. Y. Wu, The Potts model, *Rev. Modern Phys.*, 54, 235-268 (1982)
- [14]. G.C. Kuczynski, "Self-Diffusion in Sintering of Metal Particles", *Trans. Amer. Inst. Min.*, 185 169-178 (1949)
- [15]. W.D. Kingery and M. Berg, Study of the initial stages of sintering solids by viscous flow, evaporation-condensation, and self-diffusion, *J. Appl. Phys.* 26, 1205 (1955)
- [16]. H.E. Exner, "Principles of Single Phase Sintering," *Rev. Powder Metall. Phys. Ceram.*, 1 7 (1979)
- [17]. D.L. Johnson, New method of obtaining volume, grain-boundary, and surface diffusion coefficients from sintering data, *J. Appl. Phys.*, 40, 192 (1969)
- [18]. R.L. Coble, Sintering of crystalline solids, *J. Amer. Ceram. Soc.* 41, 55 (1958)
- [19]. F.B Swinkels and M.F. Ashby, A second report on sintering diagrams, *Acta Metall.*, 29, 259 (1983)
- [20]. F.A. Nichols and W.W. Mullins, Morphological changes of a surface of revolution due to capillarity-induced surface diffusion, *J. Applied Phys.* 36, 1826 (1965)
- [21]. N. Cabrera, Mechanisms of sintering, *Trans. AIME*, 188, 667 (1950)
- [22]. R.M. German and J.F. Lathrop, Simulation of spherical powder sintering by surface diffusion, *J. Mater. Sci.*, 13 921 (1978)
- [23]. R.T. DeHoff, in: *Science of Sintering: New directions for materials processing and microstructural control*, edited by D.P. Uskokovic *et al.* Plenum Press, New York (1989)
- [24]. D. Bouvard and R.M. McMeeking, Deformation of interparticle necks by diffusion-controlled creep, *J. Am. Ceram. Soc.*, 79, 666 (1996)
- [25]. J. Svoboda and H. Riedel, Pore-boundary interactions and evolution equations for the porosity and the grain size during sintering, *Acta Metall.*, 40(11), 2829 (1992)
- [26]. J. Svoboda, H. Riedel, and H. Zipse, Equilibrium pore surfaces, sintering stresses and constitutive equations for the intermediate and late stages of sintering - Part I : Computation of equilibrium surfaces, *Acta Met. Mater.*, 42, 435 (1994)
- [27]. H. Riedel, H. Zipse, and J. Svoboda, Equilibrium pore surfaces, sintering stresses and constitutive equations for the intermediate and late stages of sintering - Part II: Diffusional densification and creep, *Acta Met. Mater.*, 42, 445 (1994)
- [28]. W. S. Slaughter, I. Nettleship, M. D. Lehigh, and P. Po-On Tong, A quantitative analysis of the effect of geometric assumptions in sintering models, *Acta Materialia*, 45, 12, 5077-5086 (1997)
- [29]. M.A. Occhionero, J.W. Halloran in *Sintering and Heterogeneous Catalysis* edited by G.C. Kuczynski, Albert E. Miller, Gordon A. Sargent, Plenum Press, New York (1984)
- [30]. J. Zhao, M.P. Harmer, Effect of pore distribution on microstructure development. II First and second generation pores, *J. Am. Ceram. Soc.*, 71, 530 (1988)
- [31]. T. Ikegami, Microstructural development during intermediate- and final-stage sintering, *Acta Metall.*, 35, 667 (1987)
- [32]. P.Zeng, S. Zajac, P.C. Clapp, and J.A. Rifkin, Nanoparticle sintering simulations, *Mat. Sci. & Eng.*, A252, 301 (1998)
- [33]. K. Tsuruta, A Omeltchenko, R. K. Kalia, and P. Vashishta, Early stages of sintering of silicon nitride nanoclusters - a molecular-dynamics study on parallel machines, *Mater. Res. Soc. Symp. Proc.* vol. 408 (1996)
- [34]. W. Zhang and J. H. Schneibel, The sintering of two particles by surface and grain-boundary diffusion – A two-dimensional numerical study, *Acta Metall.*, 43, 4377 (1995)

- [35]. H. Zhou and J.J. Derby, Three-dimensional finite-element analysis of viscous sintering, *J. Am. Ceram. Soc.*, 81, 478 (1998)
- [36]. A. Jagota and P. R. Dawson, Micromechanical modeling of powder compacts - I. Unit problems for sintering and traction induced deformation, *Acta Metall.*, 36, 2551 (1988)
- [37]. J. Pan , H. Le, S. Kucherenko, and J. E. Yeomans, A model for the sintering of spherical particles of different sizes by solid state diffusion, *Acta Metall.*, 13, 4671 (1998)
- [38]. J.W. Bullard, Digital-image-based models of two-dimensional microstructural evolution by surface diffusion and vapor transport, *J. Appl. Phys.* 81 [1] 159-168 (1997)
- [39]. E.A. Olevsky, Theory of sintering: from discrete to continuum, *Mater. Sci. & Eng. R.*, 23, 41-100 (1998).
- [40]. S. Kohara and K. Tatsuzawa, Effect of Gravity on Liquid Phase Sintering, *Bull. Inst. Space Aer. Sci. Uni. Tokio B*, 17, 493-504 (1981)
- [41]. A. N. Niemi and T. H. Courtney, Settling in Solid-Liquid Systems with Specific Application to Liquid Phase Sintering, *Acta Metall.*, 31, 1393-1401 (1983)
- [42]. C. M. Kipphut, A. Bose, S. Farooq, and R. M. German, Gravity and Configurational Energy Induced Microstructural Changes in Liquid Phase Sintering, *Metall. Trans. A*, 19, 1905-1913 (1988)
- [43]. S.-C. Yang and R. M. German, Gravitational Limit of Particle Volume Fraction in Liquid-Phase Sintering, *Metall. Trans. A*, 22, 786-791 (1990)
- [44]. D. F. Heaney, R. M. German, and I. S. Ahn, The Gravitational Effects on Low Solid-Volume Fraction Liquid-Phase Sintering, *J. Mater. Sci.*, 30, 5808-5812 (1995)
- [45]. Y. Liu, D. F. Heaney, and R. M. German, Gravity Induced Solid Grain Packing During Liquid Phase Sintering, *Acta Metall. Mater.*, 43, 1587-1592 (1995)
- [46]. R. Raman and R. M. German, A Mathematical Model for Gravity-Induced Distortion During Liquid-Phase Sintering, *Metall. Mater. Trans. A*, 26, 653-659 (1995)
- [47]. R. M. German, Y. Liu, and A. Griffio, Gravitational Effects on Grain Coarsening during Liquid-Phase Sintering, *Metall. Mater. Trans. A*, 28, 215-221 (1997)
- [48]. R. M. German, *Sintering Theory and Practice*, Wiley-Interscience, New York (1996)
- [49]. R. M. German, S. Farooq, and C. M. Kipphut, "Kinetics of Liquid Phase Sintering," *Mater. Sci. Eng. A*, 105-106, 215-224 (1988)
- [50]. E.A. Olevsky and R.M. German, Effect of gravity on dimensional change during sintering, I. Shrinkage anisotropy, *Acta Mater.*, 48, 1153-1166 (2000).
- [51]. E.A. Olevsky and R.M. German, Effect of gravity on dimensional change during sintering, II. Shape distortion, *Acta Mater.*, 48, 1167-1180 (2000).

SELF-ASSEMBLY OF Ni-NANOPARTICLES IN AEROSOLS PRODUCED THERMALLY ON-GROUND AND UNDER MICROGRAVITY CONDITIONS

Stefan Lösch¹, Daniela Nolle², Eberhard Goering², Bernd H Günther¹

¹ Fraunhofer Institute for Manufacturing and Advanced Materials (IFAM)
Wiener Straße 12, D-28359 Bremen, Germany

² Max-Planck-Institut for Intelligent Systems (former Metals Research),
Heisenbergstraße 3, D-70569 Stuttgart, Germany

E-mail: loesch@ifam.fhg.de

Keywords: magnetic nanoparticles, aerosol, microgravity, sounding rocket, parabolic flight, agglomeration

Abstract

The self-assembly behavior in Ni-aerosols was studied on-ground and under microgravity conditions by using the European sounding rocket MAXUS 8 and the parabolic flight aircraft A300 Zero-G. In microgravity, convection within the thermally produced aerosols could be effectively suppressed. It is shown that due to magnetic dipole interaction the Ni-particles agglomerate in a chain-like morphology both on-ground and in parabolic flights. It is shown that the chain length increases with increasing agglomeration time. This time scale could be extended in the range of minutes by using the sounding rocket microgravity platform. In general, under microgravity condition the intrachain size distribution of the Ni-particles is narrower then gets narrower. This is reduced to the ideal flow condition in microgravity. Surprisingly the sounding rocket platform did not result in chain-like Ni-agglomerates. Instead irregular morphology of fluffy agglomerates resulted similar to those observed for non-magnetic nanoparticles. These results are explained by considering the thermal history during particle synthesis in this process.

1. Introduction

The agglomeration of gas-borne particles usually occurs under the combined effect of magnetic, electrostatic and Van der Waals interactions [1-4]. In particular for Ni, Co, and Fe, this process is clearly dominated by magnetic dipole interparticle forces [5]. As a result, often a chain-like agglomeration of the magnetic particles is observed. For applications as sensors or in magnetic data storage, these “necklaces” should be as stretched as possible and contain particles with a narrow size distribution. The evaporation/condensation method is a well-understood physical method to produce nanosized particles from inorganic material. Unfortunately the flow conditions are difficult to control for such thermally produced aerosols due to convection and sedimentation effects.

In this work we investigate the relationship between carrier gas pressure, dwell time and size/shape of the resulting agglomerates of nickel particles produced either on-ground or under microgravity, where thermally induced convection effects can be suppressed effectively. In microgravity the dwell time for agglomeration in thermally produced aerosols can be extended to the minutes range (sounding rocket).

2. Experimental Procedure

The process of evaporation/condensation in inert gases is illustrated in Figure 2. The ingot material is melted in a suitable crucible by thermal heating. Nanosized particles are formed from the evaporated material by vapour cooling in the (cold) carrier gas, particle nucleation and coalescence growth. After solidification the resulting nanoparticles stop growing and instead undergo agglomeration due to Brownian motion in the carrier gas. A laminar flow carries the particles and agglomerates towards the sampling stage. The coated substrates are removed after each experiment for ex-situ inspection.

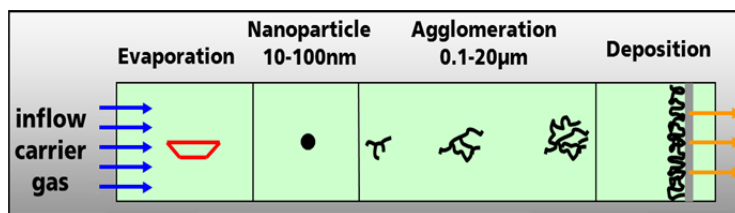


Figure 2: principle of evaporation/condensation in inert gas flow

μ -g condition) and the sounding rocket platform, respectively. Figure 1 shows a schematic of the modules used in both cases. The distance between the heating source and the sampling stage is 44 cm in both cases. However, due to technical constraints 2 different heater systems had to be used for the 2 μ -g platforms: (a) a 6 kW rf-induction heater for parabolic flight (PF) experiments, and (b) a Joule-heater for sounding rocket (SR) experiments. Using the

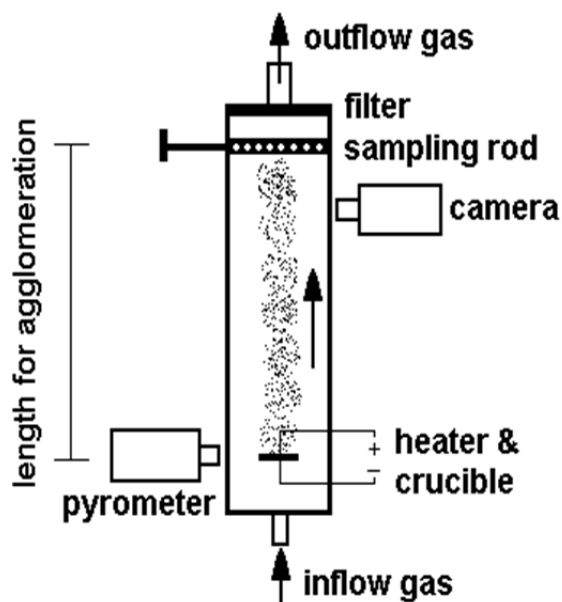


Figure 1: schematic of Ni evaporation/condensation device

laminar flow carries the particles and agglomerates towards the sampling stage. The coated substrates are removed after each experiment for ex-situ inspection. μ -g compatible experimental set-ups have been designed separately for parabolic flight (max. 22 s of

induction coil heater a Ni-ingot (5g, purity 3N5) in an alumina crucible is heated to the evaporation temperature of 1850°C within 1 minute. The inert gas (Argon) carries the developing Ni aerosol downstream. At the exit of the flow tube the solid fraction is deposited on electro-polished austenitic stainless steel substrates with a sampling time of 6s. Technical details on this set-up can be found in [7]. In the Joule-heater set-up 100mg Ni-wire (4N purity) is wound on a tungsten filament and evaporated at 1850°C. With this method a steady evaporation rate for max. 12 minutes could be achieved. The morphology of the deposited Ni-agglomerates was observed via electron microscopy (SEM/TEM). The magnetic analysis of the Ni-particles was done via superconducting quantum interference device (SQUID) measurements.

3. Results

3.1 Agglomeration Of Ni-Nanoparticles On-Ground (1-g)

Figure 3 shows typical deposits of Ni-agglomerates obtained on-ground (1-g). There is no obvious difference in morphology between agglomerates obtained with Joule-heating and those obtained with induction coil heating. TEM-inspection reveals the particles' crystallinity (Figure 4) and a ca. 2.5nm thick coating layer – probably Ni-oxide.

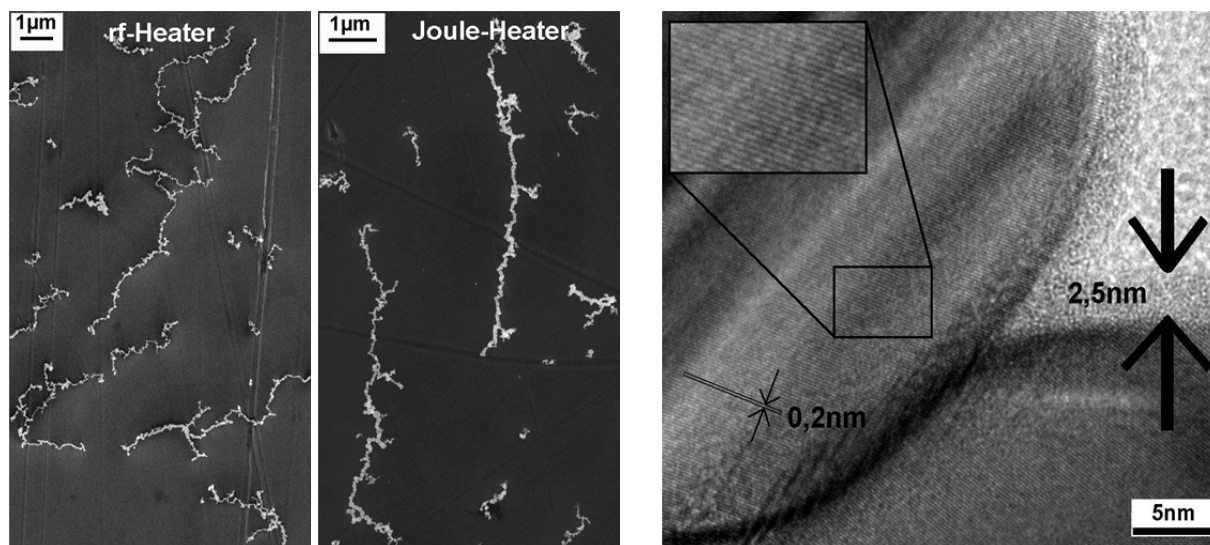


Figure 3: Ni-agglomerates obtained on ground (1-g) with induction coil heater (left) and Joule heater (right)

Figure 4: TEM image of 2 Ni-particles with single-crystalline structure; the oxide layer is 2,5nm thick

In general, the length of agglomerates increases with increasing residence times as shown in Figure 5.

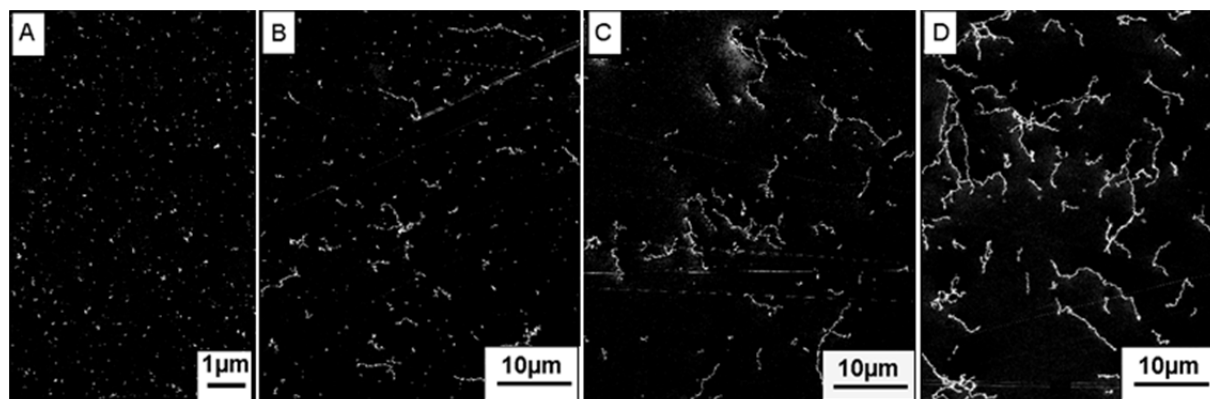


Figure 5: Ni-agglomerates obtained on-ground at different residence times A: 1s, B: 3.7s, C: 5s, D: 7.5s

The size distribution of Ni particles was determined as a function of gas pressure and velocity. The fairly broad intra-agglomerate size distribution of the Ni-particles made on-ground (Figure 6) is ascribed to convection effects in the vicinity of the evaporator, which promotes a mixing of particles having different growth histories.

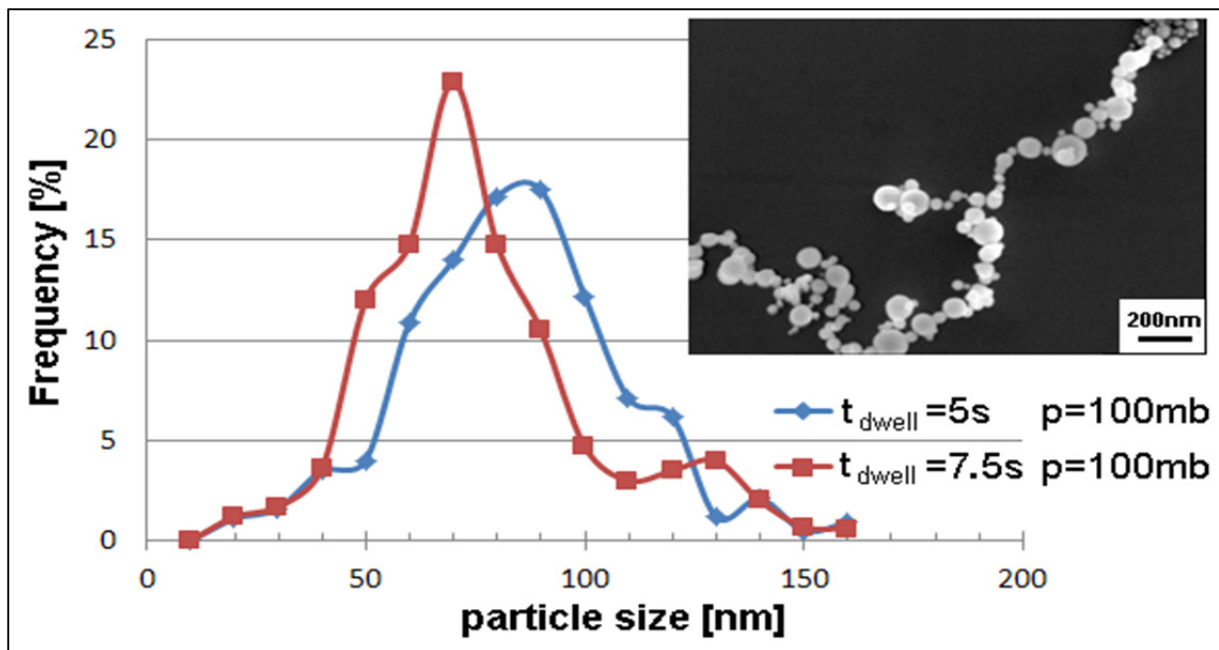


Figure 6: Intra-agglomerate size distribution of Ni-particles produced in on-ground for 2 different dwell times at a background pressure p of 100mb; insert: SEM image of a typical Ni-agglomerate

3.2 Agglomeration Of Ni-Nanoparticles In Microgravity ($\mu\text{-g}$)

3.2.1 Parabolic Flight Platform (PF)

Figure 7 illustrates the morphology of Ni-agglomerates obtained from PF-experiments. Obviously the particle chains are stretched much more perfectly compared to agglomerates produced on-ground (cf. Figure 3). With increasing “free-flow” residence time, (up to 16 sec), the agglomerates increased in length up to $30\mu\text{m}$ and contain several hundred particles. It is interesting to note that the intrachain particle size distribution obtained in $\mu\text{-g}$ (Figure 8) are much narrower compared to chains produced on-ground (Figure 6). We ascribe this to the absence of convection and sedimentation in the vicinity of the heating source in $\mu\text{-g}$, since mixing of different zones of the aerosol is absent [11].

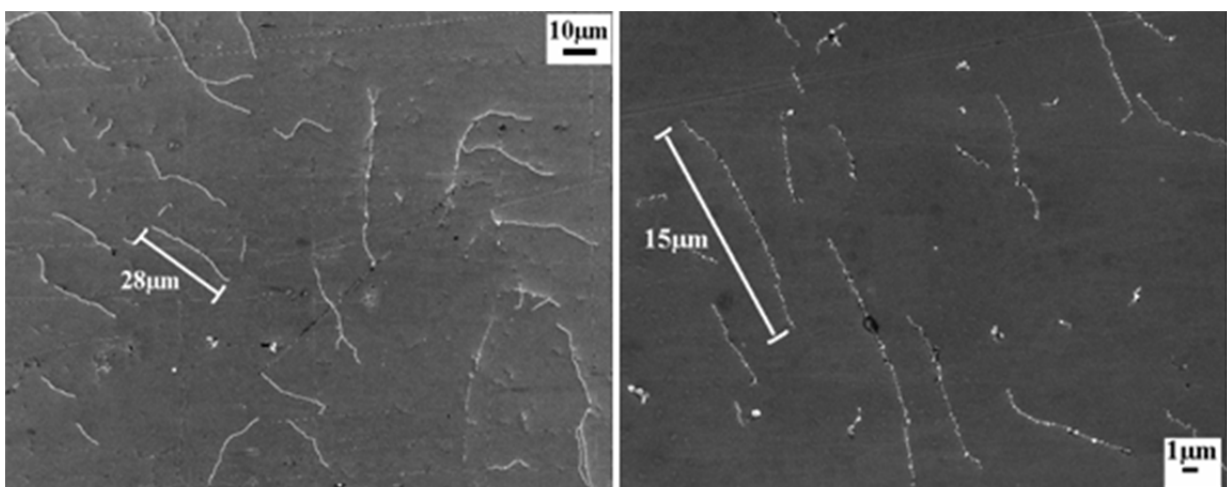


Figure 7: Ni-chains obtained in micro-gravity (PF); left: $p=100\text{mb}$, $t_{\text{res}}=16\text{sec}$; right: $p=100\text{mb}$, $t_{\text{res}}=8\text{sec}$

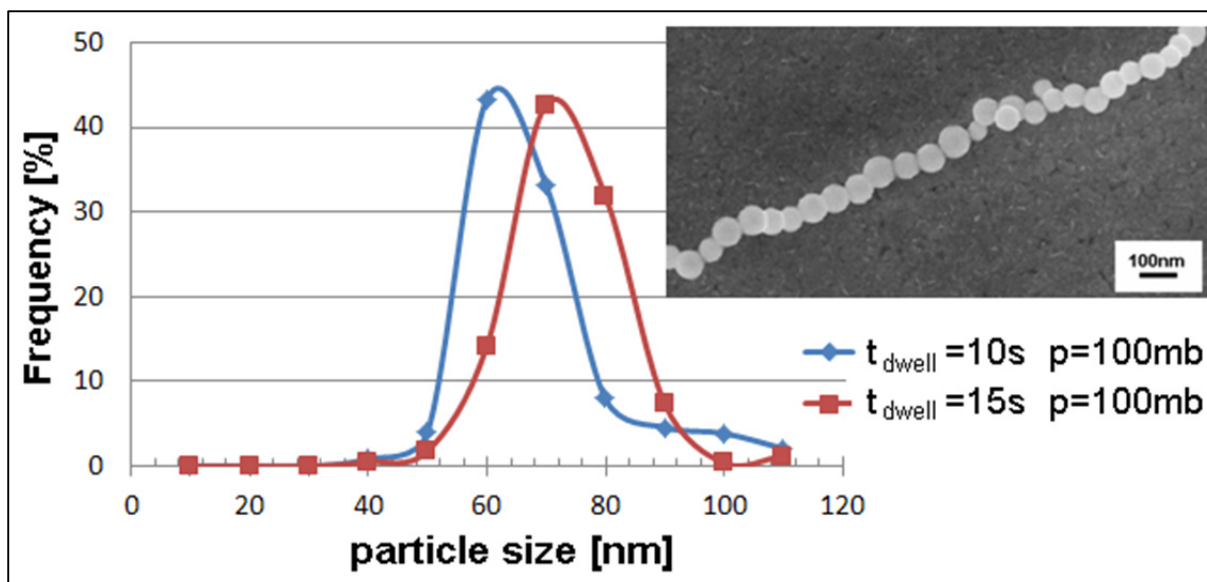


Figure 8: Intra-chain particle size distribution for 2 dwell times at a background pressure p of 100mb in μ -g (PF); insert: typical Ni-aggregate

3.2.2 Sounding Rocket Campaign MAXUS (SR)

With sounding rockets (e.g., MAXUS) the achievable residence time is extended to the minute range. We have used residence times of 7.5, 22.5, 37.5, and 55s, each at 2 pressure settings for the carrier gas, i.e. 100 and 300mbar. The μ -g quality was approximately $10^{-5}g$. The laminar flow behavior of the aerosol could be followed with a CCD-camera. Surprisingly, from the MAXUS-8 experiments in none of the sampled deposits chain-like agglomerates were found. Instead the particle aggregates' shape is similar to those usually observed in non-magnetic materials. Furthermore, no correlation was found between the 4 settings of residence time and the agglomerates' mean size (cf. Figure 9).

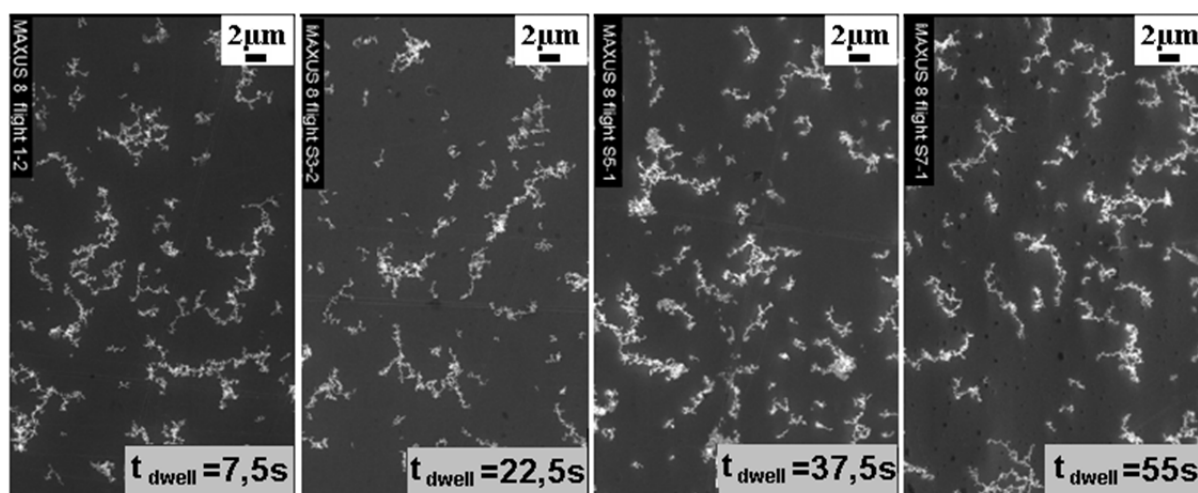


Figure 9: SEM-images of Ni-agglomerates produced on sounding rocket MAXUS 8 flight at 300mbar and residence times of 7.5s, 22.5s, 37.5s and 55s (set for samples #1,3,5,7)

Similar to the results from PF experiments the agglomerates' morphologies do not change as a function of pressure (100 vs. 300 mbar) (cf. Figure 10). Furthermore, the intra-agglomerate particle size distribution is shifted to smaller values by a factor 2 (cf. Figs.8,10).

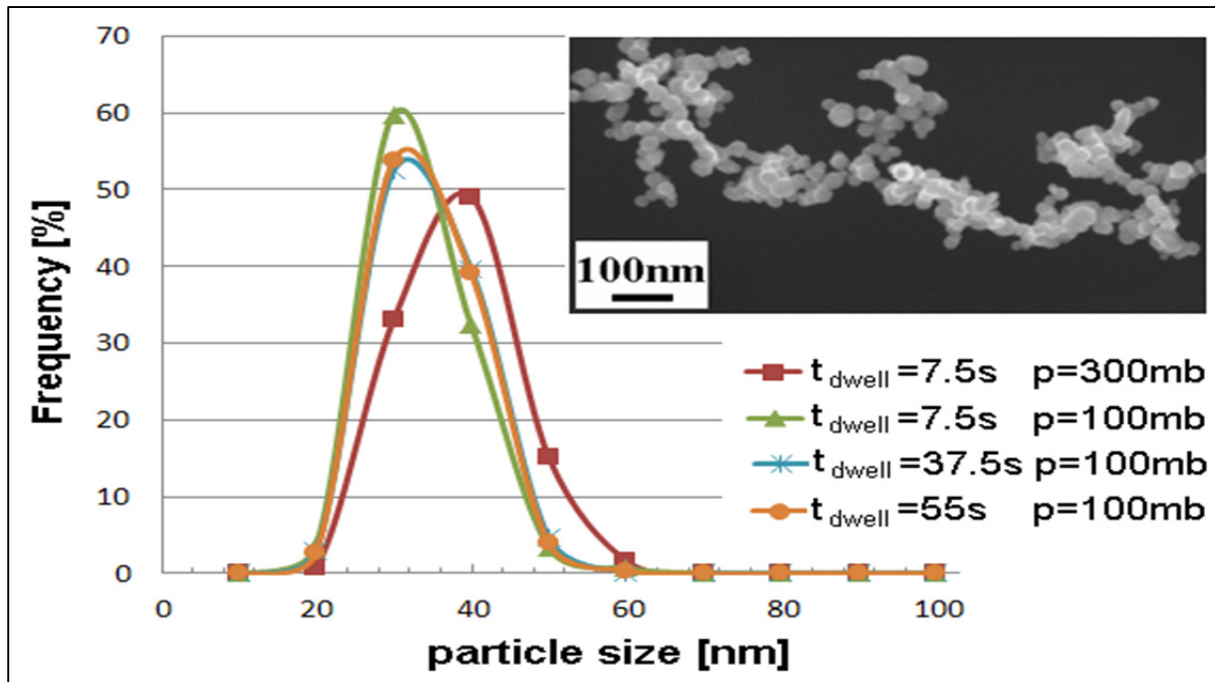


Figure 10: Intra-agglomerate size distribution of Ni-particles obtained in μ -g (SR) at different dwell times and two different background pressures; insert: typical Ni-aggregate morphology

4. Discussion

The formation of extended chains of nanoparticles is a well-known phenomena observed as a result of agglomeration within magnetic aerosols. Usually the magnetic dipole interaction is considered responsible for this type of self-organization (cf. [5]). Li et al. [8] observed morphologies of Ni-agglomerates depending on the external magnetic field strength: Applying a strong magnetic field would result in longer particle chains. Unfortunately in all these experiments the magnetic structure of the nanoparticles remains unclear. In our experimental set-up the Earth magnetic field (cf. Table 1) might influence the orientation of the magnetic dipoles and/or the chain fragments on their way towards the sampling stage.

Table 1: earth magnetic field strength $|B|$ at different locations

Bremen (lab)	Parabolic flights (during parabola)	MAXUS 8 (at launch)	MAXUS 8 (start of μ -g phase)	MAXUS 8 (at apogee)
$48.5 \mu\text{T}^1$	ca. $47.8 \mu\text{T}^2$	$52.2 \mu\text{T}^1$	$46.1 \mu\text{T}^3$	$37.2 \mu\text{T}^3$

¹<http://www.pimath.de/magnetfeld/gesamtfeld.html>, ²[10]; ³values during MAXUS flight have been calculated

Figure 11 illustrates the proposed agglomeration mechanism in the presence of dipolar magnetic interaction in lab-, PF- and SR-experiments. In Figure 12 is shown the mean chain length as a function of dwell time obtained in lab- and PF-experiments. No such data could be derived for the SR-samples, since no particle chains had formed.

To elucidate the reason for the non-chainlike Ni-aggregates obtained in the SR experiments, we had performed SQUID and MFM (Magnetic Force Microscopy) measurements on the agglomerates. Due to the size distribution evaluated via TEM-measurements, we assumed

blocked superparamagnetic behavior with related single domain particles at room temperature. Unfortunately, MFM investigations failed due to interactions between the MFM

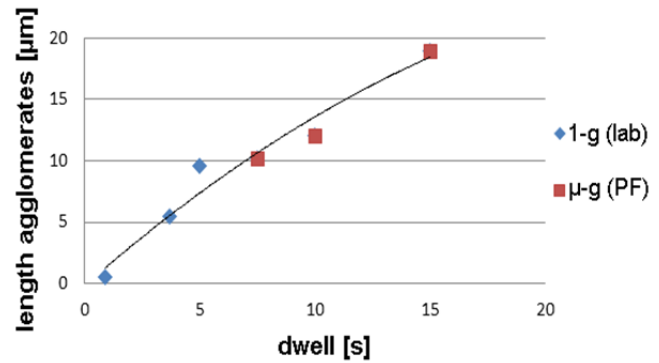
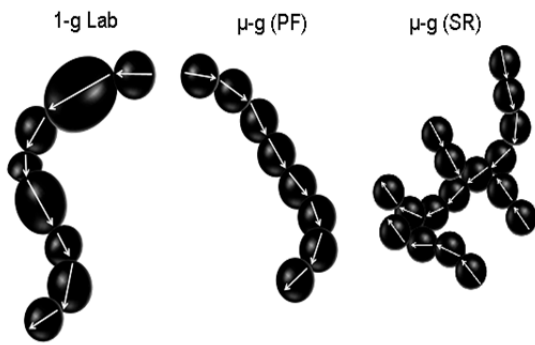


Figure 11: proposed model for agglomerate formation in 1-g and μ -g induced by dipolar interaction between Ni particles

Figure 12: length vs. dwell time of Ni-agglomerates obtained on-ground and in PF experiments

tip and the agglomerates which moved the Ni-chains during the measurements and therefore prevented usable images. SQUID analysis on samples assembled under 1-g and μ -g conditions, respectively, clearly show blocked superparamagnetic behaviour (Figure 13). We would like to mention that a small fraction of the coercive behavior could be related to the NiO induced exchange bias, provided from a small surface related contribution [9]. However, both samples show a superposition of ferromagnetic and paramagnetic behavior. We assume that due to the size distribution a mixture of blocked and unblocked superparamagnetic particles is present. Because the size of the particles assembled during the SR flight is smaller than in lab and during PF, this sample exhibits a smaller blocking temperature. Due to this and the relative low Curie temperature of Ni of about 631K one expects a stronger effect of magnetization reduction with increasing temperature at the SR made particles. Therefore it is most likely, that Ni-particles produced under μ -g conditions (SR) are not magnetic during the particle assembly phase, due to the particle size related smaller blocking temperature, which is below the material temperature after evaporation.

To summarize, the most likely explanation for the different behavior of the μ -g Ni-particles (SR) is the reduced blocking temperature due to the size dependency, yielding hot nonmagnetic Ni-clusters during the agglomeration phase. Nevertheless, the exact reason for this phenomenon is still under investigation.

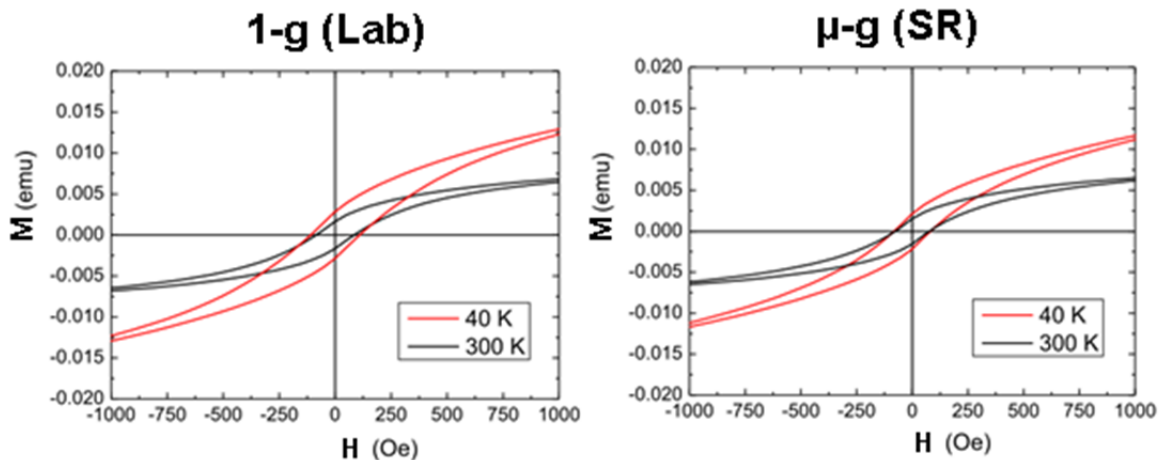


Figure 13: SQUID measurements of Ni-agglomerates developed on-ground (left) and on sounding rocket (right)

5. Conclusions

With this work we have presented new results on the agglomeration behavior of Ni-nanoparticles in aerosols produced under normal gravity and microgravity conditions. In general, necklace-like chains are obtained with primary Ni-particles being larger than about 20 nm. Agglomerates obtained in μ -g during parabolic flights are similar in morphology with those obtained on-ground. The chain length slightly correlates with the time available for agglomeration. Furthermore, the intra-chain particle size distribution is much narrower compared to those obtained on-ground. Surprisingly, the results obtained from a sounding rocket campaign (MAXUS-8) do not fit into this scheme: no particle chains were found even with Ni-particles much larger than 20 nm. This might be due to a different temperature dependent magnetic behavior of the nanoparticles and will be part of future investigation on the particles' magnetic properties.

Acknowledgements

The authors thank ESA, SSC, and Novespace for providing microgravity facilities, sounding rocket launch support, and assistance during parabolic flights, respectively. This work was partially funded by the European Commission under contract-No NMP3-CT-2004-500635.

REFERENCES

- [1] F. E. Kruis et al, *Synthesis of nanoparticles in the gas phase for electronic, optical and magnetic applications – a review*, J. Aerosol Sci. Vol. 29, No. 5/6, 1998, 511-535
- [2] S.P. Parkin et al, *Magnetic Domain-Wall Racetrack Memory*, Science 320, 2008, 190
- [3] H. Wang et al, *Size-controlled synthesis, microstructure and magnetic properties of Ni nanoparticles*, Materials Research Bulletin 43, 2008, 3529-3536
- [4] A. Oberholz et al, *Winnacker-Küchler: Chemische Technik*, 5. Auflage, (2003-2005), ISBN: 978-3-527-30430-1, K. Wegner et al, Band 2, Kapitel 9, 821-905
- [5] V. Maceira et al, *One-dimensional assemblies of silica-coated cobalt nanoparticles: Magnetic pearl necklaces*, Journal of Magnetism and Magnetic Materials 303, 2006, 163–166
- [6] C. G. Granqvist et al, *Ultrafine metal particles*, J. Appl. Phys. Vol. 47. No.5, 1976, 2200-2219
- [7] S. Lösch et al, *Microgravity compatible equipment for inert gas condensation of metals during parabolic flights*, Rev. Sci. Instrum. 80, 2009, 083907
- [8] P. Lie et al, *Well-aligned Nickel Nanochains Synthesized by a Template-free Route*, Nanoscale Res Lett 5, 2010, 597–602
- [9] M. Fraune et al, *Size dependence of the exchange bias field in NiO/Ni nanostructures*, Appl. Phys. Lett., Vol. 77, 2000, 3815 - 3817
- [10] M. Rost, *Aggregation of micron-sized magnetic dust particles in low magnetic field conditions*, Copernicus, 2006
- [11] G.W.Webb, U.S. Patent No. 4758267, 1988

Crystallographic Stability of Metastable Phase formed by Containerless Processing in REFeO₃ (RE: Rare-earth Element)

Kazuhiko Kuribayashi^{1,2}, M. S. Vijaya Kumar²

¹ Shibaura Institute of Technology,
Toyosu, Koto, Tokyo 135-8548, Japan

² Institute of Space and Astronautical Science, JAXA,
Yoshinodai, Sagamihara, Kanagawa 252-5210, Japan

Keywords: Containerless processing, Undercooling, Metastable phase,

Abstract

Undercooling a melt often facilitates a metastable phase to nucleate preferentially. Although the classical nucleation theory shows that the most critical factor for forming a metastable phase is the interface free energy, the crystallographic stability is also indispensable for the phase to be frozen at ambient temperature. In compound materials such as oxides, authors have suggested that the decisive factors for forming a critical nucleus are not only the free energy difference but also the difference of the entropy of fusion between stable and metastable phases. In the present study, using REFeO₃ (RE: rare-earth element) as a model material, we investigate the formation of a metastable phase from undercooled melts with respect to the competitive nucleation and crystallographical stabilities of both phases.

Introduction

A metastable phase is a phase that does not exist in thermal equilibrium state and, although thermodynamically unstable, can temporarily exist when some conditions are fulfilled. Research into the metastable phase began with Ostwald's prediction that a phase formed first from supersaturated liquid is not always thermodynamically stable but is close to liquid in energy [1]. This prediction is called "step rule". Later on, Stranski and Totomanov [2] suggested that the step rule is a consequence of preferential formation of a critical nucleus of the metastable phase. That is, the activation energy required to form a critical nucleus, ΔG_n^* , controls the nature of the process. Regarding this point, the classical nucleation theory [3] states that ΔG_n^* can be understood in terms of the interfacial free energy γ between the liquid and solid phases. Turnbull [4] and Spaepen [5], assuming that γ of a simple material such as metal is related not to the enthalpy change but to the entropy change at the solid-liquid interface, formulated γ as

$$\gamma = \alpha \frac{\Delta S_f T}{(N_A V_m^2)^{\frac{1}{3}}}, \quad (1)$$

where ΔS_f , T , N_A and V_m are the heat of fusion, the temperature of material, Avogadro number and the molar volume, respectively. Furthermore, Spaepen and Meyer [6] derived α , dimensionless solid-liquid interfacial energy, as 0.86 for fcc or hcp crystals and 0.71 for bcc structures, respectively. The α -factors, which strongly depend on the structure of both solid and liquid phase, are to be a critical parameter to determine ΔG_n^* . In fact, it has been reported that the phase selection of the stable γ -phase or the metastable δ -phase in Fe-Ni-Cr alloys is controlled by α [7-9]. However, almost the metastable phases formed at the first recalescence, which

change into the stable phases at the second recalescence, are not frozen into ambient temperature. In order that the metastable phase may be frozen into ambient environment, the nucleation criterion of metastable phase as well as the crystallographical stability must be fulfilled. Then, in the present investigation, using REFeO₃ as the model material, where RE means rare-earth elements, the phase selections not only in the nucleation stage but also the growth stage are discussed.

Entropy-undercooling regime criterion of phase selection

Before taking up the main subject of this paper, we mention again the hypothesis that, in ionic crystals, ΔS_f is to be a dominant factor in the determination of γ .

Spaepen [10] and Granasy [11], almost at the same time, developed rather similar models that γ at equilibrium state is given by

$$\gamma = \int_v (H(r) - TS(r)) dr, \quad (2)$$

where $H(r)$ and $S(r)$ are cross-interfacial enthalpy and entropy. Figure 1 shows a schematical illustration of Eq. 2, where (a) shows the change of the atomic order and of the order parameter in solid and liquid, and (b) schematic representation of the change in the enthalpy $H(r)$ and the product $T_E S(r)$ of melting temperature and entropy at the solid-liquid interface. The colored area corresponds to the approximate value of the interfacial energy, showing that α is not a dimensionless interfacial energy but a dimensionless interface thickness. This model can qualitatively infer the temperature dependence of the solid-liquid interfacial free energy. However, we need analytical or numerical forms of $H(r)$ and $S(r)$ in order to evaluate the interface thickness that is the key parameter of the model.

On the other hand, in a material having faceted interface, the order parameter representing the regularity of the atomic arrangement rapidly changes as the interface is crossed as shown in Fig. 2. In this case, $H(r)$ can be approximated by the near-step function as shown in Fig. 2(b). Consequently, the interfacial energy is approximated with a triangle if we assume $S(r)$ as a linear function of r at the cross-interface region. This result also means that α is a dimensionless interface thickness rather than a dimensionless interfacial energy. The recent numerical calculation of α based on the molecular dynamics and the density functional analysis suggests

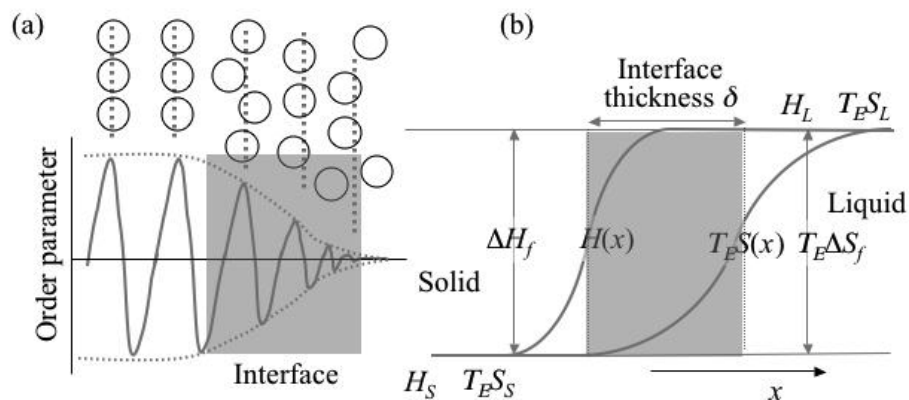


Figure 1. Schematic representation of the nonfaceted interface between solid and liquid. (a) change of the atomic order and of the order parameter in solid and liquid. (b) schematic representation of the change in the enthalpy $H(r)$ and the product $T_E S(r)$ of melting temperature and entropy at the solid-liquid interface. The colored area corresponds to the approximate value of the interfacial energy, showing that α is not a dimensionless interfacial energy but a dimensionless interface thickness.

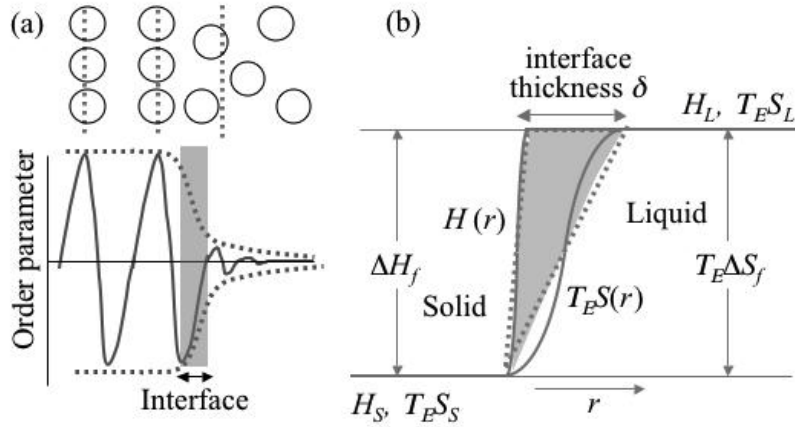


Figure 2. Schematic representation of the faceted interface between solid and liquid. (a) change of the atomic order and of the order parameter in solid and liquid. (b) schematic representation of the change in $H(r)$ and $T_E S(r)$. The colored area corresponds to the approximate value of the interfacial energy, suggesting the interface thickness is approximately half of the atomic layer spacing.

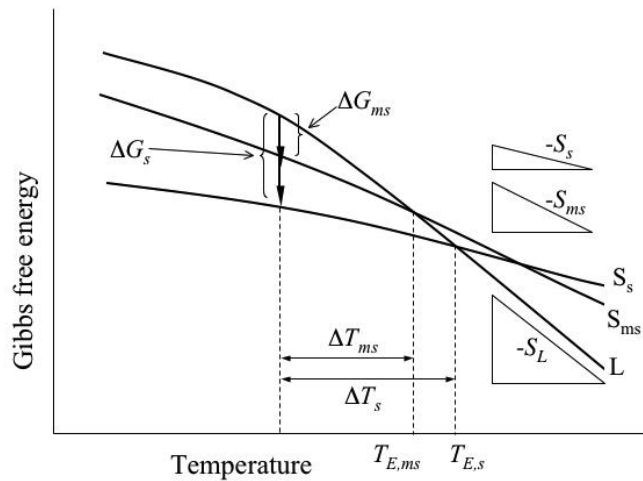


Figure 3. Schematic image of temperature dependency of free energy in liquid and solid phases (stable and metastable phases). The entropies of three phase are related $S_L > S_{ms} > S_s$. Therefore, as for entropy of fusion ΔS_f caused by solidification, the relation $\Delta S_{f,s} > \Delta S_{f,ms}$ becomes valid.

the interface thickness is approximately half of the atomic layer spacing [12], which implies that the model shown in Fig. 2 is qualitatively valid even in the nonfaceted interface.

Figure 3 schematically shows the thermodynamic relation when considering the step rule [13]. The figure depicts temperature and free energy of both liquid and solid phases (stable and metastable phases). The reason why liquid phase changes to solid phase is that the free energy of the liquid phase becomes larger than that of solid phase. The energy-balance point of both phases is the melting point. Comparing the metastable phase to the stable solid phase in terms of free energy, the free energy of the metastable phase, G_{ms} , is larger than that of stable phase, G_s , (the subscripts s and ms mean stable phase and metastable phase, respectively). Therefore, the melting point of the metastable phase, $T_{E,ms}$, becomes lower than that of stable phase, $T_{E,s}$. Meanwhile,

the absolute value of the gradient of each curve (temperature coefficient of Gibbs free energy) in Fig. 2 corresponds to the entropy when pressure is constant. From the figure, we can see the relation $S_L > S_{ms} > S_s$ between entropies of liquid phase S_L , stable phase S_s and metastable phase S_{ms} . Therefore, for the change of entropy, ΔS_f , caused by melting, we can find a relation $\Delta S_{f,s} > \Delta S_{f,ms}$ (i.e., the change of the entropy is smaller when the liquid phase changes to metastable phase). From the relative relations of the three phases above, we can see that the metastable phase is to be a higher entropy phase than the stable phase [14].

Factors determining the entropy of material are first, density of material and secondly, symmetry of arrangement of atoms and/or molecules making up the material. Therefore, high entropy phase is liquid rather than solid, and gas rather than liquid. Among solid phases, it is guessed that the low-density phase becomes higher-entropy phase. In conclusion, we can say that the metastable phase is lower density, higher symmetric material than the stable state.

Experimental procedure and results

Spherical samples of REFeO₃ were prepared from high purity (99.99%) RE₂O₃ and Fe₂O₃ powders. Levitation and melting of samples were carried out by an aerodynamic levitator, ADL, which was designed in order to solidify undercooled melts under the precisely controlled P_{O_2} . Details of the sample preparation and experimental facility are shown elsewhere [15, 16].

Goldschmidt [17] discussed the stability of the perovskite (ABO₃) structure using the tolerance factor, TF :

$$TF = \frac{R_A + R_O}{\sqrt{2}(R_B + R_O)}. \quad (3)$$

In the present investigation, ionic radii of R_A , R_B and R_O correspond to those of rare-earth element, iron and oxygen, respectively. From the systematic investigation, he summarized that the perovskite structure is stable at $TF > 0.8$ and contrary unstable at $TF < 0.8$. Using Shannon ionic radii from La (0.1216 nm) to Lu (0.1032 nm), TF 's for the REFeO₃ system were calculated to be 0.905 for LaFeO₃ to 0.841 for LuFeO₃. Therefore, the perovskite structure is expected to be stable in the REFeO₃ system.

Figure 4 shows SEM micrographs of samples of REFeO₃ solidified in containerless conditions. As shown in the photographs, their surface profiles vary according to the type of rare-earth elements. The surface of LaFeO₃ is nonfaceted and spherical while that of LuFeO₃ is faceted and polyhedral [18]. Note that the different surface features result from differences in crystal structure, not differences in rare-earth element. Specifically, the lattice structure of the LaFeO₃ sample is orthorhombic, the space group of which is $Pbnm$ (*o*-REFeO₃), while the LuFeO₃ sample is a hexagonal-symmetric of $P6_3cm$ (*h*-REFeO₃). As the *h*-REFeO₃ phase has a 10%~20% smaller

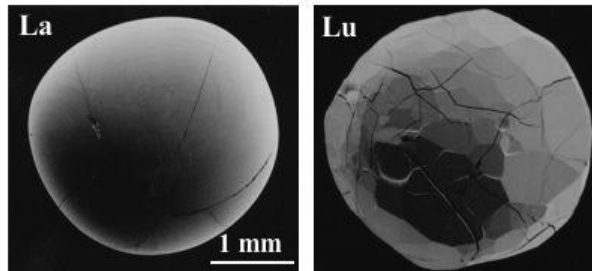


Figure 4. Surface profiles of REFeO₃ (RE=La, Lu) formed by containerless process. LaFeO₃ with large ionic radius has a smooth and spherical surface while LuFeO₃ with small radius has a rugged and polyhedral surface.

density than that of perovskite [19], it is estimated that the hexagonal crystal is a higher entropy phase than perovskite. In other words, the hexagonal crystal should have intrinsically become stable perovskite. However, having been largely undercooled to below $T_{E,ms}$ indicated in Fig. 2 by the containerless process, hexagonal crystals of high-entropy phase grew as metastable phase (Fig. 5). In fact, when we forced it to solidify at a temperature of around $T_{E,s}$ even by the same containerless process, stable-phase perovskite appears.

Figure 5 shows typical images taken sequentially during recalescence in samples of LaFeO_3 , GdFeO_3 and YFeO_3 , each of which is processed at oxygen environment. The elapsed time indicated in each image was set to 0 s for one frame before the nucleation. At oxygen environment, although single recalescence that can be ascribed to the phase transition from undercooled melt to equilibrium perovskite phase was observed in LaFeO_3 samples, double recalescences were observed in GdFeO_3 and YFeO_3 samples, where a primary phase was solidified from the undercooled melt and then the secondary phase with higher brightness was initiated at the interface between melt and the primary phase. The high brightness implies that the melting temperature of the secondary phase was much higher than that of the primary phase. This result indicates that decrease of TF facilitates the undercooled melt to solidify into the metastable $h\text{-REFeO}_3$ phase rather than the stable $o\text{-REFeO}_3$ phase. According to this result, reduction of the oxygen partial pressure P_{O_2} is expected to extend the range of TF for metastable $h\text{-REFeO}_3$ phase to be formed, because decreasing P_{O_2} increases the amount of Fe^{2+} (0.078 nm for CN=6) with larger ionic radius than that of Fe^{3+} (0.0645 nm for CN=6).

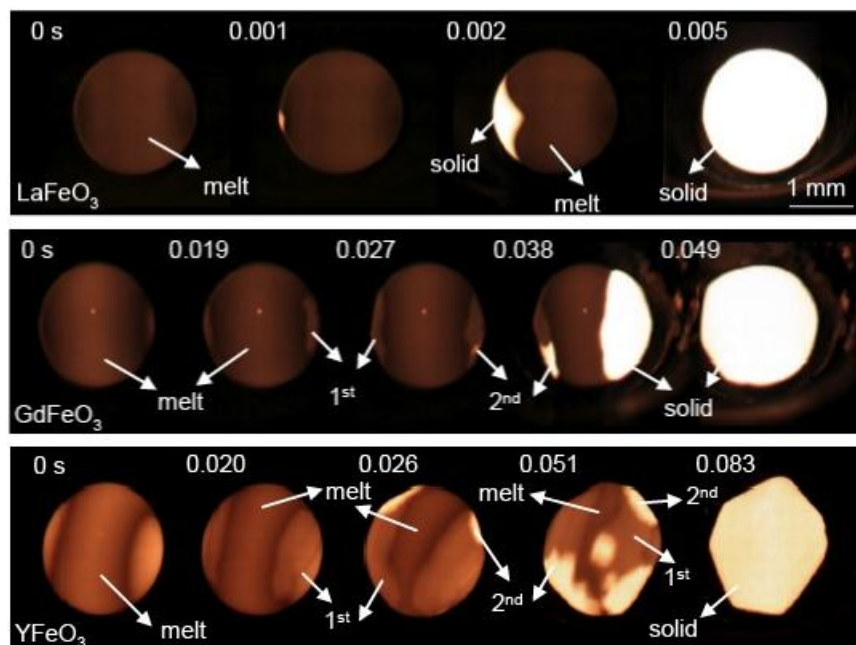


Figure 5. Sequence photographs of HSV images taken during recalescences in the REFeO_3 ($R = \text{La}$, Gd and Y) samples processed at oxygen environment. Although in LaFeO_3 single recalescence was observed, in GdFeO_3 and YFeO_3 double recalescences indicating the formation of metastable phases were observed.

In addition, YbFeO_3 was used to study the effect of ionic radii of RE elements on the formation of metastable phases, because the ionic radius of Yb^{3+} (0.1042 nm) was slightly larger than that of Lu^{3+} (0.1032 nm). Figure 6 shows the XRD patterns of YbFeO_3 samples processed at controlled P_{O_2} . At 10^5 Pa of P_{O_2} , the stable orthorhombic phase ($o\text{-YbFeO}_3$) was formed at the second recalescence as in the cases of GdFeO_3 and YFeO_3 . At 10^4 Pa of P_{O_2} , however, the

metastable hexagonal phase (*h*-REFeO₃) remained, forming the dual phase with *o*-YbFeO₃, and at 9×10^3 Pa, the *o*-YbFeO₃ phase did not appear [20].

These results suggest that the decrease of P_{O_2} facilitates the undercooled melt to solidify to metastable *h*-REFeO₃ phase rather than the stable *o*-REFeO₃ phase, particularly in samples with RE³⁺ of relatively small ionic radius.

Figure 7 shows the relation between the recalcence results and P_{O_2} as a function of the ionic radii of RE³⁺, in which Shannon ionic radii for CN=9 were used. Decrease of P_{O_2} extends the

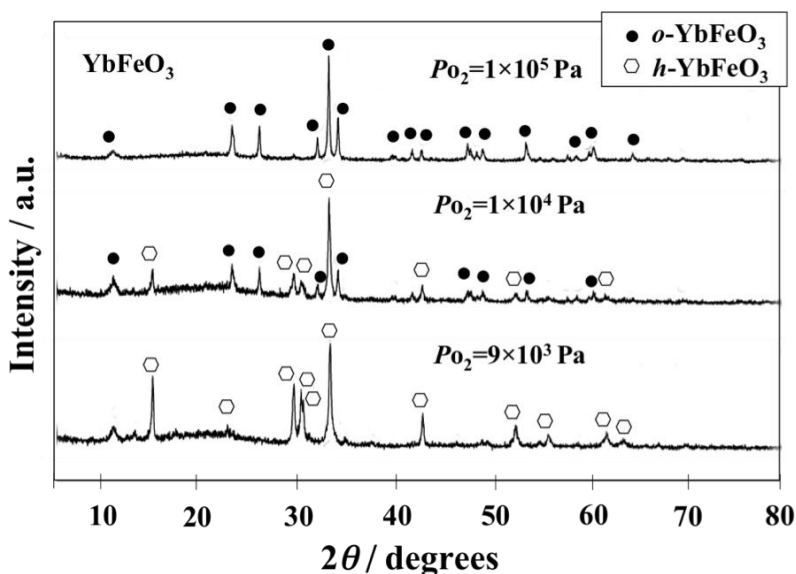


Figure 6. XRD patterns of the YbFeO₃ samples processed at $P_{O_2}=10^5$ Pa, $P_{O_2}=10^4$ Pa and $P_{O_2}=9 \times 10^3$ Pa, respectively. At 10^5 Pa of P_{O_2} , the stable orthorhombic phase (*o*-YbFeO₃) was formed at the second recalcence as in the cases of GdFeO₃ and YFeO₃. At 10^4 Pa of P_{O_2} , however, the metastable hexagonal phase (*h*-REFeO₃) remained, forming the dual phase with *o*-YbFeO₃, and at 9×10^3 Pa, the *o*-YbFeO₃ phase did not appear.

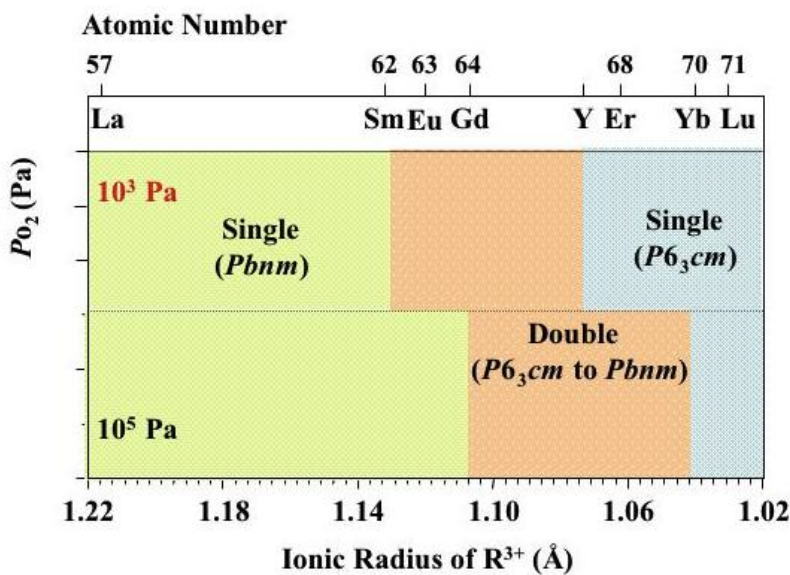


Figure 7. Relation between the recalcence results and P_{O_2} as a function of the ionic radii of RE³⁺, in which Shannon ionic radii for CN=9 were used.

range of TF for metastable h -REFeO₃ phase to be formed.

Discussion

Bertaut *et al.* [21] and Yakel *et al.* [22] have first reported the two hexagonal modifications in the ABO₃ systems, the space groups of which are $P6_3/mmc$ and $P6_3cm$, respectively. In the h -REMnO₃ system, the $P6_3cm$ type modification was formed as a low temperature phase for RE³⁺ with small ionic radius (Ho-Lu, Y and Sc), whereas the $P6_3/mmc$ type modification was reported as a high temperature phase. In our experiment, although the space group of the metastable h -REFeO₃ phase belonged to $P6_3cm$, the high temperature phase can be deduced to belong to the $P6_3/mmc$ space group because the ionic radius of Fe³⁺ is as same as that of Mn³⁺ (0.0645 nm for 6 coordination) [23]. Hence, in this investigation, the geometrical analysis of the atomic configuration in h -REFeO₃ is developed on the assumption that the space group of the primary phase is $P6_3/mmc$.

The atomic configuration of the $P6_3cm$ modification in ABO₃ system can be described as a dense oxygen-ion packing (ABCACB) with B³⁺ ions having coordination number CN=5 (five-fold distorted trigonal bipyramidal coordination), and A³⁺ with CN=7 (seven-fold monocapped octahedral coordination), forming a noncentrosymmetric structure. On the other hand, centrosymmetric $P6_3/mmc$ is assumed to be described simply with B³⁺ ions of undistorted CN=5 and A³⁺ of CN=6 (octahedral coordination).

Figure 8 shows the geometrical configuration among RE³⁺(CN=6), Fe³⁺(CN=5), and O²⁻ in a space group of $P6_3/mmc$, in which the constituent ions are packed without any spacing between neighboring ions. As shown in this figure, the relation among the ionic radii of constituent ions of h -REFeO₃ is expressed as

$$R_{RE} + R_O = \frac{\sqrt{6}}{2} (R_{Fe} + R_O). \quad (4)$$

Therefore, the h -REFeO₃ phase will be ideal when the next equation is fulfilled,

$$TF = \frac{\sqrt{3}}{2} \approx 0.87 \quad (5)$$

The experimental results showed that the h -GdFeO₃ phase is formed because TF of which is 0.867. Whereas, the h -EuFeO₃ is not formed because of slightly high TF of 0.871. This suggests

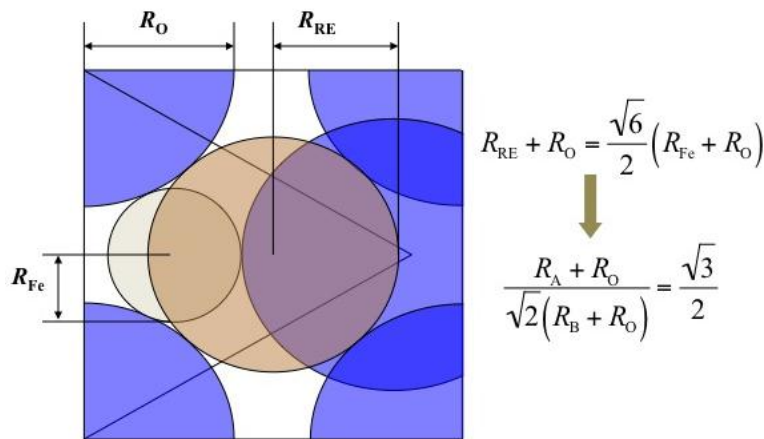


Figure 8. Geometrical configuration among RE³⁺ (CN=6), Fe³⁺ (CN=5), and O²⁻ in a space group of $P6_3/mmc$, in which the constituent ions are packed with no space between neighboring ions. The h -REFeO₃ phase will be the ideal at $TF = 0.87$.

that the aforementioned condition expressed by Eq. 5 is to be the criterion for the metastable *h*-REFeO₃ phase to be formed.

Conclusion

Using REFeO₃ (RE: rare-earth element) as a model material, containerless solidification for forming a metastable phase from undercooled melts was carried out as a function of *P*_{O₂} (oxygen partial pressure). Based on the geometrical consideration on the ionic radii of constituent ion, RE³⁺, Fe³⁺ and O²⁻, it was derived that the criterion for metastable hexagonal phase is also expressed by tolerance factor, *TF*:

$$TF < 0.87.$$

Experimental result well agreed with this criterion under reduced *P*_{O₂} as well as for ambient conditions.

Acknowledgement

This work was financially supported by a grant-in aid for Scientific Research from the Ministry of Education, Culture, Sports, Science and Technology.

References

- [1] W. Ostwald, *Z. Phys. Chem.* **22** (1897) 282.
- [2] I. Stranski and D. Totomanov, *Z. Phys. Chem. A* **163** (1933) 399.
- [3] K. F. Kelton, *Solid State Physics* **45** (1991) 75.
- [4] D. Turnbull and R. E. Cech, *J. Appl. Phys.* **21** (1950) 804.
- [5] F. Spaepen, *Acta Metall.* **23** (1975) 729.
- [6] F. Spaepen and P. B. Meyer, *Scripta Metall.* **10** (1976) 257.
- [7] Y. -Y. Chuang, C. -C. Hsieh and Y. A. Chen, *Metall. Trans. A*, **17A** (1986) 1361.
- [8] T. Koseki and M. C. Flemings, *Metall. Mater. Trans. A*, **26A** (1995) 2991.
- [9] T. Volkman, W. Loeser and D. M. Herlach, *Metall. Mater. Trans. A*, **28A** (1997) 453.
- [10] F. Spaepen, *Solid State Physics*, **47** (1994), p.1.
- [11] L. Granasy, *J. Non-Cryst. Solids*, **162** (1993) 301.
- [12] D. W. Marr and A. P. Gust, *J. Chem. Phys.* **99** (1993) 2024.
- [13] K. Kuribayashi and S. Ozawa, *J. Alloy Compd.* **408-412** (2006) 266.
- [14] K. Kuribayashi, K. Nagashio, K. Niwata, M. S. Vijaya Kumar and T. Hibiya, *Mater. Sci. Eng. A* **449-451** (2007) 675.
- [15] K. Nagashio, Y. Takamura, K. Kuribayashi and Y. Shiohara, *J. Crystal Growth* **200** (1999) 118.
- [16] M. S Vijaya Kumar, K. Nagashio, T. Hibiya and K. Kuribayashi, *J. Am. Ceram. Soc.* (2008) **91** 806.
- [17] V. M. Goldschmidt, *Die Gesetze der Krystallochemie* Math -Naturv. Kl. Oslo, Norway, **8** (1926) 1.
- [18] K. Nagashio and K. Kuribayashi, *J. Am. Ceram. Soc.* **85** (2002) 2550.
- [19] A. A. Bosak, C. Dubourdieu, J. -P. Senateur, O. Yu. Gorbenko and A. R. Kaul, *Crystal Engineering* **5** (2002) 355.
- [20] M. S. Vijaya Kumar, K. Kuribayashi and K. Kitazono, *J. Am. Ceram. Soc.* **92** (2009) 903.
- [21] E. F. Bertaut and J. Mareschal, *Compt. Rend.* **257** (1963) 867.
- [22] H. L. Yakel, W. C. Koehler, E. F. Bertaut and E. F. Forrat, *Acta. Cryst.* **16** (1963) 957.
- [23] K. Nagashio, K. Kuribayashi, M. S. Vijaya Kumar, K. Niwata, T. Hibiya, A. Mizuno, M. Watanabe and Y. Katayama, *Applied Physics Letters* **89** (2006) 241923.

ON-LINE REAL TIME DIAGNOSTICS OF A SINGLE FLUID ATOMIZATION SYSTEM

P. Delshad Khatibi, A. Ilbagi, H. Henein

Chemical and Materials Engineering Department, University of Alberta;
Edmonton, Alberta, T6G 2V4, Canada

Keywords: Online measurement, Undercooling, Radiant energy

Abstract

A drop tube-Impulse Atomization technique was used to produce copper droplets. In this method, energy is transferred to a liquid by plunger movement resulting in spherical droplets emanating from orifices. A mathematical model of the evolution of droplet velocity and temperature at various heights for different sized droplets was developed. A two-color pyrometer, DPV-2000, and a shadowgraph were used to measure droplets radiant energy, diameter and velocity. The temperature values from the model were used to assess the two color pyrometer assumption over the temperature range of measurement. The DVP 2000 measurements were found to be dependent of droplet size wavelength and position of droplets below the atomizing nozzle. By calibrating the instrument for effective emissivity over the range of measurements, the thermal history of droplets may be recorded using a single color pyrometer approach.

Introduction

The variation of undercooling or cooling rate in solidification provides the possibility to control morphology and size of crystal structures. A number of models have been reported for predicting or estimating the undercooling temperature of droplets in gas, single fluid atomization systems and drop tubes [1-3]. A systematic effort on the investigation of thermal history of falling droplets in-situ during atomization is rare [4]. In addition to the thermal history, in-situ measurement of the droplet diameter, initial velocity and instantaneous velocity is crucial in validating solidification models.

Delshad Khatibi et al. [5] used a two-color pyrometer, DPV-2000, to measure droplets effective radiant energy for different droplet sizes. It was also shown that the acceleration of falling droplets near the melting point is close to gravitational acceleration and as a result the falling droplets do not reach their terminal velocity at their melting point.

The DPV-2000 is a high-speed two colors pyrometer that measures the effective radiant energy of the particles. According to Planck's radiation law, the total energy radiated by a spherical particle can be expressed as:

$$E(\lambda_i) = \frac{C_1 \varepsilon(\lambda_i) \lambda_i^{-5}}{e^{\frac{c_2}{\lambda_i T}} - 1} \quad (1)$$

where, $C_1= 3.74 \times 10^8 \text{ W} \cdot \mu\text{m}^4/\text{m}^2$ and $C_2=1.4387 \times 10^4 \text{ } \mu\text{m} \cdot \text{K}$ [6]. $\varepsilon(\lambda_i)$ is emissivity of the particle at λ_i , wavelength, and T is temperature. In two color pyrometry a measure of the energy radiated from a body is taken at two wavelengths. It is assumed, for a two color pyrometer, that over the measured temperature range the emissivity is not a function of wavelength. In this work, we aim to test this assumption for molten copper droplets atomized into an argon gas atmosphere. Under these conditions, equation (1) would be re-written in the following form for the DVP 2000:

$$Q(\lambda_i) = \frac{C_1 \alpha(\lambda_i) d^2 \lambda_i^{-5}}{e^{c_2/\lambda_i T} - 1} \quad (2)$$

where $Q(\lambda_i)$ is proportional to $E(\lambda_i)$ and is the quantity measured by the DVP 2000, $\alpha(\lambda_i)$ is proportional to $\varepsilon(\lambda_i)$ and d is the droplet diameter in μm . The DVP 2000 reports measurements of Q at two specific wavelengths designed into the instrument. For these experiments these wavelengths are, λ_1 is $0.787 \mu\text{m}$ and λ_2 is $0.995 \mu\text{m}$. A mathematical model was also utilized to predict the temperature of falling copper droplets at different heights. Thus, for a given measurement of Q for a known droplet size and distance below the nozzle, $\alpha(\lambda_i)$ at each wavelength is the only unknown in Equation (2) and will be compared for values determined at λ_1 and λ_2 .

Experimental

Copper with 99.99% purity (Alfa Aesar) was melted in a graphite crucible using a 20kW induction furnace located at the top of a drop tube-impulse atomization (IA) tower. An argon atmosphere of 90ppm oxygen was maintained in the tower during melting and atomization. After melting the copper, it was superheated to 1400°C and the molten metal was atomized through orifices located at the bottom of the crucible, forming ligaments, which spherodized into droplets in the inert argon atmosphere. The falling droplets were cooled in free fall by the argon atmosphere.

DPV-2000 (Tecnar Automation Ltée) was used to measure effective radiant energy, $Q(\lambda_1)$ and $Q(\lambda_2)$, and a shadowgraph (Sizing Master Shadow from LaVision GmbH in Gottingen, Germany) was used to measure velocity and droplet size of the falling copper droplets. These sensors were installed on a translation stage inside the drop tube that was capable of moving in all three directions. DPV-2000 is an optical sensing device based on a patented technology developed by the National Research Council of Canada. DPV-2000 uses a dual slit optical sensor that can measure the effective radiant energy of up to 800 droplets per second with the depth of field of 1.9 mm, and it can measure radiant energy of droplets at two different wavelengths [7]. Sizing Master Shadow from LaVision uses the backlighting technique to visualize droplets for image analysis. A light source, in this case a pulsed laser combined with diffuser optics, illuminates in-flight droplets 5 times per second. Backlight of droplets inside the measurement volume of $6 \times 6 \times 6 \text{ mm}$ is captured by a high resolution high-speed imaging system. It is possible to investigate droplet sizes down to $5 \mu\text{m}$ using the shadowgraph device.

The focal point of both shadowgraph and DPV-2000 was set to an imaginary vertical line going through the center of the bottom of the crucible; therefore, any unfocused droplets would be rejected by the criteria set by the operator in the respective software of each instrument. Particle

size distribution of falling droplets (D50 and D90), velocity and effective radiant energy were measured at three distances of 10, 30 and 50 cm from the orifices.

Modeling

A mathematical model was developed to calculate droplet velocity and temperature for different sized copper droplets at different heights.

Droplets begin their downward trajectory with an initial velocity. The subsequent trajectory of the droplets depends on this initial velocity, and the forces of gravity, buoyancy and drag as shown schematically in Figure 1.

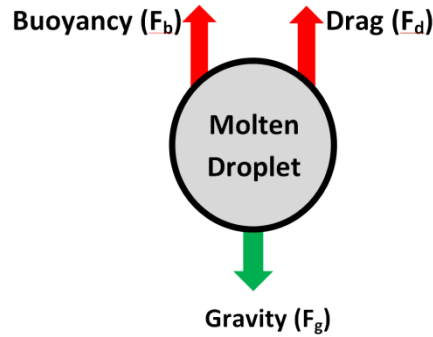


Figure 1. Schematic of the forces acting on a falling droplet.

Applying Newton's Second Law on the droplet, the instantaneous acceleration can be found as follows [8]:

$$\frac{dv}{dt} = g - \frac{3}{4} \frac{\rho_g}{\rho_p} \frac{C_d}{d} \cdot v^2 \quad (3)$$

where v is the relative velocity between the droplet and the atomization gas, (which in the case of IA $v_{gas}=0$) and ρ_p and ρ_g are the densities of the droplet and atomization gas, respectively. The gravitational acceleration is given by g and d is the droplet diameter. The discharge coefficient, C_d , for droplets in laminar flow is given by [9]:

$$C_d = \frac{18.5}{Re^{0.6}} \quad (4)$$

The Reynolds number, Re , in Equation (4) is given by:

$$Re = \frac{\rho_g \cdot v \cdot d}{\mu_g} \quad (5)$$

where μ_g is the gas viscosity.

To calculate the thermal history of a falling droplet, the heat energy loss from the surface of the droplet to the surrounding gas is given by:

$$q = h_{eff} A (T_m - T_0) \quad (6)$$

where h_{eff} is the effective heat transfer and consisting of the additive contribution of convection, conduction and radiation heat transfer mechanisms, A is the surface area of the droplet, T_m is the droplet surface temperature and T_0 is the gas temperature. It is assumed that the surface temperature of the droplet represents the entire droplet temperature, since the internal temperature gradient within the droplets are negligible (Biot <0.1) [10]. It is also assumed that the temperature increase due to surface oxidation is negligible [5]. The effective heat transfer was calculated using the modified Whitaker correlation introduced by Wiskel et al. [10], as shown in Equation 7.

$$Nu = \frac{h_{eff} d}{k_g} = 2 \frac{C}{k_s(m+1)} \cdot \frac{(T_s^{m+1} - T_g^{m+1})}{(T_s - T_g)} + (0.4 Re^{1/2} + 0.06 Re^{2/3}) Pr^{0/4} \left(\frac{\mu_g}{\mu_s} \right) \quad (7)$$

In Equation 7, Nu is the Nusselt Number, Pr is the Prandtl number and d is the droplet diameter. k_g and k_s are conductivity of gas and droplet, respectively while μ_g and μ_s are viscosity of gas and the droplet, respectively. From the variation of gas conductivity with temperature ($k_g=C \times T^m$) for argon $C = 1.86 \times 10^{-4}$ and $m = 0.7915$ [4], the model was able to closely predict the range of time and distance in which the droplets completely solidified under the condition that k_s be evaluated at the metal droplet surface temperature and the Re and Pr numbers evaluated at the free stream gas temperature. Table 1 lists the properties of pure copper and argon which were used in the model.

Table I. Thermophysical properties of copper and argon at 1400°C and 40°C, respectively [11]

	Temperature (°C)	Thermal conductivity (W/K.m)	Specific heat (J/kg.K)	Density (kg/m ³)	Viscosity (m ² /s)
Copper	1400	325	532	7722	-
Argon	40	0.01853	20.80	0.287	0.021

Results and Discussion

During atomization, the shadowgraph was continuously collecting droplet size and velocity data at 5Hz frequency. A total number of 6100 droplets were measured during the entire atomization time of two minutes. Using the shadowgraph, D10=456 μm and D50=565 μm were measured. These two particles sizes will be used as examples to show the process of droplet temperature calculations.

In our previous work [5], it was shown that the particles exit the orifices with an average initial velocity of 1 m/s. Using this initial average velocity, the temperature of droplets with diameters of 456 and 565 μm was determined using the model described above and the results are plotted as a function of distance from the nozzle plate (Figure 2). These predicted temperatures will be used below to estimate values for $\alpha(\lambda_1)$ and $\alpha(\lambda_2)$.

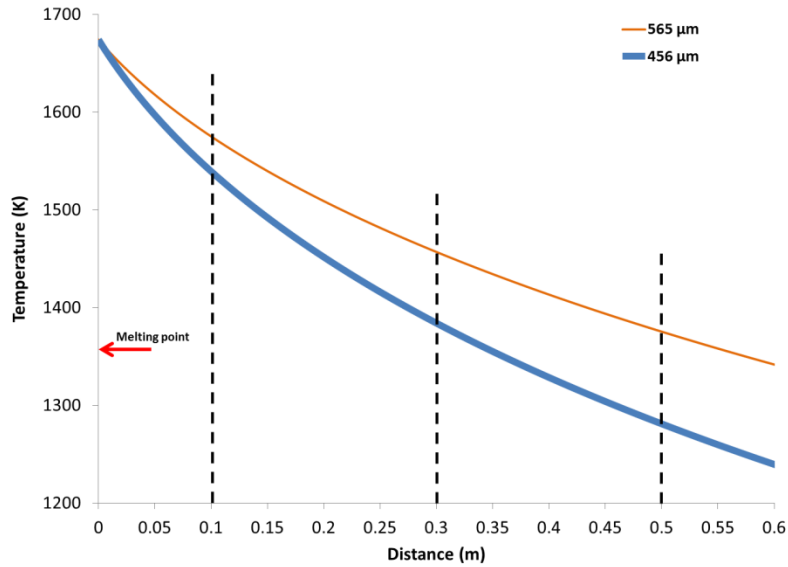


Figure 2. Temperature vs. distance from nozzle plate (plotted using the model) for two different particle sizes. Dashed line shows distance from the nozzle plate.

While the shadowgraph was collecting the velocity and diameter of falling droplets at the center of the spray, the DPV-2000 was measuring the effective radiant energy of the droplets from the same location. Figure 3(a) shows the signal counts of each droplet that DPV-2000 measured at two wavelengths. The area under the curves shown in Figure 3(a) represents the effective radiant energy and as such it is a dimensionless value. The effective radiant energies measured for different droplet sizes at two different wavelengths are shown in Figure 3(b). The measurement shown in Figure 3 was done at 10cm below the nozzle plate. It can be seen that larger droplets have higher effective radiant energy. The same trend was also observed when measurements were performed at 30 and 50cm distances from the nozzle plate.

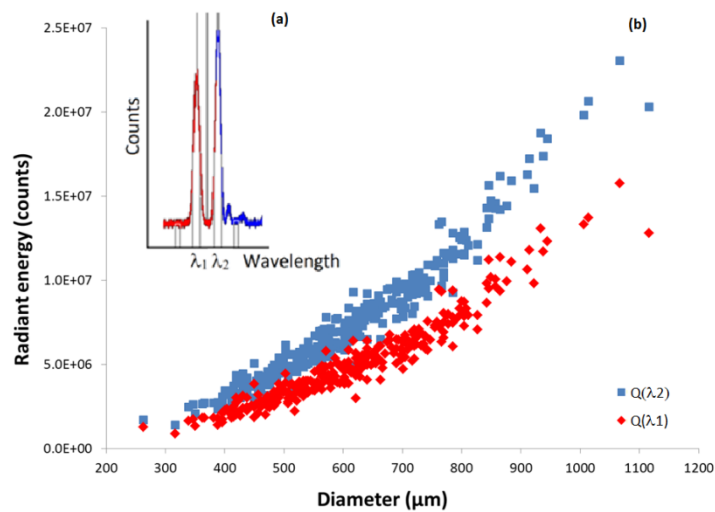


Figure 3. (a) The signal counts measured at two different wavelengths for a single droplet, (b) Radiant energy vs. droplet diameter measured by DPV-2000 at 10cm below the nozzle plate.

From Figure 3, the effective radiant intensity values for the particles with diameters of 456 and 565 μm were averaged and were plotted at three different distances in Figure 4. The error bars in this figure represent the standard deviation from the averaged radiant energy measured for each particle size. The lines connecting the data points of same distances are only for better visualization of the results.

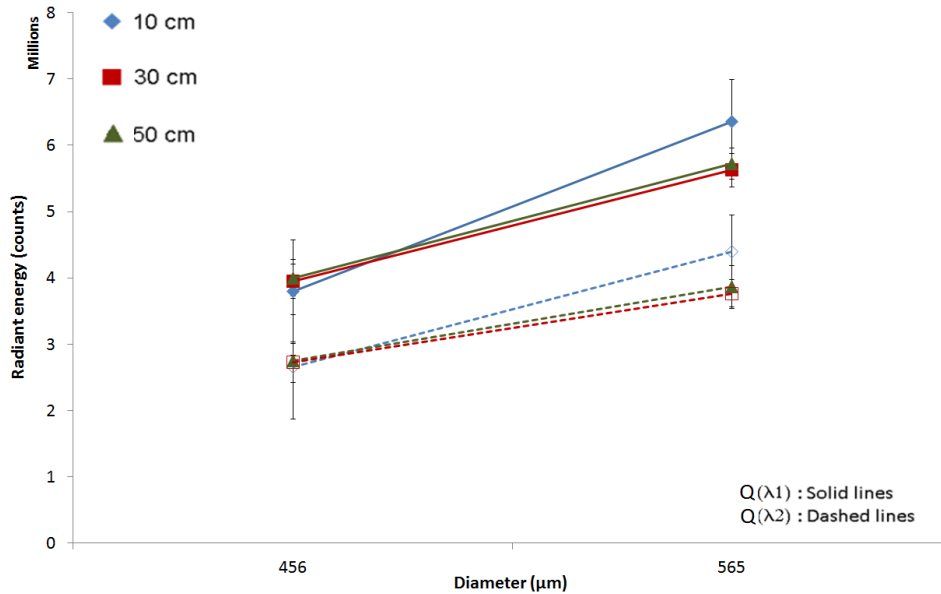


Figure 4. The radiant energies measured by DPV-2000 for 456 and 565 μm particle sizes at three different distances from the nozzle plate.

From Figure 4, it is evident that larger particles have emitted higher effective radiant energies at each wavelength.

To find effective emissivity, $\alpha(\lambda_1)$ and $\alpha(\lambda_2)$, values at λ_1 and λ_2 for different particle sizes at different heights, the effective radiant energies shown in Figure 4 and the respective temperatures from Figure 2 were used in Equation 2. The results are shown in Figure 5.

From Figure 5 it can be seen that there is a difference between $\alpha(\lambda_1)$ and $\alpha(\lambda_2)$ and by extension, $\varepsilon(\lambda_1)$ and $\varepsilon(\lambda_2)$ over the temperature range of interest in these experiments. This difference decreases with increasing temperature. Based on the two-color pyrometer's theory, it is assumed that the wavelengths are chosen so close that the change in emissivity as a result of wavelength change is insignificant. This assumption may be more precise at high temperatures where the radiant energy as a function of wavelength does not significantly change, above 1600K in Figure 5 for copper. However, below 1600K for copper, having the effective emissivity values as a function of temperature for each wavelength will allow the calibration of DPV-2000 as a one-color pyrometer. Further work is required to determine if the values of $\alpha(\lambda_1)$ and $\alpha(\lambda_2)$ are a function of material and to test this approach over a wider range of droplet sizes and temperatures.

Summary

Diameter, velocity and radiant energy of falling droplets of copper were measured using a shadowgraph and a two-color pyrometer, DPV-2000. The measurements were performed at 10, 30 and 50 cm from the nozzle. DPV-2000 measured radiant energy at two different wavelengths on atomized copper droplets. A mathematical model of droplet cooling was developed and used to predict the particle temperatures at different heights. The temperature values from the model were used with the measured values of effective radiance intensity to estimate values of $\alpha(\lambda_1)$ and $\alpha(\lambda_2)$. Both of these values are proportional to the respective emissivities. It was found that the values of α were a function of temperature and wavelength. Using these values it is feasible to calibrate the DVP instrument and use it as a single color pyrometer.

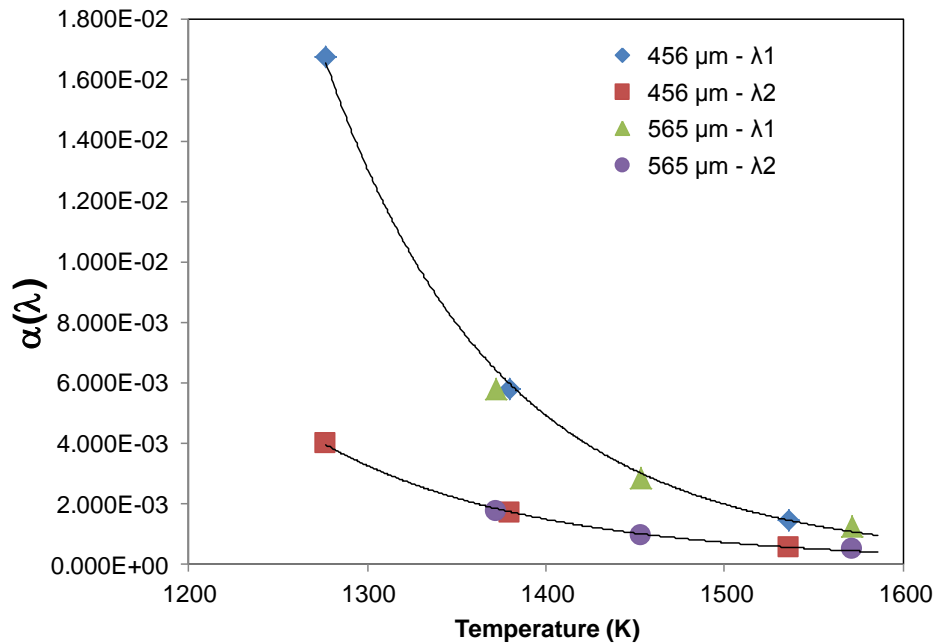


Figure 5. Effective emissivity, $\alpha(\lambda)$ as a function of temperature

Acknowledgments

The authors would like to thank Natural Sciences and Engineering Research Council of Canada (NSERC) and Canadian Space Agency (CSA) for the financial support and Nils Ellendt for the modeling.

References

- [1] A. Prasad et al., *ISIJ International*, Vol. 49 (2009), No. 7, 992.
- [2] A. Prasad and H. Henein, *Journal of Material Science*, Vol. 43 (2008), 5930
- [3] N. Zeoli, S. Gu and S. Kamnis, *International Journal of Heat and Mass Transfer*, Vol. 51, (2008), 4121
- [4] S. Whitaker, *AIChE*, Vol. 18(2), (1972), 361.
- [5] P. Delshad Khatibi et al., (Paper presented at ISPS 2011 Conference, Bonn, Germany, 2011).
- [6] J.P. Holman, *Heat Transfer*, (8th Edition, McGraw Hill Inc., 1997).
- [7] Tecnar Automation Ltée. DPV-2000 Calculation Principles, http://www.tecnar.com/images/stories/TSS/DPV/pdf/dpv_calculation_principles.pdf, Accessed: August 22, 2011

- [8] Y. Ding, H. Henein and Fallavollita, US Patent 5,609,919 (1997); Canadian Patent 2,147,407 (2003)
- [9] J.B. Wiskel et al., *Canadian Metallurgical Quarterly*, Vol. 41 (2), (2002), 193.
- [10] J.B. Wiskel, H. Henein and E. Maire, *Canadian Metallurgical Quarterly*, Vol. 41(1), (2002), 97.
- [11] J. Brillo and I. Egry, *International Journal of Thermophysics*, Vol. 24, (2003), 1155.

Electrodeposition of Metals in Microgravity Conditions

K. Nishikawa¹, T. Homma², E. Chassaing³, M. Rosso¹ and Y. Fukunaka^{2,4}

¹Laboratoire de Physique de la Matière Condensée, UMR CNRS 7643, Ecole Polytechnique, 91128 Palaiseau Cedex, France

²Dept. of Applied Chemistry, Waseda University, Japan

³IRDEP, UMR CNRS 7174, 6 quai Watier, 78401 Chatou Cedex, France

⁴JAXA, ISS Science Project Office, Tsukuba, Japan

E-mail: fukunaka@energy.kyoto-u.ac.jp

Abstract. Metal electrodeposition may introduce various morphological variations depending on the electrolytic conditions including cell configurations. For liquid electrolytes, a precise study of these deposits may be complicated by convective motion due to buoyancy. Zero-gravity (0-G) condition provided by drop shaft or parabolic flight gives a straightforward mean to avoid this effect: we present here 0-G electrodeposition experiments, which we compare to ground experiments (1-G). Two electrochemical systems were studied by laser interferometry, allowing to measure the concentration variations in the electrolyte: copper deposition from copper sulfate aqueous solution and lithium deposition from an ionic liquid containing LiTFSI. For copper, concentration variations were in good agreement with theory. For lithium, an apparent induction time was observed for the concentration evolution at 1-G: due to this induction time and to the low diffusion coefficient in ionic liquid, the concentration variations were hardly measurable in the parabolic flight 0-G periods of 20 seconds.

1. Introduction

Electrochemical interfacial phenomena in microgravity environments have not been paid much attention by electrochemical scientists and engineers. It is simply because of the apparently successful operated energy as seen even in the case of Apollo the 13th. However, the energy storage and power generation, as well as materials processing, may be planned in the international space station (ISS) and in the projects beyond ISS project after the year 2020. The study of electrochemical interfacial phenomena under microgravity conditions will be likely focused in the future.

Electrodeposition or electrochemical dissolution of metal in aqueous solution is a good subject for primary stage of microgravity electrochemical research. Its reaction mechanism is relatively well understood. Moreover, the electrochemical reaction rate can be easily controlled by changing the current density or potential. A transition from

smooth metal film to dendrite morphology is sometimes found. From the viewpoint of fundamental electrochemistry, dendritic electrodeposits may provide simple model systems to study Diffusion Limited Aggregation (DLA) phenomena. Furthermore, dendrite growth was intensively studied for practical reasons, because of its detrimental role in battery technology[2]. The surface flatness is a key issue to guarantee a longer reversibility of secondary battery during charging/discharging repetition. Thus, the coupling behavior between the morphological variations and ionic mass transfer rate must be indispensably understood.

However, for liquid electrolytes, and whatever the electrochemical system under concern, a precise study of dendrite growth mechanisms may be complicated by convective motion due to buoyancy: even in thin, quasi-two-dimensional horizontal cells with vertical electrodes, electrodeposition is accompanied by a gravity-induced fluid flow at the electrodes. This effect is due to the electrolyte stratification near both electrodes: it has been extensively studied in the recent literature, both theoretically [4-6] and experimentally [7-11]. Convective motion mixes the electrolyte and tends to homogenize the concentration. The effect depends on cell configuration, salt concentration, and current density [4]. This convection driven by buoyancy was shown to increase the instability of system [11]. Obviously, zero-gravity experiments [12] should give a straightforward mean to avoid this effect: apart from gravity, no other parameter is altered. However, these experiments are relatively difficult to work out and of short duration (around 2-25 s in the most affordable facilities: drop tower and parabolic flight).

JAMIC experiments are described at first in this paper. Then, we present a study of electrodeposition in the zero-gravity environment provided by parabolic flights. This project is supported by the Centre National d'Etudes Spatiales (CNES): it plans copper electrodeposition on copper electrode and lithium electrodeposition on Ni electrodes in the Airbus A300 from Novespace. During these flights, almost zero-gravity conditions are available over 20 to 25 seconds. The project includes the concentration measurements by laser interferometry, and similar but longer experiments performed at 1-G in the cathode over anode configuration. Both series of experimental results are to be compared with numerical calculations.

2. Experimental

2.1 JAMIC Drop Tower

A quasi two-dimensional electrolytic cell(Figure1) was used in JAMIC. A 1 mm

diam. disk cathode was placed at the center of the cell and a flat ring-shaped anode was placed at the outer edge. The thickness of the cathode made of 1 mm diam. copper wire was adjusted to $100\ \mu\text{m}$ by a polishing technique. The circular periphery area of this disk was used as the effective surface of the cathode. Copper foil of $100\ \mu\text{m}$ thickness was perforated to manufacture a flat ring-type anode with a 20 mm inner diam. Both electrodes were sandwiched by two sheets of slide glass. This electrolytic cell was filled with 0.9 M CuSO_4 aqueous solution. Electrolysis was carried out at relatively high and constant current densities in order that the interference fringe pattern would appear soon after starting the electrolysis. Thus, the diffusion layer grows in the radial direction.

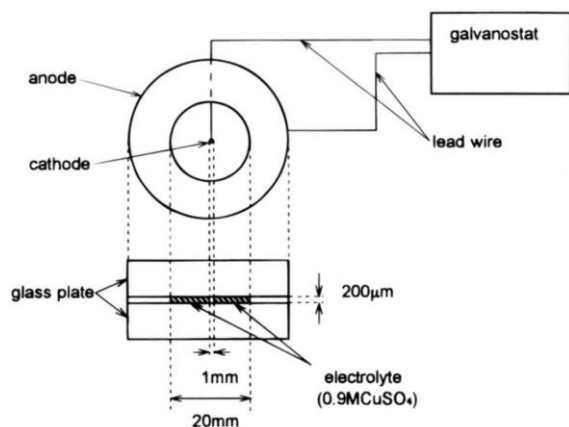


Figure 1. Quasi Two Dimensional Cell with Radial Diffusion Field

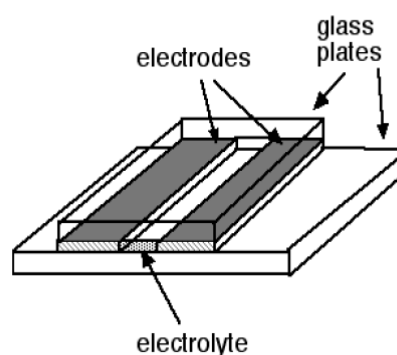


Figure 2 2-D Cell with Linear Diffusion Field

A common path microscopic interferometry was installed in JAMIC drop capsule. Laser diodes of 5 mW with 680 nm wavelength and a luminous light-emitting diode were used to observe the interference fringe pattern and the field image, respectively. The electrolytic cell was horizontally installed in this common path interferometry inside a drop capsule. The thickness of electrolyte solution in the cell was measured to be $200\ \mu\text{m}$, because both sides of cathode were coated for insulation with polyvinylchloride (PVC). The concentration dependence of refractive index of the electrolyte solution is $0.028\ \text{M}^{-1}$ and the resolution power of concentration was, therefore, $5.7 \times 10^{-2}\ \text{M}\ \text{CuSO}_4$ per fringe.

JAMIC drop capsule started to descend by gradually reducing the electromagnetic current. It was evacuated around the inner capsule, and the outer capsule was accelerated by injecting gas at an appropriate rate to compensate the friction of air inside the drop shaft. A microgravity level less than 10^{-4}G was thus attained 1 s after disengagement of the capsule. The descending capsule started to decelerate in the braking zone 10 s after free fall. It experienced about 8G as a maximum value. The

electrolysis was, therefore, initiated 1 s after the capsule had descended the shaft. Electrolysis was then terminated at 9 s in order to recover the sample electrodeposited only under microgravity conditions.

2.2 CNES Parabolic Flight

The project presented here consists in carrying out electrochemical experiments during zero-g periods provided by parabolic flights. The experiments are carried out in a pseudo 2 D-cell (Figure 2). Care is taken to obtain a well defined cell geometry: see Ref. [19] for details. Copper electrodes are used for the copper electrodeposition and nickel electrodes are for lithium electrodeposition: they are held between two glass plates enabling to observe *in-situ* the electrochemical cell.

The cell has a parallelepipedic shape, with dimensions L, the active length of the electrodes, *l*, the inter-electrode distance, and d, the thickness of the cell, respectively. Practical values are: L =0.8-1.5 cm, *l* ≈ 0.09 - 0.3 cm, d ≈ 0.012 - 0.1 cm. The lateral faces of the electrodes are coated with a hydrophobic film which limits the invasion of the electrolyte between the electrodes and the glass plates. After filling the cell with the electrolyte, it is sealed with a two-component resin before taking off: this allows to keep it under almost constant conditions for several hours [19]. During the flight, the temperature in the plane is kept at 18°C. Two electrochemical systems are studied: copper deposition from 0.1 and 0.2 mol L⁻¹ aqueous CuSO₄ solutions and lithium deposition from an ionic liquid. The ionic liquid is N-methoxymethyl-N-methylpyrrolidinium bis (trifluoro-methane-sulfonyl) imide containing 1.0 mol L⁻¹ LiTFSI.

In these microgravity experiments, a concentration variation of the electrolyte induced a variation of the refractive index which is measured by a common path laser interferometer. Laser interferometry is a well known technique for measuring the concentration changes in electrochemical processes [20-24]. This study use the interferometer described in Ref. [12] to measure *in-situ* the variations of ionic concentration in the electrolyte. Because a thin cells (0.1 or 1 mm) is used, we expect negligible light deflection due to refractive index gradients [25]. The laser source is a laser diode with 685 nm wavelength. The change in the refractive index is given by

$$d\Delta n = S\lambda \quad (1)$$

where d: the optical path length in the electrochemical cell (here the cell thickness), Δn :

the change of refractive index, S : the shift of interference fringes, and λ : the laser wavelength. The relationship between refractive index and concentration is given by:

$$\Delta n = \left(\frac{\partial n}{\partial C} \right) \Delta C \quad (2)$$

We use $(\partial n/\partial C) = 0.0279$ for a CuSO_4 aqueous solution and $(\partial n/\partial C) = 0.005$ for LiTFSI in ionic liquid. The transient behaviour of this shift is recorded with a CCD camera. Electrolytic condition is conducted at a constant current or a constant potential.

3. Results

3.1. Copper Electrodeposition in JAMIC Drop Tower

Figure 3 compares the time variation of interferograms recorded during the electrodeposition of copper at 0.2 A cm^{-2} from 0.9 M CuSO_4 solutions obtained under 1- and 0-G conditions. At 1 s after the start of electrolysis, a single fringe appears around the cathode under 1-G field, whereas no clear image of interference fringe is seen under 0-G. At 4 s, the annular fringe pattern under 1-G recedes from the cathode surface, and a fringe appears in the vicinity of the cathode surface under 0-G. After 8 s, two clear interference fringes with broader width are observed in 1-G experiments. At the same time, several fringes with narrower width appear within a distance of $100 \mu\text{ m}$ from the cathode surface under 0-G. It is difficult to count exactly the number of interference fringe with naked eye. The growth of annular interference fringe along the radial direction indicates the development of the diffusion layer of Cu^{2+} ions, when convection is not induced. The interferogram recorded at 15 s after the start of electrolysis is also illustrated. The electrolysis has already been terminated, and the capsule has started to decelerate. The less concentrated solution stays near the cathode and slightly concentrated electrolyte does near the anode (with larger surface area). The acceleration force starts to act upon the electrolyte. Then, the lighter electrolyte, constrained inside the diffusional layer adjacent to the cathode, begins to flow to induce a convection loop along two glass sheets. This is a reason why the radius of the annual interference fringe pattern suddenly increased.

In 1-G experiments, the fringes are observed at nearly constant intervals along the radial direction. The time variation of Cu^{2+} ion concentration at the cathode surface is compared with a transient diffusion model. It decreases much slower than the calculated value. The ionic mass-transfer rate from the bulk electrolyte to the cathode surface superimposed by the fluid flow induced even in such a quasi two-dimensional shallow electrolytic cell may partly contribute such a deviation as well as the optical

deflection error.

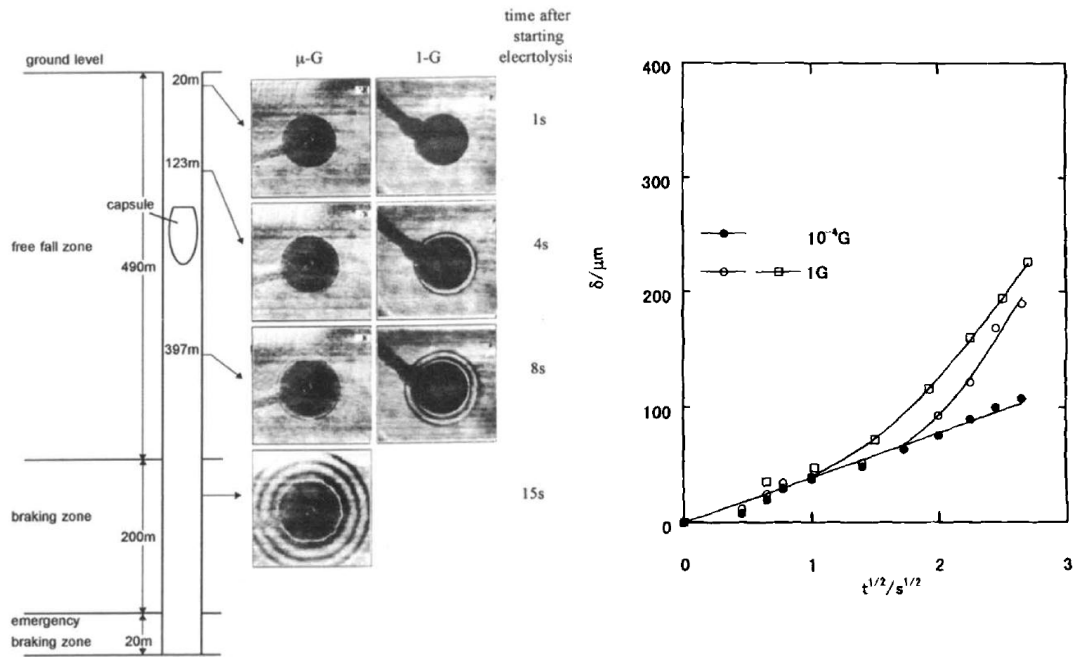


Figure 3 Transient Variations of Interference Fringes and Diffusion Layer Thickness with Progress of Cu Electrodeposition(0-G and 1-G) Followed by a Kind of Natural Convection Confined in Quasi-2D Cell in Decelerated Zone

The laser beam propagates in a straight line in the bulk electrolyte. Considering the resolution power of concentration in the present optical arrangement (0.057 M per fringe), the outer periphery of the diffusion layer may be conventionally defined as the position where the concentration is decreased by 3% of the bulk value. Thus, the time variation of the diffusion layer thickness can be reasonably measured. At 0.2 A cm^{-2} , the diffusion layer thickness increases proportionally to the square root of time in 0-G. The measured diffusion layer thickness in 1-G begins to deviate from this linearity at 1 or 3.2 s after the starting electrolysis, most probably due to induced natural convection.

The development of diffusion layer thickness under microgravity is analyzed based on the one-dimensional transient diffusion model including the migration effect. Although the physical properties of diffusivity and the transfer number vary with electrolyte composition, constant physical properties of diffusivity and the transfer number are assumed as a first-order approximation. A diffusivity of $5 \times 10^{-6} \text{ cm}^2 \text{ s}^{-1}$ and a cation transference number of 0.3 are found to give good agreement with measured thicknesses, which are very close to the reported values.²²

Figure 4 illustrates the potential difference between both electrodes. It almost stays constant at 620 mV for the first 3 s. It suddenly increases by 200 mV around 4 s, followed by a slight increase of potential difference in 0-G experiment, while the measured potential difference is slightly raised to 680 mV at 4 s and remained afterward under 1-G. The abrupt jump in the potential difference may be referred to the increase in concentration overpotential caused by depleted cupric ion at the cathode surface, since the calculated surface concentration of Cu^{2+} ion reached zero at 3 s. This behavior has been partly observed in the ground level experiment with a horizontal cathode over anode configuration. After the considerable concentration overpotential develops, copper grains grow in a dendritic manner (see Appendix below).

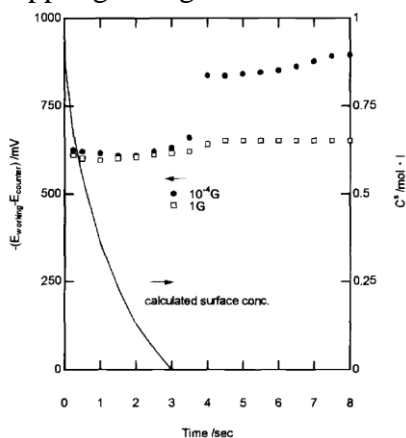


Figure 4 Time Variations of Potential Difference (0.9 M CuSO_4 , 0.3 A cm^{-2})

The effect of microgravity on the morphology of copper electrodeposited at 0.05 and 0.3 A cm^{-2} is seen in Figure 5. The electrolysis was conducted over 8 s under both environments. If copper could be precipitated densely and uniformly on the copper substrate without any voids, the average film thickness would be 0.17 and $1.0 \mu \text{ m}$, respectively. At ground level, a number of $0.5 \mu \text{ m}$ diameter grains is uniformly precipitated at both current densities. Since the averaged size of grains is close to the resolution power of the scanning electron microscope (SEM), it is difficult to distinguish any difference on the crystallographic aspect of each grain obtained at both current densities. These most likely grow in a three-dimensional nucleation manner.

Surprisingly, the significant difference of morphology of copper obtained at the same current density is noticed between 0-G and 1-G level experiments. Some grains grow with preferential growth of the lower index planes at both current densities. A similar difference is also noticed at 0.1 A cm^{-2} . At the low current density, the size of larger grains reaches about $2 \mu\text{m}$, which is about four times larger than that for the sample obtained at ground level. The preferential growth of lower index planes is more evident at the lower current density.

It is not clear why such a morphological difference is induced by the different level of gravitational acceleration. As shown above, the surface concentration of Cu^{2+} ion is more quickly lowered with time under microgravity, so long as the electrolysis conducted at the same current density. The main part of the cathode surface is thus exposed to the electrolyte with lower concentration of Cu^{2+} ion under microgravity. If we assume that the three dimensional nucleation rate becomes low with decreasing in the surface concentration of Cu^{2+} ion, we obtain fewer nuclei on the cathode under microgravity. When the electrolysis is conducted to produce the same amount of charge, more coulombic charge should be distributed on the particular grain to introduce the larger-sized grains.

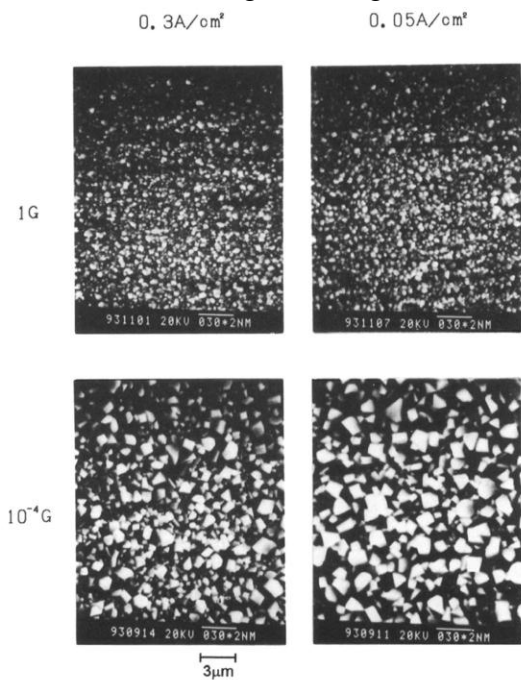


Figure 5. Comparison of Morphology of Copper Electrodeposited in Terrestrial and Microgravity Experiment: Scratched Traces by Sandpaper are Visible on Cu Disk Substrate Surface with $100 \mu\text{m}$ Thickness. (0.9M CuSO_4 Aqueous Solution, Electrodeposition Duration Period of 8s, 0.05 and 0.3 A cm^{-2})

However, the electrical conductivity is simultaneously reduced with lowered concentration of Cu^{2+} ions near the cathode. It may considerably influence the ionic mass transfer rate due to the migration effect.²⁵ Thus, the concentration gradient of Cu^{2+} ion near the cathode is no longer the same as that observed at the initial stage of

electrolysis. Further measurement of Cu^{2+} ion concentration profile is necessary to understand the morphological variations introduced by the different level of the gravitational acceleration force.

3.2. Electrodeposition of Metals in Parabolic Flight

3.2.1 Copper Electrodeposition

The concentration profile in the electrolyte for various current density and bulk concentrations were measured. Figure 6 shows an example of interference fringes recorded before and 15 seconds after the beginning of cell polarization. The fringes are bent in the vicinity of the cathode, at the bottom of the Figure, because of the variation of concentration. These concentration variations were also numerically calculated, using general equations describing transport phenomena in electrochemical systems [30], and taking into account the variation of the diffusion coefficients with concentration in CuSO_4 aqueous solution [31]. The time variation of surface concentration during and after one parabola is shown in Figure 7, and compared with theory. A good agreement between experimental and theoretical results was found. After the end of the parabola, the concentration at the cathode rapidly returned to its initial value: this was due to the large G ($\sim 1.5\text{G}$) imposed at this time in order to drive back the plane to its normal flying conditions.

We have reported elsewhere [28] the concentration measurements obtained in 1-G conditions in a C/A cell. A similar agreement with theory was found for measurements performed before the onset of dendritic growth. On the other hand, in experiments performed in horizontal cells [4, 7-10], the concentration variations were markedly different.

We did not observe dendritic growth of copper, however, because the dendrites only appear after an induction time t_s , the so-called Sand time [29]. Sand time varies as

$$t_s = \frac{\pi e^2 D (1 + \mu_c / \mu_a) C_0^2}{J^2} \quad (3)$$

where e is the electronic charge, D the diffusion constant, μ_c and μ_a the cationic and anionic mobilities respectively, C_0 is the initial ionic concentration and J the current density. To obtain a Sand time shorter than 10 seconds for example, would require a high current density (larger than 20 mA cm^{-2}) and still, the time available for observing dendritic growth would be very short. Experimental environment did not provide such conditions in this parabolic flight campaign. Further experiments are thus necessary to explore dendritic growth itself.

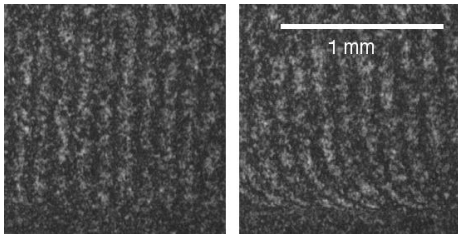


Figure 6. Interference Fringes before of and 15 s after Cu Electrodeposition. (0.1 mol L^{-1} ; 8 mA cm^{-2} ; Cell Thickness is 0.1 cm.)

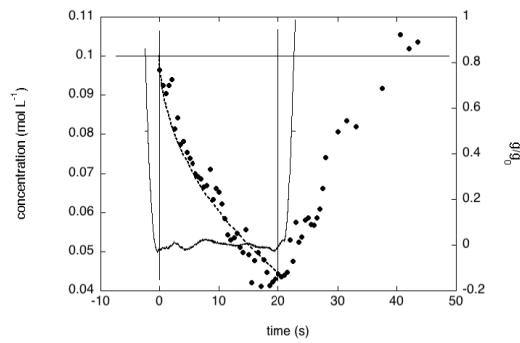


Figure 7. Surface Concentration Variations Cu^{2+} Ion during Parabolic Flight (Closed Circles: Measured, Dashed Line: Calculated)

3.2.2. Lithium Electrodeposition

As mentioned earlier, a series of experiments were performed at 1-G. A typical result is given in Figure 8, showing the variation of the cathode surface concentration as a function of the square root of time. In this experiment, the applied current density is 1 mA cm^{-2} and cell thickness is $d = 0.1 \text{ cm}$. One clearly sees a first stage, where the concentration variation is very small. Then, after 90 s, the variation is much more rapid. Such an induction time was already reported [16]. In the present case, the observed induction time might be due to side reactions of the electrodeposited lithium metal. The diffusion coefficients in the ionic liquids are very low: from the variation of the diffusion layer thickness in the experiment illustrated in Figure 8, we estimated a diffusion coefficient $D \sim 10^{-7} \text{ cm}^2 \text{ s}^{-1}$. This value is in good agreement with that reported by other methods [32]. The concentration variations are compared in Figure 8 with theoretical values [30], which are calculated without taking into account the concentration dependence of the diffusion coefficient. The result obtained for the above value of D and a transport number of 0.35 for Li^+ ion is shown in Figure 8 as a straight continuous line.

Due to the very low diffusion coefficient and to the induction time mentioned above, the concentration variations due to Li deposition during the first 20 seconds are very small, and the concentration boundary layer thickness is at most $10 \text{ }\mu\text{m}$: thus concentration variations are hardly detectable by our interferometer. The Li deposition experiment would thus require longer zero-g times.

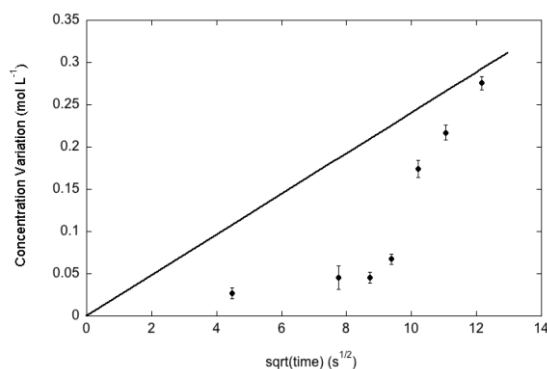


Figure 8. Li Electrodeposition in Ionic Liquid: Time Variations of Cathode Surface Concentration with Electrolysis(Experimental: Circles, Calculated: Straight Line).

4. Conclusion

A common path microscopic interferometry was used in a drop shaft experiment. The growth of the diffusion boundary layer of Cu^{2+} ions associated with electrodeposition of copper in CuSO_4 solution was successfully measured in situ under microgravity. When the electrolysis is conducted at 1-G, natural convection is induced even in such a shallow electrolyte layer of $200 \mu\text{m}$ thick. Measurements of voltage drop between both electrodes show the abrupt increase in potential difference, just after the surface concentration of Cu^{2+} ion reaches zero under 0-G. A significant difference of morphology appears after only 8s of electrodeposition at constant current density. Larger grains with preferential growth of lower indexes are obtained in 0-G. The coupling effect of the diffusion and migration mechanism to the electrocrystallization phenomena under 0-G must be further examined. It is necessary to monitor the transient variation of cathodic overpotential with the progress of electrodeposition.

Although of limited duration, parabolic flight experiments can provide interesting results on the early stage of electrodeposition. The evolution of concentration profiles is consistent with the theoretical calculation curves. However, a more complete study would require further zero-g experiments: for studying dendritic growth of copper, or for deposition of lithium from ionic liquids, longer times would be necessary (such as those available in sound rockets or in the International Space Station). These improvements are considered in the framework of a project developed by an “Electrochemical Nucleation & Growth” ESA Topical Team.

5. References

- [1] Witten T A and Sander L M 1981 *Phys. Rev. Lett.* **47** 1400
- [2] Tarascon J-M and Armand M 2008 *Nature* **451** 652

- [3] Laitinen H A and Kolthoff I M 1939 *J. Am. Chem. Soc.* **61** 3344
- [4] Chazalviel J-N, Rosso M, Chassaing E and Fleury V 1996 *J. Electroanal. Chem.* **407** 61
- [5] Marshall G, Mocskos P, Swinney H L and Huth J M 1999 *Phys. Rev. E* **59** 2157
- [6] Kawai S, Nishikawa K, Fukunaka Y and Kida S 2007 *Electrochim. Acta* **53** 257
- [7] Rosso M, Chazalviel J-N, Fleury V and Chassaing E 1994 *Electrochim. Acta* **39** 507
- [8] Barkey D P, Watt D, Liu Z and Raber S 1994 *J. Electrochem. Soc.* **141** 1206
- [9] Huth J M, Swinney H L, Mc Cornmick W D, Kuhn A and Argoul F 1995 *Phys. Rev. E* **51** 3444
- [10] Argoul F, Freysz E, Kuhn A, Léger C and Potin L 1996 *Phys. Rev. E* **53** 1777
- [11] Marshall G, Mocskos E, González G, Dengra S, Molina F V and Iemmi C 2006 *Electrochim. Acta* **51** 3058
- [12] Fukunaka Y, Okano K, Tomii Y, Asaki Z and Kuribayashi K 1998 *J. Electrochem. Soc.* **145** 1876
- [13] González G, Marshall G, Molina F and Dengra S 2002 *Phys. Rev. E* **65** 051607
- [14] Marshall G, Perone E, Tarela P and Mocskos P 1995 *Solitons and Fractals* **6** 315
- [15] Sagués F, López-Salvans M Q and Claret J 2000 *Phys. Reports* **337** 97
- [16] Nishikawa K, Fukunaka Y, Sakka T, Ogata Y H and Selman J R 2007 *Electrochim. Acta*, **53** 218
- [17] González G, Rosso M, Chassaing E and Chazalviel J-N 2007 *Electrochim. Acta* **53** 141
- [18] Morisue M, Fukunaka Y, Kusaka E, Ishii R and Kuribayashi K 2003 *J. Electroanal. Chem.* **559** 155
- [19] Rosso M, Chassaing E, Chazalviel J-N and Gobron T 2002 *Electrochim. Acta* **47** 1267
- [20] McLarnon F R, Muller R H and Tobias C W 1976 *Electrochim. Acta* **21** 101
- [21] Denpo K, Okumura T, Fukunaka Y and Kondo Y 1985 *J. Electrochem. Soc.* **132**, 1145
- [22] Eriksson R 1995 *Electrochim. Acta* **40** 725
- [23] Konishi Y, Tanaka Y, Kondo Y and Fukunaka Y 2000 *Electrochim. Acta* **46** 681
- [24] Fukunaka Y, Nakamura Y and Konishi Y 1998 *J. Electrochem. Soc.* **145** 3814
- [25] Beach KW, Müller R H and Tobias C W 1973 *J. Opt. Soc. Am. A* **63** 559
- [26] Hawkes J B, Astheimer R W 1948 *J. Opt. Soc. Am.* **38** 804
- [27] Nishikawa K, private communication
- [28] Nishikawa K, Chassaing E and Rosso M 2011 *Electrochim. Acta* **56** 5464
- [29] Sand H J S 1901 *Phil Mag* **1** 45

- [30] Marciano S L and Arvia A J 1983 Diffusion in the absence of convection: steady state and nonsteady state *Comprehensive Treatise of Electrochemistry* Ed Yeager E, Bockris J O'M, Conway B E, Sarangapani S (New York: Plenum Press) vol.6, pp. 65-132,
- [31] Miller D G, Rard J A, Eppstein L B and Robinson R A 1980 *J. Solution Chem.* **9** 467
- [32] Nishikawa K, Naito H, Kawase M and Nishida T 2011 *Lithium Batteries Discussion* Arcachon (France)

6. Acknowledgements

The authors thank Drs. H. Yasuda (Osaka University), Y. Inatomi (Japan Aerospace Exploration Agency - JAXA), K. Kinoshita (JAXA), M. Takayanagi (JAXA), S. Yoda (JAXA) and T. Maki (Olympus Corporation), for providing the interferometer especially designed for zero-g experiments that we used in this study. The authors also wish to thank Dominique Clément for the mechanical realization of the experimental setup and for the many technical solutions which he brought to the problems involved in the operation of this experiment in parabolic flight. Centre National d'Etudes Spatiales is acknowledged for its financial support and Novespace for help in preparing the experiments.

PROPAGATION REGIME OF IRON DUST FLAMES

François-David Tang¹, Samuel Goroshin², Andrew J. Higgins²

¹European Space Agency, ESTEC; Kaplerlaan 1, Noordwijk, The Netherlands

²McGill University, Department of Mechanical Engineering
817 Sherbrooke St. West, Montreal, Quebec, Canada

Keywords: Iron powder, Combustion, Reduced gravity

Abstract

A flame propagating through an iron-dust mixture can propagate in two asymptotic regimes. When the characteristic time of heat transfer between particles is much smaller than the characteristic time of particle combustion, the flame propagates in the continuum regime where the heat released by reacting particles can be modelled as a space-averaged function. In contrast, when the characteristic time of heat transfer is much larger than the particle reaction time, the flame can no longer be treated as a continuum due to dominating effects associated with the discrete nature of the particle reaction. The discrete regime is characterized by weak dependence of the flame speed on the oxygen concentration compared to the continuum regime. The discrete regime is observed in flames propagating through an iron dust cloud within a gas mixture containing xenon, while the continuum regime is obtained when xenon is substituted with helium.

Introduction

While the combustion of powdered metals is typically associated in solid-fueled rockets, metallic fuels have recently been suggested as a potential energy carrier for transport vehicles as a sustainable alternative to fossil fuels [1]. To exploit these applications, a fundamental understanding of the metallic dust flames is essential, but experimental results on fundamental flame parameters are scarce. As a result, current models of laminar flames propagating in heterogeneous media are simply based on a continuum assumption, which underlines the fact that the interparticle spacing l_p is much smaller than the flame width l_d . This assumption permits the function describing the heat release in the reaction zone to be described as a continuous function in space and the governing equations to be expressed as a set of partial differential equations [2,3].

However, if the interparticle distance l_p is on the same order of magnitude as the flame width l_d , then the continuum fails to describe the propagation of the flame. The flame exhibits so-called discrete characteristics where the propagation of the front is dominated by local ignition interactions between neighboring particles. The heat release function becomes dependent on the spatial distribution of the particles and the flame can no longer be described by the continuum theory [4,5]. The parameter quantifying the regime of propagation is the dimensionless combustion time defined as:

$$\tau_c = \frac{t_r \alpha}{l^2}, \quad (1)$$

where t_r is the characteristic particle reaction time, α is the thermal diffusivity of the gas mixture and l is the interparticle spacing. The discrete regime is realized when $\tau_c < 1$, while the continuum is when for $\tau_c \gg 1$ [5].

In this work, the discrete regime is realized in an experiment where flames propagating through clouds of iron particulates are observed in low-thermal diffusivity, oxidizing environment, namely xenon-oxygen. In contrast, the continuum regime is achieved in a helium-oxygen mixture, which is characterized by a high thermal diffusivity. The continuum and discrete regimes are differentiated using the response of the flame speed to variations of the oxygen concentration.

Experimental Details

The dust combustion experiment uses a flame in an open-ended tube methodology that allows observation of a constant-pressure laminar flame. Experiments were performed onboard a reduced-gravity parabolic flight aircraft to minimize particle settling and buoyancy-induced convective flows. The schematics of the apparatus are shown in Fig. 1.

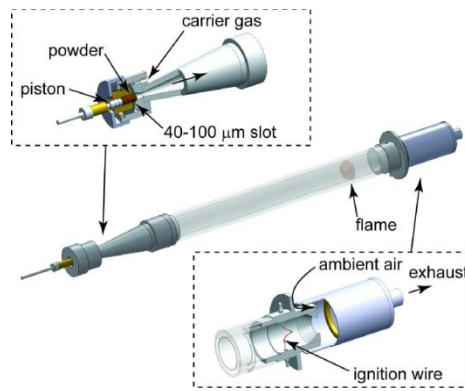


Figure 1: Schematic of the dust combustion experiment. The top left inset illustrates the design of the dust dispersion system and the bottom right inset the design of the first stage cooling and filtering systems.

The powder dispersion unit (see top inset in Fig. 1) consists of a dust feeder and a disperser. The initially compacted dust is fed via a small syringe-type device. As it is fed by the piston, the dust column is continuously dispersed via the impact of a transverse sonic gas jet produced by a 40-100 μm circular slot at the base of the conical dispersion chamber (see top inset in Fig. 1). The conical diffuser connecting the dust dispersion unit with the combustion tube provides expansion and laminarization of the initially highly turbulent flow containing the dispersed dust. The combustion tube is a Pyrex glass tube with an internal diameter of 48 mm and 70 cm in length. The fuel suspension was ignited by an electrically heated, 100- μm -diameter tungsten wire at the open end of the tube, with the flame propagating toward the closed end (dispersion system).

The fuel concentration in the suspension is controlled by varying the piston speed via an electromechanical linear actuator. The fuel concentration in the suspension can be calculated from the feeding rate of the piston, the packing density of the powder and the flow rate of the dispersing gas. The mass concentrations of iron powder varied in a range of 900-1,200 g/m^3 .

The exhaust from the combustion tube is passed through a series of cooling and filtering systems and ultimately discharged into the aircraft cabin to accommodate the absence of overboard vents. The combustion products were drawn into the inlet of the cooling and filtering system by a vacuum blower. A wide annular opening between the combustion tube and the filtering system

(see Fig. 1, right bottom inset) ensures unobstructed access of the ambient air to maintain ambient pressure inside the combustion tube.

The combustion rack installed onboard the airplane contains four replaceable combustion tube assemblies (see Fig. 2). Each assembly is comprised of a combustion tube integrated with an individual powder dispersion unit. Four tube assemblies are mounted horizontally parallel to each other on the combustion rack, providing an unobstructed view for the optical diagnostics.



Figure 2: Photograph of the dust combustion apparatus installed on board parabolic flight aircraft.

The propagation of the flame was recorded by a high-speed digital camera viewing the entire length of the combustion tube at 300 frames per second.

The use of iron, that burns entirely in the condensed phase was motivated to ensure that the reaction occurred in the absence of the formation of vapors in the attempt to reflect the heterogeneous characteristics of the modeling. Five different iron powders were used in this investigation and are designated A to D in the Table I. Scanning electron microscope photographs of the iron powders are shown in Fig. 3.

Table I: Characteristics of iron powders used.

Powder	Particle shape	Purity	d_{10} (μm)	d_{32} (μm)
(a)	Spherical	99.9	3.3	4.3
(b)	Spherical	99.5	7.0	9.6
(c)	Spherical	99.5	9.9	13.7
(d)	Spherical	99.9	26.8	44.7

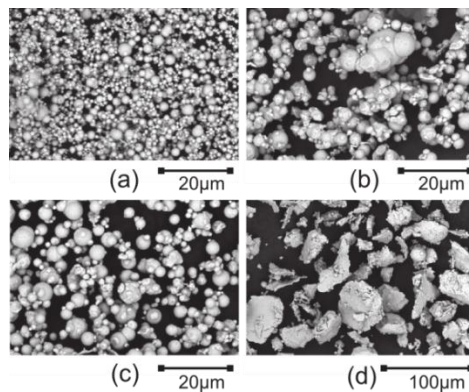


Figure 3: Scanning Electron Microscope (SEM) pictures of iron particles.

The experiments were performed using four separate gas mixtures containing helium or xenon at 21% and 40% oxygen concentration. The mixtures were supplied by a commercial gas supplier and were certified to be within an accuracy of 2%.

Results

The measured flame speeds from experiments performed in xenon and helium with 21% and 40% oxygen concentration are shown in Fig. 4. The flame speeds were obtained from the analysis of the high-speed videos. The error bar represents the standard deviation from 5 to 11 repeated measurements performed with the same gas mixture.

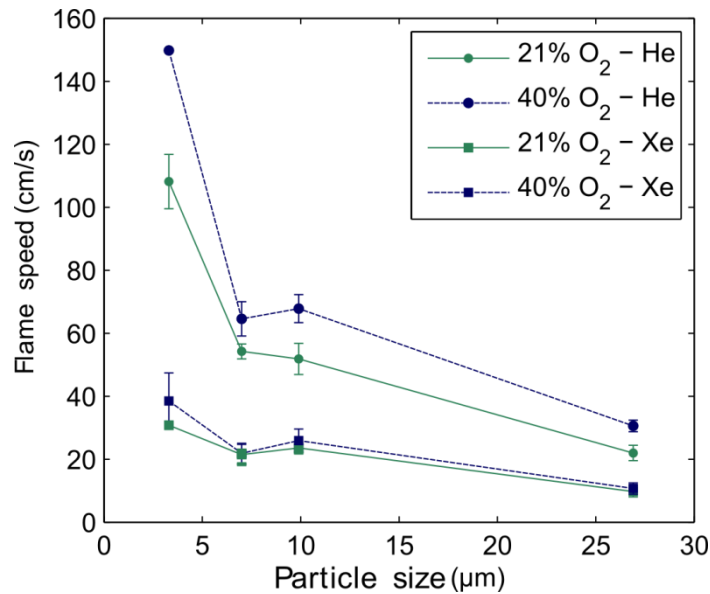


Figure 4: Flame speed measurements for iron powders A, B, C and D in He-O₂ and Xe-O₂ in 21% and 40% oxygen concentrations.

The flame speed is consistently larger in mixtures containing 40% compared to 21% oxygen. However, the difference is more pronounced in mixtures containing helium, compared to mixtures containing xenon.

Discussion

The ratios between the flame speeds in 40% and 21% oxygen concentration are shown in Fig. 5 for helium- and xenon-balanced mixtures and for the different particle sizes. The ratios corresponding to measurements performed in xenon mixtures are consistently lower than those for helium mixtures for all particle sizes. These measurements highlight the fact that flames propagating in xenon mixtures are less sensitive to variations of the oxygen concentration C_{O_2} compared to flames in helium mixtures.

Using the shrinking core model of particle combustion, the oxygen concentration C_{O_2} is related linearly to the particle combustion time t_r ($C_{O_2} \sim t_r$) [6]. Hence, flame speeds measured in xenon mixtures are less sensitive to changes of the particle reaction time t_r compared to mixtures containing helium.

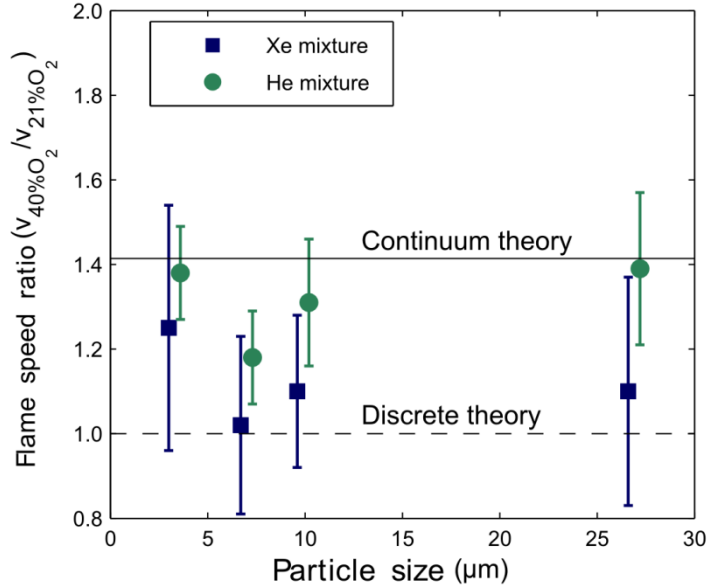


Figure 5: Ratio of the flame speeds between 21% and 40% O₂ in helium and xenon mixtures.

The stronger dependence of the flame speed on the reaction time t_r in mixtures containing helium compared to mixtures balanced with xenon can be attributed to a transition of the propagation regime from continuum to discrete. When substituting the balance inert gas from helium to xenon in 21% O₂, the dimensionless combustion time τ_c decreases from approximately 3.4 (continuum) to 0.6 (discrete).

Previous numerical work has shown that the discrete regime is characterized by a front speed that is independent of the reaction time t_r [7]. In other words, variations of the oxygen concentration do not affect the flame speed in the discrete regime. The flame speed ratio characteristic of the discrete regime reflects the insensitivity of the flame speed on the reaction time t_r :

$$\left. \frac{v_{40\%O_2}}{v_{21\%O_2}} \right|_{disc.} = 1. \quad (2)$$

The distinctive relationship between the flame speed and the reaction time t_r in the discrete regime is in sharp contrast with the front speed predictions in a continuum. Using thermal theory, the flame speed v is expected to vary with the reaction time t_r as $v \sim 1/\sqrt{t_r}$ [8]. This behavior results in a ratio of the flame speeds $v_{40\%O_2}/v_{21\%O_2}$:

$$\left. \frac{v_{40\%O_2}}{v_{21\%O_2}} \right|_{cont.} = \sqrt{\frac{t_r(21\%)}{t_r(40\%)}} = \sqrt{\frac{40}{21}} \approx 1.4. \quad (3)$$

In the discrete regime, the fact that flames exhibit a different behavior to change of the oxygen concentration from the predictions of the thermal theory highlights the breakdown of the continuum assumption. In the discrete regime, the heat release around particles becomes

localized to the point that the propagation of the flame becomes limited by the heat diffusion between neighboring particles. When the flame is controlled mainly by heat diffusion, the increase of the reaction rate of particles does not cause an increase of the flame speed.

In contrast, in a continuum, the limiting mechanism is assumed to be the particle reaction rate. This assumption underlines the fact that the reaction rate is treated as continuous function in space, where particles form a dense cloud of particles characterized by an interparticle spacing much smaller than the flame width.

Conclusion

The regime of propagation was investigated by varying the transport properties of the gas mixture as a means to change the dimensionless combustion time. Reduced experiments were performed in xenon- and helium-balanced mixtures to observe discrete and continuum flames, respectively. It was found that flames propagating in xenon-balanced mixtures were less sensitive to the oxygen concentration than flames propagating in helium-balanced mixtures. This observation reflects the distinct behavior of the flame propagation between the discrete and the continuum regimes.

Acknowledgement

This work was supported under Canadian Space Agency contract 9F007-052073/001/ST. The authors would like to thank the Flight Research Laboratory of the National Research Council of Canada.

References

1. K. Kleiner, "Powdered Metal: The Fuel of the Future," *New Scientist*, 2522 (2005), 34-
2. S. Goroshin, M. Bidabadi, J.H.S. Lee, "Quenching Distance of Laminar Flame in Aluminum Dust Clouds," *Combustion and Flame*, 105 (1996), 147-160.
3. A.G. Merzhanov, E.N. Rumanov, "Physics of Reaction Waves," *Reviews of Modern Physics*, 71 (1999), 1173-1211.
4. J.M. Beck, V. Volpert, "Nonlinear Dynamics in a Simple Model of Solid Flame Microstructure," *Physica D*, 182 (2003), 86-102.
5. S. Goroshin, J.H.S. Lee, Y. Shoshin, "Effect of the Discrete Nature of Heat Sources on Flame Propagation in Particulate Suspensions," *Symposium (International) on Combustion*, (27) 1998, 743-749.
6. J.C. Yang. "Heterogeneous Combustion," *Environmental Implications of Combustion Processes*, ed. I.K. Puri (Boca Raton, FL: CRC Press, 1993), 127-128.
7. S. Goroshin, F.D. Tang, A.J. Higgins, "Reaction-diffusion fronts in media with spatially discrete sources," *Physical Review E*, 84 (2011), 027301.
8. L.P. Yarin and G. Hetsroni, *Combustion of Two-Phase Reactive Media* (Berlin: Springer-Verlag, 2004), 301.

Containerless Processing on ISS: Ground Support Program for EML

Angelika Diefenbach¹, Stephan Schneider², Rainer Willnecker¹

¹DLR Microgravity User Support Centre, Linder Hoehe, 51149 Cologne, Germany

²DLR, Institute for Material Sciences in Space, Linder Hoehe, 51149 Cologne, Germany

Keywords: electromagnetic levitation, containerless processing, reduced gravity, experiment preparation

Abstract

EML is an electromagnetic levitation facility planned for the ISS aiming at processing and investigating liquid metals or semiconductors by using electromagnetic levitation technique under microgravity with reduced electromagnetic fields and convection conditions. Its diagnostics and processing methods allow to measure thermophysical properties in the liquid state over an extended temperature range and to investigate solidification phenomena in undercooled melts.

The EML project is a common effort of The European Space Agency (ESA) and the German Space Agency DLR. The Microgravity User Support Centre MUSC at Cologne, Germany, has been assigned the responsibility for EML operations. For the EML experiment preparation an extensive scientific ground support program is established at MUSC, providing scientific and technical services in the preparation, performance and evaluation of the experiments. Its final output is the transcription of the scientific goals and requirements into validated facility control parameters for the experiment execution onboard the ISS.

Motivation for electromagnetic processing in space

Containerless processing in the earth laboratory is an attractive way to provide high-purity environment to high-temperature or highly reactive materials. It is particularly suited to give access to the meta-stable state of an undercooled melt. In the absence of container walls, the nucleation rate is greatly reduced and high levels of undercooling can be obtained. Electromagnetic levitation is also suited for the in-situ study of properties of metallic melts. It allows to levitate bulk samples of several grams at high temperatures (well above 2000°C) and to measure the thermophysical properties of freely suspended liquid melts.

However, there are limitations to terrestrial electromagnetic levitation, due to sample deformation, turbulent currents and high process temperatures caused by the required high electromagnetic fields. Most of these effects can be avoided if performing electromagnetic levitation under reduced gravity conditions.

For the electromagnetic positioning of a sample against external residual forces in the microgravity environment, only weak field strength is required. Therefore, disturbances of the liquid sample by the magnetic field such as stirring or shape deformation are avoided. It becomes possible to reach very low process temperatures and to access deep levels of undercooling, respectively. Furthermore, thermophysical data of materials can be derived over a large temperature range including the undercooling regime.

EML Payload and Experiment Overview

The electromagnetic levitation Facility EML is planned to fly in the Columbus Module of the International Space Station in ESA's European Drawer Rack. The EML accommodation in EDR

is depicted in Fig. 1. EML is a successor of the German payload TEMPUS, which has been successfully flown on the Spacelab Missions IML-2, MSL-1 and MSL-1R. In recent years, EML development models have repeatedly been flown on parabolic flight and TEXUS missions.

The EML facility is equipped with the so called SUPOS (Superpositioning) coil system, which allows to decouple heating and positioning of the sample. Several diagnostics are available for the experiment performance. From the top, the temperature is measured with a pyrometer and two digital video cameras are used for the process control and scientific aims. The side view camera is a high speed camera and will be used for frames rates up to 30 kHz.

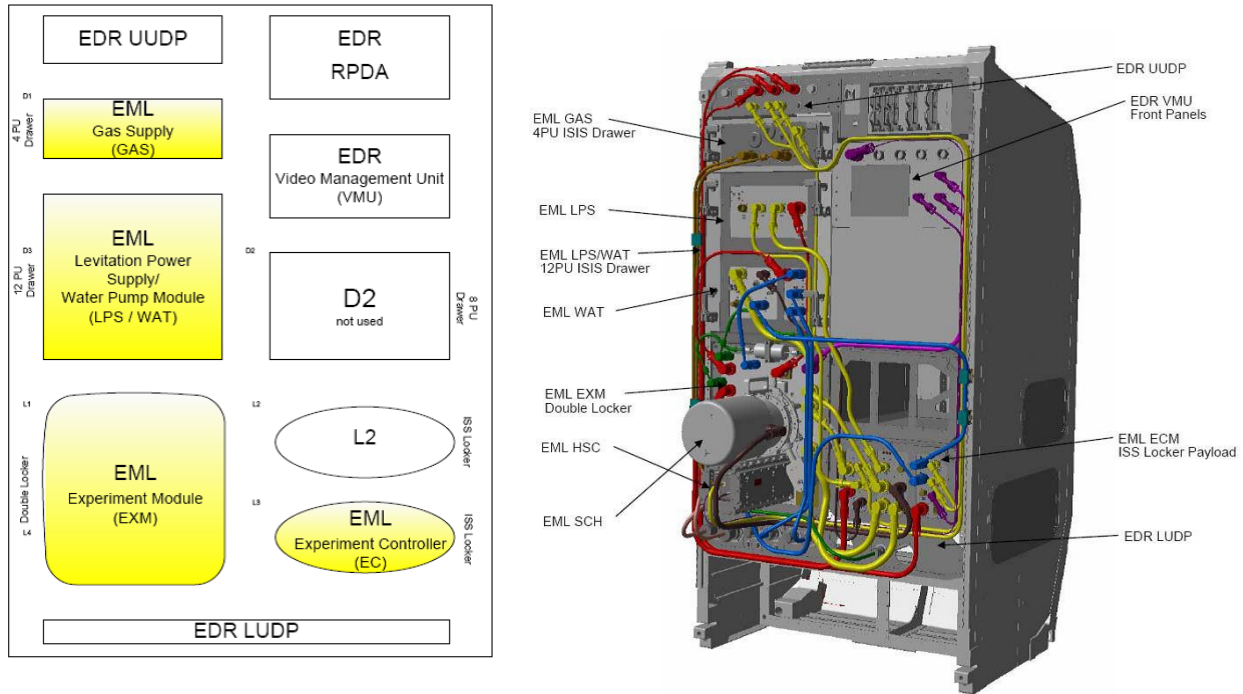
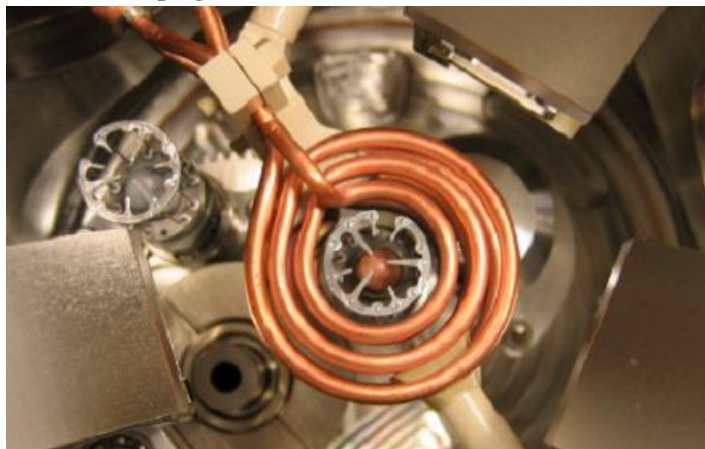


Fig. 1: EML Accommodation in European Drawer Rack (figures provided by Astrium)

Fig. 2: EML coil and CuCo sample in a sample holder (TEXUS campaign)



The planned experiments cover two major groups measurement of thermo-physical properties (viscosity, surface tension, density, thermal expansion, etc.) and solidification. For investigation of the sample solidification the solidification can be triggered at an aimed undercooling level, the growth velocity of the solidification front can be measured via the high speed camera and after the experiment the micro-structure of the in microgravity solidified sample can be analyzed.

EML is able to process liquid metals or doped semiconductors containerless by the electromagnetic levitation technique in the range of 600 to 2000°C. The absence of gravity allows to decouple heating and positioning and to work under an environment with reduced

electromagnetic fields and convection conditions. The experiments are divided into the following classes:

Class A: Undercooling and solidification speeds

Measurement of undercooling temperature (with pyrometer)

Measurement of solidification velocity with optional high-speed video

Triggering of solidification by touching the undercooled sample with a nucleation trigger needle (part of sample holder)

Class B: Heat capacity, effective thermal conductivity, enthalpies, solid fraction

Modulation of the heating input power into the sample, measure temperature response

Measurement of the electrical power loss to the sample

Class C: Surface tension and viscosity

Pulsing the heating field to induce surface oscillations in the molten sample to observe surface oscillation frequencies and decays by video cameras

Class D: Thermal expansion

Measure the sample size with video cameras using subpixel resolution techniques

Class E: Electrical conductivity

Measure electrical data of the levitation system and optionally additional electrical diagnostic circuits to detect the changes of the coupling between the RF magnetic fields with sample temperature.

All experiment classes require an ultra clean processing environment in form of either ultrahigh vacuum or high purity noble gas atmosphere at reduced pressure inside the hermetically tight process chamber.

EML Operations Overview

As an ESA payload, EML will be operated by the Microgravity User Support Center in Cologne, Germany, which is one of the nine User Support and Operation Centers (USOCs) in Europe. The European USOCs are responsible for the different ESA racks and experiments onboard the International Space Station. The tasks of the USOCs are to prepare on-orbit operations, conduct these and also act as a link between the responsible investigators and the experiments. Before the experiments are operated the ground segment has to be prepared and procedures need to be developed and validated. These depend on the experiment and can also involve the scientists as to what they want to achieve. Another important task is to support the crew training that has to happen on ground long before the actual experiment takes place. During on-orbit operations it is the USOCs responsibilities to receive telemetry from “their” payloads and send the necessary telecommands to perform the experiments. Also the scientists get their data usually from the USOCs.

EML will be integrated in Columbus Rack EDR. This drawer rack will be operated from the ERASMUS USOC in Noordwijk. Both USOCs are part of the established ESA Ground Segment in which MUSC acts as the Center responsible for EML operation. As such MUSC is responsible for planning and preparation of the EML on-orbit activities and for executing these and ERASMUS, as Facility Responsible Center for the EDR Rack, provides the single point-of-contact for all EDR real-time operations.

EML is planned for an in-orbit lifetime of 6 batches with 18 samples each, shared between a broad international scientific community. For the first batch of experiments, ten research teams are planning for 36 individual investigations, all requiring multiple melt and solidification cycles on one sample.

Data services to and from EML (Commanding, Telemetry and file uplink) are based on the utilization of the standardised systems available to all European USOCs - customised for EML requirements. In that scenario, MUSC will be responsible for the operation preparation for the experiments in EML, e.g. the development of crew and ground command procedures and all additional operational products (e.g. ground displays) needed to perform the experiments onboard the ISS.

For the operation of the latest parabolic flight and sounding rocket campaigns, MUSC has developed an EML specific evaluation software for science telemetry and video which is already in use during current campaigns. With this software – TeVi – the scientists can monitor the video and housekeeping data of his experiments in parallel. For the process analysis the video data can be displayed in slow motion or frame by frame synchronously with the sample and facility data. A subroutine for the oscillation analysis of oscillating samples was added. It allows to measure the edge of the sample and to calculate two perpendicular radii, the area, center of mass etc. of the sample for each frame. From this data viscosity and surface tension data can be derived. A FFT from a selected region of the data can be performed and the oscillation frequency measured. In a further step the surface tension is calculated from the oscillation frequency. Fig. 3 shows screen shots of the TeVi tool for a parabolic flight experiment.

The EML data are archived in a data archive based on the Hypertest platform. This archive was adapted to the structure of EML data and archives, video and facility data and documents from the historic missions. The data are stored together with metadata, which enables the user to search the data after sample material, principal investigator, campaign etc. The data can be distributed easily and fast via this archive and can be downloaded into the TeVi tool. The archive serves also as long term data archive fulfilling ESA and DLR data holding policies.

The existing tools will be adapted to serve the science teams during EML ISS operations.

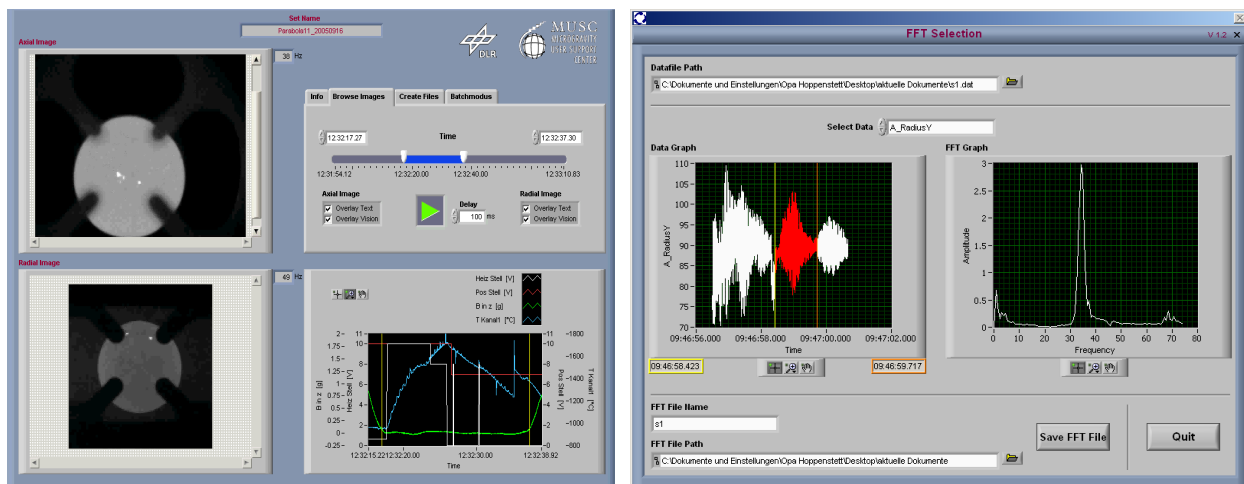


Fig. 3: Screenshot of the TEVI software. Left: synchronous display of video and facility data, Right: FFT analysis and oscillation frequency

Experiment Preparation: Ground Support Program

The experiment preparation is embedded in the overall operations preparation at MUSC. The so called ground support program covers all the activities needed to transcribe the individual scientific ideas into verified experiment and facility control parameters and files. It provides the

scientific users with technical and scientific services in the preparation, performance and evaluation of the experiments.

The ground support program consists of three major parts:

Sample Characterization:

The determination of certain sample properties which are mandatory for the individual EML experiment execution process are provided as a service to the science teams.

The knowledge of the amount of sample material evaporating from the sample surface during processing is essential because the evaporated metal dust is a resource in the EML. The deposited metal layer growing on the coil is limited and the evaporated metal must not exceed certain limits. Therefore the evaporation rate of the each flight sample composition is measured by MUSC in a dedicated ground model on sample material provided by the science teams.

The set-up consists of a UHV chamber in which a sample is heated to specified temperature. The mass loss is determined by an oscillating quartz crystal, refer to Fig. 4 and Fig. 5.

The obtained data are later used for experiment planning purposes and finally the experiment execution in-orbit. During the real-time experiment operation, the evaporation rate is used to observe that the element specific limit values are not exceeded and to monitor the layer thickness growing on the coil.

For the detailed planning of the experiments the coupling of each sample to the RF field has to be known. Since EML is not designed to levitate samples under terrestrial conditions all ground based measurements are performed on samples suspended in the coils. Due to the longstanding history of EML, a number of experimental data stemming from parabolic flight and sounding rocket campaigns are available and will support the experiment development.



Fig. 4 (left): UHV Chamber with oscillating quartz crystal for mass loss/evaporation rate determination

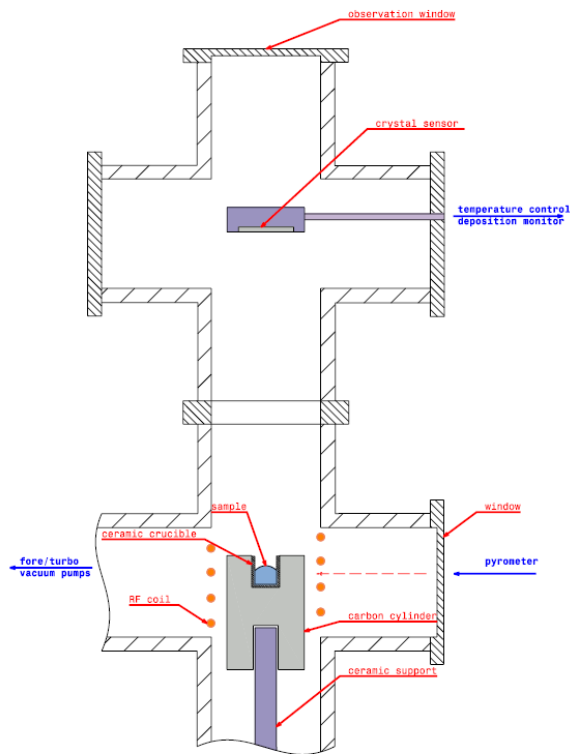


Fig. 5 (right): Sketch of the vacuum chamber; the lower part shows the sample placed in the ceramic crucible and the graphite cylinder within the HF coil. The oscillating quartz crystal is placed in the upper part.

The obtained coupling data are later used in order to simulate the required temperature time profile of the sample with an EML simulator software.

For a correct temperature measurement with the pyrometer onboard, the sample emissivity is measured in the EML ground model. The sample is heated until melting sets in and by a comparison of the measured and literature melting point the emissivity can be derived. The optical setup and used pyrometer of the ground model is comparable to the EML facility.

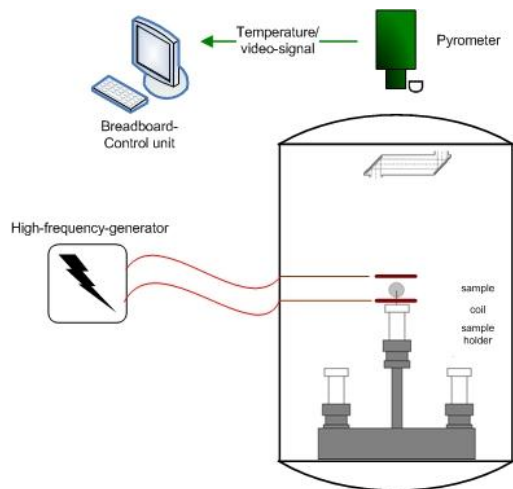


Fig. 6: EML Bread Board for Coupling Efficiency Measurements

Experiment development

The first step in the experiment development is the definition of the individual operational process flow for each experiment, yielding the outline of all nominal and contingency operation. For that purpose, so called science protocols are prepared on behalf of and in cooperation with the science teams, describing key temperatures of the samples to be reached, facility settings (camera, pressure, etc.) and a detailed experiment planning. These science protocols are the base for the further development of the parameter sets.

EML experiments consist of two sets of parameters. The experiment parameters EPs define the experiment as planned. The so called limit parameters LPs provide an independent guard rail envelope of RF values for each experiment that can never be exceeded.

The core parameters for both EP sets are developed with the EML experiment simulator, which currently predicts temperature time profiles from applied RF parameters and the coupling behaviour of the sample to the RF field. The EML experiment simulator will be upgraded by a facility part and enables MUSC to simulate the facility behaviour for an experiment run and to schedule the experiments accordingly.

Experiment verification

After development of the parameter sets they must be validated in a representative EML model. For this purpose, the Operational Model (OM), which also acts as flight spare will be used. During the validation the parameter sets will be processed on a suspended high melting sample and thus the parametersets and the experiment performance can be validated. Especially the timing and interleaving of the two independent sets of parameters will be checked. This task will be performed in close cooperation with the involved scientists, using the verification runs for

user training on the operational environment they will use later during on-board experiment performance.

Summary and outlook

The EML facility is currently under development and is planned to be launched in 2013. The scientific users of the EML are supported by the DLR MUSC, which performs an extensive scientific ground support program. This covers the sample characterisation, experiment preparation and validation of experiment parameters.

The experiments onboard the ISS are controlled and operated from the control room at DLR MUSC in Cologne via a dedicated ground segment.

After the experiments the scientists are supported by the data evaluation and long term archiving of the data.

Acknowledgements

The EML Ground Support Program is funded by the European Space Agency (ESA).

References

[1] Electromagnetic levitation in microgravity: EML on parabolic flights, TEXUS and ISS, Schneider, Engelhard, Heuskin, Diefenbach, 4th International Symposium on Physical Sciences in Space (ISPS 4), 11. - 15. Juli 2011

[2] Support tools for TEMPUS / EML campaigns, Schneider, Engelhard, Heuskin, Diefenbach, 4th International Symposium on Physical Sciences in Space (ISPS 4), 11. - 15. Juli 2011

[3] Structuring and Visualizing Microgravity Material Science Data in a Topic Maps Ontology. Grimbach, Alois und Wever, Philipp und Schneider, Stephan und Willnecker, Rainer PV International Conference 2009, 1. - 3. Dezember 2009, Castillo de Villafrance, Spanien.

[4] Measurement of thermophysical properties of liquid metallic alloys in a ground- and microgravity based research programm. The Thermolab Project. Fecht, Schneider, Wunderlich, Battezzati, Papandrea, Palumbo, Egry, Mills, Quested, Brooks, Giuranno, Novakovic, Passerone, Ricci, Seetharaman, Aune, Vinet, Garandet, J.-P. (2005) Metallurgica Italiana, 3, p 47-51.

[5] Preparation for Containerless processing on ISS: parabolic Flights with the TEMPUS facility, Diefenbach, Lohöfer, Dreier, Piller, 53rd IAC,2002

HIGH-PRECISION TEMPERATURE CONTROL OF A CRYSTAL GROWTH FURNACE AT 1500°C

Ch. Stenzel¹, A. Hess², A. Cröll², D. Bräuer³, H. Sauermann³

¹Astrium GmbH, D-88090 Immenstaad

²Kristallographie, Institut für Geowissenschaften, Universität Freiburg, D- 79104 Freiburg

³Institut für Automatisierungstechnik, TU Bergakademie Freiberg, D- 09596 Freiberg

Keywords: Temperature control, Crystal growth, High-temperature furnace

Abstract

For crystal growth of semiconductor materials a short-term temperature stability of 0.1°C at 1500°C is one of the essential parameters to be addressed for achieving high-quality crystals.

Hence, for temperature monitoring and control with high precision in a floating zone furnace two sets of thermo-sensors, type B thermocouples and optical fibre thermometers, have been implemented and successfully operated in the furnace for more than 2000 h. The optical fibre thermometers consist of an optical system made of sapphire (two fibres plus a prism in between for deflection) and transmit the infra-red radiation of the heater to the outside of the hot core of the furnace for pyrometric temperature measurement.

A dedicated control algorithm has been set up which controlled the power settings to the individual heaters. Both sensor types showed no degradation after this period and yielded a short-term stability at 1200°C of 0.05°C (optical fibre thermometers), respectively 0.08°C (thermocouples).

Introduction

For float zone crystal growth experiments onboard the International Space Station (ISS) the implementation of a dedicated heater insert for the Materials Science Laboratory (MSL) is envisaged - the Float Zone Furnace with Magnetic Field (FMF) [1]. One of the essential parameters to control inhomogeneities in the crystal growth of semiconductor materials is the short-term temperature stability (in the range of several minutes) of the furnace [2]. To set up a high-precision temperature control system requires an appropriate combination of fast actuators (heaters) and sensors as well as the implementation of a sophisticated temperature control system. This furnace is especially designed to provide enhanced short-term temperature stability in addition to the ability of adjusting the temperature gradient at the solid-liquid interface over a wide range. The specification on the short-term stability of the furnace was set to $\Delta T < 0.05^\circ\text{C}$. In a laboratory model of this furnace the above mentioned features have been addressed in the design and the performance has been verified in an experimental test programme.

In the following sections of this paper the detailed design of the respective subsystems of the FMF furnace to achieve a short-temperature stability - the heating system, the thermometry and the control system - will be introduced, the results of the performance tests reported, and a summary given.

Heating system

In order to provide a zone profile at 1500°C with a variable gradient at the solid/liquid interface, the FMF is laid out as a furnace with 7 individually controlled heating zones. In the area of the central zone the melt zone is established. Figure 1 shows a conceptual sketch of the FMF.

The single heaters consist of encapsulated graphite heaters where a meandered graphite layer ($50\ \mu\text{m}$ thick) is deposited onto a pBN substrate. The heating layer is covered by a second pBN CVD layer to protect it against mechanical, electrical, and chemical injuries. The resulting thickness of wall of less than 2 mm provides a rather low thermal mass enabling fast heating rates and temperature changes. Due to the excellent material compatibility between the different materials and similar values for thermal expansion this type of heater can bear up a power density of more than $30\ \text{W}/\text{cm}^2$ leading to a compact design for high-temperature applications and also to long operation times of more than 2000 h. Figure 2 shows a photograph of the central heater of the FMF.

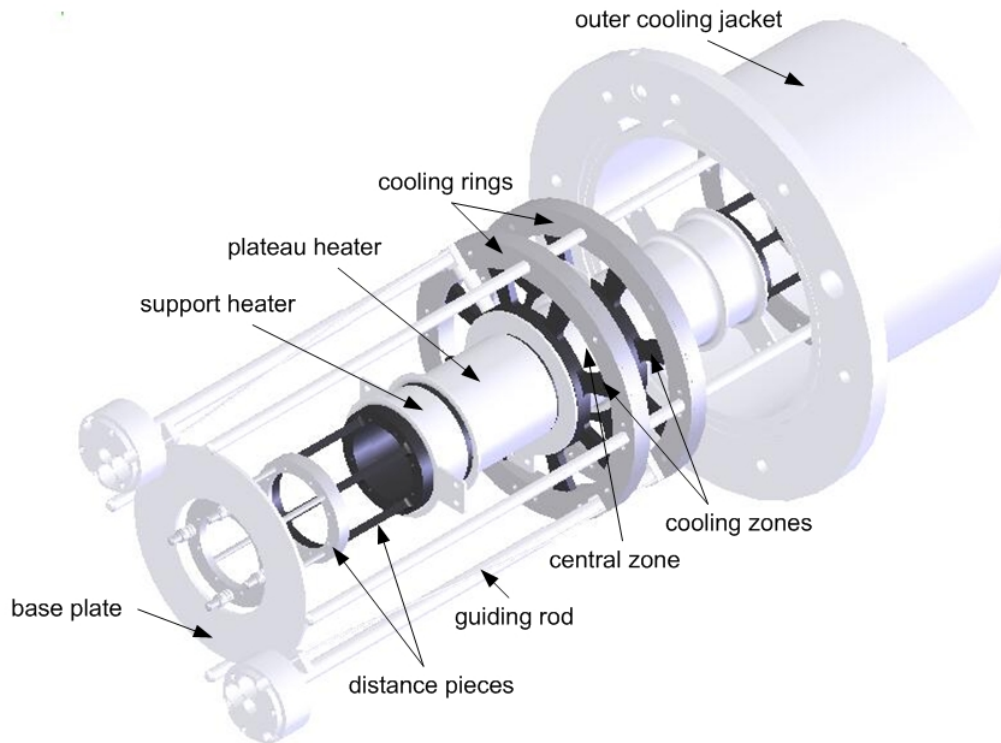


Figure 1. Conceptual sketch of the FMF exhibiting the inner structure of the furnace: The furnace provides a symmetrical thermal profile with seven individual heating zones. Six zones are placed symmetrically at both sides of the central heater (on each side a cooling zone, a support, and a plateau heater is placed).

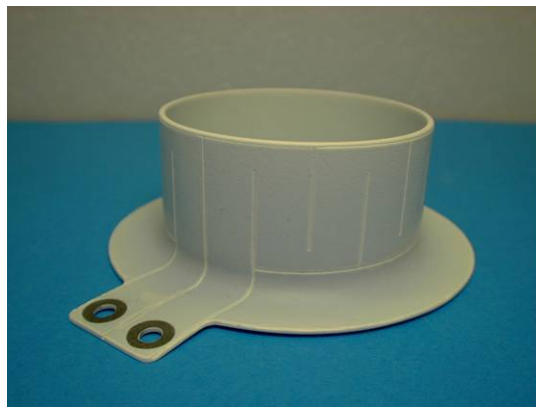


Figure 2. Encapsulated graphite heater for the central zone of the FMF: The thermal load of 1000 W provides a maximum temperature of 1500°C in this area

To improve the radial homogeneity of the temperature profile in the FMF tubular thermal diffusors for each zone consisting of a graphite tube have been employed; thereby the heaters are placed directly around the diffusors tubes.

Thermometry

For temperature measurement and control each zone is equipped with two thermocouples. Additionally, one optical sensor is employed in the three inner zones of the furnace. The temperature control system of the furnace could thereby use signals of both sensor types as input.

Thermocouples

The application of sheathed thermocouples represents the standard technique for temperature measurement and control in furnaces. The achieved stability amounts to about 0.1 K [3]. For temperature above 1200°C only type C (W-Re) or type B (Pt-Rh) thermocouples can be applied. Because of the better drift behaviour type B thermocouples with the following specifications have been selected:

- Type B (Pt-PtRh)
- Insulation material: MgO
- Sheath Pt (\varnothing : 1,0 mm)
- Protection tube Ta (\varnothing : 1,6 x 0,1 mm)

The thermocouples were implemented into axial borings in the diffusors. In order to prevent a degradation of the Pt sheath due to a reaction with the graphite diffusor they were inserted into protection tubes of Ta. The compatibility of this protection tube with a graphite environment has been tested in advance for several hours at 1600°C in vacuum (1×10^{-5} mbar). No drifts or degradation have been observed.

Optical Sensors

According to Planck's law higher temperature resolution can be obtained by utilising optical fibre thermometry with sapphire fibres at elevated temperatures [4, 5]. These sensors consist of an optical waveguide to transmit the IR radiation emitted from a small spot of the object to be measured out of the hot region to a photo detector which converts the radiation signal into a temperature reading following Planck's law. For application in high-temperature facilities these waveguide are made of sapphire. Using straight fibres in a 4-zone laboratory furnace a short-term stability of 0.015°C has been achieved [6].

Due to constructional boundary conditions of the MSL facility the sensors may not be routed in a straight line within the furnace, one 90° bend of the sensors has to be included. For the FMF optical sensors this is realised by the Optical Deflection System (ODS) which is built up by straight sapphire waveguides. The path of rays is being deflected by a sapphire prism which is embedded in a support structure out of ceramic. To enhance transmission by focussing a sapphire lens is implemented behind the prism. Similarly to the thermocouple design the sapphire fibres are integrated into protection tubes out of alumina. The distance to the heater surface amounts to 2 mm. The final transmission for the ODS was measured to amount to 40%. Three out of 7 heating zones of the FMF have been equipped with an ODS as illustrated in Fig. 3.

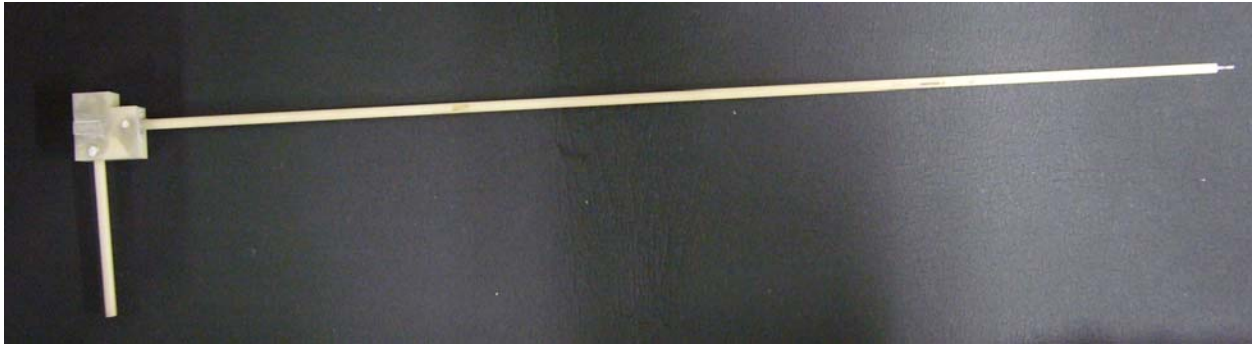


Figure 3. Example of an ODS sensor: The short arm is directed to the hot side, the long arm is routing the IR signal out of the hot core; at its end a conventional quartz fibre leads the signal to a Si photo diode located outside the furnace.

Temperature Control Algorithm

The developed high-precision temperature control system is based on a holistic view of the furnace, reflecting sensors, heaters, software, and control algorithm. Since the individual zones are not adiabatically separated from each other, an initial temperature difference between the zones causes thermal fluxes which affect the temperatures of the zones again. Hence, there exists a strong thermal coupling between zones and the furnace is to be regarded as a multiple-input multiple-output (MIMO) plant. In order to develop an optimised feedback controller the thermal properties of each zone as well as the couplings have to be known exactly. In a first step a theoretical furnace model based on conduction and radiation between the zones is established, and then the unknown parameters are experimentally determined by process identification. This means measuring the dynamic temperature changes as response to well-defined power signals (Pseudo Random Binary Signal). These semi-empirical data represent the input for the parameter estimation algorithm which finds optimised model parameters. The obtained model is basis for feedback controller synthesis [7]. The final controller consists of a separate, standard PID (Proportional-Integral-Differential)-algorithm for each zone with pre-filter, pilot control, decoupling and anti-reset-wind-up. This structure and the V-canonical plant are depicted in Fig. 4. A V-canonical structure means that the loop interactions are regarded as feedback couplings, hence modifying the input signal.

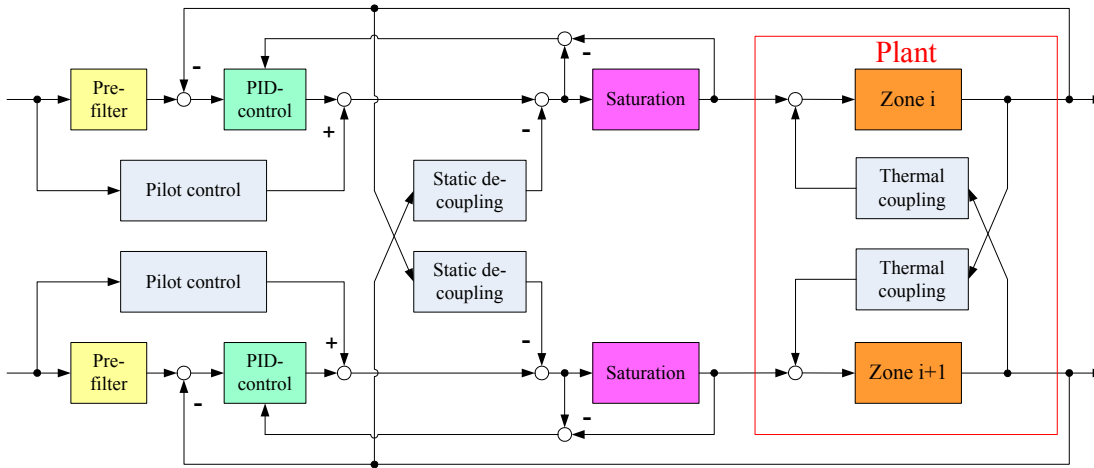


Figure 4. Structure of the feedback controller and the V-canonical MIMO plant as example for two zones: Thereby the power setting to zone I depend on the temperature of this zone and of its neighbouring zones via the thermal coupling which have to be experimentally determined.

Tests

At 1200°C the short-term stability has been investigated for both type of sensors control (thermocouples or ODS). The central heaters were set to 1200°C and the cooling zone to 1100°C to establish a temperature gradient of 50 K/cm. The test was performed over a time period of 18 h (ODS) and 20 h (TC). In the central zone temperature fluctuations of $\Delta T = 0.05^\circ\text{C}$ could be achieved for control with the ODS sensors, and $\Delta T = 0.051^\circ\text{C}$ for control with thermocouples as shown in Fig. 5. In the cooling zones even better values of $\Delta T = 0.026^\circ\text{C}$ (ODS) and $\Delta T = 0.05^\circ\text{C}$ (TC) could be obtained.

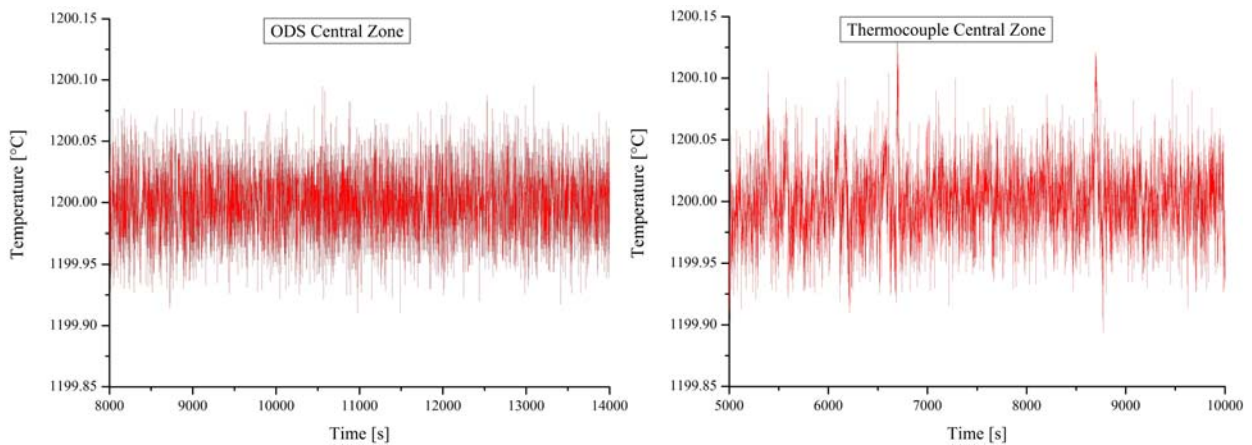


Figure 5: Measured short-term temperature stability for control with ODS sensors (left) and with thermocouples (right)

Conclusion

Temperature control within a multi-zone furnace for semiconductor crystal growth has been realised with thermocouples and optical sensors as input signals for the control algorithm. With both systems a superior short-term stability of less than $\Delta T < 0.05^\circ\text{C}$ could be achieved in a multi-zone high-temperature furnace. No significant performance difference between the two types of sensors could be detected in the investigated temperature range. However, for environments with strong EMC perturbations the optical sensors reveal some advantage.

References

- [1] Hess, A., Cröll, A., Stenzel, C., Bräuer, D., Sauermann, H., Uhlig, V., *Floating Zone Furnace with Rotating Magnetic Field*. Poster Presentation DGKK 2010
- [2] Müller, G., *Convection and Inhomogeneities in Crystal Growth from the Melt*, in: *Crystal Growth, Properties and Applications*, Vol. 3, III-V Semiconductors, Springer-Verlag, Berlin, Heidelberg, New York, 1980
- [3] Sauermann, H., Schneider, K., Janda, O., Gröll, L., Bretthauer, G., Linn, H., *Das Gradient-Freeze Verfahren und seine regelungstechnische Umsetzung*. 39. IWK der TU Ilmenau, 1994, p. 809-817
- [4] Schietinger, C.: *Temperature measurements using optical fibers*, in: *Thermal Measurements in Electronics Coolings*, ed. K. Azar CRC Press, 1997, Boca Raton
- [5] Dils, R. R., *J. Appl. Phys.*, **54**, 1983, p. 1198
- [6] H. Sauermann, Ch. Stenzel, S. Keesmann, B. Bonduelle, *Cryst. Res. Technol.* **36**, 2001, p. 1329-1343
- [7] Hermann, K., Rehkopf, A., Sauermann, H., *Betrachtungen zur Identifikation einer Gradient-Freeze-Anlage zur Einkristallzüchtung*, *Automatisierungstechnik*, Vol. 54 2006, p. 566-573

Investigation of Thermocapillary Convection of High Prandtl Number Fluid Under Microgravity

Ruquan Liang, Guangdong Duan

Key Laboratory of National Education Ministry for Electromagnetic Processes of Materials,
Northeastern University, No.3-11, Wenhua Road, Shenyang 110819, China

Keywords: Liquid Bridge, Thermocapillary Convection, Velocity, Temperature

Abstract

Thermocapillary convection in a liquid bridge, which is suspended between two coaxial disks under zero gravity, has been investigated numerically. The Navier-Stokes equations coupled with the energy conservation equation are solved on a staggered grid, and the level set approach is used to capture the free surface deformation of the liquid bridge. The velocity and temperature distributions inside the liquid bridge are analyzed. It is shown from this work that as the development of the thermocapillary convection, the center of the vortex inside the liquid bridge moves down and reaches an equilibrium position gradually. The temperature gradients in the regions near the upper center axis and the bottom cold corner are higher than those in the other regions.

1. Introduction

Thermocapillary flow is often encountered in the production of single crystals using the floating-zone method, and the oscillatory thermocapillary convection is responsible for the periodic variations in striations in the production process. The oscillatory thermocapillary convection becomes significant and causes detrimental striations in the chemical composition of the finished crystal. Schwabe and Scharmann¹ and Chun and Wuest² observed, for the first time, the three-dimensional time-dependent state in thermocapillary convection in their experiments. Since the first observation, many studies have been done on the half-zone model where a liquid drop is held between two coaxial rods remained at different temperatures to impose an axial temperature gradient on the free surface, and the liquid drop is held by surface tension force between two rods. The studies found in the literature mainly concerned with the following aspects,

1. The transition and the successive mode structures of the flow field³⁻⁶,
2. The flow structures at a region close to the critical point of the transition,
3. The information regarding the flow fields far beyond the critical point⁷.

In the high Pr range ($Pr > 10$), although many experimental data can be found in literature, no accurate stability analyses nor numerical simulations of the oscillation phenomenon are currently available. One important aspect is that the dynamic free surface deformation was not considered, although it may play an important role in the oscillation mechanism. In the present paper, the temperature and velocity fields in the liquid bridge under zero gravity are investigated numerically considering the free surface deformation and the ambient air by using the level set method. The present study aims at understanding the time dependent thermal fluid phenomena with dynamic free surface deformation in the half-zone liquid bridge by a direct nonlinear numerical simulation.

2. Governing Equations

The half-zone model consists of an initially cylindrical liquid bridge suspended between the hot and cold circular disks as shown in Figure 1. The ambient air is included in the computational region. The diameter of the top and bottom disks (D) is 5.0 mm, and the aspect ratio of the liquid bridge (H/D) is 0.7, where H is the height of the liquid bridge. The temperature difference between two disks is defined as ΔT . The general governing equations of the problem

for Newtonian incompressible flow conditions under zero gravity are given by the following non-dimensional Navier-Stokes, the continuity and the energy conservation equations⁸.

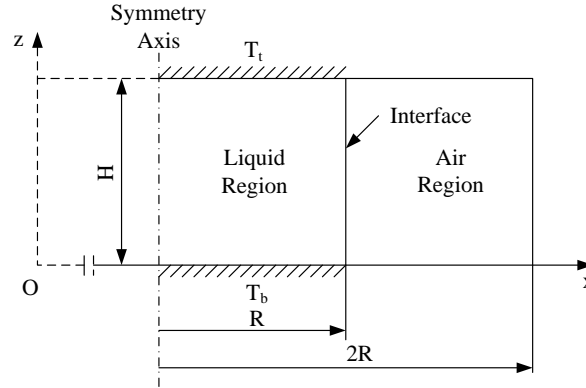


Figure 1. Schematic of a thermocapillary convection model

$$\mathbf{u}_t + (\mathbf{u} \cdot \nabla) \mathbf{u} = \frac{1}{\rho} \left(-\nabla p + \frac{1}{\text{Re}} \nabla \cdot (2\mu \mathbf{D}) + \left(\frac{1}{\text{We}} - \frac{\text{Ca}}{\text{We}} \Theta \right) \kappa \delta(d) \mathbf{n} \right) \quad (1)$$

$$\nabla \cdot \mathbf{u} = 0 \quad (2)$$

$$\frac{\partial \Theta}{\partial t} + \nabla \cdot (\mathbf{u} \Theta) = \frac{1}{\text{Re Pr}} \nabla^2 \Theta \quad (3)$$

where $\mathbf{u} = (u, v)$ is the fluid velocity, $\rho = \rho(\mathbf{x}, t)$ is the fluid density, $\mu = \mu(\mathbf{x}, t)$ is the fluid viscosity, \mathbf{D} is the viscous stress tensor, κ is the curvature of the interface, d is the normal distance to the interface, δ is the Dirac delta function, \mathbf{n} is the unit normal vector at the interface, t is the time, p is the pressure. The key parameters are $\text{Re} = \rho_l U_\infty D / \mu_l$, Reynolds number, where D is the initial diameter of the liquid bridge and U_∞ is the characteristic velocity defined as $U_\infty = \sigma_T \Delta T / \mu_l$ in microgravity conditions, where σ_T is the temperature dependency of surface tension, $\Delta T = T_t - T_b$ is the temperature difference between the top and bottom disks; $\text{We} = U_\infty^2 D \rho_l / \sigma$, Weber number; $\text{Pr} = \mu_l / \rho_l a$, Prandtl number, where a is the thermal diffusivity; $\text{Ca} = \mu_l U_\infty / \sigma$, Capillary number; $\text{Ma} = \text{Re Pr}$, Marangoni number. We denote σ as the surface tension, $\sigma = \sigma_c - \sigma_T (T - T_b)$, where σ_c is a reference value of surface tension, and Θ as the excess temperature, $\Theta = (T - T_b) / \Delta T$. Here ρ_l and μ_l are the dimensional liquid density and viscosity, respectively. ρ_g and μ_g are the dimensional density and viscosity of ambient air, respectively.

3. Level Set Function and Its Formulation

The level set method was originally introduced by Osher and Sethian (1988)⁹ to numerically predict the moving interface $\Gamma(t)$ between two fluids. Instead of explicitly tracking the

interface, the level set method implicitly captures the interface by introducing a smooth signed distance from the interface in the entire computational domain. The level set function $\phi(\mathbf{x}, t)$ is taken to be positive outside the liquid bridge, zero at the interface and negative inside the liquid bridge. The interface motion is predicted by solving the following convection equation for the level set function of $\phi(\mathbf{x}, t)$ given by¹⁰,

$$\phi_t + \mathbf{u} \cdot \nabla \phi = 0 \quad (4)$$

$$\mathbf{u} \cdot \nabla \phi = (u\phi)_x + (v\phi)_y \quad (5)$$

$$(u\phi)_x + (v\phi)_y = \frac{1}{2h} (u_{i+1/2,j} + u_{i-1/2,j}) (\phi_{i+1/2,j} + \phi_{i-1/2,j}) - \frac{1}{2h} (u_{i+1/2,j} - u_{i-1/2,j}) (\phi_{i+1/2,j} - \phi_{i-1/2,j}) + \frac{1}{2h} (v_{i,j+1/2} + v_{i,j-1/2}) (\phi_{i,j+1/2} + \phi_{i,j-1/2}) - \frac{1}{2h} (v_{i,j+1/2} - v_{i,j-1/2}) (\phi_{i,j+1/2} - \phi_{i,j-1/2})$$

For smooth data, we have $(\phi_{i+1/2,j} + \phi_{i-1/2,j}) \approx (\phi_{i,j+1/2} + \phi_{i,j-1/2})$. In addition, we have $(u_{i+1/2,j} - u_{i-1/2,j}) \approx (v_{i,j+1/2} - v_{i,j-1/2})$ because \mathbf{u} is numerically divergence free. Thus,

$$(u\phi)_x + (v\phi)_y \approx (u_{i+1/2,j} + u_{i-1/2,j})(\phi_{i+1/2,j} - \phi_{i-1/2,j}) / (2h) + (v_{i,j+1/2} + v_{i,j-1/2})(\phi_{i,j+1/2} - \phi_{i,j-1/2}) / (2h)$$

In addition, the model of Continuum Surface Force (CSF) is employed to treat the surface tension force on the interface, which interprets the surface tension force as a continuous body force across the interface rather than as boundary conditions in normal and tangential directions to the interface. By using the level set function, body force due to surface tension can be expressed as,

$$\frac{1}{We} \kappa \delta(d) \mathbf{n} = \frac{1}{We} \kappa(\phi) \delta(\phi) \nabla \phi$$

The curvature of the interface is evaluated from

$$\kappa(\phi) = -\nabla \cdot (\mathbf{n})$$

$$\nabla \cdot \mathbf{n} = \nabla \cdot \left(\frac{\nabla \phi}{|\nabla \phi|} \right)$$

The Dirac delta function is defined as

$$\delta_\alpha(\phi) \equiv \begin{cases} \frac{1}{2} (1 + \cos(\pi\phi/\alpha)) / \alpha, & \text{if } |\phi| < \alpha \\ 0, & \text{otherwise} \end{cases}$$

4. Boundary and Initial Conditions

The flow in the liquid bridge is assumed to be axis-symmetric initially, and the hot and cold disks are maintained at constant temperature T_i and T_b , respectively.

$$\Theta = 0 \quad (z = 0)$$

$$\Theta = 1.0 \quad (z = 1.0)$$

The adiabatic condition is adopted on the all other boundary walls except for the hot and cold disks. The initially stationary liquid bridge and the ambient air are considered with the initial condition

$$\mathbf{u}(t = 0) = 0$$

The non-slip condition is used for all walls of the computational domain

$$\mathbf{u} = 0$$

The present strategy is further summarized below. The mass conserving level set methods is applied to analyze the free surface motion of the liquid bridge. The Navier-Stokes equations in primitive variable formulations and energy conservation equation are solved on a staggered grid by the method of lines. The advection terms are discretized by the quadratic upstream interpolation for convective kinematics (QUICK) method and the other terms by the central finite difference method except for the body force, and a second-order Adams-Bashforth method is used as the time integration scheme. The higher essentially non-oscillatory (ENO) scheme is also adopted to solve the convection term of the level-set function. The Poisson equations are solved by means of the Successive Over Relaxation (SOR) approach. The Continuum Surface Force (CSF) model is employed to treat the surface tension force at the interface.

5. Code Validation

In present study, the numerical model and code have been carefully tested again by comparing the isotherms and velocity vectors in the liquid bridge of 2cSt silicone oil obtained from the present study with those reported by Kawamura et al.¹¹. In the comparison, the initial liquid bridge and the ambient air are denoted to be stationary and axis-symmetric. The radii and height of the liquid bridge are $R = 5 \text{ mm}$, $H = 5 \text{ mm}$, respectively. The temperature difference between the top and bottom disks is $\Delta T = 30^\circ \text{C}$. The Marangoni number is $Ma = 4 \times 10^4$, and the Prandtl number is $Pr = 28.0$. The temperature contour and velocity vectors obtained from the present work under zero gravity is shown in Figure 2, and the agreement between the present results and those from Kawamura et al. can be qualified as quite acceptable (see Fig. 5(b) of Kawamura et al. (2007)).

6. Results and Discussion

The mechanism of thermocapillary convection in a liquid bridge of high Prandtl number under zero gravity is investigated. The key parameters used are as follows: $Pr = 50$, $Ma = 5000$, $We = 15$, $T_t = 328 \text{ K}$, $T_b = 298 \text{ K}$. Diameter of the top and bottom disks is $D = 5.0 \text{ mm}$, and the aspect ratio (H / D) is 0.7. In this section, we study the flow structure inside the liquid bridge under the present computational conditions.

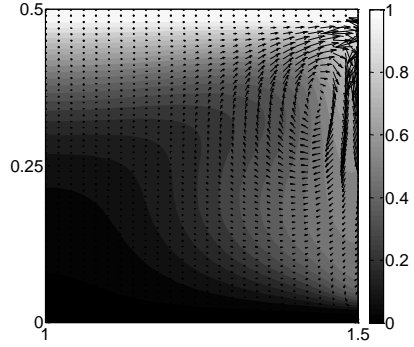


Figure 2. Temperature contour and velocity vectors (2cSt silicone oil, $Ma = 4 \times 10^4$, $Pr = 28.0$)

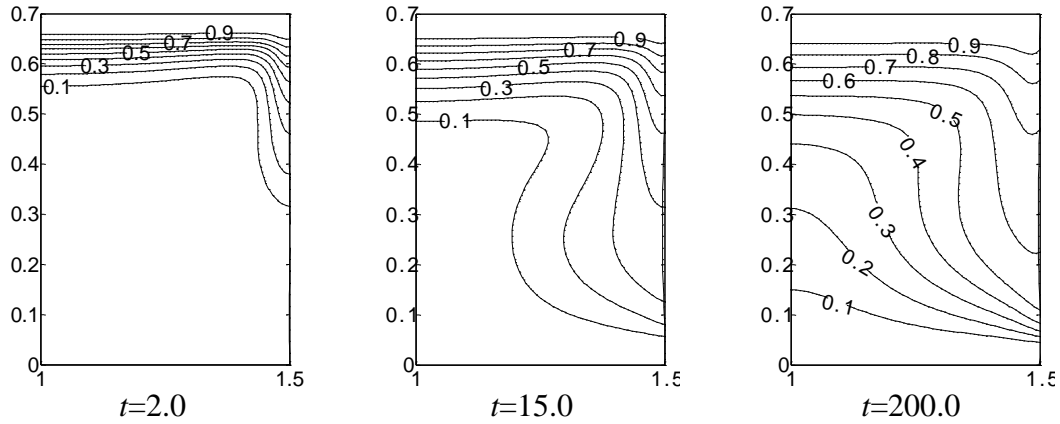


Figure 3 Time evolution of isothermals ($Pr = 50$, $Ma = 5000$, $We = 15$, $T_t = 328K$, $T_b = 298K$, $D = 5.0mm$, $H / D = 0.7$)

Figure 3 illustrates time evolution of isothermals inside the liquid bridge, where only half of the liquid bridge is plotted. Since the temperature of the top disk is higher than that of the bottom disk, the heat flux moves from the top disk toward the bottom disk, and the flow is driven in the hot corner. On the other hand, the surface flow is developed due to the temperature gradient on the free surface, which results in a return flow inside the liquid bridge. The return flow generates a radial convection, which tends to make the bulk fluid temperature distribution rather uniform near the free surface. It can be found from Figure 3 that the temperature gradients in the regions near the upper center axis and the bottom cold corner are higher than those in the other regions.

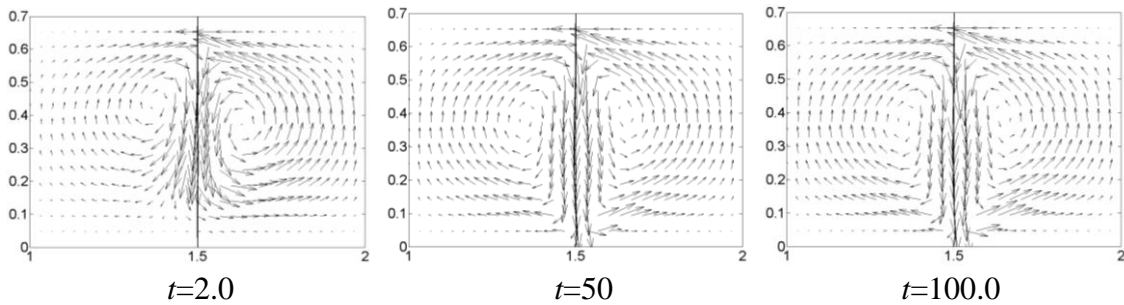


Figure 4 Time evolution of velocity vectors ($Pr = 50$, $Ma = 5000$, $We = 15$, $T_t = 328K$, $T_b = 298K$, $D = 5.0mm$, $H / D = 0.7$)

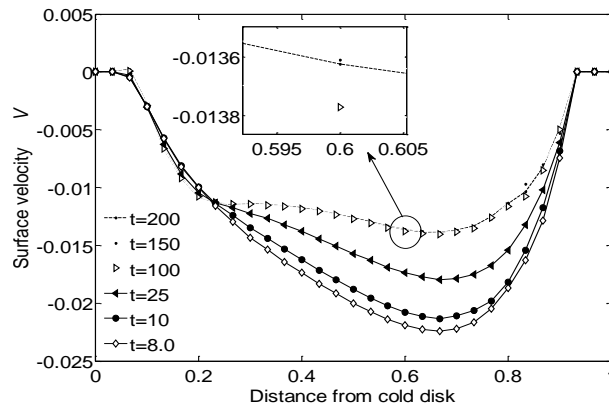


Figure 5 Time evolution of surface velocity in axial direction ($Pr = 50$, $Ma = 5000$, $We = 15$, $T_t = 328K$, $T_b = 298K$, $D = 5.0mm$, $H / D = 0.7$)

The velocity vectors in the liquid bridge and ambient air at $t=2.0$, $t=50.0$, and $t=100.0$ are presented in Figure 4. Note that only half of the computational domain is plotted in Figure 4 due to the symmetric property. The free surface remains straight shape due to the zero gravity. Two vortices are generated due to the thermocapillary convection inside the liquid bridge and ambient air, respectively, and the vortex center inside the liquid bridge locates near the hot corner initially ($t=2.0$) as shown in Figure 4. As the development of the thermocapillary convection, the vortex center inside the liquid bridge moves down and reaches an equilibrium position gradually ($t=50.0$, $t=100.0$). The larger velocity vectors can be found mainly around the free surface because the flow is driven by the surface flow generated near the free surface. Figure 5 shows the surface velocities in axial direction. It can be seen that the values of the surface velocities in axial direction are all negative, showing that the direction of the surface flow is from the top disk toward the bottom disk. The surface velocities in axial direction at the top disk and the bottom disk are zero due to the no-slip conditions in there. As the time proceeds ($t=8.0$, $t=10.0$, $t=25.0$, $t=100.0$), the levels of the surface velocities in axial direction rise, showing the enhancement of the surface flow gradually. After that, the profiles at $t=100.0$, $t=150.0$, and $t=200.0$ are very close, showing the surface flow approaches the equilibrium state after $t=100.0$. The maximum of the surface velocities in axial direction can be obtained on the surface position of about $z=0.65$ at every time, where z is the non-dimensional distance from the cold disk.

7. Conclusions

Thermocapillary convection in a liquid bridge of $Pr = 50$ under zero gravity has been investigated numerically. From this work, the following conclusions can be drawn.

1. The temperature gradients in the regions near the upper center axis and the bottom cold corner are higher than those in the other regions.
2. As the development of the thermocapillary convection, the vortex center inside the liquid bridge moves down and reaches an equilibrium position gradually.
3. As the time proceeds, the levels of the surface velocities in axial direction rise, showing the enhancement of the surface flow gradually. After that the surface flow approaches the equilibrium state. The maximum of the surface velocities in axial direction can be obtained on

the surface position of about $z=0.65$ at every time, where z is the non-dimensional distance from the cold disk.

Acknowledgement

The present work is supported financially by the National Natural Science Foundation of China under the grant of 11072057 and the Natural Science Foundation of Liaoning Province under the grant of 20092002.

References

1. D. Schwabe, A. Scharmann, "Steady and oscillatory Marangoni convection in floating zones under microgravity," *J. Cryst. Growth*, 6(1979), 125.
2. C. H. Chun, W. Wuest, "Experiments on the transition from the steady to the oscillatory marangoni-convection of a floating zone under reduced gravity effect," *Acta Astronaut.*, 6(9)(1979), 1073-1082.
3. F. Preisser, D. Schwabe, and A. Scharmann, "Steady and oscillatory thermocapillary convection in liquid columns with free cylindrical surface," *J. Fluid. Mech.*, 126(1983), 545-567.
4. Y. Kamotani, S. Ostrach, and M. Vargas, "Oscillatory thermocapillary convection in a simulated floating-zone configuration," *J. Cryst. Growth*, 66(1984), 83-90.
5. R. Velten, D. Schwabe, and A. Scharmann, "The periodic instability of thermocapillary convection in cylindrical liquid bridges," *Phys. Fluids*, 3(A) (1991), 267-280.
6. J. Masud, Y. Kamotani, and S. Ostrach, "Oscillatory thermocapillary flow in cylindrical columns of high Prandtl number fluids," *J. Thermophys. Heat Transfer*, 11(1997), 105.
7. S. Frank, D. Schwabe, "Temporal and spatial elements of thermocapillary convection in floating zones," *Exp. Fluids*, 23(1997), 234.
8. R. Q. Liang, Z. Chen, "Dynamics for droplets in normal gravity and microgravity," *Microgravity Sci. Technol.*, 21(2009), 247-254.
9. S. Osher, J. Sethian, "Fronts propagating with curvature-dependent speed: Algorithms based on hamilton-jacobi formulations," *J. Comput. Phys.*, 79(1) (1988), 12-49.
10. M. Sussman, P. Smereka, and S. Osher, "A level set approach for computing solutions to incompressible two-phase flow," *J. Comput. Phys.*, 114 (1994), 146-159.
11. H. Kawamura, E. Tagaya, and Y. Hoshino, "A consideration on the relation between the oscillatory thermocapillary flow in a liquid bridge and the hydrothermal wave in a thin liquid layer," *Int. J. Heat Mass Tran.*, 50(2007), 1263-1268.

REAL TIME IN-SITU OBSERVATIONS OF EQUIAXED DENDRITE COHERENCY IN AL-CU ALLOYS USING HIGH BRILLIANCE 3rd GENERATION SYNCHROTRON SOURCES

Andrew G. Murphy¹, David J. Browne¹, Wajira U. Mirihanage², Ragnvald H. Mathiesen²

¹Engineering and Materials Science Centre, University College Dublin, Ireland

²Department of Physics, Norwegian University of Science and Technology, N-7491 Trondheim
Norway

Keywords: Aluminum alloys, Dendrite coherency, Solidification, Synchrotron radiation

Abstract

In the last decade synchrotron X-ray sources have fast become the tool of choice for performing in-situ high resolution imaging during alloy solidification. This paper presents the results of an experimental campaign carried out at the European Synchrotron Radiation Facility, using a Bridgman furnace, to monitor phenomena during solidification of Al-Cu alloys - specifically the onset of equiaxed dendrite coherency. Conventional experimental methods for determining coherency involve measuring the change in viscosity or measuring the change in thermal conductivity across the solidifying melt. Conflicts arise when comparing the results of these experimental techniques to find a relationship between cooling rate and coherency fraction. It has been shown that the ratio of average velocity to the average grain diameter has an inversely proportional relationship to coherency fraction. In-situ observation therefore makes it possible to measure these values directly from acquired images sequences and make comparisons with published results.

Introduction

Many casting defects, e.g. microsegregation, hot tearing, gas porosity and solidification shrinkage, develop in mush after the point of coherency is reached. Traditionally dendrite coherency has been determined by one of two methods, namely rheological [1–4] and thermal analysis [5]. Rheological methods are based on measuring the increasing viscosity of the melt, as solid becomes coherent, and ultimately the shear strength of the dendritic network. Experimental details of the rheological setup have been well described by others [6] so it will not be discussed here. Thermal analysis is based on the principle of differing thermal conductivities between solid and liquid in the solidifying melt. In both rheological and thermal experimental methods the coherency fraction solid is calculated from the thermal data and compared to various alloy and process parameters for correlation [7]. Early coherency studies compared both methods for industrial grade aluminum alloys, ultimately showing good agreement [8, 9]. Increasing either cooling rate or solute content exhibited earlier coherency and thus lower fraction solid. The addition of grain refiners decreased grain size, delaying coherency and thus increasing coherency fraction solid. Chai [6] *et al.* performed a detailed theoretical analysis, based on diffusion-controlled equiaxed growth models, predicting coherency fraction solid, which was found to depend on the competition between nucleation and growth. Typically, for alloys with solute concentrations between zero and the solubility limit, as solute concentration increases both grain size and growth rate decrease. It is, however, the faster of the two decreasing variables, i.e. grain size or growth rate, which dictates final coherency fraction solid. An inversely proportional

relationship is found for cooling rate, growth restriction fraction and coherency time, the time at which the coherency-torque curve first deviates from steady state, as well as varying proportionally with d/V , where d is the grain diameter at coherency and V is the average dendritic growth rate. Although these theoretical predictions have been shown to underestimate the coherency fraction solid observed, they still display qualitative agreement with experimental results [9]. The most recent study of Veldman [10] *et al.* showed significant deviation between both experimental methods for Al-Si-Cu ternary alloys. In rheological experiments cooling rate was observed to have little effect on coherency fraction solid as opposed to thermal analysis which suggested the reverse. Similar results were observed when comparing solute additions with increasing silicon content observed to reduce coherency fraction solid. Silicon content is also observed to dominate, over cooling rate, the microstructure morphology, with lower levels exhibiting small globulitic structure and higher levels, larger orthogonal dendritic grains. A fullness morphological parameter, which is defined as the ratio of internal grain volume solid fraction, V_{GS} , to grain envelope volume, V_{GE} , or more traditionally the internal solid fraction, f_s , (equation (2)) [11, 12] showed high correlation with coherency fraction solid and solute additions indicating grain morphology as a controlling factor of coherency.

Many detailed solidification studies have now been conducted using binary alloy systems and synchrotron radiation and much quantitative data has been gathered and analyzed [13–15]. Following on from previous X-ray studies, this paper compares the experimental rheological and thermal coherency analysis with preliminary real time in-situ observations of equiaxed grain coherency, showing qualitative agreement with recent rheological studies.

Experimental Methods

This experimental campaign was carried out on the ID15A beamline at the European Synchrotron Radiation Facility (ESRF) in Grenoble, France. The experimental, Bridgman furnace, set up was principally the same as described in previous campaigns [16–18] and thus has been well documented. Specific parameters unique to this campaign and salient features of the rig are herein described. Two alloy sample types, Al-15wt%Cu and Al-25wt%Cu, measuring 30 x 15 x 0.2 mm, were used in this study. Grain refinement was achieved by the addition 0.5 g/kg of Al-Ti-B as described previously. Samples, once oxidized and coated with a boron-nitrite spray, are encased between two 150 μm quartz glass plates. This assembly is fitted to a translation device allowing the sample to be pulled through an imposed thermal gradient. The thermal gradient is supplied by two heater elements surrounding the crucible and separated by an adiabatic zone, where the incident X-ray beam intersects the sample. Temperature readings from the heaters are continuously measured by embedded thermocouples during the course of solidification, allowing for mid-run manual adjustment of the temperature gradient. The field of view (FOV) for captured images is set to 1.3 x 1.3 mm. Image capture was performed by a Sarnoff fast readout 512 x 512 pixel CCD, with image acquisition every 0.045 seconds. The ID15A is a high energy beamline delivering incident photons in the range [30 keV, 750 keV]. For this particular experiment the full polychromatic incident beam was employed. In terms of X-ray absorption contrast in the radiograms, however, only the lower photon energies will give a measurable contribution.

Solidification was performed by translating the sample through a constant or varying thermal gradient at a constant velocity, anti-parallel to gravity. Post experimental image enhancement and analysis is carried out using MATLAB from MathWorks, ImageJ, a java based open source image manipulation toolbox and the GNU Image Manipulation Program. Adaptive, linear and

nonlinear spatial filtering algorithms are used in conjunction with adaptive contrast enhancement and flat fielding techniques augment visible contrasts. Figure 1 shows a schematic layout of the heater/sample section of the Bridgman furnace used in the experiments. Also indicated is the location and scale of the field of view in contrast with the sample dimensions.

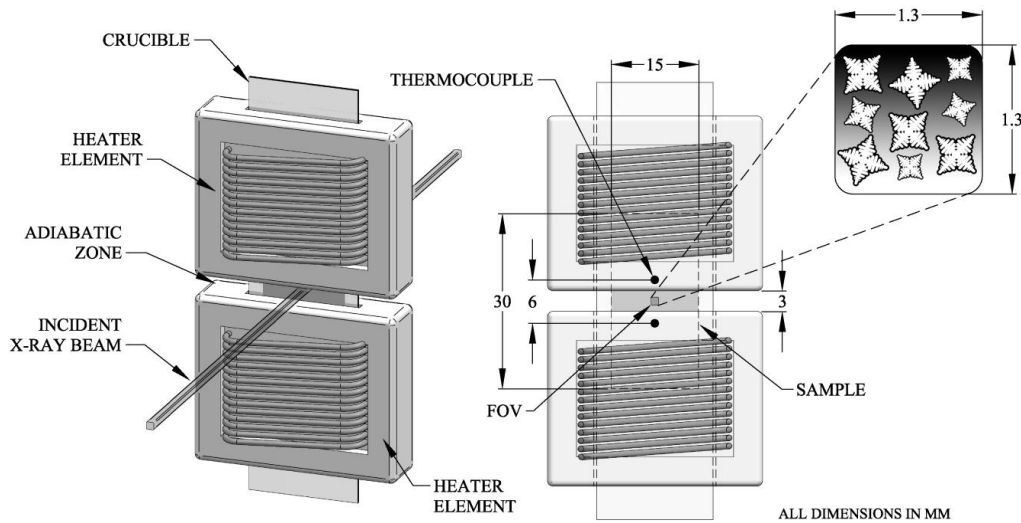


Figure 1. Schematic layout of the Bridgman type gradient furnace and sample orientation

Results & Discussion

Examples of the images obtained are shown in figure 2. Figure 2 (a) shows the original captured image, before image enhancement, for an Al-15wt%Cu sample run. The poor image contrast is found to be indicative of the entire experimental run. This discrepancy is attributed to the extremely high energy of the ID15 beamline. Even for the lowest energies, between 30 and 90 keV, the majority of the photons pass through the sample unabsorbed giving approximately 1.5 – 2% in total integrated absorption contrast between 200 μm of α -Al solid and Al-Cu liquids between 15-25wt%Cu. This puts the contrast close to the intrinsic noise level of the image acquisition system.

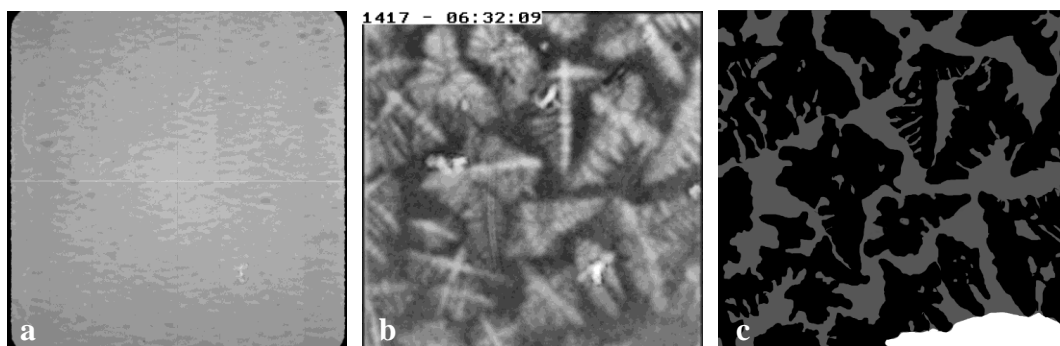


Figure 2. Al-15wt%Cu image acquisition data; (a) Original image; (b) Contrast enhanced image; (c) Envelope and Grain masking

Figure 2 (b) shows (a) post image enhancement through, flat fielding, noise cancellation, adaptive histogram adjustment and spatial convolution filtering. The spatial filtering method used was designed and implemented specifically for these images. While noise is still evident,

grains structures are clearly visible. Figure 2 (c) shows the process of envelope definition and solid α -Al extraction, with solid aluminum in black, coherency envelope in grey and outside envelope as white. In the case of rheological and thermal analysis [6], the point of coherency is determined at a discrete time based on changes in measured parameters, i.e. torque and temperature. In reality however, grain coherency is a transient process strongly governed by local undercoolings, solutal constitution and gravity-induced thermosolutal convection. Therefore degrees of coherency are occurring in any non-isothermal melt throughout the solidification process with no absolute time. It is also understood that once impingement occurs, primary growth ceases and dendritic coarsening dominates. With real time in-situ image acquisition it is possible to observe grain growth after nucleation, grain motion and finally impingement at the point of coherency. It is observed from these captured sequences that once individual grains become coherent, no further growth, either coarsening or preferential, occurs while grains are passing through the FOV. It is certain that post transport through the FOV, predictable solidification processes occur, however whilst visible, grains appear frozen in time at the point of coherency. It is proposed, therefore, to define a coherency envelope from which coherency fraction solid (f_{coh}) will be determined, based on the ratio of internal envelope solid area, V_S , to internal envelope total area, V_{EV} , equation (1).

$$f_{coh} = \frac{V_S}{V_{EV}} \quad (1)$$

Figure 3 illustrates the coherency concept. Isolated nucleated grains grow and eventually impinge, creating coherent network clusters, as was apparent in this study. In cases where solid growth encompasses the entire FOV, as in figure 2(b), the FOV will serve as the envelope boundary.

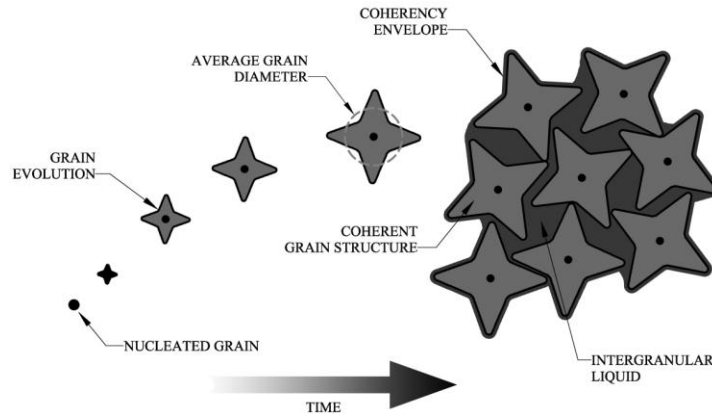


Figure 3. Coherency envelope definition

Due to the quasi-2D nature of the sample certain factors must be taken into consideration in the analysis. For instance, calculated solid fractions are based on area ratios, rather than volume ratios. This introduced unavoidable error into measurements as grains were observed to have varying thicknesses, less than or equal to the sample thickness. This was evidenced by instances of grain superposition observed during solidification. This error can be minimized in some respects by virtue of the ability to track grains from nucleation to impingement, continuously monitoring individual grain evolution. Also grains were observed to impinge mechanically on the crucible walls, i.e. get trapped between quartz slides, possibly distorting coherency events. Measurement reproducibility error was also evident due to manual definition of grain envelopes. To quantify this error a number of grain measurements were repeated several times to determine

average variation. This was calculated to be approximately 2.5%. Qualitatively, however, using consistent analytical methods the data showed minimal variation. Figure 4 shows a graph of the cooling rate across all samples versus coherency fraction solid. Cooling rate, in the case of a Bridgman furnace, is calculated as the product of thermal gradient and translation velocity. It is apparent from the data that change in cooling rate has no significant effect on f_{coh} , which supports the most recent published rheological/thermal comparisons [10]. Al-15wt%Cu samples were solidified initially at a low cooling rate, increasing step wise and then gradually increased to higher cooling rates. Al-25wt%Cu samples were solidified initially at low cooling rates and gradually decreased. Statistical correlation (r) was performed in the cooling rate/ f_{coh} data and low values (<0.5) were observed for both alloy types suggesting a low degree of linearity between both variables. The coefficient of determination (r^2) for both samples was calculated at approximately 20% again supporting negative interdependence.

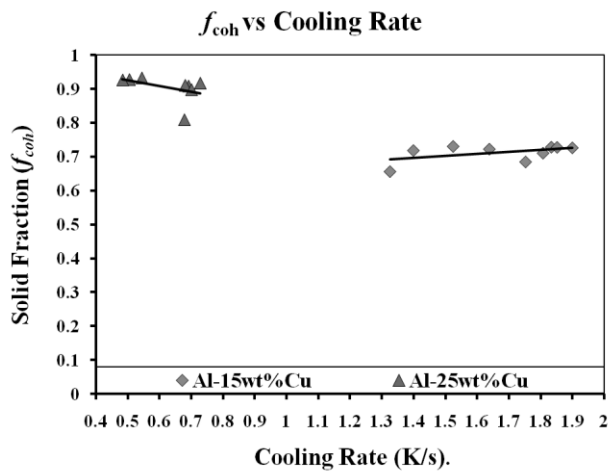


Figure 4. Cooling rate versus coherency fraction solid

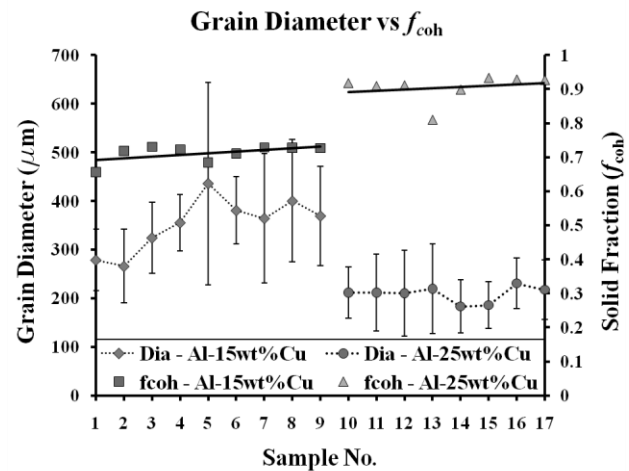


Figure 5. Grain diameter versus coherency fraction solid

Figure 5 shows the relationship between grain size and coherency fraction solid. Larger, and thus more dendritic, grains exhibit lower coherency fraction solid than the smaller cellular-equiaxed structures. This, again, supports previous experimental data as it is suggested smaller more numerous grains, exhibit slower growth thus impingement is delayed, increasing f_{coh} . It is also evident from figure 5 that there is significant deviation in grain size measured in individual coherency envelopes. Solidification sequences show grain nucleation at various locations and times ahead of the coherent network. It has already been suggested that movement of growing solid through the melt changes the local undercooling and composition, affecting subsequent growth. Evidence has also been presented of effects of so called solutal poisoning [19] caused by sedimenting solute ejected from growing grains. The combination of these solidification effects appears to be the cause of the observed grain size deviation. Finally figure 6 shows the so called fullness parameter, f_s , in relation to f_{coh} . It is not expected that this value should show any significant difference in trend however, it is expected to be higher than f_{coh} , as observed. The fullness, equation (2), parameter itself appears to be an appropriate measure of grain morphology, with large highly dendritic grains showing lower fullness and small globular grains exhibiting a large value of fullness.

$$f_s = \frac{V_{GS}}{V_{GE}} \quad (2)$$

Figure 7 shows an example of the differences observed in morphological evolution. In figure 7 (a), a more elongated dendritic growth morphology is observed, with well defined secondary dendrite arm spacings. Figure 7 (b) shows, on average, a more circular and smaller grain size exhibiting the so called equiaxed-cellular morphology. Apparent from figure 7 is the higher granular solid fraction in (b), which stems from smaller grains allowing for more efficient coherent packing ultimately increasing the coherency fraction solid.

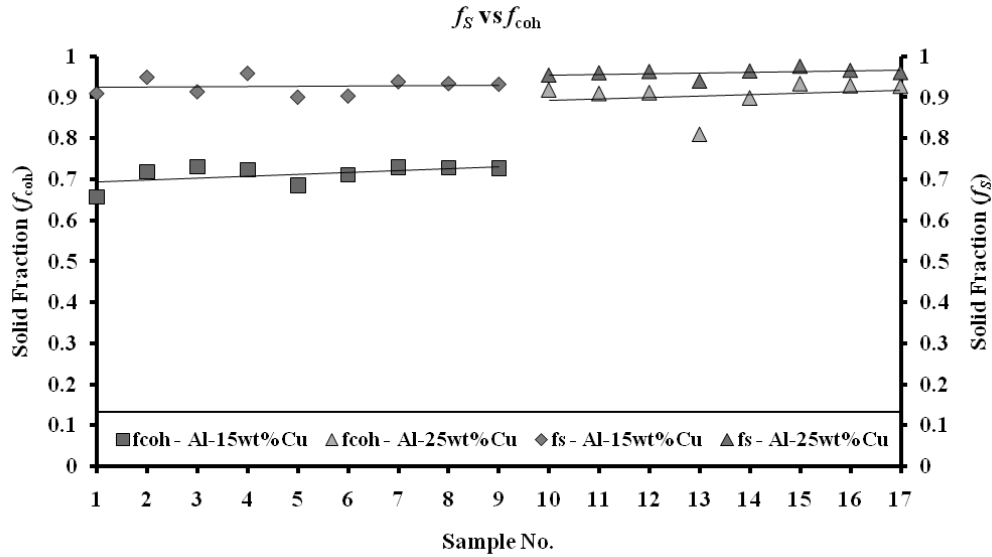


Figure 6. Fullness versus coherency fraction solid

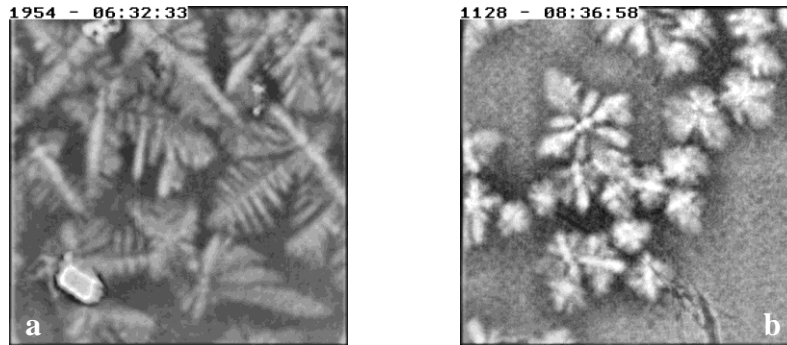


Figure 7. Al-15wt%Cu (a) and Al-25wt%Cu (b) morphological comparison

A first order approximation method of calculating the volume coherency fraction solid is proposed. Assuming the 2D solid fraction can be modeled as a spherical volume of solid proportional to the solid area and 2D coherency envelope can be modeled as a cubic volume element proportional to envelope area, the conversion is derived as follows:

$$V_s = \frac{4}{3\sqrt{\pi}} (A_s)^{3/2} \quad (3)$$

where V_s is the equivalent spherical solid volume based on the total captured solid area, A_s . Similarly V_{EV} , the cubic equivalent coherency envelope is determined using equation (4).

$$V_{EV} = (A_{EV})^{3/2} \quad (4)$$

where A_{EV} is the total area of the defined coherency envelope. The 3D coherency fraction, $f_{coh\ 3D}$, is thus defined as the ratio of V_S to V_{EV} as expressed in equation (5).

$$f_{coh\ 3D} = \frac{V_S}{V_{EV}} \quad (5)$$

Figure 8 shows the newly calculated volume coherency fraction solid for the captured data. As expected these values are consistently lower than the values calculated for equivalent areas however, they are still higher than published data. It should be noted, however, in-situ studies show direct observation of solidification phenomena in real time and there have been significant inconsistencies between rheological and thermal data suggesting deviation may be systematic.

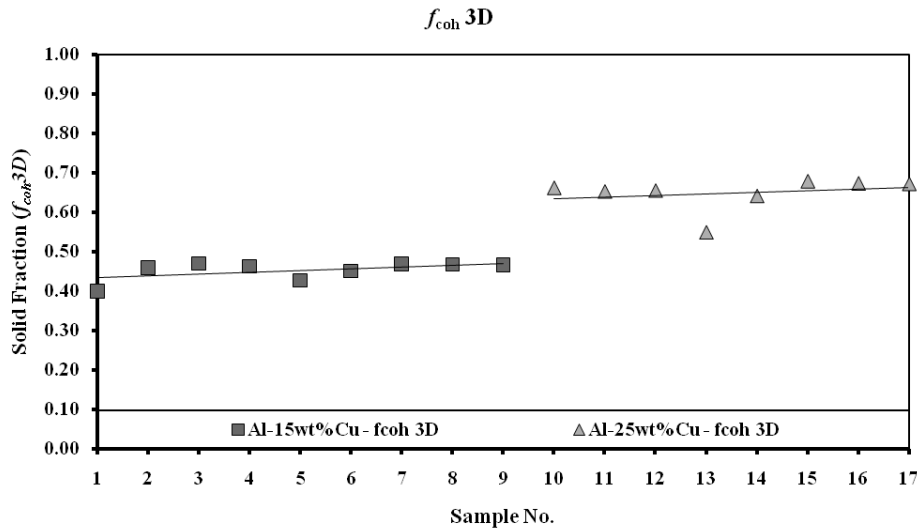


Figure 8. Volume based coherency fraction solid

Conclusions & Future Work

This document presents a preliminary study into the determination of fraction solid at the point of coherency. Qualitative agreement was found between this work and the work of Veldman *et al.* [10] in relation to cooling rate independence and increasing coherency fraction solid with decreasing grain size. It is observed here however, that decreasing grain size follows an increase in solute concentration which contradicts previous work. Previous solute concentrations analyzed however have been limited to low concentration and industrial compositions [6, 8], which may account for the discrepancy. Based on this study, further work is a required with alloy composition more consistent with previous rheological and thermal experimental campaigns in order to make quantitative comparisons. Correlations between coherency fraction solid and other grain attributes, i.e. aspect ratio, grain rotation and grain motion, are proposed for future investigation. The 2D to 3D conversion described here also requires further investigation and definition. The nature of the thin sample has the effect of distorting grain growth, as growth in the plane of the beam is suppressed while grain cross-sections become artificially enlarged. 2D to 3D conversions can therefore result in cumulative errors in predicting volumetric solid fractions. Microgravity experiments are also warranted to determine the significance of thermosolutal convection and buoyancy on coherency fraction solid.

Acknowledgements

The authors wish to acknowledge the financial support of the European Space Agency (ESA) under the PRODEX program, (Contract No. 90392). This work is part of the ESA-MAP (Microgravity Applications Promotion) project XRMON. Also the authors wish to thank Dr. Marco Di Michiel (Exp. Division, ESRF) for his assistance with the experiment, Dr. Shaun McFadden (now at Dublin Institute of Technology, Ireland) and Dr. Paul Schaffer (now at Hydro Aluminium, Norway) for their efforts in capturing the experimental data.

References

1. S. A. Metz and M. C. Flemings, *AFS Trans.*, (78) (1970), 453.
2. J. Claxton, *J. Metal.*, (1975), 14.
3. D. B. Spencer, R. Mehrabian, and M. C. Flemings, *Metallurgical Transactions*, 3 (1972), 1925-1932.
4. D. Brabazon, D. J. Browne, and A. J. Carr, *Materials Science and Engineering: A*, 356 (1-2) (2003), 69-80.
5. L. Backerud and B. Chalmers, *Trans Met Soc AIME*, 245 (2) (1969), 309-318.
6. G. Chai et al., *Metallurgical and Materials Transactions A*, 26 (1995), 965-970.
7. J. Tamminen, *Chem. Comm., Stockholm*, 2 (1988), 8-33.
8. L. Arnberg, G. Chai, and L. Backerud, *Materials Science and Engineering: A*, 173 (1-2) (1993), 101-103.
9. A. K. Dahle and L. Arnberg, *Materials Science and Engineering: A*, 225 (1-2) (1997), 38-46.
10. N. L. M. Veldman et al., *Metallurgical and Materials Transactions A*, 32 (2001), 147-155.
11. I. Dustin and W. Kurz, *Z. Metallkd*, 77 (1986), 265-73.
12. M. Rappaz and P. H. Thevoz, *Acta Metallurgica*, 35 (12) (1987), 2929-2933.
13. R. H. Mathiesen et al., *Physical Review Letters*, 83 (24) (1999), 5062.
14. H. N. Thi et al., *Journal of Physics D: Applied Physics*, 36 (10A) (2003), A83-A86.
15. H. Yasuda et al., *Journal of Crystal Growth*, 262 (1-4) (2004), 645-652.
16. R. H. Mathiesen et al., *Metallurgical and Materials Transactions B*, 33 (4) (2002), 613-623.
17. R. H. Mathiesen and L. Arnberg, *Materials Science and Engineering: A*, 413-414 (2005), 283-287.
18. R. H. Mathiesen and L. Arnberg, *Acta Materialia*, 53 (4) (2005), 947-956.
19. A. Bogno et al., *Transactions of the Indian Institute of Metals*, 62 (4-5) (2009), 427-431.

TRUNCATED DUAL-CAP NUCLEATION SITE DEVELOPMENT

Douglas M. Matson and Paul J. Sander

Tufts University;
Department of Mechanical Engineering;
200 College Avenue; Medford, MA 02155, USA

Keywords: critical nucleus shape, heterogeneous nucleation, mushy-zone

Abstract

During heterogeneous nucleation within a metastable mushy-zone, several geometries for nucleation site development must be considered. Traditional spherical dual cap and crevice models are compared to a truncated dual cap to determine the activation energy and critical cluster growth kinetics in ternary Fe-Cr-Ni steel alloys. Results of activation energy results indicate that nucleation is more probable at grain boundaries within the solid than at the solid-liquid interface.

Introduction

Undercooled hypoeutectic ternary Fe-Cr-Ni steel alloys solidify in a two-step process known as double recalescence [1]. The metastable ferritic bcc-phase forms first with subsequent transformation to the stable austenitic fcc-phase. The delay between these two nucleation events represents the incubation time for the stable phase and this delay is a strong function of melt convection. In classical nucleation theory [12-14], the steady-state nucleation rate, I_s , and time dependent nucleation rate, I , are related by the equations

$$I = I_s \exp \left[-\frac{\tau}{t} \right] \quad \text{for} \quad I_s = I_o \exp \left[-\frac{\Delta G^*}{k_B T} \right] \quad (1)$$

where τ is a characteristic incubation time, t the observed delay time, I_o a pre-exponential factor, ΔG^* the Gibbs free energy for formation of a critical nucleus of n^* atoms of a pure material, and T the transformation temperature. The Boltzmann constant has a value of $k_B = 1.38 \times 10^{-23}$ J/atomK. Steady-state nucleation does not become appreciable until $\Delta G^* > 60 k_B T$ while transient nucleation does not become appreciable until $t \gg \tau$. Turnbull estimated that for condensed phases the incubation time was a function of the size of the cluster and the rate at which atoms cross the interface, β^* , between the surrounding matrix and the cluster [2].

$$\tau = \frac{(n^*)^2}{\beta^*} \quad (2)$$

The attachment rate β^* has variously been related to the jump frequency [2] and the lattice diffusivity [3-5]. By invoking the principle of time reversal, where the statistical fluctuations in cluster size follow the same path during growth and decomposition, Feder *et al* [6] determined the incubation time to be

$$\tau = \frac{-4 k_B T}{\beta^* \left. \frac{\partial^2 (\Delta G)}{\partial n^2} \right|_{n^*}} \quad (3)$$

Russell [7] evaluated condensed phase nucleation for binary systems to account for the influence of solute partitioning and found that clusters approaching the critical size were surrounded by an enriched solute shell, contrary to expectation, and that diffusivity of the slower moving species controls the attachment rate with an interchange frequency β' .

$$\beta' = \frac{x}{a_o^2} \left(\frac{2 D_A D_B}{D_A + D_B} \right) \quad \text{for } x = C_A \left(\frac{A_S}{a_o^2} \right) \quad (4)$$

where x is the number of atoms jumping a jump distance a_o and the subscripts on the diffusivity D represent solute A and solvent B. The number of atoms jumping can be evaluated from the surface concentration C_A , the interface area A_S , and the area per atom. A key finding for multi-component systems is that the rate controlling step for linked flux evaluations is replacement of shell atoms of the controlling species and not the interfacial jump frequency.

In an effort to identify the mechanism for stable-phase nucleation in ternary Fe-Cr-Ni steel alloys, Koseki [1] showed that a dual cap cluster forming within the metastable solid along a bcc-bcc boundary was more probable than (1) homogeneous nucleation of a sphere in the melt, (2) heterogeneous nucleation as a single spherical cap protruding from the bcc-solid and into the melt, (3) heterogeneous nucleation of a spherical cap protruding into the solid, and (4) heterogeneous nucleation of a dual cap along the solid-liquid interface. In these analyses, the time to form a potential nucleation site is taken as zero. Homogeneous nucleation in the melt requires no site development time. Homogeneous nucleation within the solid and heterogeneous nucleation in the form of a spherical cap at the solid-liquid interface requires only that the pre-existing solid exist. Since the solid/liquid interface forms immediately during primary recalescence there is no delay for site formation.

A transient site, such as the solid-solid grain boundary dual cap, is one that forms sometime after primary solidification. Two processes become important in the evaluation of transient site development. First, we must assess how long it takes to form a suitable heterogeneous nucleation site and then, second, we must define how long it takes for a critical nucleus to grow after a suitable site has formed. The sum of these two events determines the incubation period which corresponds to the delay time between primary metastable recalescence and subsequent initiation of the conversion to the stable phase.

Hanlon [8] proposed that fluid drag and dendrite bending can lead to secondary arm collision which will create the required bcc-bcc grain boundary. Matson [9] extended these analysis by showing that nucleation of the stable phase could only occur once a suitable site had formed on,

or in, the pre-existing metastable solid thus explaining how convection can influence predictions using classical nucleation theory. Sites that form due to collision include the bcc-bcc grain boundary and the liquid-filled crevice formed by the intersection of two parallel cylindrical arms. Since the predicted delay time required for cluster growth for both the dual cap and crevice clusters was several orders of magnitude faster than the observed delay, the formation of the grain boundary crevice, and not cluster growth, was identified as the controlling process.

One additional geometry needs to be considered. The current paper looks at the potential for interaction between a dual cap and the liquid due to growth near the grain boundary/liquid interface. Dual cap cluster formation was primarily limited due to diffusion along the grain boundary since diffusion through the solid was sluggish and thus grain boundary diffusion dominated. The activation energy was low due to the favorable low surface/volume ratio. Crevice cluster formation was significantly more rapid due to enhanced diffusion through the surrounding liquid but the activation energy was higher due to an increase in surface/volume. The intersection of a dual cap with the liquid surface combines these processes and must be evaluated to complete the picture. The geometry that forms is known as a truncated dual cap.

Geometry of a truncated dual cap

A dual cap consists of two identical spherical sections with a characteristic intersection angle, 2θ , defined by the relative interfacial free energies, γ . Along the grain boundary mirror plane, equilibrium is maintained if

$$\gamma_{MM} = 2 \gamma_{MS} \cos \theta \quad (5)$$

with subscripts MM for metastable/metastable and MS for metastable/stable. The activation barrier at the critical radius, ΔG^* , is evaluated based on equating surface and volume terms, A and V respectively, at the critical cluster radius r^* where dG/dn goes to zero such that

$$\Delta G^* \Big|_{r^*} = 2 A_{MS} \gamma_{MS} - A_{MM} \gamma_{MM} - V \Delta G_V \quad (6)$$

$$\Delta G_V = \frac{\Delta H \Delta T}{T_m}$$

with ΔH the enthalpy of fusion, ΔT the undercooling set by the melting points of the metastable and stable phases, and T_m the melting point of the stable phase. The area and volume terms are readily evaluated from equations for spherical sections. If we assume typical values for thermophysical properties for steel alloys[9] to be $\gamma_{MM} = 0.468 \text{ J/m}^2$, $\gamma_{ML} = 0.212 \text{ J/m}^2$, $\gamma_{SL} = 0.302 \text{ J/m}^2$, $\Delta G_V = 2.56 \times 10^7 \text{ J/mol}$, $D_{GB} = 1 \times 10^{-10} \text{ m}^2/\text{s}$, $D_S = 1 \times 10^{-14} \text{ m}^2/\text{s}$, $D_L = 3 \times 10^{-9} \text{ m}^2/\text{s}$, and a grain boundary thickness of $t = 5 \text{ \AA}$, then the angle is $2\theta = 41.2^\circ$, the activation barrier is $\Delta G^*/kT = 102$ for a nucleus containing 15000 atoms with a delay time of $\tau = 5.9 \times 10^{-8} \text{ sec}$.

Note that the value for the interfacial free energy between stable and metastable phases is highly speculative given the inability to experimentally define this value. Thus a value of $\gamma_{MS} = 0.250 \text{ J/m}^2$ was selected as representative. Throughout the remainder of this paper, the errors associated with this selection are investigated.

When a dual cap intersects the liquid, the common circular basal surface is truncated. This is shown in Figure 1 where the overall shape of the transformed volume is seen in (a) and each of the three sub-volumes which comprise the shape are visually blown apart in (b). Note that top and bottom represent the converted section of the dual cap within the metastable solid while the pointed ellipsoid extends out into the liquid.

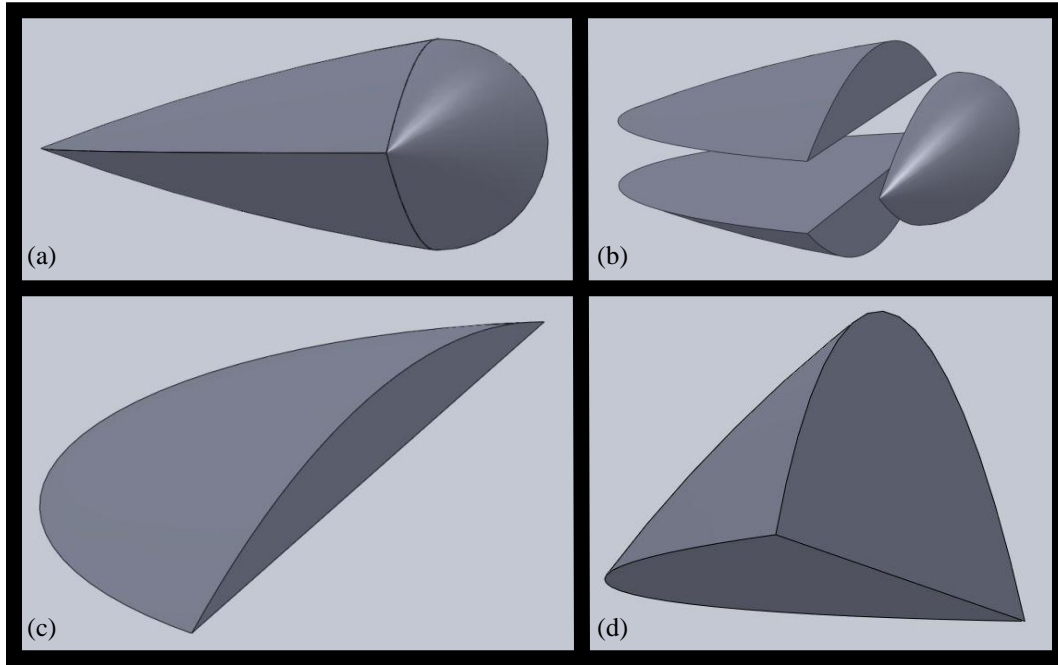


Figure 1. Geometry of a truncated dual cap. (a) overall volume (b) exploded view to show upper and lower truncated cap sections and the ellipsoid protruding out into the liquid (c) truncated cap for typical properties and $\gamma_{MS} = 0.25 \text{ J/m}^2$ (d) truncated cap for typical properties and $\gamma_{MS} = 0.37 \text{ J/m}^2$

In Figure 1 the influence of the value of the interfacial free energy between metastable and stable phases is illustrated where in (c) the interfacial free energy is set at $\gamma_{MS} = 0.25 \text{ J/m}^2$ while in (d) $\gamma_{MS} = 0.37 \text{ J/m}^2$. Of particular interest is the strong influence of the value of the γ_{MS} parameter on the ellipsoid dimensions. As seen in Figure 1(c), at low values the interfacial properties dominate and the point where metastable solid/metastable solid/liquid are in equilibrium is pronounced. In Figure 1(d) the volume properties dominate and the point is less pronounced. This point is of critical concern because at this location surface frustration, a local instability caused by anisotropy of surface tension, causes modeling of the geometry to break down. Isotropic interfacial energies require that the boundary between metastable solid and liquid have the same wetting angle which means that the “ellipsoid” should, in fact, be a spherical cap section with a-axis and b-axis the same. This is certainly not true in (c) but the

geometry comes closer to this shape in (d). Surface frustration is due not only to the elliptical cross-section of this face but also due to the definition of surface angles.

Along the solid/solid interface (left side of the shape) equation 5 is used to define the interior angle 2θ relative to the horizontal mirror plane as before. At the point where the metastable solid-solid boundary intersects the liquid-stable solid boundary (the point in the ellipsoid) the interfacial free energy balance results in the definition of two equations in two unknowns along horizontal and vertical axes

$$\gamma_{LM} = \gamma_{MS} \cos \theta_S + \gamma_{LS} \cos \theta_L \quad (7)$$

$$\gamma_{MS} \sin \theta_S = \gamma_{LS} \sin \theta_L \quad (8)$$

These define the angle the truncated section makes to the vertical, θ_S , and the angle the exterior surface of the ellipsoid makes to the vertical, θ_L . Note that ideally the angle should be identical along the a-axis and b-axis of the ellipsoid but surface frustration makes this not possible due to the required existence of the pointed intersection. To estimate the surface area and volume it was assumed that the shape could be represented by rotating the destroyed metastable solid-liquid interface about the solid-solid line resulting in a shape similar to half a football.

The truncated dual cap and ellipsoid shapes cannot be characterized readily analytically and a graphical approach was used to estimate areas and volumes. Using the predicted characteristic lengths and angles, a model was developed in SolidWorks[®] to evaluate areas and volumes as a function of the interfacial free energy γ_{MS} . Defining the base of the truncated cap as A_{MM} , the front as A_{ML} , the surface as A_{MS} , and the exterior of the ellipsoid as A_{SL} , the activation barrier can be evaluated from

$$\Delta G^*|_{r^*} = 2A_{MS}\gamma_{MS} + A_{SL}\gamma_{SL} - 2A_{ML}\gamma_{ML} - A_{MM}\gamma_{MM} - V\Delta G_v \quad (9)$$

Using typical thermophysical properties presented earlier, $\theta = 41.2^\circ$, $\theta_S = 81.2^\circ$, $\theta_L = 54.9^\circ$, and the ellipsoid has major axis length $a = 19.9 \times 10^{-9}$ m and minor axis length $b = 3.3 \times 10^{-9}$ m. The activation barrier is calculated to be $\Delta G^*/kT = 3315$ for a nucleus containing 156000 atoms with a delay time of $\tau = 2.8 \times 10^{-9}$ sec. The results of calculations of this type for all three mechanisms as defined over the entire range of possible interfacial free energies are presented in Figure 2 and Figure 3.

Discussion

Prediction results show that all three mechanisms are possible but only for low values of the interfacial free energy. At these energies, the shape of both the dual cap and truncated dual cap are thin saucer-shaped volumes due to the small interior angle along the metastable solid grain boundary. The truncated portion thus has a highly anisotropic elliptical shape with major axis to minor axis ratio varying from 11 to around 6 over the range of interfacial free energies investigated. The sensitivity to selection of values for interfacial energies can readily be investigated beyond what has been presented here as part of a larger evaluation of error associated with use of this type of technique. For example, if the value of the interfacial free energy of the metastable solid-solid boundary is reduced from the nominal value of $\gamma_{MM} = 0.468$

J/m^2 to $\gamma_{\text{MM}} = 0.212 \text{ J/m}^2$ (the value for γ_{ML}) then major to minor axis ratio is reduced to around 1.6 and is insensitive to the selection of γ_{MS} . This ratio represents geometries closer to the desired isotropic, circular shape. Note that all interfacial free energy values have a high inherent uncertainty and thus the results should be viewed as indicating trends and not as numerical predictions. Results are ordinal and not cardinal.

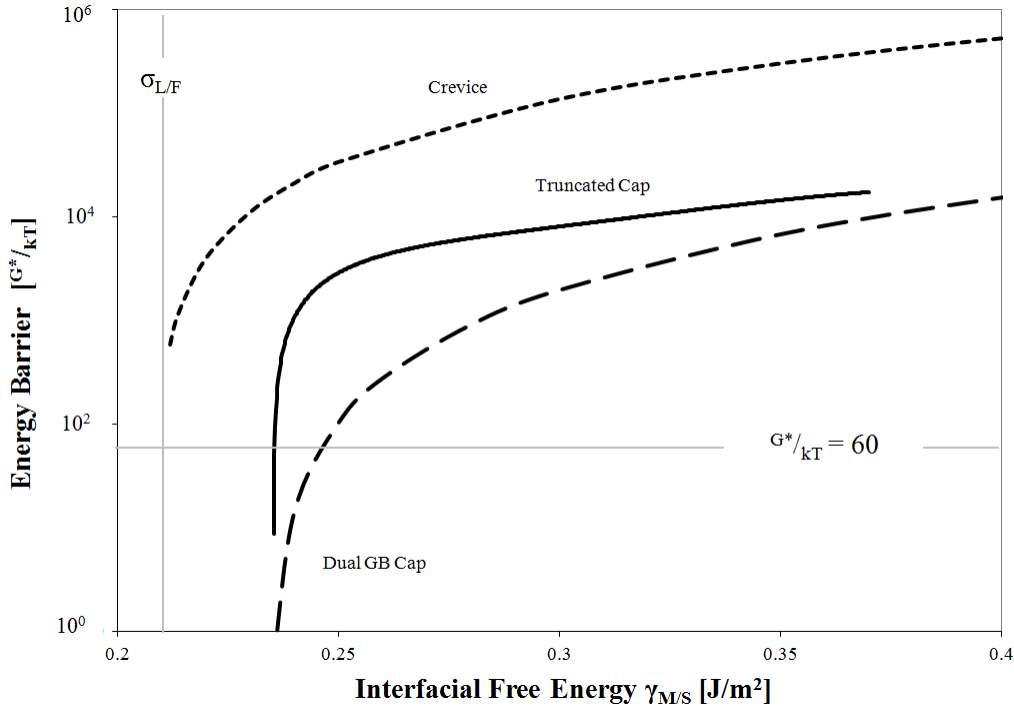


Figure 2. Energy barrier for nucleation of each cluster shape over the range of possible interfacial free energy values.

Figure 2 also clearly shows that the truncated cap geometry does successfully combine elements of both the solid-solid dual cap mechanism and the solid-liquid crevice mechanism. Predictions for the truncated dual cap tend to lie between the extremes calculated for the other two mechanisms however if all were operational this mechanism would dominate since the *fastest possible* mechanism is favored and the truncated cap is kinetically fastest over the entire range, as seen in Figure 3. However, since the energy barrier is higher for the truncated dual cap than for the embedded dual cap it is unlikely to be operative except at interfacial free energies less than a value of around $\gamma_{\text{MS}} = 0.24 \text{ J/m}^2$.

One additional weakness of the approach used to estimate the surface area and volume for the pointed ellipsoid section for this geometry is that in order to obtain a tractable solution for the ellipsoid form, the foot-ball shaped rotation element was selected. This technique was used because SolidWorks[®] can readily generate this shape. Unfortunately, this ignores the calculated angle $\theta_L = 54.9^\circ$ for $\gamma_{\text{MS}} = 0.25 \text{ J/m}^2$ which should be constant along the three-phase interface.

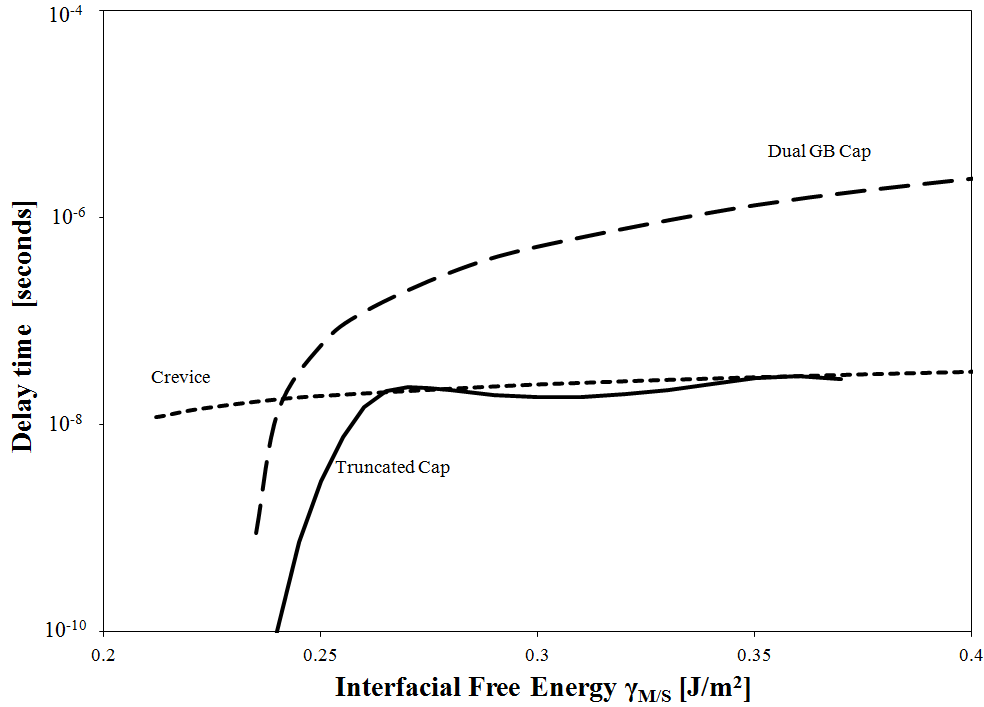


Figure 3. Kinetics of cluster formation for each shape over the range of possible interfacial free energy values.

Note that the rotated shape has a continuously changing surface angle. The extremes occur at the point along the major axis where the angle is $\theta_L^{min} = 18.9^\circ$, and at the top along the minor axis where the angle is $\theta_L^{max} = 90^\circ$. The effect of this change in angle is a continuously changing curvature of the surface which, as previously noted, results in surface frustration. This warping of the ideal geometry also results in a slight overestimation of the surface area and volume – estimated to be on the order of 37% and 58% respectively for these conditions – with the error decreasing because the difference between major and minor axis decreases significantly with increasing γ_{MS} . One interesting result of this surface frustration is that the decreased angle at the point strains the equilibrium at the three-phase junction and creates an additional resistance to cluster formation. This effect is commonly observed by children blowing up a balloon – if a strain is induced along one axis by pinching, the increase in anisotropic surface tension only allows expansion of the balloon along orthogonal axes. Thus for our application there is a strain term which must be added to the free energy balance and growth along the major axis is hindered. The polarity of this term suggests that the resulting activation energy will be greater than anticipated. These observations further strengthen the conclusion that clusters will form along the grain boundary within the metastable solid and not at the intersection of the metastable boundary and the undercooled liquid.

These theories must be validated over a wide range of convection conditions as is only possible through electromagnetic levitation experimentation in microgravity [10].

Summary

Evaluation of the predicted delay times for all mechanisms shows that the incubation time to grow a critical cluster is several magnitudes faster than observed. This supports the theory that, following formation of the metastable array, the controlling kinetic mechanism is formation of a site where nucleation may occur rather than growth of a critical cluster. Evaluation of the energy barrier indicates that over a select and limited range of interfacial free energy values, all of the mechanisms – spherical cap, crevice nucleation, and truncated cap – are possible. However, since the barrier for formation of a truncated cap is greater than that for a dual cap for all interfacial energies evaluated in this study, cluster formation is more likely along a grain boundary within the solid rather than at the intersection of the boundary and the liquid.

Acknowledgements

This project is sponsored by NASA under grants NNX08AL21G and NNX10AV27G. The authors would like to thank the members of the ThermoLAB International Topical Team sponsored by ESA under AO-2009-1020 for valued collaboration.

References

1. T. Koseki and M. C. Flemings, "Solidification of undercooled Fe-Cr-Ni alloys: Part I. Thermal behavior" *Metall. Mater. Trans.* A26[11] (1995) 2991-2999.
2. J. H. Hollomon, D. Turnbull, "Nucleation", *Prog. Met. Phys.* **4**, (1953) 333-338.
3. D. Turnbull, J.C. Fisher, "Rate of nucleation in condensed systems", *J. Chem. Phys.* **17** (1949) 71-73.
4. R. Becker, "Nuclear formation in the separation of metallic mixed crystals" *Anal. Phys.* **32**[1-2] (1938) 128-140.
5. A. Kantrowitz, "Nucleation in very rapid vapor expansions", *J. Chem. Phys.* **19**, (1951) 1097-1100.
6. J. Feder, K. C. Russell, J. Lothe, G. M. Pound, "Homogeneous nucleation of droplets in vapours" *Adv. Phys.* **15** (1966) 111-178.
7. K. C. Russell, "Linked flux analysis of nucleation in condensed phases" *Acta Metall.* **16**, (1968) 761-769.
8. A.B. Hanlon, D.M. Matson, and R.W. Hyers, "Internal Convective Effects on the Lifetime of the Metastable Phase Undercooled Fe-Cr-Ni Alloys," *Philosophical Magazine Letters*, vol. 86, no. 3, (2005), 165-174.
9. D.M. Matson, "Ch 10 – Nucleation within the Mushy-zone", in *Solidification of containerless Undercooled Melts*, D. M. Herlach and D. M. Matson eds., Wiley-VCH, (2012) *in press*.
10. D.M. Matson, R. W. Hyers, T. Volkmann, and H.-J. Fecht, "Phase selection in the mushy zone: LODESTARS and ELFSTONE Programs", *Physics IOP*, Proceedings of *ISPS 2011 Conference*, July 14, 2011, Bad-Godesberg DE, (2011) *in press*.

REPORT DOCUMENTATION PAGE

Form Approved
OMB No. 0704-0188

The public reporting burden for this collection of information is estimated to average 1 hour per response, including the time for reviewing instructions, searching existing data sources, gathering and maintaining the data needed, and completing and reviewing the collection of information. Send comments regarding this burden estimate or any other aspect of this collection of information, including suggestions for reducing this burden, to Department of Defense, Washington Headquarters Services, Directorate for Information Operation and Reports (0704-0188), 1215 Jefferson Davis Highway, Suite 1204, Arlington, VA 22202-4302. Respondents should be aware that notwithstanding any other provision of law, no person shall be subject to any penalty for failing to comply with a collection of information if it does not display a currently valid OMB control number.

PLEASE DO NOT RETURN YOUR FORM TO THE ABOVE ADDRESS.

1. REPORT DATE (DD-MM-YYYY) 01-09-2012			2. REPORT TYPE Conference Publication			3. DATES COVERED (From - To)		
4. TITLE AND SUBTITLE Materials Research in Microgravity 2012						5a. CONTRACT NUMBER		
						5b. GRANT NUMBER		
						5c. PROGRAM ELEMENT NUMBER		
6. AUTHOR(S) R. Hyers, Ed;* V. Bojarevics, Ed;** J. Downey, Ed; H. Henein, Ed;*** D. Matson, Ed;† A. Seidel, Ed;‡ D. Voss, Ed¶ and M. SanSoucie, Compiler						5d. PROJECT NUMBER		
						5e. TASK NUMBER		
						5f. WORK UNIT NUMBER		
7. PERFORMING ORGANIZATION NAME(S) AND ADDRESS(ES) George C. Marshall Space Flight Center Huntsville, AL 35812						8. PERFORMING ORGANIZATION REPORT NUMBER M-1342		
9. SPONSORING/MONITORING AGENCY NAME(S) AND ADDRESS(ES) National Aeronautics and Space Administration Washington, DC 20546-0001						10. SPONSORING/MONITOR'S ACRONYM(S) NASA		
						11. SPONSORING/MONITORING REPORT NUMBER NASA/CP-2012-217466		
12. DISTRIBUTION/AVAILABILITY STATEMENT Unclassified-Unlimited Subject Category 29 Availability: NASA CASI (443-757-5802)								
13. SUPPLEMENTARY NOTES Prepared for the Materials and Processes Laboratory, Engineering Directorate *University of Massachusetts, **University of Greenwich, ***University of Alberta, †Tufts University, ‡EADS Astrium, ¶ESA-ESTEC								
14. ABSTRACT Reducing gravitational effects such as thermal and solutal buoyancy enables investigation of a large range of different phenomena in materials science. The Symposium on Materials Research in Microgravity involved 6 sessions composed of 39 presentations and 14 posters with contributions from more than 14 countries. The sessions concentrated on four different categories of topics related to ongoing reduced-gravity research. Highlights from this symposium will be featured in the September 2012 issue of JOM. The TMS Materials Processing and Manufacturing Division, Process Technology and Modeling Committee and Solidification Committee sponsored the symposium.								
15. SUBJECT TERMS materials science, microgravity, modeling, thermophysical properties, combustion, sintering, phase transformations, solidification								
16. SECURITY CLASSIFICATION OF:			17. LIMITATION OF ABSTRACT		18. NUMBER OF PAGES		19a. NAME OF RESPONSIBLE PERSON	
a. REPORT	b. ABSTRACT	c. THIS PAGE	UU		212		STI Help Desk at email: help@sti.nasa.gov	
U	U	U					19b. TELEPHONE NUMBER (Include area code) STI Help Desk at: 443-757-5802	

National Aeronautics and
Space Administration
IS20
George C. Marshall Space Flight Center
Huntsville, Alabama 35812
